Swansea University
Prifysgol Abertawe

Cronfa
Setting Research Free

Swansea University E-Theses

The relationship between the microstructure and corrosion resistance of Galfan coated steels.

Elvins, Jonathon

How to cite:

Elvins, Jonathon (2005) *The relationship between the microstructure and corrosion resistance of Galfan coated steels..* thesis, Swansea University.
http://cronfa.swan.ac.uk/Record/cronfa43202

Use policy:

This item is brought to you by Swansea University. Any person downloading material is agreeing to abide by the terms of the repository licence: copies of full text items may be used or reproduced in any format or medium, without prior permission for personal research or study, educational or non-commercial purposes only. The copyright for any work remains with the original author unless otherwise specified. The full-text must not be sold in any format or medium without the formal permission of the copyright holder. Permission for multiple reproductions should be obtained from the original author.

Authors are personally responsible for adhering to copyright and publisher restrictions when uploading content to the repository.

Please link to the metadata record in the Swansea University repository, Cronfa (link given in the citation reference above.)

http://www.swansea.ac.uk/library/researchsupport/ris-support/

THE RELATIONSHIP BETWEEN THE MICROSTRUCTURE AND CORROSION RESISTANCE OF GALFAN COATED STEELS

Submitted for the degree of Engineering Doctorate (EngD)

Jonathon Elvins

EPSRC Engineering Doctorate Centre for Steel Technolgy, Wales
University of Wales Swansea

ProQuest Number: 10821594

All rights reserved

INFORMATION TO ALL USERS
The quality of this reproduction is dependent upon the quality of the copy submitted.

In the unlikely event that the author did not send a complete manuscript
and there are missing pages, these will be noted. Also, if material had to be removed,
a note will indicate the deletion.

ProQuest 10821594

Published by ProQuest LLC (2018). Copyright of the Dissertation is held by the Author.

All rights reserved.
This work is protected against unauthorized copying under Title 17, United States Code
Microform Edition © ProQuest LLC.

ProQuest LLC.
789 East Eisenhower Parkway
P.O. Box 1346
Ann Arbor, MI 48106 – 1346

UNIVER
LIBRARY
WALES SWANSEA

Declaration/Statements page to be included in Higher Degree Theses.

DECLARATION

This work has not previously been accepted in substance for any degree and is not being concurrently submitted in candidature for any degree.

Signed...(candidate)

Date..21/7/05...................................

STATEMENT 1

This thesis is the result of my own investigations, except where otherwise stated.

Other sources are acknowledged by footnotes giving explicit references. A bibliography is appended.

Signed .(candidate)

Date..21/7/05..........................

STATEMENT 2

I hereby give consent for my thesis, if accepted, to be available for photocopying and for inter-library load, and for the title and summary to be made available to outside organisations.

Signed..(candidate)

Date..

NB: *Candidates on whose behalf a bar on access has been approved by the University (see Appendix 2), should use the following version of Statement3:*

I hereby give consent for my thesis, if accepted, to be available for photocopying and for inter-library loans **after expiry of a bar on access approved by the University of Wales on the special recommendation of the Constituent Institution/University College.**

Signed . ...(candidate)

Date..21/7/05..........................

ACKNOWLEDGEMENTS

Well after such a long time there are so many people to thank for the truly great support I have received. A huge thanks to my family without whom none of this would be possible. Thanks to Sam (you have the patience of a saint!), Mum, Dad and Deb for all the support, encouragement and general willing to put up with a cranky so and so for the final few months of .... well torture! I am in debt to one and all.

Thanks also to my friends who have been there along the way (and also to those I have met along the way). Special appreciation to Chris, Cullen & Dom, to the guys and gals in my year and to those who have arrived and departed from the world famous corrosion group. At this point I would also like to mention Geraint for continued knowledge input and Pete for his expertise in all photographic.

To my support from Corus I send many thanks. The two Dave's at Shotton, Alan, Joh, Vernon and Mr. Simulator, John Demmel. The support was excellent and much appreciated.

Finally I would like to say a special thanks to Dave and John who have been there every step of the way. I could not have asked for finer support and guidance.

Well it's not possible to end on song... so as the lights go down on my University career, Ladies and Gentlemen...

Elvins has left the building.

Thankyou all

Jon

Abstract

The drivers for the work detailed within this thesis are twofold. Firstly the overwhelming goal of the project was to determine if a relationship existed between the microstructure of the Galfan galvanising coating and the subsequent corrosion protection it provided to the steel substrate. The secondary driver was to act upon the information obtained and improve the corrosion resistance by variations in chemistry or altering the processing conditions. To this end a novel method for quantifying Galfan microstructure was developed and used in conjunction with the Scanning Vibrating Electrode Technique (SVET) to measure the performance of a series of Galfan Coatings. A combination of samples produced at Corus Colors, Shotton and samples produced using a Rhesca Hot Dip Simulator were used to complete the studies.

Initial work was undertaken using line produced samples from the original British Steel Galfan trials. The microstructural analysis of these samples revealed variations in the volume percentage of primary zinc, along with significant variations in primary zinc dendrite number and size. SVET testing was performed along the cut edge of these organically coated samples. Analysis of these experiments revealed a linear trend such that increasing the volume percentage of primary zinc led to an increase the SVET recorded zinc loss. Combining this data with zinc runoff and organic coating delamination data from external weathering experiments, revealed that the SVET is a versatile tool by being able to indicate zinc runoff levels and consequently providing limited accelerated weathering data.

The affect of variations in processing cooling rates were subsequently investigated. Here, by increasing the power of the cooling rig solidifying the coating, the nucleation of both the primary phase and the eutectic was increased. In this

circumstance the volume percentage of primary zinc remained constant. However, the increased nucleation led to an increased number of smaller primary zinc crystals and smaller eutectic cell sizes in the fast cooled samples. SVET analysis revealed that the corrosion occurring on the cut edges of the fast cooled samples was significantly lower than that on the slow cooled samples. This was ascribed to an increase in 'long life' anodes in the slow cooled samples corroding at a faster rate. The increase in nucleation of the eutectic cells meant that a greater length of depressed eutectic boundary was formed. Since the corrosion was found to be localised within this boundary, the greater length in the fast cooled samples led to greater zinc losses.

As a drive towards cost reduction, experiments were undertaken on samples of reduced coating weight. Here it was found that the number and size (area) of the primary zinc dendrites remained the same in all samples. However, due to reducing the thickness of the coating, the relative volume percentage of primary zinc was increased as the coating weight was reduced. This coating reduction also exposed primary zinc on the coating surface of the thinner coatings. SVET analysis on both the cut edge and surface showed that reducing the coating weight, increased the amount of zinc loss recorded in both areas.

The addition of Mg to the Zn-Al alloy induced a microstructural change leading to an increase in the volume percentage of primary zinc with increasing Mg content. An increase in dendrite number was also observed. The SVET data again showed an increase in corrosive activity with increasing amounts of primary zinc. Across the surface, low level Mg additions initially reduced the corrosion rate but as the Mg content increased a secondary corrosion mechanism became dominant and increased the corrosion observed.

Contents

Chapter 1: Introduction and Literature review

Chapter 2: Experimental Methods

Chapter 3: Short term predictive testing for cut edge corrosion resistance in zinc aluminium alloy galvanised steels

Chapter 4: Influence of cooling rates on the microstructure and corrosion resistance of Galfan coated steels

Chapter 5: Influence of coating weight on the microstructure and corrosion resistance of Galfan coated steels

Chapter 6: The influence of Mg on the microstructure and corrosion resistance of Galfan coatings

Chapter 7: Conclusions and future Work

1.0 Introduction

The perfect partnership® of HPS200® and Celestia® (see section 1.3 for descriptions) has been the flag ship for Corus Colors for a number of years. Both products are organically coated steel (OCS) systems designed for use in the construction and cladding sector. Examples of use of these products are shown in figure 1.1. In order to keep ahead of the competition, the continuous redevelopment and improvement of these products is essential and, hence, this body of work focuses upon the development of a component common to both products, the metallic galvanising layer Galfan.

The construction and cladding industry accounts for ~73% of the European strip steel consumption with Corus being the second biggest OCS producer in Europe and the seventh biggest in the world.

Corus Colors produce 1 million tonnes of OCS products each year. Of this figure 10% is HPS200 ® product and from these figures it is evident why the continued development of these products is a priority – not only to keep ahead of the competition but to reassure the existing customers.

1.1 Organically coated steels (OCS)

Organically coated steels are widely used within the construction industry. A typical OCS product is a composite of a number of layers each providing key elements which contribute to the overall system. A typical breakdown of an OCS system is shown in figure 1.2. For the construction sector a standard mild steel substrate is generally used. Depending upon application (roofing or wall cladding) the

Figure 1.1 – Organically Coated Steels in operation

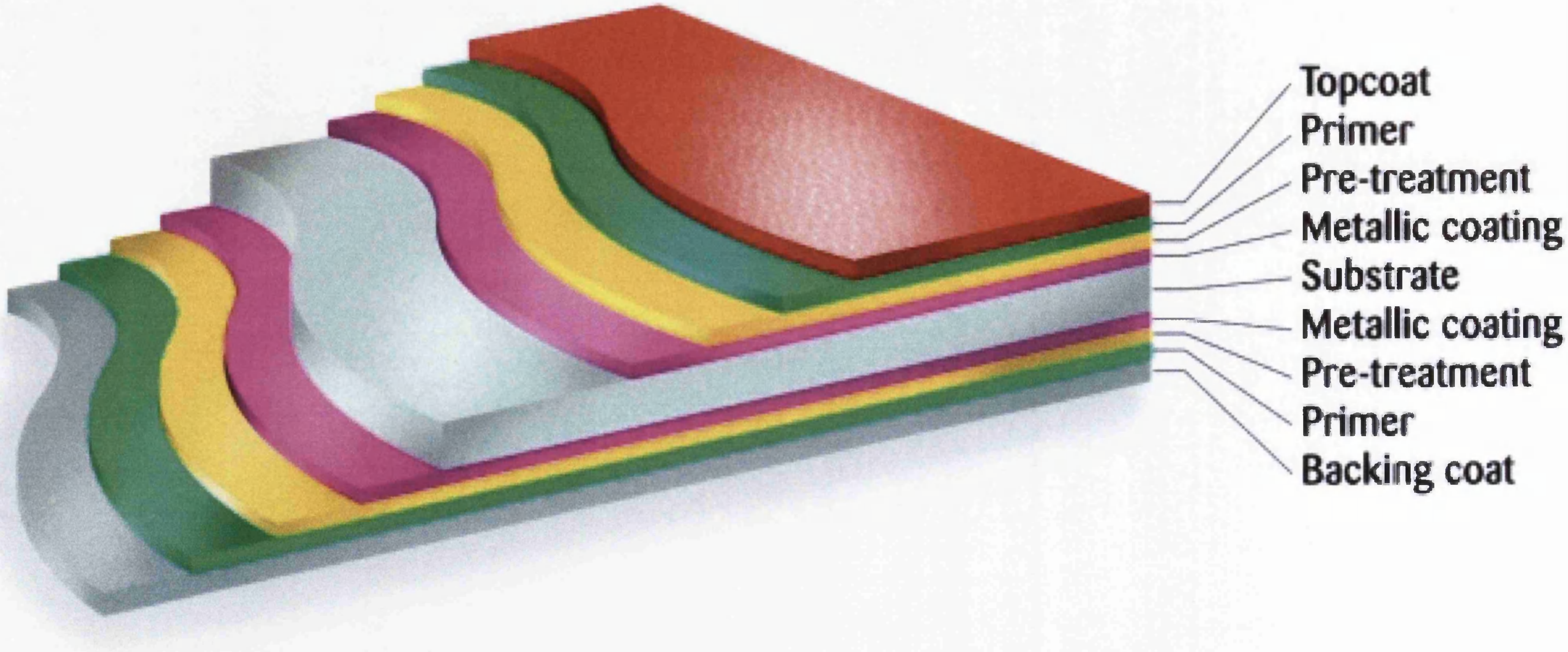

Figure 1.2 – Schematic of Organically Coated Steel product

steel substrate is typically 0.55mm – 0.7mm in gauge providing a number of key properties vital for producing a stable yet cost effective structure. On top of this steel substrate a zinc or zinc – aluminium alloy metallic layer is adhered. This coating, the focus of the current research, is a galvanising layer used to sacrificially protect the base steel substrate. A more in depth consideration of this coating is discussed later (section 1.4). On top of the galvanising layer is the pre-treatment layer. This latter layer, typically a few microns in thickness, serves two functions. Firstly it provides a layer onto which the succeeding coatings can readily adhere and secondly provides corrosion protection due to the chromates contained within it. Above the pre-treatment layer is the primer layer. The primary function of this layer is corrosion protection which it provides via corrosion inhibiting pigmentation. The thickest layer (between 100-200μm) is the top coat. This layer provides the aesthetics for the product, and also provides barrier protection by restricting the ingress of water. OCS products are coated on both sides of the steel. Typically the products reverse side contains the aforementioned pre-treatment and primer layers but is topped with a thin (typically 15μm) organic coating to provide barrier protection and rudimentary aesthetics.

1.2 Production of galvanised and OCS steels

The easiest and oldest method of applying a zinc or zinc alloy coating to strip steel is via the hot dipping process. To achieve the desired goal, dedicated lines have been developed to ensure optimum processing conditions are achieved in the safest manner possible.

The hot dip process is universally standard (in design and layout as opposed to processing conditions) and as such, the description below can be ascribed to any line used for these processes. A typical galvanising bath is shown in figure 1.3. The process is a continuous process with typical line speeds approaching 200m/min in which the strip steel is passed through a molten zinc bath to allow the coating to occur.

The galvanising process is typically split into three regions; the entry section, the coating section and the exit section. Upon receiving the strip steel (as a coil) it is attached to the tail end of the previous coil by means of a laser welder. It is essential that the steel is chemically clean before entering the galvanising bath otherwise the molten zinc layer will not adhere to the surface. Hence the strip is initially cleaned using an acid or alkaline solution, rinsed and then pickled at room temperature (using 15% HCl) to remove scale build-ups. Subsequently, the strip is passed into a direct fired non-oxygen furnace[1]. Within this furnace a carbon monoxide rich flame is directed at the strip to remove any remaining oxides thus preparing the strip for the coating process. Before immersion into the bath, the strip is heated to a temperature around 470°C ensuring optimum wettability of the zinc or zinc alloy coating. Upon passing through the galvanising bath the coating adheres to the steel via diffusion of atoms between the substrate and molten alloy forming an inter-metallic[2] layer which provides the bond between the substrate and the coating. Exiting the bath the coating weight is controlled by high pressure, low volume air knives set at a required distance from the strip. Varying this distance results in different coating thicknesses. The coated steel will then pass through a cooling rig (shown in figure 1.4) to solidify the coating at a rate controlled by the line operators. The coated strip is then water

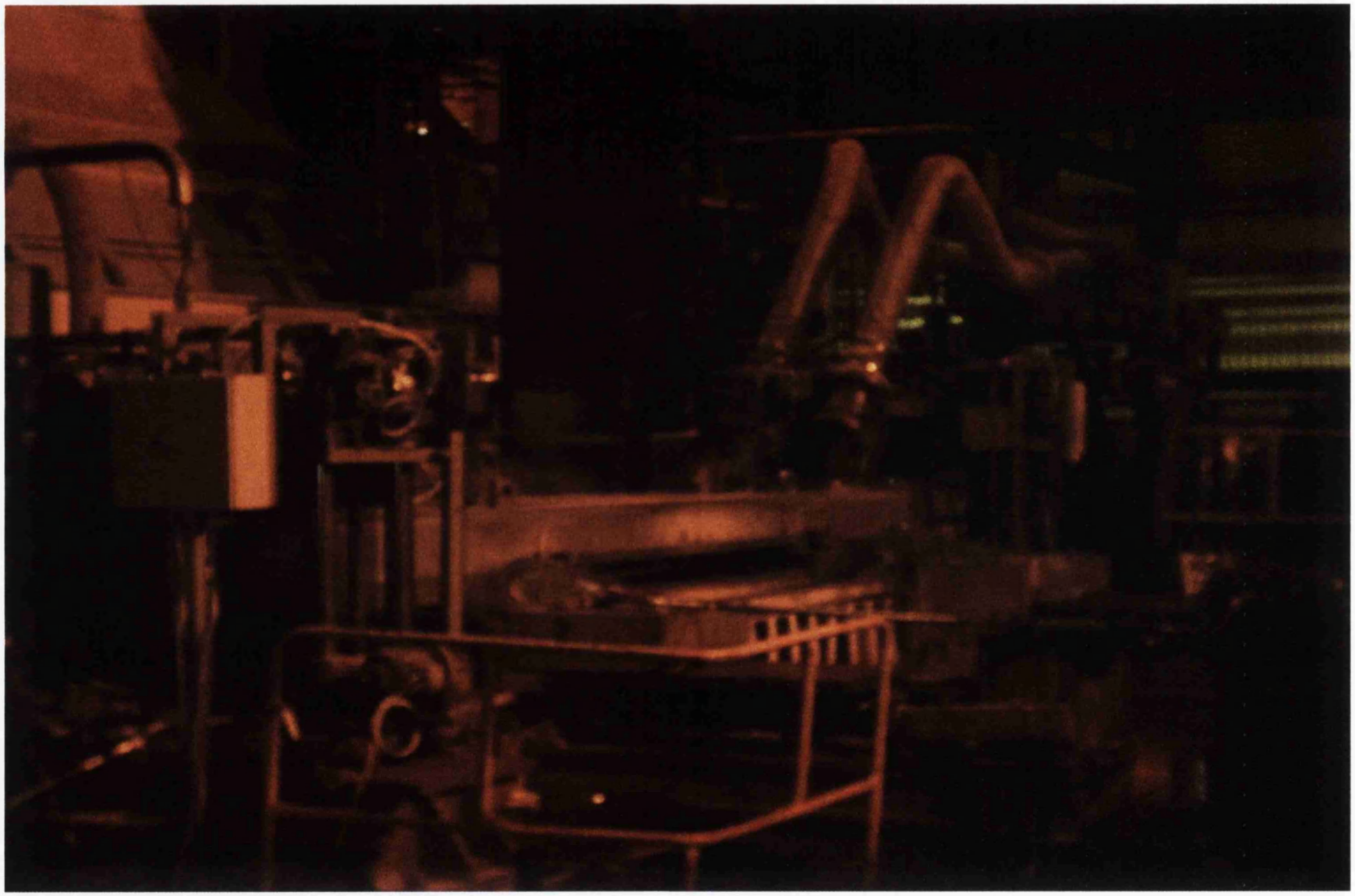

Figure 1.3 – Typical galvanising bath – Corus Colors, Shotton

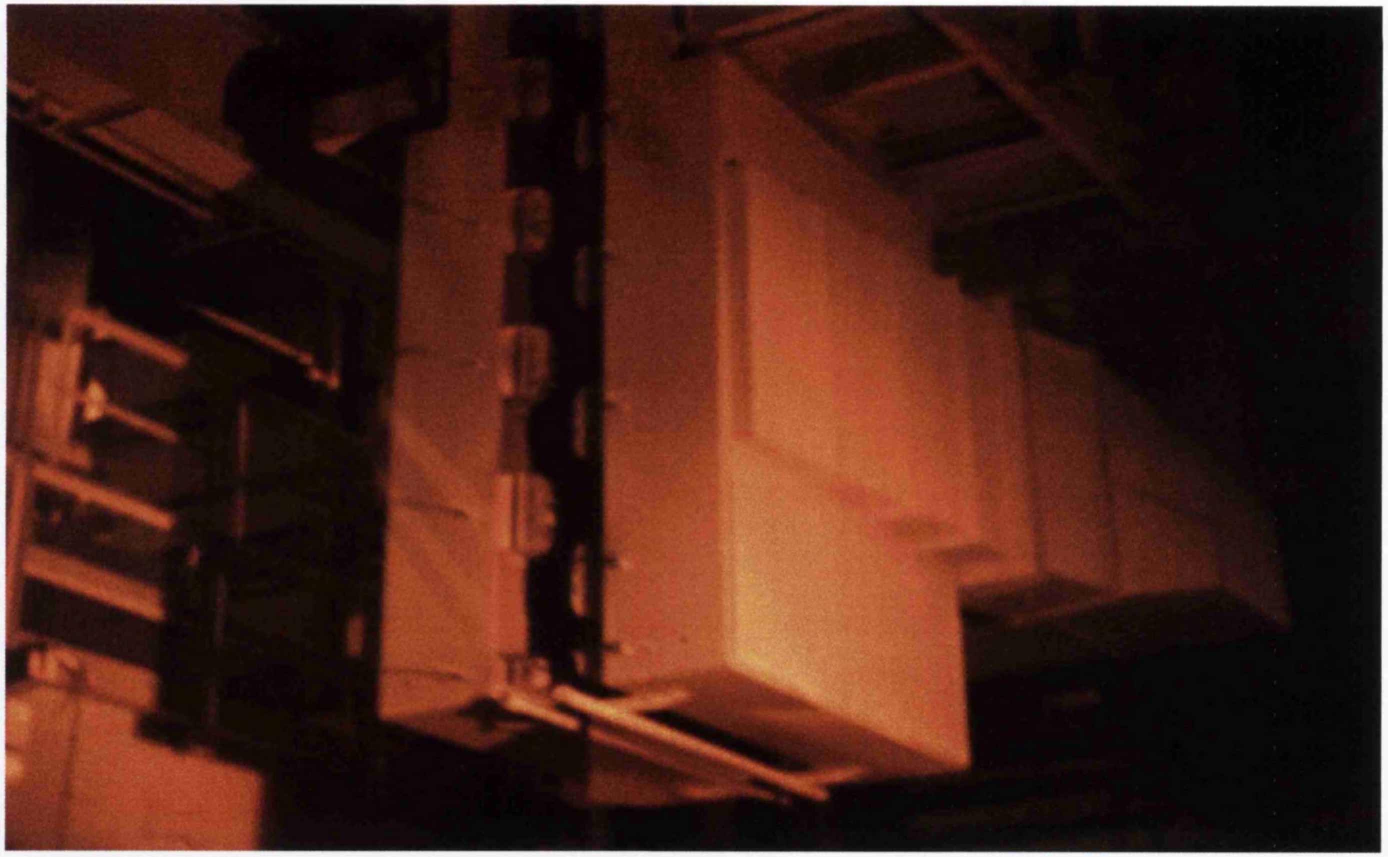

Figure 1.4 – Typical galvanised coating cooling rig – Corus Colors, Shotton

quenched to 30°C and passed through a bridle to homogenise the tension within the strip. A thin chromate passivation layer is frequently added to allow further processing before the strip is re-coiled and dispatched to the required processing line. In certain cases the coating can be temper rolled to give a smoother finish.

1.3 Production of organically coated steels

Similar to the galvanising process, the coating process of steels with organic coatings is again split into three zones: Entry, process and exit.

At the entry point, the lead end of the strip is stitched to the tail end of the previous strip. To ensure complete adhesion of the organic layer to the galvanised strip the surface must be chemically clean. Hence the strip will pass through two cleaning zones, the first being a heated alkaline solution and the second where an inorganic coating (~10-60nm) is applied and then subsequently rinsed in chromic acid. This completes the pre-treatment. The strip will then pass through the prime heads. These are rollers used to apply the primer coating which is typically an epoxy, acrylic or polyester based paint of thickness ~5μm. The primer layer provides two functions, firstly easier adhesion for the main coating and, secondly, corrosion resistance by strontium chromate corrosion inhibitors. The product will then pass through the primer ovens and cooling region and into the main coating house. Here the coating depends upon the product required. For a HPS200 product, a 200μm PVC top coat and a 15μm Polyester backing coat are applied simultaneously using a three head coating system on both sides. For the Celestia product a 100μm modified PVC top coat is applied, again with a 15μm Polyester backing coat. Typical curing temperatures (peak metal temperatures) approach 240°C for these products. A range of embosses can then be applied to provide aesthetics and in use identification. A schematic of the OCS line is shown in figure 1.5

1.4 Galvanising coatings

Several galvanised coatings are used for OCS all with different compositions. The main difference is the aluminium content with Galvatite (0.15% Al) < Galfan (5% Al) < Galvalume (55% Al). These are described below.

1.4.1. Galvatite

The Galvatite (GI) (see figure 1.6) coating is considered to be the base standard for galvanising coatings. Having a composition of 99.85% Zn and ~ 0.15% Al this coating is extremely effective at sacrificially protecting the base steel substrate. A pure zinc coating has low formability due to reaction diffusion, which results in the formation of a range of Fe/ Zn inter-metallics between the substrate and the coating during the galvanising process. However, it was discovered that this formation could be controlled via the addition of Al (forming a $Fe_2(Al, Zn)_5$ inter-metallic which is very thin and ultimately more formable. The addition of Al also serves to improve the aesthetics of the coating[3] due to oxide formation on the coating surface. The structural appearance of Galvatite is that of 'spangles'. These are grains resulting from individual nucleation events which grow to form the coating. The spangle size is related to cooling conditions (or the addition of grain refiners such as zinc dust) where increasing the cooling rate (or more dust) increases nucleation and subsequently reduces the grain size.

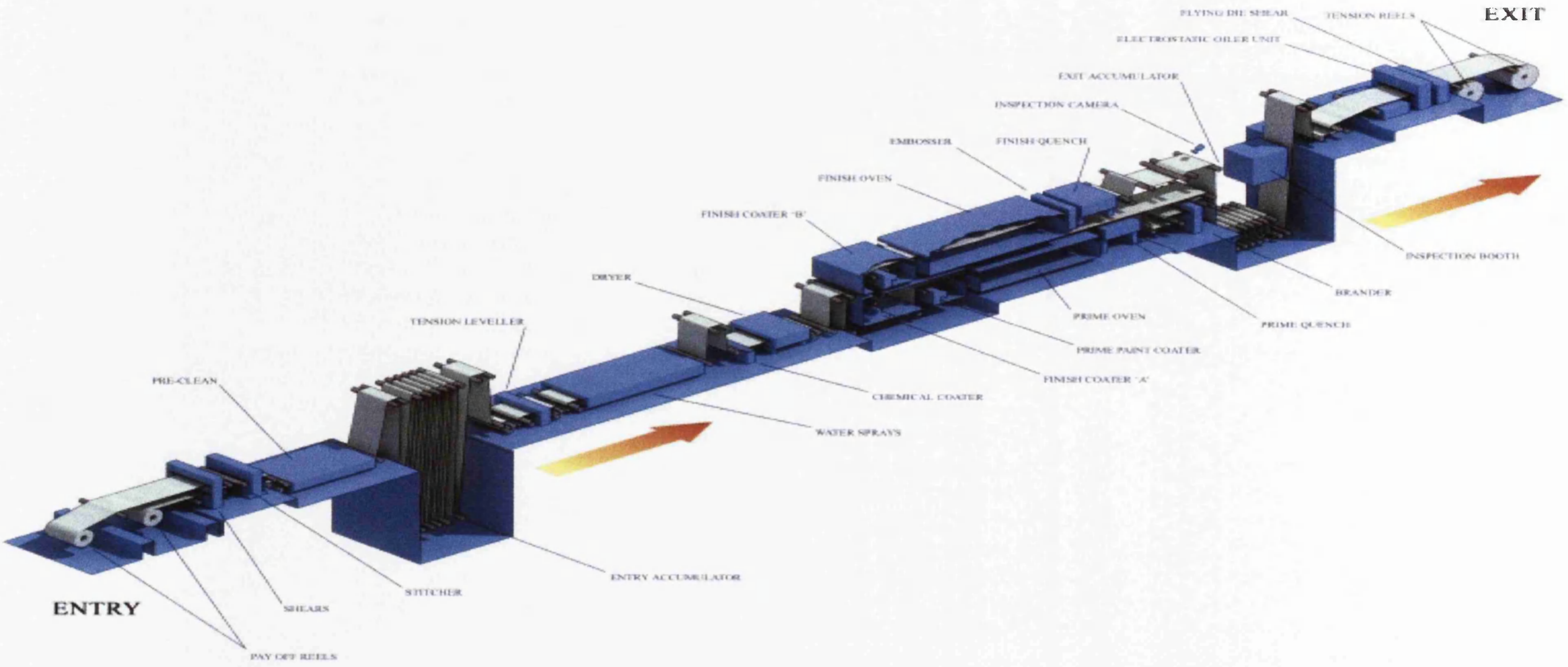

Figure 1.5 – Schematic of typical Organic coating line

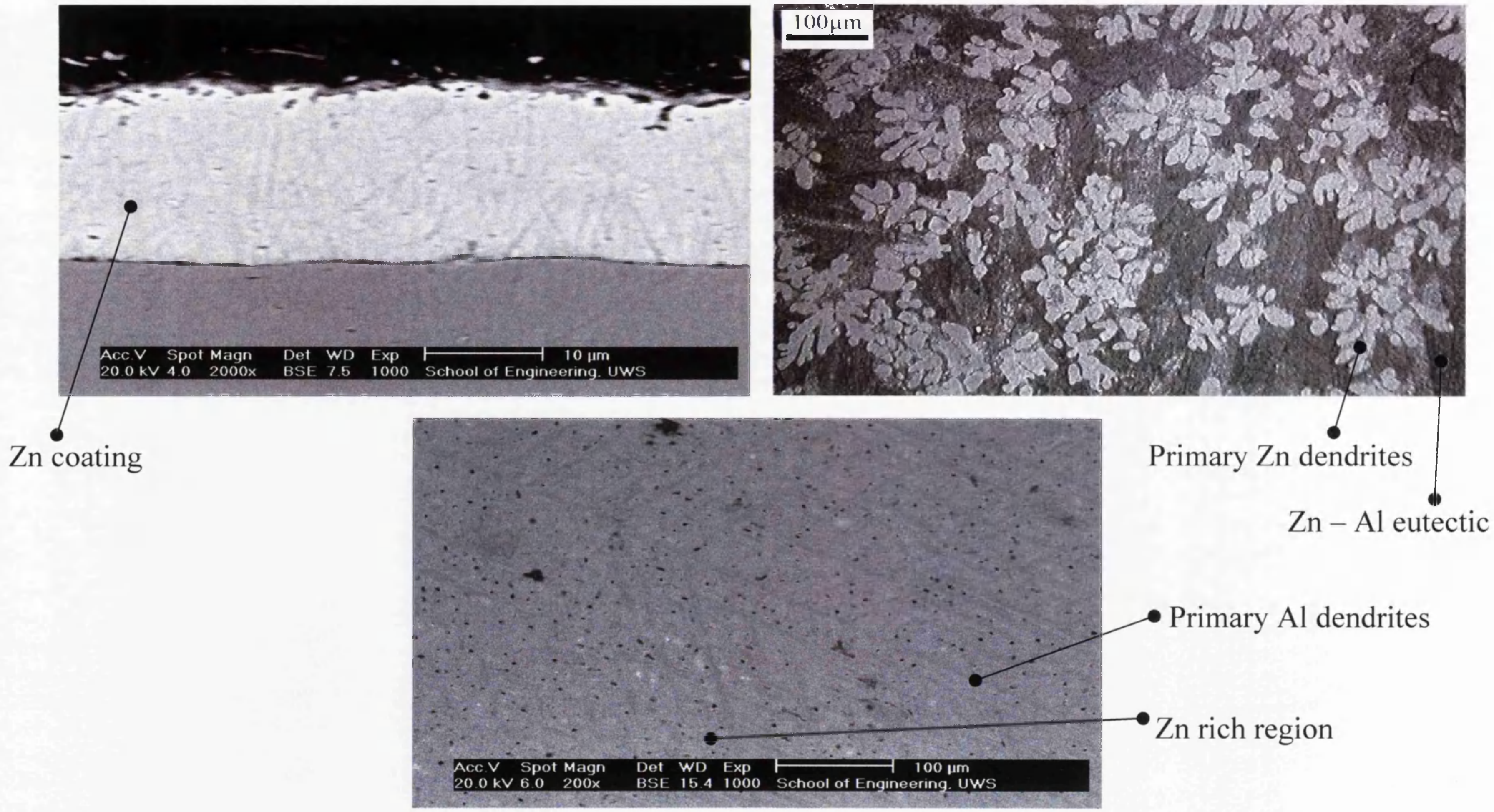

Figure 1.6 – The microstructures of Galvatite, Galfan and Galvalume

1.4.2. Galfan

Galfan is a galvanising metallic coating applied to a steel substrate with a composition generally of 95.5% Zn – 4.5%Al, the significance of which is that 4.5% Al is the eutectic point of the Zn-Al binary eutectic system. The eutectic point of two alloyed metals is a unique temperature and under equilibrium conditions this is the temperature at which the alloy will completely freeze. Under non-equilibrium conditions solidification will occur below this point (i.e. there is a degree of under cooling).

The microstructure of a Zn – Al off-eutectic Galfan (<5% Al) is a two phase microstructure consisting of primary zinc solid solution dendrites with are encased by a Zn – Al lamellar eutectic (or rod eutectic). The fineness of the microstructure (i.e. the size and number of dendrites and the inter-lamellar spacing) is dependent upon the cooling rates during solidification and becomes wholly eutectic when fast cooled[4] (>20°C/s).

Once solidified, Galfan forms a coating which has been shown to be extremely formable and considerably less susceptible to cracking[5,6] than conventional galvanised coatings.

The increased formability has been ascribed to the inherent ductility of the eutectic structure which constitutes the bulk of the coating. Galfan also displays a superior cut edge and surface corrosion resistance to traditional galvanising coatings. Subjected to accelerated corrosion testing, painted scribed panels with 4.5% aluminium galvanising layers show superior corrosion resistance[7] generally displaying two to three times the performance of conventional coated galvanised steel sheet. The unique microstructure of the Zn/Al alloy coating is the reason for its increased corrosion resistance. The zinc/aluminium eutectic retains the cathodic protection capability seen in pure zinc coatings but demonstrates a better intrinsic corrosion resistance due to the development of an adherent aluminium oxide layer over exposed areas[8]. The corrosion of this coating is dealt with in more detail in section 1.23. Typical micrographs of the Galfan coating are shown in figure 1.6

1.4.3 Galvalume

Galvalume coatings are typically comprised of 55% Al, 43.5 % Zn and 1.5% Si[9,10] (Figure 1.6). Si is added to the melt to control inter-metallic formation, as with Al in the Galvatite coating.

When solidified the Galvalume coating forms a microstructure of Al dendrites which are encased in Zn-rich inter-dendritic eutectic regions and a fine dispersion of Si particles. Galvalume displays enhanced corrosion protection over all other forms of galvanising coating. This is due to the unique corrosion mechanism associated with this structure. Initially corrosion is focused upon the zinc rich region (which is the minor constituent) and this continues until a build up of corrosion products form a passive layer preventing further attack. As this constituent is depleted the corrosion protection is increased via the Al rich dendrites through an oxide/ hydroxide method commonly associated with Al alloys[11]. Hence Galvalume gives enhanced corrosion protection but at a significantly increased production cost. However Galvalume coatings are not as ductile as Galfan coatings, due to the Si particles and the increased porosity.

As with Galfan, Galvalume coatings are commonly used within the construction and cladding sector, most specifically in the Australasian market.

1.5 Equilibrium solidification of alloys in the Zn – Al binary system.

Under equilibrium conditions the solidification of a Zinc – Aluminium binary alloy is simple to follow. Considering a hypereutectic alloy (less than 5% Al) of composition, Co, the solidification can be followed on the equilibrium phase diagram shown in figure 1.7.

Above the liquidus the binary alloy is completely liquid. On cooling, at the liquidus temperature, pro-eutectic zinc solid solution, β, crystals are nucleated. As they grow the remaining liquid becomes richer in Al. At the eutectic temperature (382°C) the alloy will be of eutectic composition and the eutectic reaction will occur transforming the remaining liquid into a Zn (β) – Al (α') eutectic (differing from α by a change in composition).

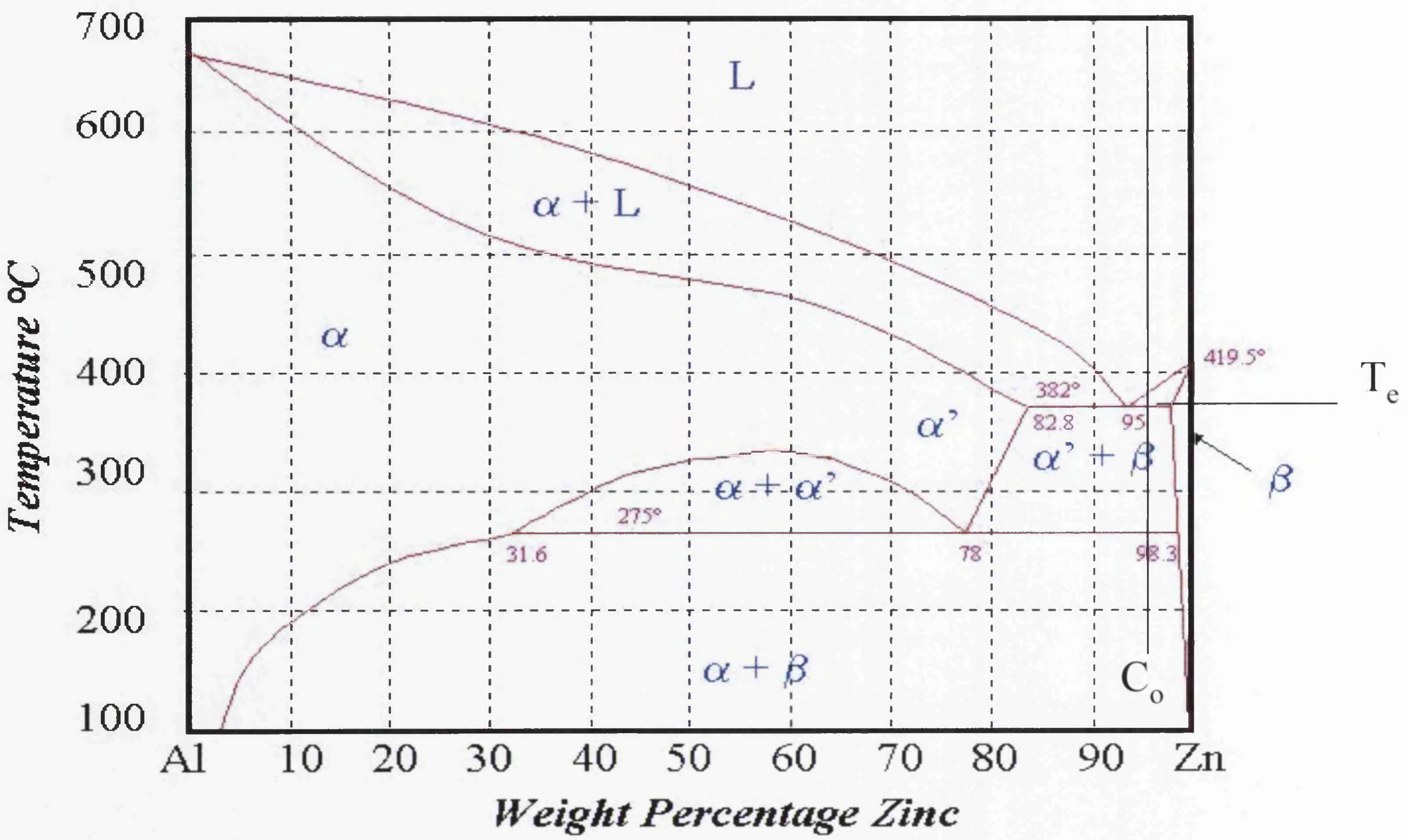

Figure 1.7 – The Zn – Al equilibrium phase diagram

1.6 Classical heterogeneous nucleation theory for a pure metal

The removal of latent heat from the metal leads to a change in state from liquid to a solid. This process, solidification, under non-equilibrium conditions will occur just below the equilibrium freezing (or melting) temperature T_e. The process of solidification dramatically alters the arrangement of atoms from short-range order (i.e. atoms in the local region appearing ordered) to long-range order where the atoms appear in regular unit cells as a crystal structure. The solidification process requires two stages: the nucleation of solid from the base liquid metal, and then growth when the remaining liquid atoms attach to the nuclei to form the long range crystal structure.

The driving force for solidification is the difference in free energy between the liquid and the solid state. The transformation from the liquid to solid is accompanied by a decrease in the free energy, and this provides the aforementioned driving force. The magnitude of the energy change is expressed as:

$$\Delta G = \Delta H - T\,\Delta S \qquad (1.1)$$

Where:

ΔG = change in free energy = $G_{liquid} - G_{solid}$

ΔH = change in enthalpy = $H_{liquid} - H_{solid}$

ΔS = change in entropy = $S_{liquid} - S_{solid}$

T = Temperature (K)

At T_e, $\Delta G = 0$, the latent heat (L) = ΔH and therefore:

$$\Delta G = \Delta H - T_e\,\Delta S = 0$$

Rearranging:

$$\Delta S = \frac{L}{T_e} \tag{1.2}$$

For small undercoolings (ΔT) combining equations 1.1 and 1.2

$$\Delta G_v \approx \frac{L\,\Delta T}{T_e} \tag{1.3}$$

Where:

ΔG_v = Free energy change per unit volume

1.7 Heterogeneous nucleation

Classical theories describe two different forms of nucleation: homogenous[12] (formation of critically sized solid from the liquid by the clustering together of a large number of atoms at a high undercooling and in the absence of any existing solid surface) and heterogeneous (formation of a critically sized nucleus from the liquid on a solid surface).

Invariably all nucleation occurs heterogeneously. The model involves the formation of a hemispherical particle upon a solid surface. A schematic of this is shown in figure 1.8. The free energy change accompanying the formation of an embryo is the difference between the change in volume free energy of the two phases and the interfacial energy required to form the new liquid – solid interface[13]. For a hemi-spherical cap of radius, r, the interfacial energy balance is:

$$\gamma_{ML} = \gamma_{SM} + \gamma_{SL} \cos\theta$$

Where:

γ_{ML} = Interfacial energy between mould wall and liquid
γ_{SM} = Interfacial energy between mould wall and spherical cap
γ_{SL} = Interfacial energy between spherical cap and liquid

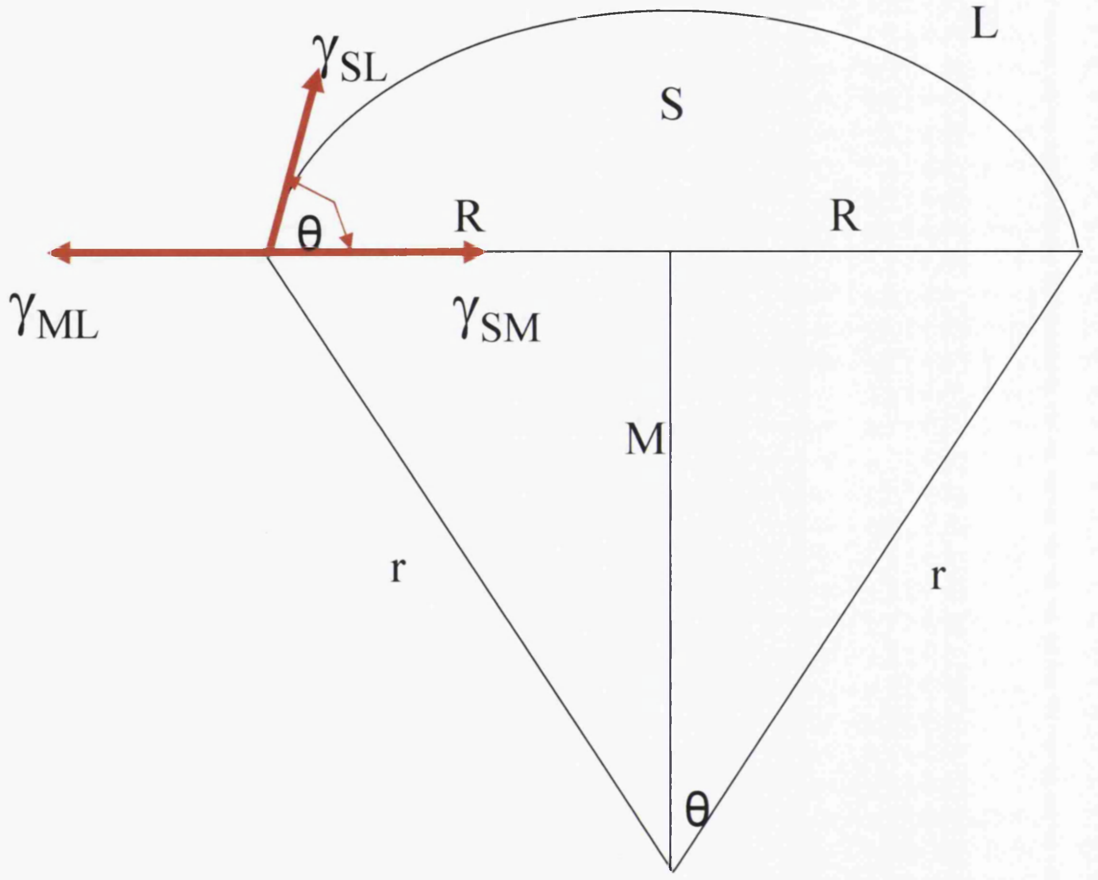

Figure 1.8 – Schematic of hemi-spherical nucleus on mould wall

$$\therefore \mathrm{COS}\,\theta = \frac{\gamma_{ML} - \gamma_{SM}}{\gamma_{SL}} \tag{1.4}$$

The free energy change accompanying the formation of the particle is:

$$\Delta G_{HET} = -V\,\Delta G_v + A_{SL}\,\gamma_{SL} + A_{SM}\,\gamma_{SM} - A_{SM}\,\gamma_{ML} \tag{1.5}$$

$$V = \text{volume of spherical cap} = \frac{\pi\,r^3(2+\cos\theta)(1-\cos\theta)^2}{3} \tag{1.6}$$

$$A_{SL} = 2\pi\,r^2\,(1 - \cos\theta) \tag{1.7}$$

$$R = r\sin\theta \tag{1.8}$$

$$A_{SM} = \pi\,R^2 = \pi\,r^2\sin^2\theta = \pi\,r^2\,(1 - \cos^2\theta) \tag{1.9}$$

Substituting (1.6) – (1.9) into (1.4)

$$\Delta G_{HET} = \frac{-\pi r^3(2+\cos\theta)(1-\cos\theta)^2}{3}\Delta Gv + 2\pi r^2(1-\cos\theta)\,\gamma_{SL} + \pi r^2(1-\cos^2\theta)(\gamma_{SM} - \gamma_{ML}) \tag{1.10}$$

From (1.4) $\gamma_{SM} - \gamma_{ML} = -\cos\theta\,\gamma_{SL}$

Substituting into (1.10)

$$\Delta G_{HET} = \frac{-\pi r^3(2+\cos\theta)(1-\cos\theta)^2\Delta G_v}{3} + 2\pi r^2(1-\cos\theta)\gamma_{SL} - \pi r^2(1-\cos^2\theta)\cos\theta\gamma_{SL} \tag{1.11}$$

$$= \left(\frac{-4\pi r^3}{3}\Delta G_v\right)\left(\frac{(2+\cos\theta)(1-\cos\theta)^2}{4}\right) + 4\pi r^2\gamma_{SL}\left(\frac{(1-\cos\theta)}{2} - \frac{(1-\cos^2\theta)\cos\theta}{4}\right) \tag{1.12}$$

$$= \left(\frac{-4\pi r^3}{3}\Delta G_v\right)\left(\frac{(2+\cos\theta)(1-\cos\theta)^2}{4}\right) + 4\pi r^2\gamma_{SL}\left(\frac{2-3\cos\theta+\cos^3\theta}{4}\right) \tag{1.13}$$

$$= \left(\frac{-4\pi r^3}{3}\Delta G_v\right)\left(\frac{(2+\cos\theta)(1-\cos\theta)^2}{4}\right) + 4\pi r^2\gamma_{SL}\left(\frac{(2+\cos\theta)(1-\cos\theta)^2}{4}\right) \tag{1.14}$$

$$= \left(\frac{-4\pi r^3}{3}\Delta G_v + 4\pi r^2\gamma_{SL}\right)\left(\frac{(2+\cos\theta)(1-\cos\theta)^2}{4}\right) \tag{1.15}$$

$$\therefore \Delta G_{HET} = \left(\frac{-4\pi r^3}{3}\Delta G_v + 4\pi\gamma_{SL}\right)S(\theta) \tag{1.16}$$

The graphical representation of this equation is shown in figure 1.9. It can be seen that the interfacial energy increases proportional to r^2 and the volume free energy with $-r^3$. The resultant is shown to increase to a certain point (denoted r*) and then subsequently reduce. r* is a point that for a given undercooling is associated with the maximum excess free energy ΔG^*_{HET}. Hence when a cluster (an initial collection of atoms forming an embryo or nuclei) is formed with a radius less than r*, the system free energy is lowered via the re-melting of the cluster. However, when a cluster of radius greater than r* is formed, the free energy of the system is reduced by the growth of the cluster. Therefore, r* is known as the critical size for a nuclei to grow and it has an associated energy (the free energy barrier to nucleation) of ΔG^*_{het}.

The differentiation of equation 1.16 gives:

$$r^* = \frac{2\gamma_{SL}}{\Delta G_v} \tag{1.17}$$

and substituting into 1.16 gives

$$\Delta G^* = \frac{16\pi\gamma^3{}_{SL}}{3\Delta G_v{}^2} S(\theta) \tag{1.18}$$

Hence, by substituting 1.17 into 1.3

$$r^* = \frac{2\gamma_{SL} T_e}{L\Delta T} \tag{1.19}$$

Consequently both the critical radius and the free energy barrier for nucleation decrease with increasing undercooling.

1.8 Non-reciprocal nucleation theory

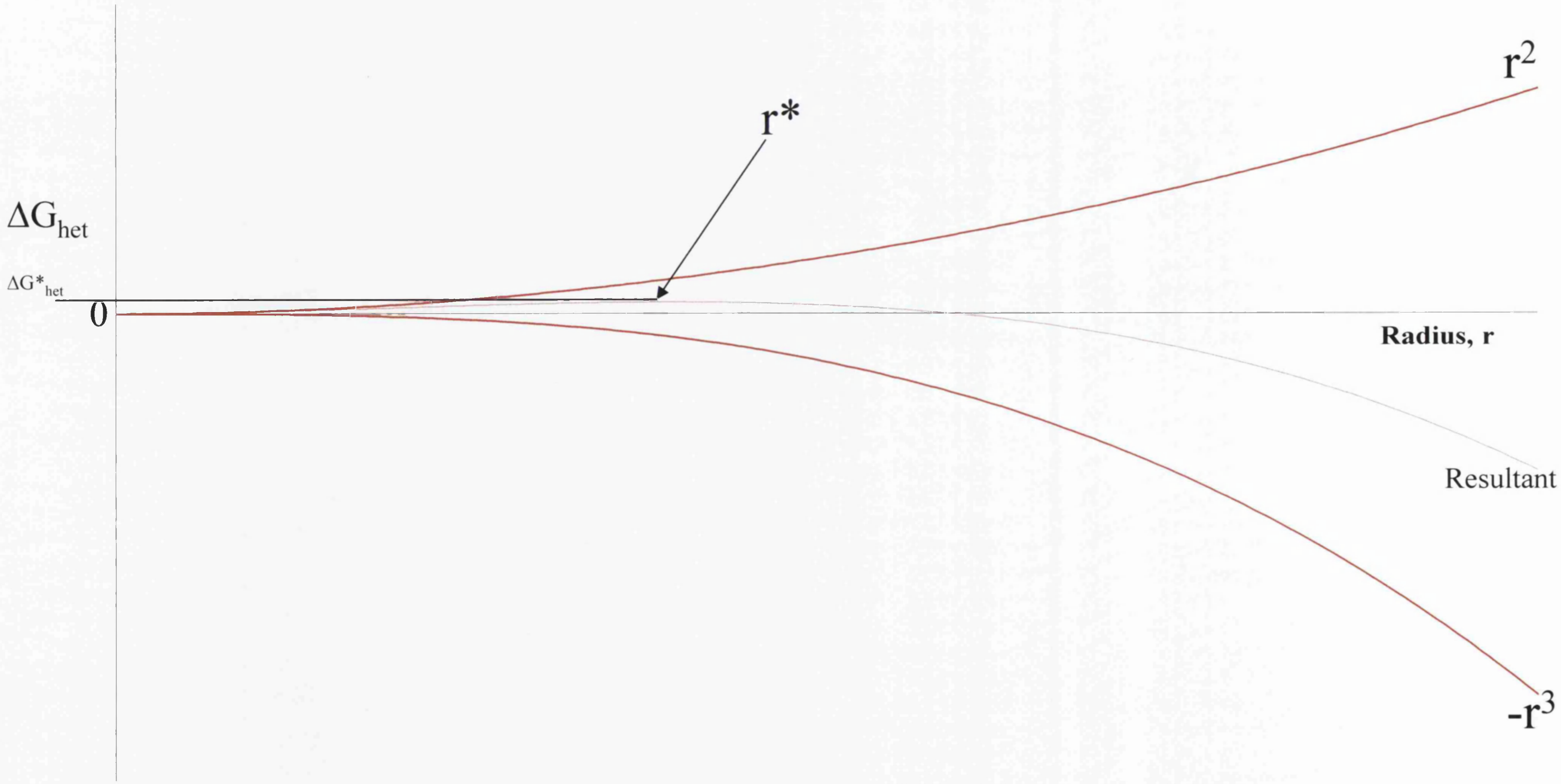

Figure 1.9 – Excess free energy of solid clusters

Studies of the undercooling associated with heterogeneous nucleation in eutectic systems (taken from the nucleation of a secondary phase from the liquid by a solid primary phase) were undertaken by B.E. Sundquist and L.F. Mondolfo[14]. The experimental procedure was clearly stated within the associated publication and it was generally found that in a binary (α and β) eutectic system α would nucleate β at low undercooling, but β would not nucleate α (except possibly at an undercooling approaching that for homogenous nucleation). The results contained within Sundquist and Mondolfo's paper concentrate upon the lead- tin (Pb- Sn) system. Using tin solid solution as the nucleant for lead solid solution it was found that the nucleation occurred at an undercooling of 0.25°C below the eutectic temperature. In the reverse case it was found that the nucleation of tin by lead occurred at undercoolings greater than 40°C. Thus the Sn rich phase is a good nucleant of the Pb rich phase but not vice versa. Therefore the phrase 'non-reciprocal' was used to describe the findings. The results for all the eutectic systems studied were categorised by the authors. It was found that metals with complex structures are difficult to nucleate, but will readily nucleate. In contrast, metals said to have simple structures were easy to nucleate but were poor nucleating agents. Other properties of the nucleating metals were that they have high entropies of fusion and high interfacial energies between liquid and solid. The results presented do not include any mention of binary Zn – Al alloys.

The nucleating characteristics of the Zn - Al system were first proposed by Spittle[15]. Investigations of the macro- and microstructures of Zn – Al castings (variation of the Al levels around the eutectic point producing hypo- and hypereutectic alloys) led to some interesting conclusions. With respect to the phase diagram, Figure 1.7, Spittle reported the formation of zinc solid solution halos around the primary Al solid solution dendrites of the hypo-eutectic (greater than 5wt% Al) system. No halos were observed upon the dendrites found within the hypereutectic region. This result has been noted in many binary systems and the phenomenon is a result of the location of the coupled zone of eutectic growth. The position of the coupled zone and the formation of haloes in alloys in eutectic systems have been discussed at length[16,17]. Within all of the discussed systems it was found that haloes of the poor nucleant form around the primary crystals of the better nucleant but not vice versa. Therefore, from the macro- and microstructures Spittle concluded Al is the better nucleant of Zn than vice versa. Bluni et al[18] conducted experiments to measure the degree of undercooling associated with the nucleation of each phase by the other in the Zn – Al system. The conclusions from these experiments were that the nucleation of zinc by aluminium occurred at an undercooling of only 0.25°C. In the reverse case the undercooling was 4°C. The conclusions agreed with those of Spittle.

1.9 Solidification of the Galfan coating

The solidification of hypereutectic Zn – Al alloy coatings under non-equilibrium conditions requires two distinct nucleation events. Initially the primary phase, β, a HCP (hexagonal close packed) zinc solid solution containing ~ 1% Al nucleates. Hinterberger[19] et al have shown that the nucleation of these primaries occurs in the vicinity of the steel substrate with the number, size and dispersion dependent upon processing parameters such as cooling rate.

At some under-cooling below the eutectic temperature, the nucleation of the second phase of the eutectic occurs. Spittle has shown the growth of the eutectic occurs within the coupled zone, which is probably asymmetric and skewed to the Al rich side of the phase diagram.

The majority of the primary zinc is contained within the bottom third of the coating (i.e. close to the steel) while the coating surface is comprised almost totally of eutectic. At the boundaries of the eutectic cells on the surface, depressions can be seen. These depressions occur as a result of the volume contraction when the liquid to solid transformation occurs. This contraction, unless fed, results in depressions between the eutectic cells (spangles). Other associated features of the solidification shrinkage include triple points (junctions between three growing cells) and cracks in the surface. Bluni et al have proposed a mechanism for crack formation within the boundaries. Impurities within the alloy, having a partition coefficient less than unity, are rejected into the melt during solidification. As the cell boundaries are the final regions to solidify, the impurities, such as lead, are segregated to these regions. Induced stresses will result in cracking within these regions.

1.10 Inter-metallic formation in Galfan.

Reaction diffusion occurring between the steel substrate and the liquid coating will lead to the formation of inter-metallic compounds. These reactions need to be predicted and analysed to be able to control the microstructure and the coating surface quality.

Predicting these transformations is extremely difficult with standard hot dip coatings. The addition of Al into the melt to form Galfan creates a new set of complexities. These complexities are due to three key factors: several reactions will occur at the same time, the reactions are very quick and that the transformation fronts regularly become unstable[21].

A wide range of experiments have been conducted upon the formation of the inter-metallic layers. Lin et al[20] produced results for the variations of the layers at different temperatures and the subsequent effects on surface quality. The experiments were conducted in the temperature range 460-520°C. The results indicated that at higher temperatures the growth of the inter-metallic was promoted. The rate of growth was rapidly accelerated above 500°C and at the lower temperatures a rougher coating was produced due to less fluidity in the liquid alloy, which produced wave like features upon solidification. If allowed to grow the inter-metallic became an extremely porous layer .

Further work has shown the presence of a $Fe_5Al_5Zn_x$ layer at short dip times.

1.11 The addition of aluminium.

As stated previously the alloying of aluminium and zinc will lead to an improved galvanising coating. The research from ILZRO, CRM and Nippon steel has produced a number of conclusions regarding the effects of the variation in aluminium content.

Firstly the results agree with the initial studies from ILZRO that the ideal composition for improved corrosion resistance is between 4.5 – 10%[21]. However it must also be noted that in order to keep a predominantly eutectic structure the Al content must be kept between 4.7 and 6.2 wt%[21].

The concentration of Al within the coating has a beneficial effect on the corrosion resistance, the viscosity of the galvanising bath, the structure formed and the quality of the coating. The viscosity of the bath is important when determining the adhesion properties of a particular coating. When Al is added to the Zn bath the viscosity of the bath should theoretically drop. However, in practice, this does not occur as, when tested, the viscosity remains generally high in most situations. Two reasons have been postulated for this. Firstly it is known that dross forms in the melt pot due to iron dissolution. The oxidation of aluminium to Al_2O_3 coats the surface of the galvanising bath adding to the increased viscosity.

It is summarised that if the Zn-Al bath is kept around the eutectic composition (5% Al in Zn), then the coating operation will be performed at its most fluent at a temperature lower than that for a conventional hot dip coating. (The eutectic temp being 382°C).

Reducing the content of the aluminium below 5% will lead to an improved surface finish. This is due to the compensating effects of larger amounts of zinc rich primary phase on depression formation between eutectic cells. In contrast increasing the Al content above approximately 8% will lead to a poorer surface quality due to the increased ability of the dross particles in the bath to adhere to the substrate.

Hypoeutectic alloys form a different microstructure to those observed in standard Galfan coatings. In this circumstance a halo of zinc solid solution is observed around the primary Al solid solution dendrites. The halo formation is thought to be due to the fact that Zn is a poorer nucleant of Al than vice versa and the coupled zone arguments(see figure 7.2). The eutectic morphology has been shown to be predominantly rod-like in hypoeutectic alloys.

The test results of corrosion due to variations in Al provided by Nippon steel are thus:

0.15% Al	total weight loss	30-35g/m^2/year
4.5-10% Al	total weight loss	20-25g/m^2/year

As the Al increases the corrosion changes from generalised corrosion (general HDG (Galvatite)) to localised corrosion on the galfan structures.

1.12 The addition of magnesium to Galfan.

Along with aluminium a lot of work has been undertaken to observe the effects of magnesium upon the microstructure and corrosion resistance of Galfan.

The addition of Mg into the galvanising pot is thought to decrease the fluidity of the liquid alloy. This has possibilities in helping with adhesion of the coat to the substrate. The alloy is thought to suppress bare spot formation[22]. Bare spots are areas where the alloy has not coated the steel. The discontinuous layer will lead to obvious problems with enhanced corrodibility.

Research has been conducted by Nippon steel investigating an alloy addition to counteract the effect of intergranular corrosion caused by the presence of lead and tin. Magnesium provided the best results in reducing their effects whilst adding benefits in other areas.

It would appear that small additions (< 0.05 wt%) reduce grain boundary irregularities and the surface becomes smooth with a silver white appearance. However as the additions increase to beyond 0.5wt% the eutectic cells will coarsen. The microstructure in other areas of the coat will also coarsen due to the interaction with aluminium and the magnesium which segregate to the surface. This leads to a poor surface finish with detrimental effects upon the paintability and formability.

Experiments conducted by Lamberigts et al[23] on the effects of Mg content (in Galfan) between 0 and 0.8% concluded that the addition of Mg always resulted in a decrease in ductilility. Other research has shown that a change in microstructure was observed with increasing Mg content. The primary phase volume percentage increased and the eutectic became rod like[24] with higher Mg content.

More recent experiments conducted through Corus and University of Wales Swansea[25] have shown that additions of Mg between 0.01 – 0.05% improve the surface corrosion resistance, formability and paintability. However SVET data has also shown that the increase in Mg also leads to increased cut edge corrosion. In each case (Nippon steel and Swansea university / Corus) the addition of Mg shows an improvement of corrosion performance on the coating surface.

1.13 The effect of other alloying additions

The accepted typical composition of Galfan is approximately 4.X% Al (X = 4.2-7.2%) with a small percentage of other alloying elements and the remainder zinc. Small amounts of alloying additions are included to alter the physical characteristics of the microstructure and the corrosion properties of the coating. The license from ILZRO describes a general composition for traditional Galfan coatings. This composition is:

Element		UNS Z38510
		Comp Wt%
Aluminium		4.2 - 7.2
Misch Metals		0.03 - 0.1
Iron	Min - Max	0.005 - 0.075
Silicon	Max	0.015
Lead	Max	0.005
Cadmium	Max	0.005
Tin	Max	0.002
Others, Total	Max	0.04
Zinc	Max	Remainder

Table 1.1 Recommended maximum elemental additions to Galfan

The additions of aluminium and magnesium have marked effects on the microstructure as has been described. Other elements in smaller amounts do however have a significant effect on the final structure and the properties of the coat. These will be briefly reviewed below.

1.13.1 The addition of Lead

The addition of lead has been used for the formation of spangles (eutectic cells) which form the Galfan eutectic structure[25]. Secondary benefits for lead ensure that under the high speed coating process the formation of the coat is smooth and continuous.

However opposing the clear benefits that lead brings, the drawbacks are significant. Previous research has shown that the addition of lead can lead to inter granular corrosion.

1.14.1 The addition of Tin

Tin has been found to have two adverse effects on Galfan. Firstly it is regarded along with lead as a major cause of inter granular corrosion. There is also evidence suggesting that tin causes delamination of the organic coating.

1.15.1 The addition of Silicon

Silicon is added to the Galfan melt to control the formation of the inter-metallic layer. The silicon partially inhibits reactions that would naturally occur between the zinc in the coating and the iron within the substrate. Preventing this reaction increases the formability of the overall product. The inter-metallic is generally brittle, thus significantly reducing the final product formability. Consequently this provides a more versatile product. The work of Lamberigts et al has shown a direct relationship between the silicon content and the formation of cracks in the coating.

1.16.1 The addition of Berylium

This is a rarely used alloying addition. It is occasionally used to counteract the damaging effects of lead and tin. It can also be used to reduce the surface defect known as streaking.

1.17.1 The addition of Cadmium

The addition of Cd causes similar effects to the addition of lead. Cadmium can be used as a grain refiner to promote nucleation of the spangles. A smooth and continuous coating is also ensured when coating at high speeds. There are no known adverse effects to the microstructure as long as the additions are below 0.05 wt%.

1.18 Influence of Cooling rate on Galfan coatings

Production of the coated galvanised product allows for processing conditions to influence the structure of the Galfan coating. One such condition is the rate at which the coating is solidified. Described in section 1.3, the solidification of the coating may be controlled via the use of a fast cooler situated above the galvanising bath. Due to the nucleation and growth characteristics of Zn – Al binary alloys the size and number of the eutectic cells and also those of the primary zinc dendrites will be altered by the rate of solidification of the coating[26, 19]. As well as altering the size and number of eutectic cells, the cooling rates will alter the distribution of solidification shrinkage at the eutectic cell boundaries. Accelerated cooling will increase the smoothness of the coating by up to 30% when compared to a slow cooled sample. Previous research at ILZRO[27] has determined that the rapid solidification of the Galfan coating is beneficial in so much as the relevant physical properties are enhanced and the corrosion resistance of the coating is improved[28]. Typical cooling rates provided by ILZRO (for the ideal structure) are around 30°C/s[29]. The rapid cooling of the coating will also limit the formation of inter-metallics at the steel/ coating interface improving the overall formability of the coating. It has been shown that this is more important in heavy gauge steels.

1.19 Failure modes of OCS

Of the numerous reported[30] failure modes for OCS products, by far and away the most common problems occur with cut edge corrosion and organic coating delamination. The Confidex® guarantee offered by Corus ensures that the supplied material (as long as it is maintained correctly) will be guaranteed to perform for 27 (soon to be extended to 30) years. In as much, the product must comply with the performance criteria detailed in the compass durability index[31] and if it fails to comply will be restored at Corus' expense. In 2003 cut edge corrosion was the cause of 64% of Corus Colors customer complaints on the HPS200 product. Typically over a 10 year period, cut edge corrosion has been responsible for ~54% of all failures. In figure 1.10 the effects of firstly cut edge corrosion and secondly organic coating delamination are clearly shown.

Cut edge corrosion can be defined as corrosion which is initiated and focused at the exposed cut edge of the OCS product. Essentially when the OCS product is guillotined for manufacturing purposes, a certain amount of the steel substrate is exposed to the local atmosphere. This exposed area will provide a ready initiation point for the corrosion cell and hence corrosion occurs. Since it is virtually impossible

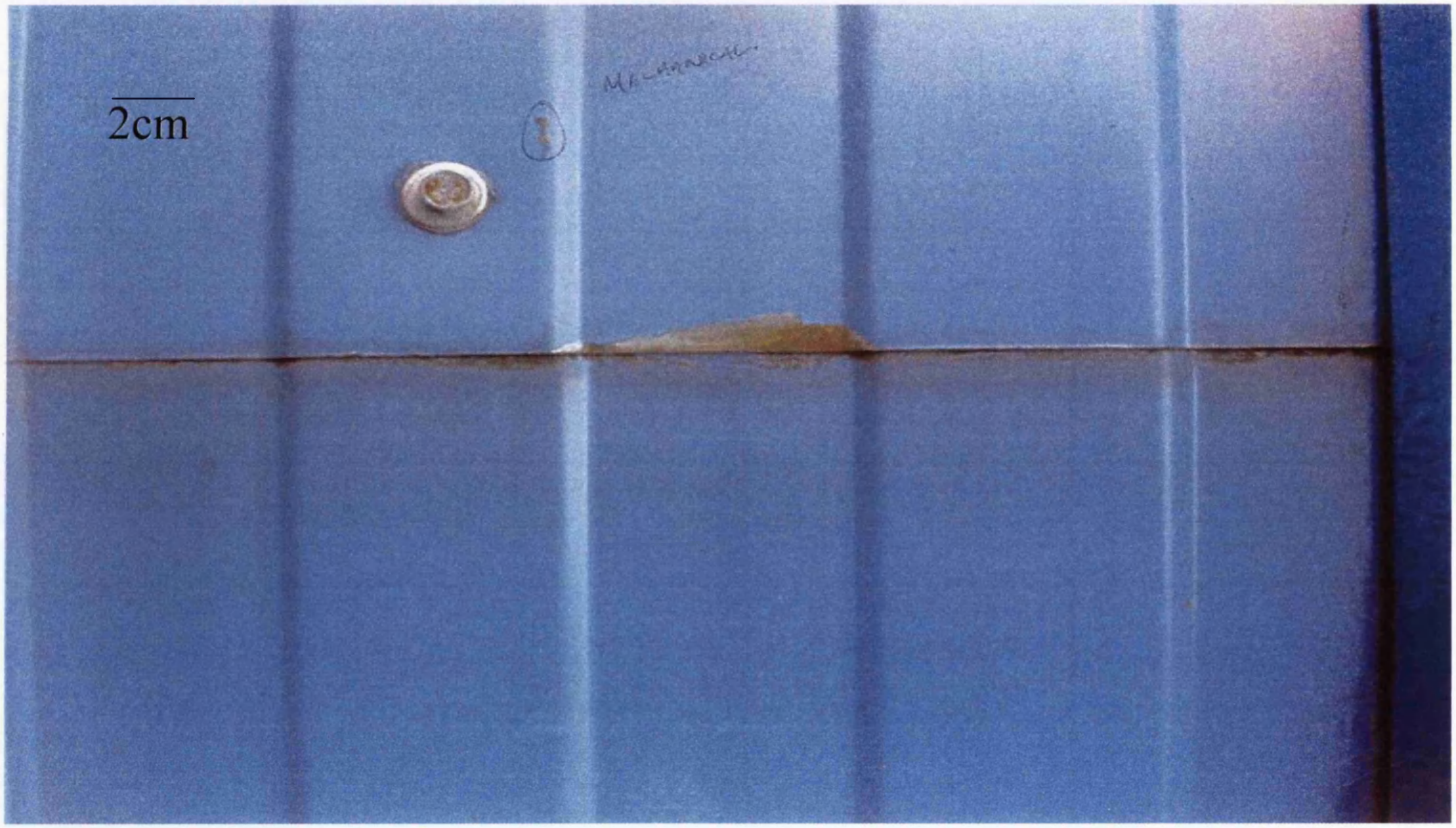

Figure 1.10 – Example of cut edge corrosion and coating delamination

to design out these features, coatings (such as galvanising coatings) have been used to minimise their effect. This provides the basis for the studies within this body of work.

Organic coating delamination can be defined as the premature removal of the organic coating due to electrochemical processes. With this problem the disbondment of the organic coating from the steel is brought about by either the anodic or cathodic reactions of an active corrosion cell. Once the coating is removed it leaves the exposed steel/metal susceptible to increased corrosive attack.

Therefore the continued development of the OCS system is required to limit the effects of these two forms of failure, and ensure the continued protection of all products produced.

1.20.1 Theory of Aqueous corrosion

The degradation of a metal within its environment by means of an electro-chemical reaction is known as corrosion. The driving force for corrosion is for a metal to exist in its lowest natural energy state. Most naturally occurring metals are found in the form of an oxide, this being assumed to be the lowest natural energy state. The removal of a metal from the oxide form (known as an ore) takes a great deal of energy usually supplied in the form of heat, for example in a blast furnace when extracting iron from iron ore (haematite). Thus a metal that has been separated exists in a higher energy form, and has a strong driving force to return to the lowest energy form. The return to the lowest energy state through combination with components of the environment is corrosion.

The energy difference between the metal in the pure form and that of the ore/corrosion product is known as the *free energy difference,* ΔG. The value of ΔG, in all circumstances represents the tendency for a metal to corrode. The actual reaction-controlling step is the *free energy of activation,* ΔG^*. Before a metal can corrode, energy must be supplied into the system. The energy barrier is ΔG^*, enough energy must be supplied in the system to overcome this barrier and allow the corrosion reaction to occur. Hence the driving force for corrosion is ΔG, but the corrosion rate is limited by ΔG^*.

1.20.2 Wet corrosion

Corrosion may occur in many forms ranging from dissimilar metal corrosion to corrosion via erosion processes. By far the most common form of corrosion when dealing with metallic elements is that of wet (aqueous) corrosion.

As the name suggests wet corrosion occurs in the presence of a conducting electrolyte. The reaction occurring is a mass-charge exchange reaction. Mass is transferred between the solid metal and the liquid environment[32], as charge is exchanged between the atoms (in the solid metal) and the dissolved oxygen and ions (in the electrolyte and the corrosion products). A basic wet corrosion cell requires four components, an anode where metal dissolution occurs (and electrons are produced), a cathode (usually oxygen or hydrogen reduction) where the electrons are consumed, a flow of electrons between these two sites, and of course an electrical connection to carry the flow of electrons and ions. Inhibiting one of these four components will stop the corrosion cell occurring and consequently stop corrosion. A typical corrosion cell is shown in figure 1.11

The anodic reaction, which is the oxidation of metal (M) atoms into the form of aqueous metal ions is represented below.

$$M_{(s)} \rightarrow M_{(aq)}^{n+} + ne^- \qquad (1.20)$$

The ions produced by this reaction have one of two fates. They will either be taken into the solution or react with other species around the component interface forming insoluble solid or gel corrosion products.

The corresponding cathodic reaction is essential to consume the electrons produced by the anodic reaction. This reaction can take on two forms. The first reaction involves the evolution of hydrogen from the system which dominates at low pH(1-7):

$$2H^+_{(aq)} + 2e^- \rightarrow H_{2\,(g)} \qquad (1.21)$$

The more general reaction under aerobic conditions and normal pH (7-14) is the reduction of oxygen generating hydroxyl ions:

$$2H_2O_{(l)} + O_{2(g)} + 4e^- \rightarrow 4OH^-_{(aq)} \qquad (1.22)$$

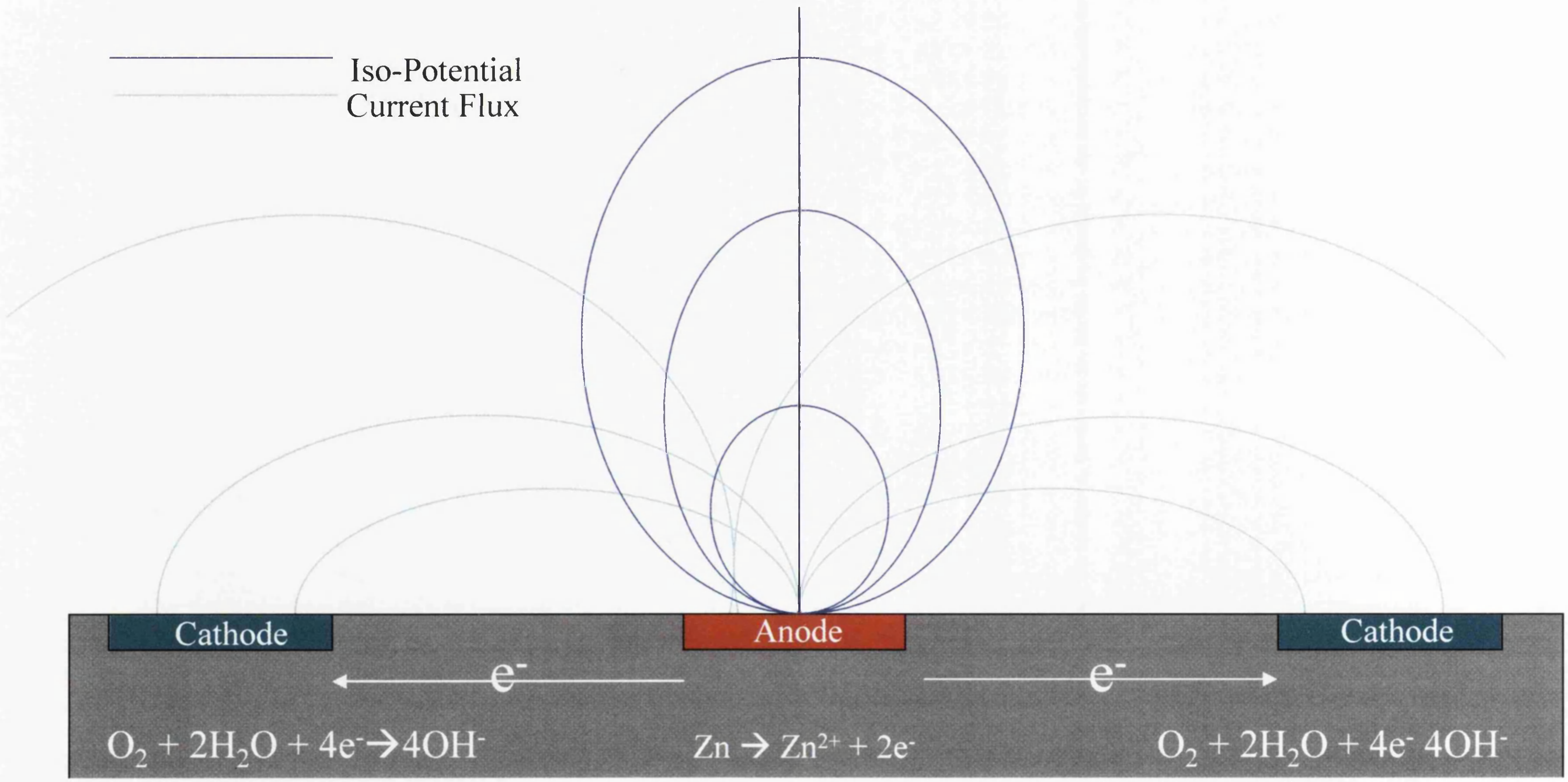

Figure 1.11 – Schematic of corrosion cell

Figure 1.11 shows a schematic of a wet corrosion cell occurring on a pure zinc surface.

The formation of a corrosion cell upon the surface of a metal can be the result of many different variations in local conditions. The reaction can vary with:

1. Local pH and electrolyte composition changes
2. Oxygen levels dissolved in the solution
3. Crystallographic features (grain boundaries, defects etc)
4. Changes in local metallic composition (e.g. different alloy phases or intermetallics)

The chance of corrosion occurring can therefore be succinctly defined:

Corrosion arises when a chemical process is made possible by a net release of free energy across a metal/electrolyte interface. The energy difference manifests as an electrical potential and this potential is the tendency for corrosion

The majority of the work contained within this Thesis deals with the galvanic protection of a steel substrate via the use of a metallic coating upon the substrate surface. The coating sacrificially protects the steel thus allowing the load bearing part of the system to do the job it was designed to do. The protection is known as galvanic protection. The previous section alluded to the fact that if one of the four required components for corrosion was removed then it would be impossible for the corrosion cell to form. The galvanic coating and other organic layers also act as a barrier separating the substrate from the electrolyte. This process is known as barrier protection.

1.21.2 Galvanic corrosion

Galvanic corrosion is more commonly known as dissimilar metal corrosion or bimetallic corrosion. This corrosion is created through the coupling together of two different metals. Any resulting corrosion is a product of the two metals holding different positions in the galvanic series. The galvanic series is a standard list of free corrosion potentials, E_{corr}, of a number of different metals compared against a standard hydrogen electrode (SHE). A selected list is shown below:

Metal	E_{corr} /V (vs SHE) (10)
Copper	+0.02
Tin	-0.26
Steel	-0.46
Aluminium	-0.51
Zinc	-0.86

Table 1.2. Typical free corrosion potentials for pure metals immersed in 3.5% NaCl at 20°C vs SHE

Both electrode potential and free corrosion potential are a thermodynamic indication of the tendency to corrode and the greater the separation of the electrode potential of coupled materials the greater the corrosion occurring upon the surface of the more active metal (the metal with the more negative E_{corr} value in table 1.1). To determine the activity of the metals we again consider the electrode potential. The selected results above are potentials taken in seawater at 20° C vs SHE. Zinc has a free corrosion potential that is below that of steel. Thus if the two were coupled together in an environment described above, corrosion would preferentially occur upon the zinc and the steel would be protected from any damage. Therefore we have the basis for cathodic protection of steel. The corrosion occurs upon the coating protecting the steel substrate.

1.21.4 Crevice corrosion

This form of corrosion occurs when part of the metal surface is deemed to be in a shielded or restricted environment, when compared to the rest of the surface which is exposed to a large volume of electrolyte. A mechanism to describe this form of corrosion has been presented when applied to stainless steels, however, broadly the mechanism is much the same for most systems. The crevice site required would have typical dimensions of 20 – 100 μm in width. The mechanism is known as the Fontana Greene mechanism[32]. The corrosion occurs over three stages.

1. The initial corrosion occurs as a result of the standard anodic and cathodic reactions. The electrolyte has a uniform composition and corrosion proceeds across the entire exposed region. The reactions in this stage were dealt with earlier.
2. The second stage is controlled by diffusion rates through the electrolyte. The cathodic reaction requires oxygen to continue. The rate at which the oxygen within the solution is consumed controls the rate of the reaction. As the reaction consumes the oxygen in local area more must diffuse from the

surrounding areas. It is obvious since the diffusion paths are shorter and there is a greater area that it is easier to replace the oxygen on the exposed surface than that in the crevice. Thus more oxygen is replaced at the surface than in the crevice. Thus, the reduction reaction within the crevice begins to slow due to depletion of local oxygen. The slowing of the reduction reaction does not affect the anodic reaction, due to the increase in hydrogen ion concentration accelerating the anodic reaction. Consequently, the region in which there is a lower concentration of oxygen becomes a focal anode due to the differential aeration process (see later) and the net charge in the crevice becomes more positive than that of the surrounding electrolyte.

3. The potential difference created by this event attracts negative ions from the surrounding areas, in order to try and balance the local charge. However the negative ions flowing into the region are usually chloride ions which themselves actively enhance corrosion within the region. The ions will increase the rate of metal dissolution and solubilise the protective oxide layer which forms on the metal surface. Another result to enhance corrosion is the formation of acid in the locale. The metal ions produced by the anodic reaction combine with the chloride ions forming complexes. In turn the complexes react with water to produce acid. The acid then increases the rate of corrosion within the crevice.

1.21.5 Pitting Corrosion

Pitting corrosion is a form of localised corrosion very similar to crevice corrosion. Selective attack occurs upon the corroding surface as a result of a scratch (or mechanically induced break), an emerging dislocation (boundary between slipped and non- slipped material) or a composition inheterogeneity[32]. The difference between a pit and the crevice corrosion previously described is in the initiation procedure. Once nucleated the pit will either survive (known as a stable pit) or die (said to be unstable). Once a pit has survived the nucleation process it must continue to propagate by building up an oxide layer over the hole. The build up (completely shrouding the hole) prevents the diffusion of oxygen into the corroding area setting up a differential aeration cell as in crevice corrosion. These pits surviving the nucleation process are known as meta-stable pits. In order to continue the growth of the pit, the oxide layer must remain intact. Any breaches of this layer will allow oxygen diffusion into the pit and it will deactivate.

1.21.6 Differential Aeration corrosion

This form of corrosion partially contributes to both of the above processes. The corroding metallic surface requires both an anode and a cathode. Both these sites are controlled by the amount of oxygen within the solution, and able to diffuse to the local area. Metal dissolution (anodic activity) will dominate in areas where there is little oxygen and the cathodic activity will dominate in regions of high oxygen content. Thus when regions become depleted in oxygen (possibly due to differing oxygen diffusion path lengths) anodic activity will become localised and corrosive attack occurs.

1.21.7 Kinetics of Corrosion

When anodic and cathodic sites are initiated upon a single piece of corroding metal, the sites are acting as a polyelectrode, a system of two or more couples, not in mutual equilibrium, occurring on a single electrode surface[33,34,35]. The additivity principle (postulated by Wagner and Traud[36]) defines that the total current flowing within a circuit is the summation of the individual couples upon the corroding surface, hence:

$$\Sigma\, i_{\text{anodic}} = -\,\Sigma\, i_{\text{cathodic}} = i_{\text{corr}} \qquad (1.23)$$

Where:

$\Sigma\, i_{\text{anodic}}$ = Current density due to anodic reaction

$\Sigma\, i_{\text{cathodic}}$ = Current density due to cathodic reaction

i_{corr} = rate of corrosion (expressed as a current)

As the electrochemical currents are potential dependent the corroding substrate will adopt a unique potential which is known as E_{corr}, the free corrosion potential. The relationship between the current (i) and potential (E) occurring was defined by Tafel[37] and shows that:

$$i_{\text{anodic}} \propto \exp(E) \qquad (1.24)$$

and

$$i_{\text{cathodic}} \propto \exp(-E) \qquad (1.25)$$

From these equations a theoretical Tafel plot may be created which will show that plotting E against lg i is a straight line. In practice a typical Tafel plot will curve from the zero potential point.

When combining two systems (such as a metallic component and aerated electrolyte), the combination of Tafel plots from these systems (forming a mixed potential plot) produces an Evans diagram which shows a simple corrosion process for the metal in the electrolyte. This is shown schematically in figure 1.12. The Evans diagram summarises the electrochemical environment the metal adopts. The plot

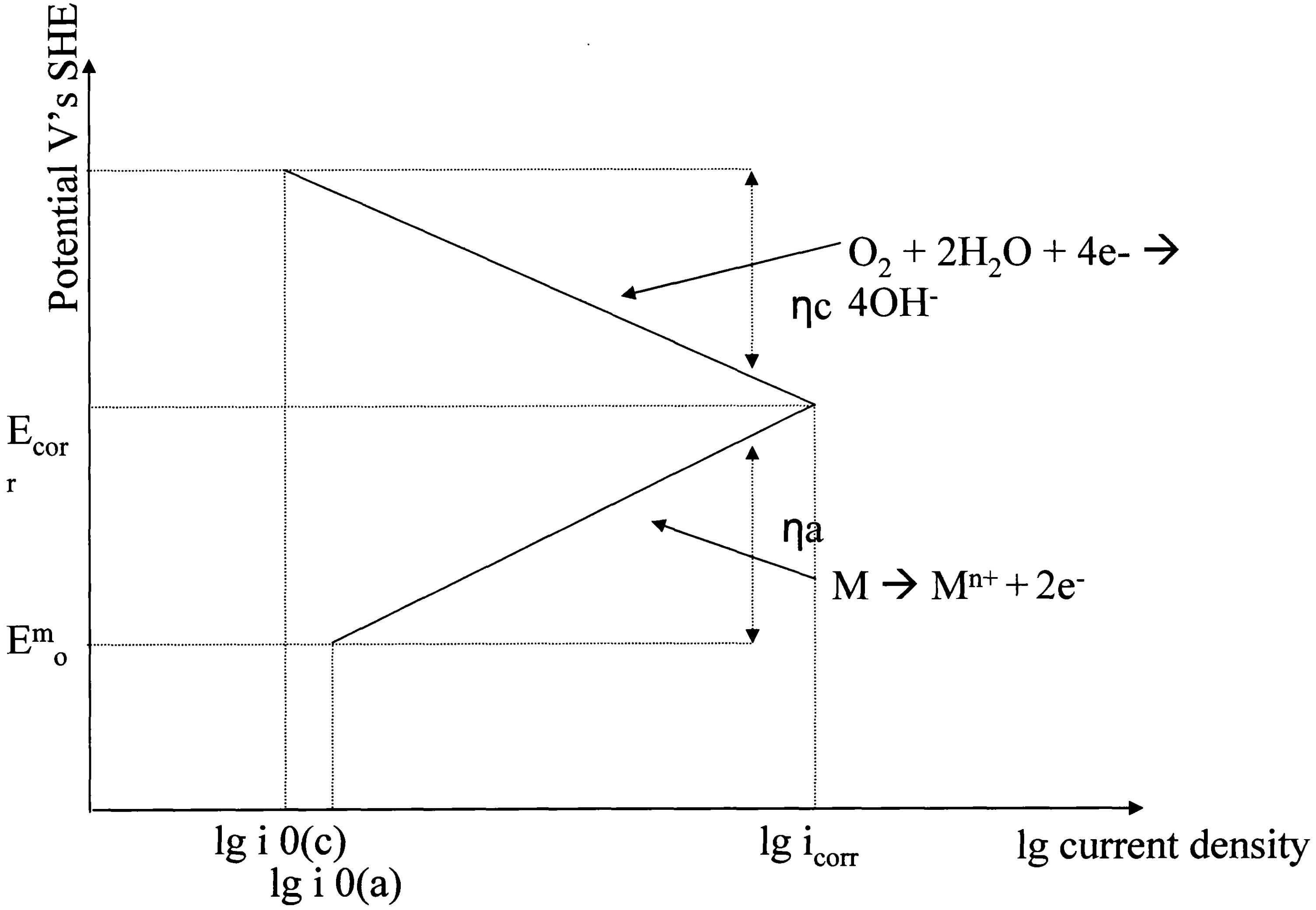

Figure 1.12 – Evans diagram for a metal in an aerated solution

shows that the metal will typically adopt a more positive potential when exposed compared to it's E^0 value measured under standard conditions. This value (E_{corr}) is the free corrosion potential and is a reflection of the true thermodynamic driving force for corrosion as described in table 1.1. Additions of inhibitor species to reduce the cathodic or anodic current can be used to slow down corrosion and lead to a shift in $E_{corr.}$

1.21.8 Pourbaix Diagrams

The visualisation of how the stability of different species is affected by pH and potential was presented by Marcel Pourbaix[32]. Pourbaix separated the corroding and non- corroding conditions by means of a threshold potential, defining that a metal is in the corroding state when the concentration of its ions is $\geq 10^{-6}$ M. In conditions where the ionic concentration is less than this value the system is said to be in a condition of immunity. The basics of corrosion reactions are described by equations 1.20. and 1.21. The underlying principles behind these equations assume that the ionic species produced via corrosion enter the electrolyte as soluble species. However, many species produced under corrosive conditions are insoluble (such as Al in the corrosion products of Galfan) and will form a layer upon the corroding surface. This layer can act as a barrier, preventing contact between the electrolyte and the corroding surface subsequently reducing the rate of corrosion. Under these conditions, the corroding system is said to be in a state of passivity.

The typical Pourbaix diagram for iron in water is shown in figure 1.13. Pourbaix, and subsequent researchers have essentially produced diagrams for many metallic systems which predict the condition of the metal under different condition of potential and pH. It can be seen from the schematic Pourbaix diagram (figure 1.13)

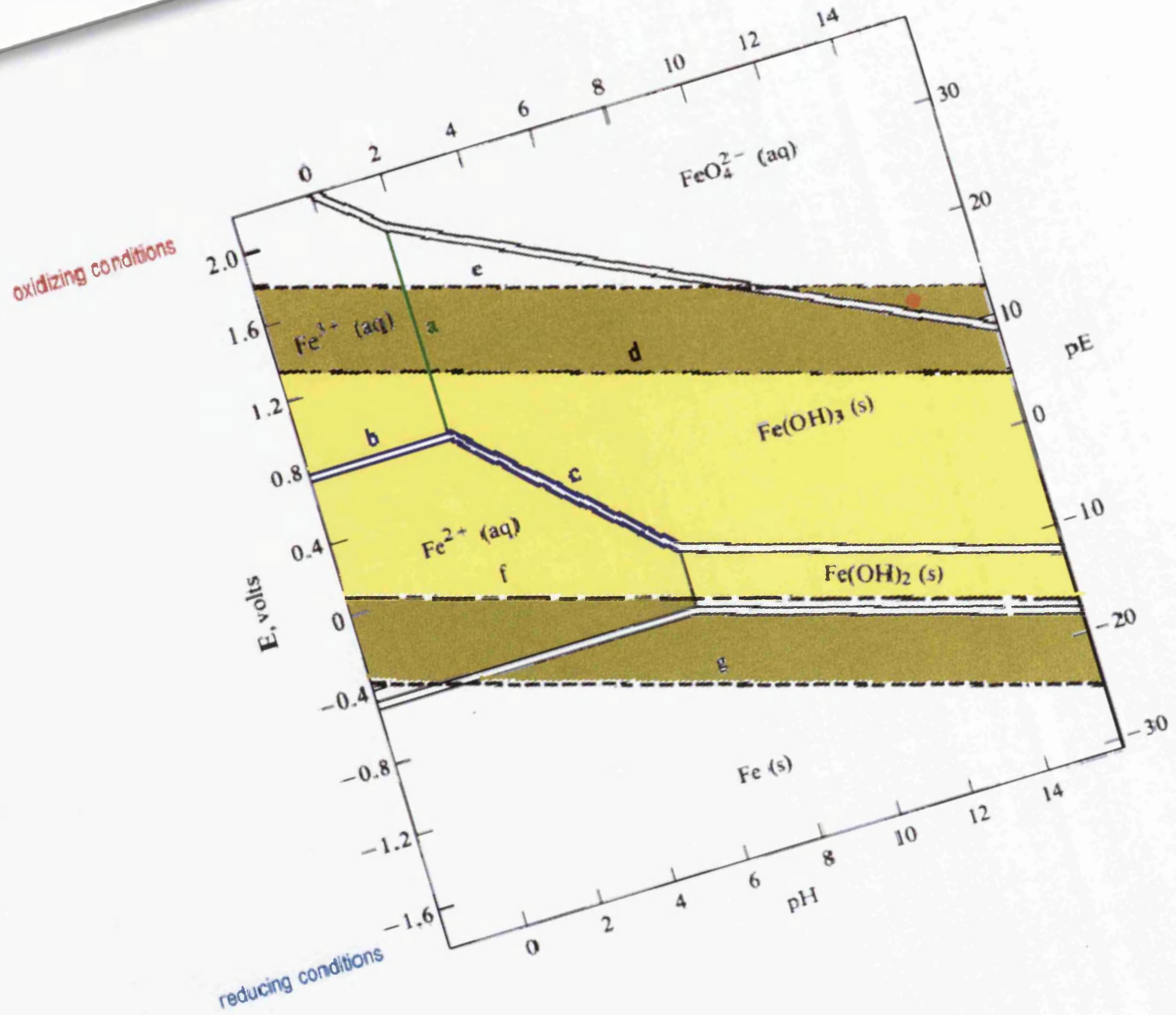

diagram for Fe in water

that in a typical sea water iron will corrode. Corrosion prevention through galvanising pushes the iron potential close to that of zinc, where iron is immune.

1.22 Corrosion prevention

1.22.1. Barrier protection

As previously discussed the corrosion cell is a combination of four distinct entities: the anodic and cathodic reactions, an electrolyte and the transport of electrons through the electrolyte between the anodic and cathodic sites. The removal or prevention of one of these entities will result in the inhibition of the corrosion process. Consequently, when designing for the prevention of corrosion, it is important to consider these principles and act upon them.

The easiest way to prevent corrosion occurring is through barrier protection. In this circumstance the potential corroding surface is separated from the electrolyte by a coating such as paint (on cars) or by organic coatings on buildings. An un-interrupted coating will protect the surface of the base metal from any corrosive attacks, however scratches of defects (to the base metal) within the coating will allow corrosion to be initiated and rusting will occur.

1.22.2 Sacrificial coating protection

A more advanced form of corrosive protection is provided through sacrificial coatings. In this method the concept of dissimilar metal corrosion (section 1.21.2.) is utilised, where the more reactive metal (typically zinc or zinc alloy when protecting steel) is coated onto the metal being protected and the metal coating will corrode preferentially to the base metal providing total protection. In the case of zinc protecting iron the free corrosion potentials of zinc and iron in seawater (typically 3.5% NaCl) are -0.86V and -0.46V (vs SHE). Hence, considering the underlying principles (section1.20.1) the zinc is more electrochemically negative (i.e. more reactive) and will corrode preferentially to the steel.

1.23 Corrosion Inhibition

Corrosion inhibitors, added to the pre-treatment and primer layers of an organic coating system, limit the corrosion occurring by lowering the rate of corrosion normally associated with a particular environment. The inhibitor additions are added in very small quantities, but are remarkably effective in reducing the corrosion occurring. The inhibitors may either be organic (such as polyaniline) or inorganic (such as strontium chromate) although environmental legislation is forcing a move away from chromated systems.

Commonly used inhibitors for OCS systems are metal salt (inorganic) inhibitors. These inhibitors act to reduce the rate of either the anodic or cathodic reactions and are most favoured due to their sparingly soluble nature. The anodic inhibitors work by producing passive films or salt layers of low solubility upon the anodic sites via reactions with the corroding metals ions. The reactions serve to increase the polarisation of the anode and hence allow the film to be deposited. Cathodic inhibitors operate by reducing the corrosion current and the free corrosion potential. This reduction is brought about via the precipitation of insoluble compounds upon the areas of cathodic activity which limit the access of electrolyte and oxygen to the cathodic site. Hence limiting the oxygen, slowing the overall rate of reaction.

1.24 The corrosion of Galfan

The corrosion of any coating can occur within two regions; the cut edge and the surface. Recent work has been conducted upon both of these regions for the Galfan coating. In both studies mechanisms have been postulated for both the surface corrosion and the cut edge corrosion. With both cases the influence of microstructure had a dramatic effect.

In the case of the cut edge, zinc rich regions will corrode preferentially to the surrounding eutectic microstructure. Thus it is possible to straight away see the advantages over standard Galvatite (Zn – 0.15% Al) where typically (if pitting does not occur) the entire coating corrodes uniformly. The selective localised corrosion upon the primary will reduce the overall rate of corrosion. Evidence for the selective corrosion is shown in figure 1.14.

The majority of surface corrosion occurs within the depressed grain boundaries. The corrosion is thought to be a result of three different factors. Firstly, it is accepted theory[32] that corrosion will preferentially occur within defects upon the surface. The depressed boundaries may be seen as natural defects. Within these boundaries are two initiation sites for anodic activity. Firstly studies by Elvins et al[38] have shown the appearance of primary Zn dendrite arms. These arms appear as a result of the solidification shrinkage, but may be seen as initiation points. It must be noted that the volume fraction of these arms is tiny compared to that of the bulk eutectic. Predominantly situated at triple points, cracks also appear within the cell

Before corrosion

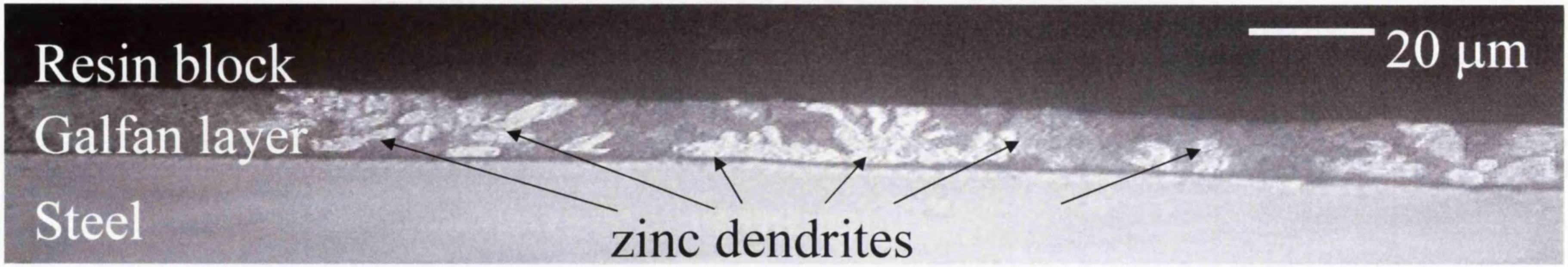

After corrosion

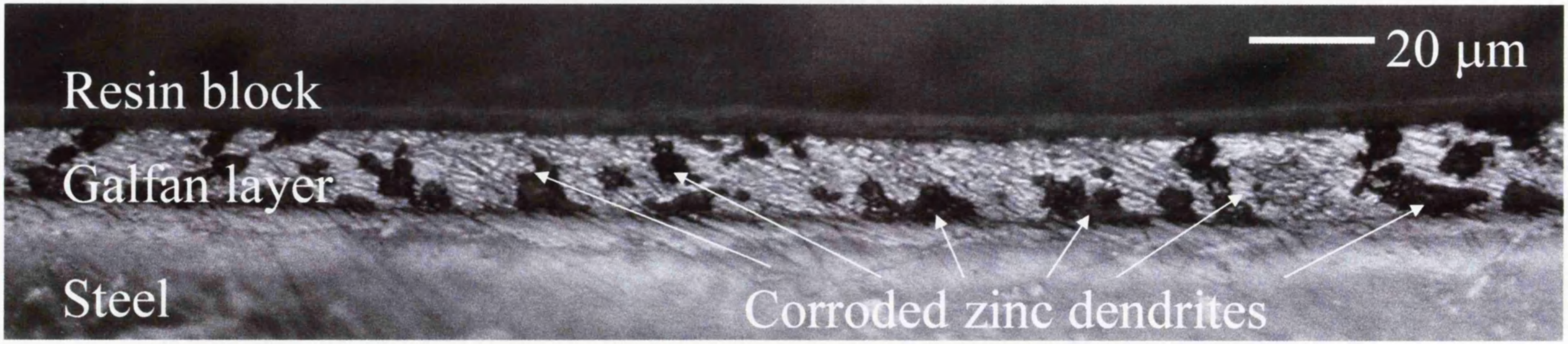

Figure 1.14 – Examples of selective corrosion in galfan coatings

boundaries. These points act as initiation sites for differential aeration (crevice corrosion) cells.

This work (detailed in subsequent chapters) will show that the corrosion occurring upon the surface and the cut edge is directly linked to the microstructure and solidification conditions.

1.25 Accelerated tests

When supplying guarantees against corrosion the expected duration (i.e. corrosive resistance life) of the product is predicted via accelerated testing. Natural weathering tests will give the most precise data but require a product to be tested over a number of years. Hence, for any meaningful data to be produced the launch of a product would only occur after a significant time. Therefore the need to rapidly predict the corrosive resistance of a product has led to the development of a number of accelerated tests which give extrapolated data on the performance of a coating in a much smaller time frame. These tests simulate the natural mechanism of corrosion as closely as possible whilst accelerating the damage caused to the coatings. As such, a number of criteria[39] have been specified when developing accelerated tests:

1. The test must accelerate the process without altering the corrosion mechanism.
2. How will the acceleration be achieved?
3. What are the testing limits?
4. What are the properties to take into consideration?: humidity, rainfall, dry periods…etc

The following sections briefly describe a few widely used tests and the performance of Galfan under such tests.

1.25.1. SO_2 Tests

Sulphur dioxide tests are used to model corrosion in industrial atmospheres. Under these conditions SO_2 from the industrial process may be dissolved in rain water forming acid rain. Consequently the acid rain will accelerate the natural corrosion processes occurring upon metallic substrates and therefore the predicted performance of galvanised coatings is essential.

The work of M.P. Roman[40] has shown that in 10ppm SO_2 tests, which are designed to simulate industrial exposure, the life expectancy of Galfan is 5 or 6 times greater than that of the standard galvanising coating. In a set of harsher tests the appearance of red rust was twice as quick in the standard coating.

These results were confirmed again with the results of blistering tests showing that the blistering was reduced when a Galfan coating was used.

1.25.2. Salt Spray tests.

The salt spray test involves exposing numerous samples of the required substrate to a mist of either 3, 5 or 20% NaCl at a temperature generally between room temperature and 40°C. The salt spray tests are generally evaluatred by the amount of time required to produce red rust. The results of a number of tests on

Galfan show that the life expectancy (i.e. the amount of time for red rust to appear) is approximately 2-3 times greater than the conventional coating[41].

1.25.3 Natural weathering

The natural weathering results are produced by exposing the samples to different environments over a period of years. Marine tests have shown that the Galfan coating will out last galvatite due to the levelling off of the coating reduction at a much earlier time[42].

The edge creep in these environments is also reduced. 9 year experiments have shown that edge creep in Galfan is between 2 and 3mm (depending on pre-treatment) whereas that for galvatite over a period of 5.5 years is between 15 and 16mm (again depending on the pre-treatment).

The initial tests conducted with the CRM (centre de research metallurgique) pilot Galfan material began in 1978. The five year results correlate with the laboratory tests showing the corrosion rates are between half and a third slower than the conventional hot dip coat. Three year weathering results also show the same results.

1.26. Scanning Electrochemical techniques

Scanning electrochemical techniques are becoming evermore popular methods of studying aqueous corrosion in laboratory environments[43,44]. All of these techniques operate via the movement of a probe above the corroding surface which is immersed in solution. In this way the probe can detect local variations in potential or potential gradient occurring and the locations at which these changes occur. Hence the corrosion kinetics and anodes can be observed and analysed. The data received from these probes can be represented as area maps or other spatially resolved representations which can be used to infer local differences in surface current density, reactivity and topography[45]. The major benefit of these techniques is the ability to spatially resolve and quantify local changes in the surface activity and differences in the rate of the reaction. More conventional techniques[46] provide an average value of the entire exposed surface area.

There are three variants in use most commonly; The SRET (Scanning reference electrode technique), the SVET (scanning vibrating electrode technique) and the SKP (scanning Kelvin probe). Both SRET and SVET allow local corrosion assessment on immersed samples and SKP allows investigation of corrosion activity beneath organic coatings or moisture films.

The SRET was the first scanning electrochemical technique and is the simplest and provides the most limited information. The basic mode of operation for this instrument is the measurement of potential in solution which are generated ohmically due to the ionic current flux provided by localised corrosion cells.

The SVET is a development of the SRET and provides the instrumentation for the corrosion studies described later. The SVET measures potential gradients in solution using a vibrating probe electrode. A detailed description of this technique is provided in section 2.2. The theory behind the SVET operating principles is detailed below and the corrosion cell is shown pictorially in figure 1.15. Lines of iso-potential are perpendicular to the current flux and in this schematic the cathode is remote

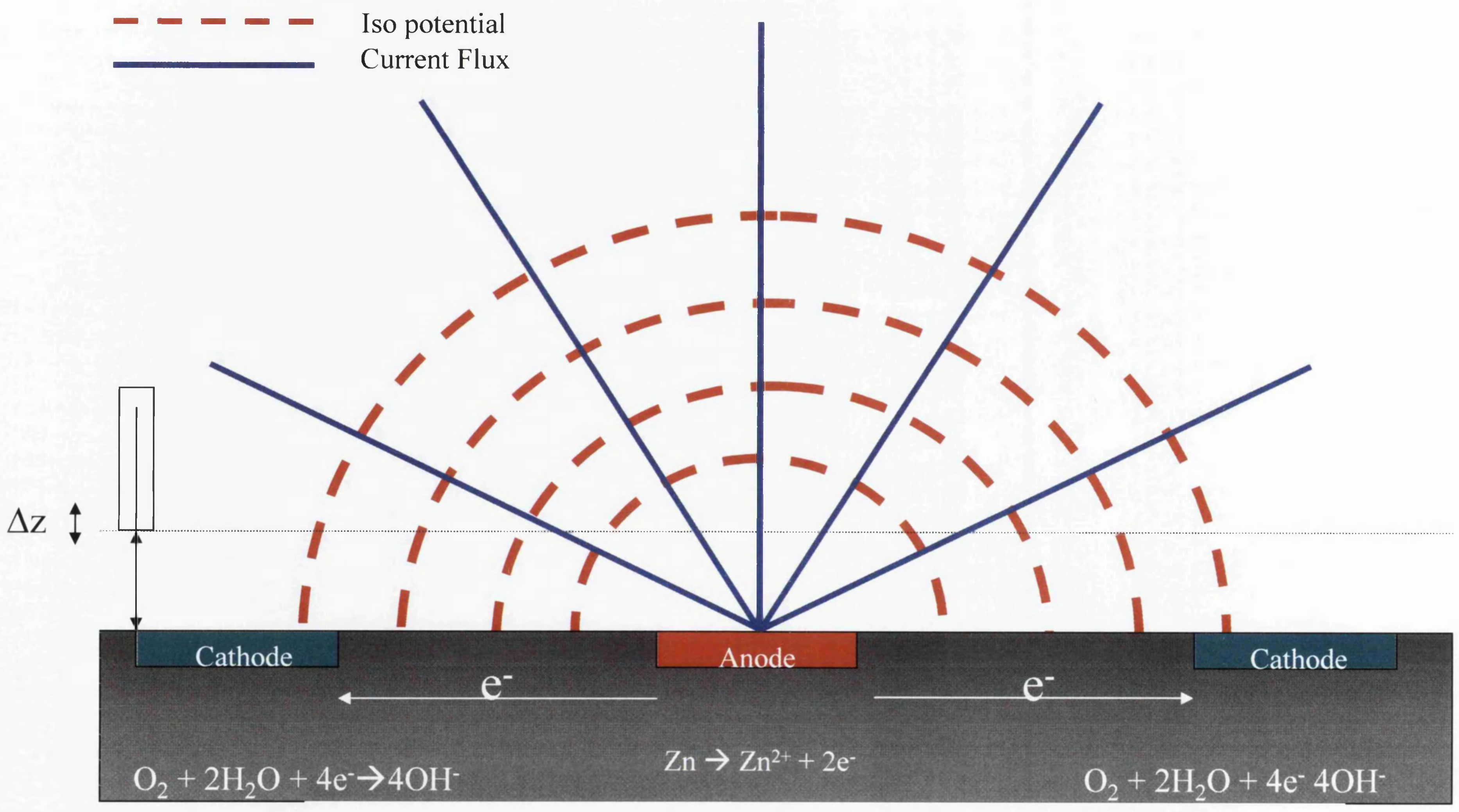

Figure 1.15. The operating principles of the scanning vibrating electrode technique

leading to radially symmetric current distribution. The distribution of the potential and ionic currents is theoretically derived by the Laplace equation:

$$\nabla^2 E = 0 \tag{1.26}$$

Where:

E = potential

and ohms law:

$$i = -\kappa \nabla E \tag{1.27}$$

Where:

i = current

κ = conductivity of solution

Considering a point anode current source with remote cathodes (as shown in figure 1.15) ensuring that when a current is passed through the point source the current distribution is radial, the relationship between the potential difference and current is:

$$F = \frac{dE}{dz} = \frac{iz}{2\pi\kappa(x^2 + y^2 + z^2)^{1.5}} \tag{1.28}$$

F = field strength

E = potential

i = Current

z = probe height

κ = conductivity

The maximum field strength from a point source occurs directly above the emitting origin and therefore components x and y in equation 1.27 equal 0. Hence the maximum field strength:

$$F_{max} = \frac{i}{2\pi\kappa z^2} \tag{1.29}$$

This equation displays an inverse square relationship between the field strength F_{max} and the probe height, z. therefore it is critical to ensure that during all experimentation the scan height remains at a set distance above the corroding sample.

The spatial resolution (at a particular height) of the SVET is determined by the single peak width at half maximum (*whm*). The spatial resolution of the vibrating probe is the smallest distance between two distinct anodes or cathodes that can be visualised by the SVET. Still considering our point source, r is the distance along the x, y plane from the point source:

$$r = (x^2 + y^2)^{0.5} \tag{1.30}$$

The value of r at half the maximum field strength is given by:

$$0.5F_{max} = \frac{iz}{2\pi\kappa(r^2 + z^2)^{1.5}} \tag{1.31}$$

The ratio of equations (1.30) and (1.31) gives

$$r = z(2^{2/3} - 1)^{0.5} \tag{1.32}$$

The width of the SVET response peak is 2r hence,

$$whm = 2r = 1.533z \tag{1.33}$$

Considering a scan height of 100µm the theoretical maximum spatial resolution of the SVET is 153µm.

The SVET has been used to study a variation of phenomenon associated with corrosion[47]. It has been shown to be particularly useful in studying modes of corrosion associated with the cut edge of galvanised steels[48,49]. It has been particularly useful in determining the distribution of anodic and cathodic activity across corroding surfaces and hence should prove to be a particularly useful tool in the following studies.

The SVET has been used to great effect to study cut edge corrosion on a number of occasions. Powell et al[50] used this technique to elucidate the corrosion mechanisms occurring along Galvatite coated steel cut edges under asymmetrical organic coatings. By plotting the changes in localised current density across the steel samples, the authors were able to conclude that high levels of anodic activity were focused upon the galvanising layer under the thicker organic coating. Further interpretation of the results led to the theory that this form of coating produces coatings which are highly susceptible to differential aeration corrosion mechanisms. Further studies were continued in this vain by where the effect of coating permeabilities and porosity's were studied. Williams et al[47] determined that the anodic activity occurring on the galvanised coating (again a Galvatite coating) will focus proximal to a coating with greater barrier properties as opposed to one with lesser properties (assuming that the two coatings have differing barrier properties). Again the distribution of the anodic and cathodic activity implies a differential corrosion mechanism occurring and in this circumstance prevents passivation of corrosion occurring.

The SVET technique has previously been used to study corrosion on Galfan coated steels. Challis et al[51] used this technique to quantify the effects of Mg content in Galfan on the surface and cut edge corrosion resistance. In these studies it was found that by increasing the Mg content, the surface corrosion performance was improved due to reduced eutectic nodule boundaries which act as initiation sites for corrosion. In contrast, the increase in Mg, led to worsened corrosion performance along the cut edge. This was ascribed to the increase the primary zinc phase providing a more persistent and intense corrosive activity.

1.27 Conclusions and Project aims

The most corrosion resistant coating available which is easily over-coated with organic coatings is the 5% Al Galfan coating. It is now being used at Corus, Shotton for all HPS200 and Celestia products. What is clear from some of the information shown earlier is that the primary phase in Galfan corrodes preferentially. It is also clear from previous work that the SVET is a useful technique with appropriate resolution to investigate the link between microstructure and corrosion in these alloys.

In this programme of work the aims were to:

1.) Control the microstructure through variation in the processing conditions
2.) Control the microstructure through variation in the Galfan coating composition
3.) Establish links between microstructure and corrosion using SVET
4.) Establish whether SVET testing is a reliable test method for evaluating performance.

1.27 REFERENCES

---

[1] D. Reynolds, Corus. *Private Communication*

[2] Y. De Abreu, A. Da Silva, A. Ruiz, R. Rέquiz, N. Angulo and R. Alanis, Surface and Coatings Technology,120-121, 682 (1999).

[3] A.R. Marder, Progress in Materials Science 45, 191(2000)

[4] J. Hostetler, Progress report no. 24. Galfan Technical Resource Centre, ILZRO, (1992)

[5] D. Christian, Proc. Of Eighth Galfan Licencees Meeting, International Lead and Zinc Research Organisation (ILZRO), (1986)

[6] F. Goodwin, 'Galfan Galvanising Alloy Technology', 2nd Edition, ILZRO, (1984).

[7] M. Lamberights, V. Leroy and F. Goodwin, Proc. of the Third International Zinc Coated Sheet Steel Conference (INTERGALVA), SID/7 (1991)

[8] F. Goodwin, A.F. Skerazi and R. Lynch: 25th Annual Conference of Metallurgists, The Canadian Institute of Mining and Metallurgy (1986)

[9] BSS, Zalutite – Zinc/Al alloy coated steel – Technical manual, (1989).

[10] J.H. Selverian et al, J. Mater. Eng, 9, 133, (1987)

[11] J.H. Sullivan, Thesis (Ph.D.) - University of Wales Swansea, (2003).

[12] D.A. Porter and K.E. Easterling, 'Phase transformations in metals and alloys'. New York : Van Nostrand Reinhold, 1981

[13] R. Elliott, Eutectic solidification processing : crystalline and glassy alloys. London : Butterworths, 1983.

[14] B.E. Sundquist & L.F. Mondolfo, Trans A.I.M.E. 221,157 (1961)

[15] J.A. Spittle, Metal Sci. 12, 578 (1977)

[16] A. Kofler, J. Australian. Inst. Metals, 10, 132 (1965)

[17] J.D. Hunt and K.A. Jackso, Trans A.I.M.E.,239, 864 (1967)

[18] S.T. Bluni, M.R. Notis and A.R. Marder, Acta Metal.Mater 43, 1775 (1995)

[19] F. Hinterberger, W. Maschek and J. Faderl, Zinc Based Steel Coating Systems: Production and Performance, 281, (1998)

[20] K.L. Lin, J.K. Ho, C.S. Jong and J.T. Lee, Physical Metallurgy of zinc coated Steels, 89 (1993)

[21] K. Tano and S. Higuchi, Nippon Steel Technical Report, No. 25, 29 (1985)

[22] F. Goodwin, In, Zinc Based Steel Coating Systems: Metallurgy and Performance, 183 (1990)

---

[23] M. Lamberigts, Continuous Galfan coating of steel sheet and wire, ILZRO project ZM-285

[24] K. Masuhara and F. Kumon, Proceedings of the International Conference on Zinc and Zinc Alloy Coated Sheet Steel (Galvatech), 596, (1989)

[25] V. Stevenson. Corus report. WL/SMP/R/DO6/4/99/D

[26] Comparing Galfan and Galvalume as anti-corrosion coatings for pre-painted steel sheets, ILZRO.

[27] F. Goodwin, GALFAN galvanising Alloy and technology, ILZRO, 2nd Ed. (1984)

[28] A.F. Skerazi: Proceedings of the 14th International Galvanising Conference, Munich Germany, (Zinc Development Association), 51(1986)

[29] The Galfan Handbook, ILZRO publication

[30] P.A. Ryan, R.P. Wolstenholme and D.M. Howell, Durability of cladding- A state of the art report, Thomas Telford, (1994)

[31] Celestia & HPS200, Individual Solutions. Guaranteed Partnerships. Corus Colors. (2004)

[32] K R Trethewey, J Chamberlain, "Corrosion for Science and Engineering", Longman publishing, 1996

[33] R. Parsons, Pure Appl. Chem., 37, 512, (1974)

[34] J. O'M. Bockris, in Modern Aspects of Electrochemistry, J. O'M. Bockris and B. E. Conway (Eds.), Butterworths; London, Ch. 4, (1954)

[35] P. Van Rysselburg, Electrochem. Acta, 9, 1343, (1964)

[36] C. Wagner and W. Traud, Z. Electrochem., 44, 391, (1938)

[37] J. Tafel, Z. Physik. Chem., 50, 641. (1905)

[38] J. Elvins, J.A. Spittle and D.A. Worsley, Corrosion Engineering, Science and Technology,38, 197,(2003)

[39] K. Barton. Protection against Atmospheric corrosion, John Wiley & Sons (1976)

[40] M.P. Roman, Proceedings of the International Conference on Zinc and Zinc Alloy Coated Sheet Steel (Galvatech), 5, (1989)

[41] S. Radke, D. Herrshaft, J.Less Common Metals, 93, 253, (1983)

[42] M. Lamberigts, V. Leroy and F. Goodwin. Third International Zinc Coated Sheet Conference. (1991)

[43] S. Bohm, H.N. McMurray, S.M. Powell and D.A. Worsley: Electrochimica Acta, 45, 2165, (2000)

[44] R. Akid and D. J. Mills Corrosion Science, 43,1203,(2001)

[45] H.N. McMurray and D. Worsley: in Advances in Chemical Kinetics, (ed. R.G. Compton and G. Hancock), 4, 149, (1997)

---

[46] F. J. Maile, T. Schauer and C. D. Eisenbach, Progress in Organic Coatings, 38, 117,(2000)

[47] M. J. Franklin, D. C. White and H.S. Isaacs, Corrosion Science,33, 251(1992)

[48] S. Böhm, H. N. McMurray, S. M. Powell and D. A. Worsley, Electrochimica Acta, 45, 2165, (2000)

[49] D. A. Worsley, D. Williams and J. S. G. Ling, Corrosion Science, 43,2335(2001)

[50] D. A. Worsley, A. Belghazi and S.M. Powell, Ironmaking and Steelmaking, 26, 387 (1999)

[51] D A Worsley and M Challis, British Corrosion Journal, 36, 297, (2001)

Chapter 2

Experimental Methods

2.1 Microstructural Investigations

2.1.1. Preparation of coating samples

To investigate the microstructural evolution in the coating as a function of distance from the air/ coating interface, the larger panels (either produced online or via the hot dip simulator) were guillotined into 20mm x 10mm coupons. In the case of organically coated materials (used for investigations detailed in chapter 3) the coupons were immersed in dichloromethane to remove the PVC top coat. The coupons were subsequently pressure mounted in conducting bakelite. The bakelite served a dual purpose of allowing examination of the microstructure via a scanning electron microscope and providing a hard casing ensuring even polishing across the surface. Each sample was then subjected to rigorous investigations described below.

2.1.2. Investigation of microstructural evolution

2.1.2.1. Volume percentage of primary zinc

Samples for microstructural investigation were prepared as above. Initial investigations involved determining the average volume percentage of primary zinc solid solution phase within each coating. Each sample was polished down to a 1 μm diamond slurry and then etched using chromic acid to reveal the microstructure. By initially indenting a Vickers hardness diamond into the coating surface a method for measuring depth through the coating was facilitated. Using the diamond's indentation angle (136°) and applying simple trigonometry, the depth through the coating can be calculated from the size of the square imprint observed on the surface during polishing as shown in Figure 2.1. Hence images can be recorded and compared at like positions in different samples. Micrographs were recorded at different depths using a

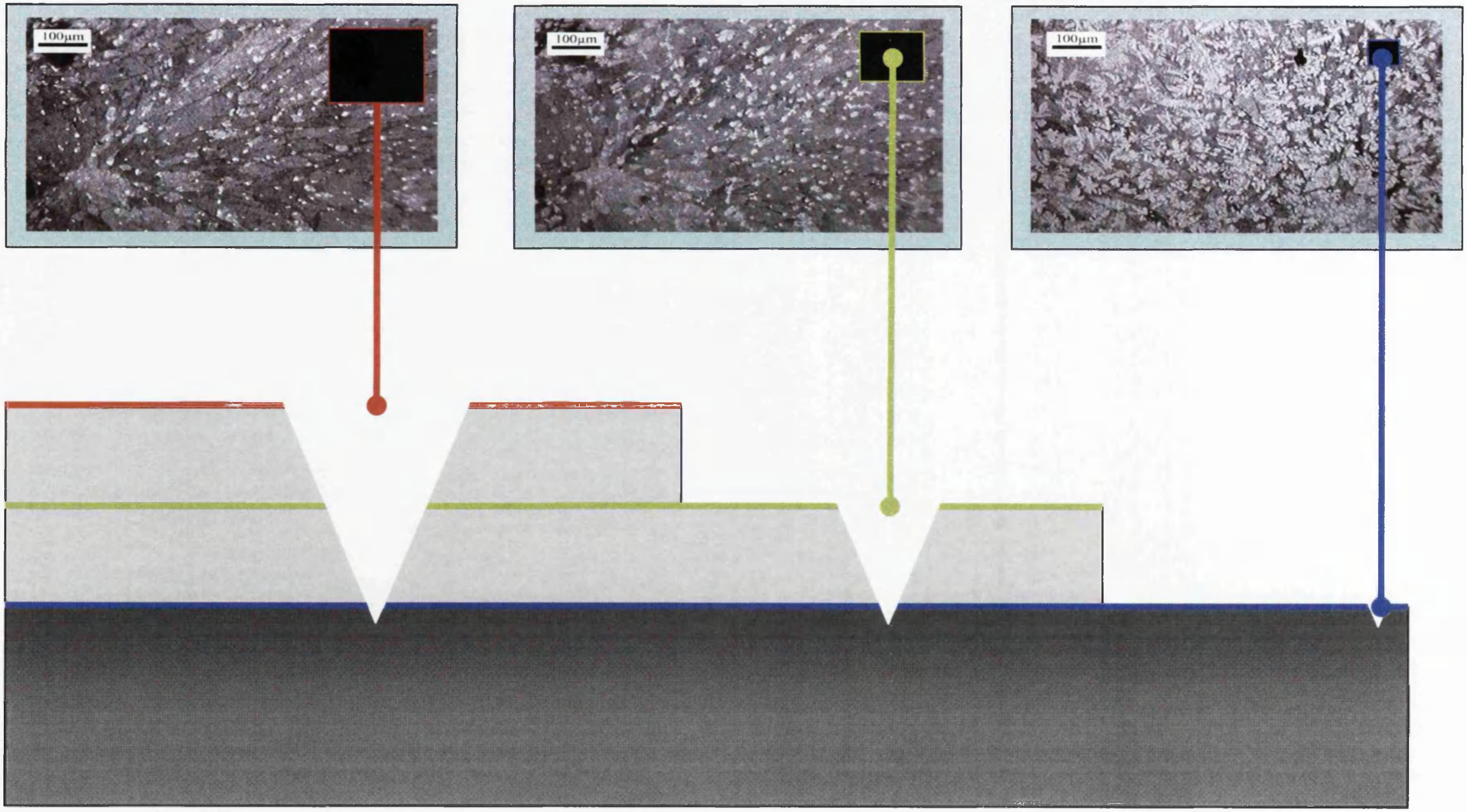

Figure 2.1. Calculation of depth through the metallic coating

Nikon coolpix digital camera (2.1 Mega pixel, 1600 x 1200 resolution) attached to a Reichert optical microscope. The images were then subjected to image analysis routines (using Sigma Scan Pro version 5.0) to calculate firstly the area percentage of the primary zinc phase at each level in the coating as in figure 2.2 and secondly the overall volume percentage by averaging all the values at all levels in the coating.

2.1.2.2. Average number of dendrites per mm^2

Images recorded as close as possible to the steel/coating interface (typically similar to those in figure 2.2) for the above calculations have been used to estimate the average number of primary zinc solid solution dendrites per square mm. Using the enhanced images, Sigma Scan Pro v.5 is able to count the number of enhanced objects designated by the user by means of overlaying an intensity threshold (shown in figure 2.2(3). Since the images are calibrated, the number of objects (in this case dendrites) are returned as a number per unit area. This figure is subsequently normalized to give the dendrite number per square mm.

2.1.2.3. Average dendrite size

In this circumstance the size of the dendrite refers to the average surface area (mm^2) of each solid crystal at the steel/ coating interface rather than the average size of the envelope surrounding each branched dendrite. To calculate the dendrite size, the area percentage of primary zinc at the steel/ coating interface (taken from calculations 2.1.2.1) was divided by the total number of dendrites (calculations 2.1.2.2.) within the aforementioned area. Assuming that the size of the dendrites remains relatively constant throughout the sample, an average size is determined.

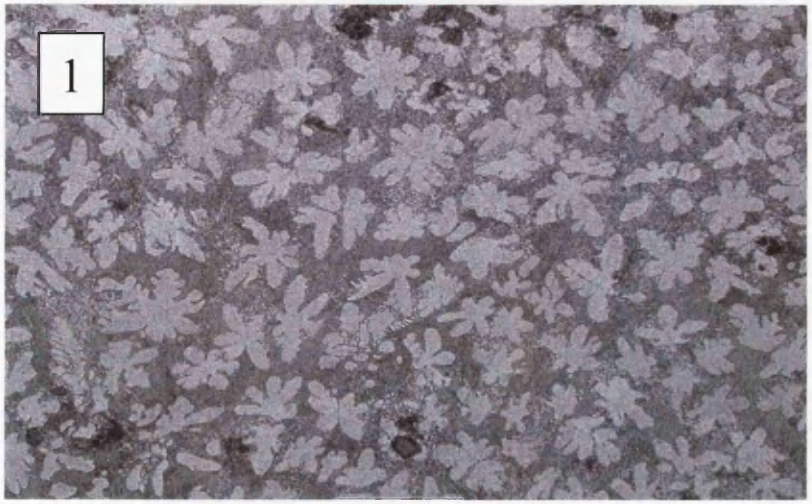

1. Image as recorded
2. Image after initial analysis
3. Area of primary zinc calculated by Sigma scan pro (V.5)

Figure 2.2 Calculation of area percentage of primary zinc

2.1.2.4. Measurement of the inter- lamellar and inter- rod eutectic spacing

As previously described (section 1.4.1) the expected structure of a binary Zn – Al eutectic is of lamellar morphology. Variations in the processing conditions or the addition of a ternary element may bring about a forced change from lamellar eutectic to a rod morphology. In both cases, a measure of the inter- lamellar or inter- rod spacing will yield information about the growth of the coating. Simple linear analysis was employed to accurately measure such spacings. Images of the eutectic were recorded at the steel/coating interface ($x1000$ magnification) using the Reichert optical light microscope. Each image was calibrated using a 1mm (divided into 100 divisions) standard (Ticules LTD, cs515) at the appropriate magnification. Importing the images into Sigma Scan Pro V.5 allows user defined lengths (using two point scaling) to be measured. In this instance, the distance across ten lamellae (or rods) was recorded and subsequently the mean average calculated. This process was repeated twenty times at various areas within the image. Finally the mean average of the twenty results was calculated and this value deemed to be the average inter-lamellar (or rod) spacing.

2.1.2.5. Calculation of the eutectic cell size ('spangle' size)

Measurement of the eutectic cell size again allowed information regarding nucleation of the two phase eutectic to be obtained. Defined areas of the unpolished air/ coating interface surface were digitally recorded using a Hewlett Packard Scanjet 5200C. The images were calibrated using a 1mm standard (Ticules LTD, cs515) and imported into Sigma Scan Pro V.5. Again linear analysis was employed to find the average cell (spangle) size. The distance across four cells was measured and the mean average calculated. The process was repeated ten times over various regions of the image and from these the mean average eutectic cell (spangle) size was derived.

2.2 Investigation of corrosion via the Scanning Vibrating Electrode Technique (SVET)

The SVET is an electrochemical technique which operates through the measurement of the vertical component of current flux in solution, at known points, above a corroding metal surface via a movable vibrating microtip electrode [1,2]. The basic wet corrosion cell is detailed in section 1.20.2. Due to reactions induced in the corrosion cell, the electrical connection provided by the metal substrate allows transport of electrons from the anodic to the cathodic sites. The discrete ions produced either form insoluble corrosion products or more often enter the electrolyte. The ionic current flow is again from the anodic to cathodic sites this time through the electrolyte. Since the conductivity of the metal is many orders of magnitude greater than that of the electrolyte, the distribution of ionic current facilitates ohmic potential gradients[3]. These potentials are generated by the ionic current flow (current flux). The vibrating probe converts the normal component of the potential into ac voltage by means of mechanical motion and can therefore register a signal [3]. The magnitude of the current flux is directly proportional to corrosion intensity and therefore the changes in corrosion activity are recorded.

2.2.1. Preparation of samples

2.2.1.1 Cut edge corrosion testing

For the cut edge corrosion measurements, panels were guillotined into 20 x 10mm coupons and were then embedded in Metset (polyester casting resin) so as to avoid any geometrical effects that might have been introduced as a result of differential organic coating thickness[4]. The resultant sample was then ground to reveal one metallic edge with the rest of the sample completely insulated from exposure to the electrolyte used for SVET testing. Before immersion in the electrolyte the edge to be exposed was polished using increasingly fine carborundum paper (down to 1200 grade). The edge was then subject to optical microscopic investigation to ensure that sample preparation had not lead to the formation of any crevices at the metal mounting material interface and that the exposed edge remained completely flat and scratch free. N.b. Metset was chosen rather than Bakelite since the latter has conducting capabilities making it unsuitable for corrosion measurements.

2.2.1.2. Surface corrosion testing

Samples prepared for surface corrosion investigations were first guillotined into 50mm x 50mm coupons. The SVET scan area used was typically a 9 x 9 mm in the centre of this coupon. To avoid corrosion activity occurring anywhere outside of the scan area, the samples were sealed with an extruded PTFE self adhesive tape (3M 5490). This tape was chosen since, in testing, it prevented any crevice corrosion occurring beneath it and also could be removed from the coupon after exposure without leaving an adherent residue. The transparency of the tape also allowed inspection to ensure no corrosion occurred in areas other than the exposed region. Hence one 50 x 50 mm coupon could be used to make several measurements of corrosion activity.

2.2.2. Measurement of corrosion using Scanning Vibrating Electrode Technique (SVET)

The SVET has been shown to be an invaluable tool in the mechanistic investigation of corrosion in organic coated steels[5,6,7,8] and specifically cut edge corrosion[9,10,11,12]. A schematic illustration of the equipment is shown in figure 2.3. The signal is measured by a 125μm platinum microdisc electrode which is encased in a 250μm glass sheath. The electrode is vibrated at a frequency of 140 Hz normal to the plane of the scan by a speaker isolated within the mu-metal (ensuring no magnetic flux leakage) head. The amplitude of vibration, measured using strobe lighting, is approximately 30μm at the applied drive voltage. This value can be compared with a mechanical amplitude of vibration derived theoretically.

$$F_{max} = \frac{i}{2\pi\kappa z^2}$$

Since $F_{max} = \Delta E / \Delta z$

$\Delta z = \Delta E / (i / 2\pi\kappa z^2) = \kappa /$ calibration factor

In such case as $\kappa = 70.1 \times 10^{-3}$ ohm^{-1} cm^{-1} and the derived calibration factor = 338000 Am^{-2} V^{-1}

$\Delta z = 20.7\mu m$

Δz is equivalent to the root mean square of the voltage implying that the actual amplitude is $2^{0.5}$ larger, giving an actual amplitude of 29.3μm.

The vibrational frequency is set by the lockin amplifier which is also used to record the measured signal. Computer controlled tri-axial stepper motors control the movement of the probe through the X,Y and Z directions, ensuring a consistent area is scanned over the surface.

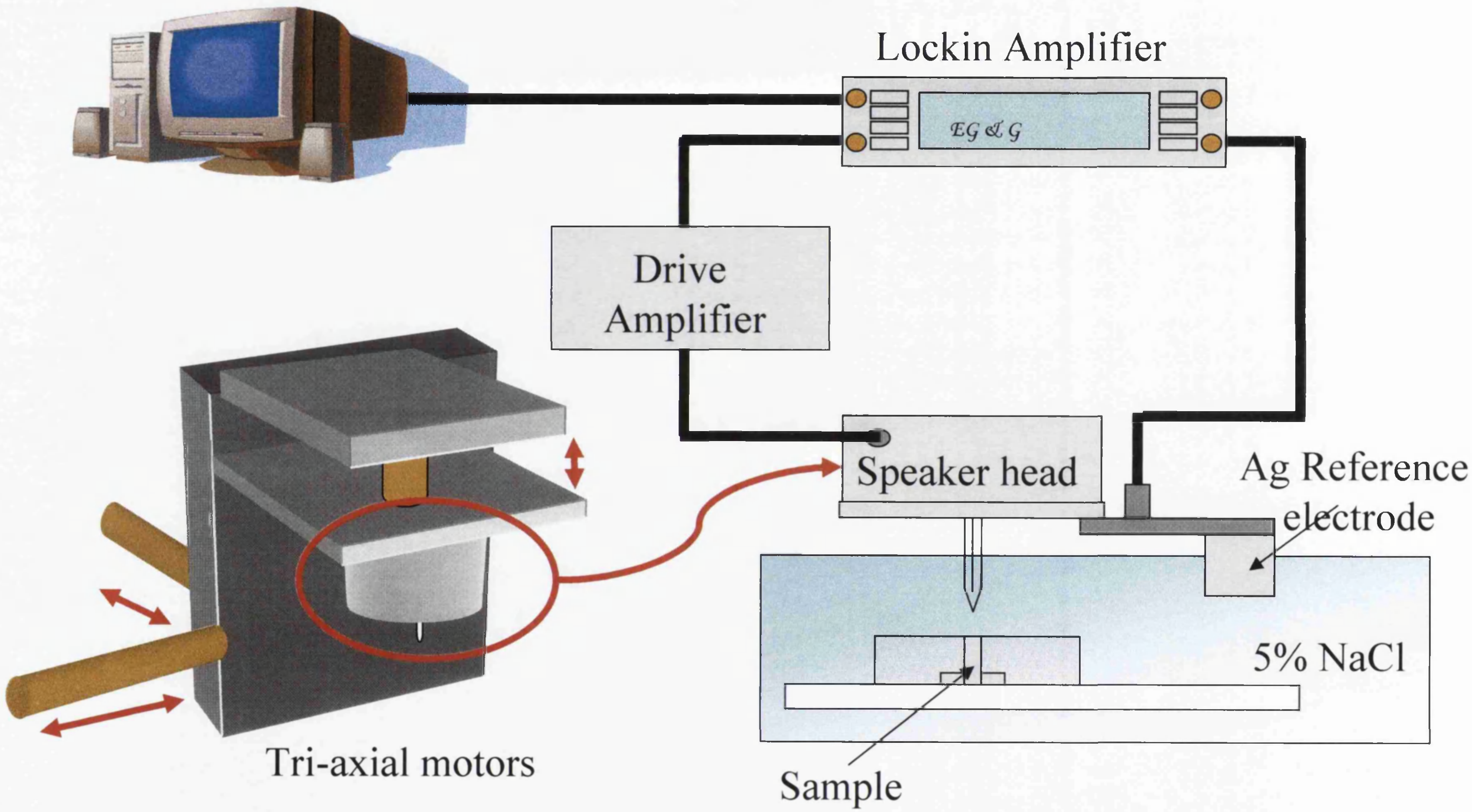

Figure 2.3. Schematic of SVET equipment

The sample under test is held vertically with the corroding surface horizontal and uppermost, immersed in a tank of aqueous sodium chloride electrolyte typically (5% (0.86 mol dm^{-3})), which is unstirred and open to the air. The dissolved oxygen concentration (in bulk solution) was assumed to be constant at 2.8 x 10^{-4} mol dm^{-3} (i.e. the equilibrium concentration for air saturated water)[13].

During the experimental period the sample is held upon a Perspex levelling table, shown schematically in figure 2.4. The triangular design allows independent height control of the sample through the X and Z planes. When used in conjunction with the vibrating probe, the height control allows the sample to be levelled ensuring it is perfectly horizontal. The height is determined by screws situated at the three corners of the triangle.

2.2.2.1 SVET Response for a Point Current Source

The SVET tip registers an alternating potential at the vibration frequency that is proportional to the electrical field strength, F, or potential gradient in the direction of vibration. It has been shown[14] for a point current source (i), the value of F at any distance x, y and z from the point source in a medium of conductivity κ is given by:

$$F = \frac{dE}{dz} = \frac{iz}{2\pi\kappa(x^2 + y^2 + z^2)^{1.5}} \qquad (1)$$

Furthermore, the maximum field strength (F_{max}) will be obtained when the SVET electrode is directly over the point source (x = y = 0):

$$F_{max} = \frac{i}{2\pi\kappa z^2} \qquad (2)$$

The SVET apparatus is calibrated using a point current source consisting of a platinum microdisc anode (25 μm diameter) set in an insulating plane and a remote, large area (2 cm^2), platinum gauze cathode. The calibration cell was immersed in

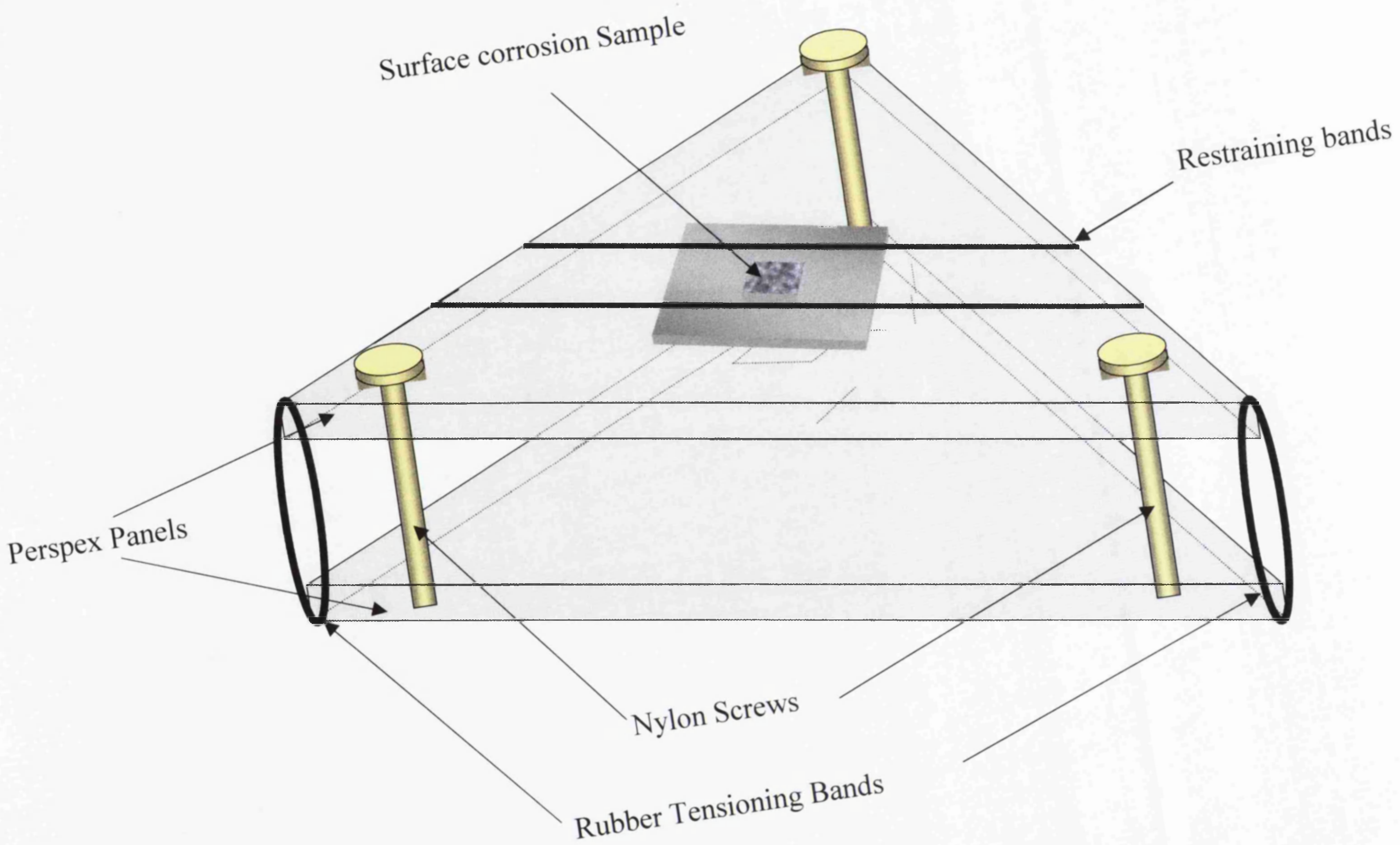

Figure 2.4. Schematic of levelling table used for SVET experimentation

0.86 mol dm^{-3} (5%) aqueous NaCl and known currents i (0.1-0.6μA) were passed through it using a galvanostat. The SVET probe was then scanned above the Pt microdisc anode at a constant height of 100 μm. The field strength distribution above the microdisc electrode exhibited the characteristic bell shape proportions reported previously [10,11] with a width at half maximum (*whm*) height of 0.27mm shown in figure 2.5. The maximum electrical field strength values, F_{max} were recorded when the SVET probe was directly above the microdisc anode and increased linearly with applied cell current, i (correlation coefficient 0.998). This produced a calibration factor of 3.38×10^5 $AV^{-1}m^{-2}$ (Figure 2.6.). This value was checked prior to each experiment using a point source incorporated within the sample holder.

The conductivity of 5% (0.86 mol dm^{-3}) NaCl at 20°C is 70.1×10^{-3} Ωcm^{-1} and substituting this value into equations (1) and (2) gives a theoretical value of the *whm* at $z = 100$ μm of 0.153 mm. This is approximately half of the experimental value of 0.27 mm (Figure 2.5,c). This departure from theoretical performance derives from the finite dimensionality of the SVET probe since the probe tip consists of a 125 μm microdisc electrode. As the calibration cell anode may be considered as a point current source with a *whm* value of 0.27 mm this value is an indication of the limiting spatial resolution of our SVET.

2.2.2.2 Data collection from the SVET

Raw data collected from the SVET is returned as grid files in the units of nV which can be converted to V. By multiplying this data by the calculated calibration factor and realising using cartography software (surfer v.6) a 'map' of corrosion activity in Am^{-2} is produced (Figure 2.5 a & b, anodic activity shown as yellow,

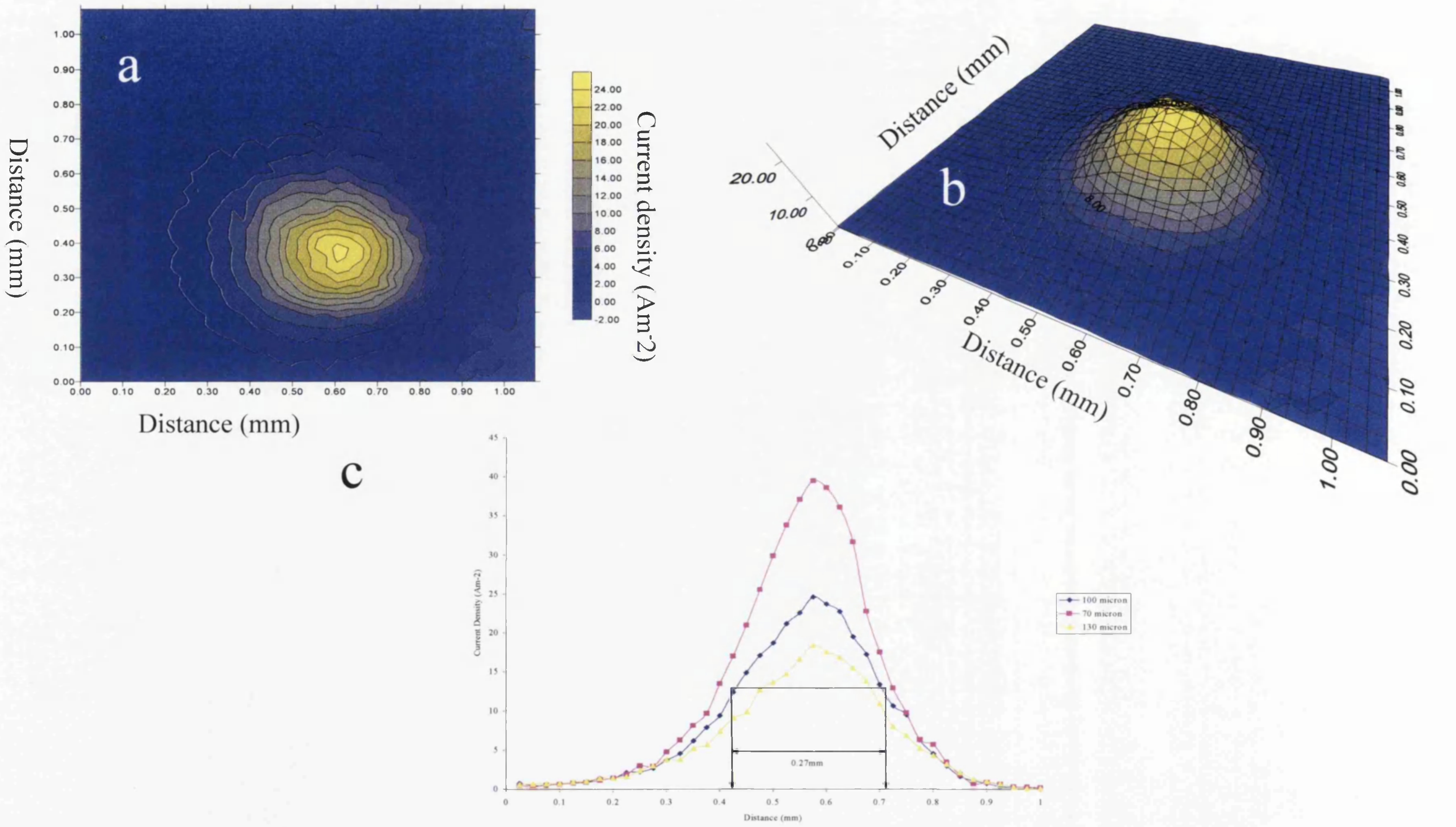

Figure 2.5. Characteristic bell shape distribution of current density around point source

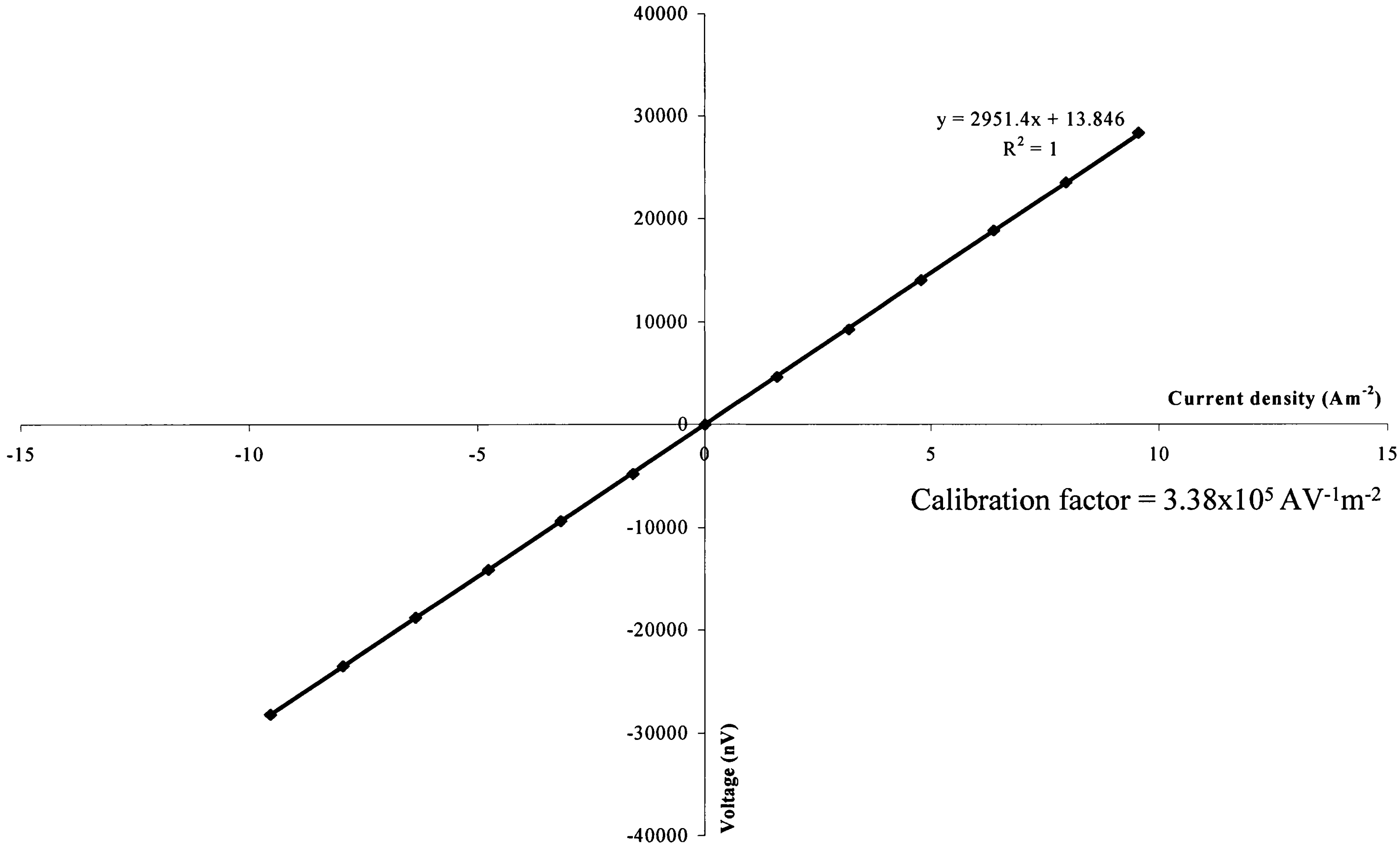

Figure 2.6. Typical calibration plot for the SVET, 1/m = calibration factor

cathodic activity shown as blue). These maps will be subsequently referred to as Iso-current density maps. Hence, by comparing iso-current density maps produced over a 24 hour period, it is possible to determine changes in the corrosion activity occurring across the surface throughout the experimental life. The data retrieved from such maps is useful (the intensity (current density, Am^{-2}) of corrosion activity can be compared between samples) but without greater in-depth analysis is limited. Therefore novel methods have been devised to adapt the raw data and iso-current density maps into meaningful results describing not just the corrosion activity but lifetimes and intensities of individual anodes and the respective metal loss associated with such events.

Previous work[15,16] has determined that preferential corrosion occurs upon the primary zinc dendrites in Galfan. Therefore the metal loss associated with corrosion events throughout this body of work will be described as total zinc loss (*tzl*). This value is calculated from the grid files under the assumption that the corrosion activity remains constant over the period between scans. Integration of the raw data (nV) (again using surfer v.6) returns the data values in $nVmm^2$. The software is able to distinguish between positive and negative values hence separating the positive anodic activity (in terms of ionic current) from negative cathodic activity. The 'volume' of positive and negative data from each scan is therefore calculated. Positive data (i.e. the anodic volume) is converted from $nVmm^2$ into nVm^2 and subsequently multiplying by the calculated calibration factor gives a value in amps. Multiplying this value by the time of 1 hourly scan (3600 seconds) converts the data into charge. The charge can be converted into mass using Faraday's law and the knowledge of the corroding ions' charge and atomic weight, i.e.:

$$tzl = (Q/\ nF)\ x\ A$$

where Q = charge (C)

F = Faraday's constant, (96485 C/mol)

n = no. of electrons lost during corrosion (2 for Zn)

A = atomic weight, (65 for Zn)

Thus, the total zinc loss is the sum of each scan through the experimental life.

Although a number of assumptions are made for this calculation, recent studies[17] have shown that for Galfan and for zinc galvanised steels the calculation gives a reasonable approximation of zinc loss in chloride solution. This reflects the predominance of local corrosion in spatially resolved situations. One potential limitation is when the anodic and cathodic sites are physically close to each other and cannot be resolved by SVET.

By determining the location of each new anodic event it is possible to compare the variation in intensity of corrosion at a single point during each hour of the experimental period. Hence, it is possible to a.) Determine the lifetime of each anode and b.) Assess the variation in intensity of corrosion during the lifetime of each anode. This data is graphically represented in the form of 'residual plots' detailing corrosion intensity, anodic lifetimes and the number of active anodes throughout the experimental period. From these results the change in corrosion mechanisms relating to variation in the local microstructure can be investigated further.

Further to highlighting the importance of anode lifetimes and intensities the residual plots can also indicate the contribution to the overall zinc loss of each corroding site. Due to the unique isolation of primary zinc along the cut edge, it can be assumed that each anodic site is equivalent to a single point source. Hence, from fig 1.11, (chapter 1) it can be seen that the field of current flux radiates hemispherically about the anodic site. Given a constant SVET scan height of 100μm, it is possible to measure the average intensity (Current density, Am^{-2}) of each anode. Therefore by dividing the current density by the surface area of a hemi-sphere a value is returned in amps. From this value in amps it is possible to calculate a zinc loss from the individual anodes via the methodology described above.

2.2.2.3 Limitations of SVET

As with most novel techniques the SVET and associated analysis routines have a few limitations of usage. The iso-current maps detailed earlier can essentially be viewed as a 'snapshot' of corrosion at a given time. A single scan is produced over approximately 15 minutes. Due to the nature of activation and passivation of corrosion activity it is possible that certain anodic events are missed by the scanning probe. Therefore, the value of corrosion recorded by the SVET is somewhat smaller than the actual activity occurring. Hence, the SVET is described as semi- quantitive, giving an indication of the trends of corrosion activity as opposed to actual values. That said, for galvanised steels in sodium chloride solution the SVET measured and ICPMS measured zinc losses differ only by ca 20%.

2.3 Hot Dip Simulator (HDS)

Recent work [18,19,20,21] completed using the hot dip simulator (HDS) has proven it to be an excellent method of recreating hot dip coatings observed in continuous galvanising within a laboratory environment. The Iwatani Rhesca machine is able to simulate a wide variety of processing conditions from changes in coating mass through to increased line speeds and cooling rates. Suitable for use with a wide range of commercial steel gauges, it was deemed to be an excellent method of experimenting with the Galfan composition without the need for potentially expensive line trials.

The simulator comprises of three main parts: the simulating unit shown in Figure 2.7, a gas mixing station and the computer controlled processing station.

The entire dipping process is controlled via a computer. Details of the required simulation routine (e.g. bath entry temperature, pot temperature, dwell time etc) are inputted into a program from which the relevant instructions are relayed to the various units within the simulator. Selected details (i.e. times and temperatures) of the sample's progress are logged graphically and can be viewed to ensure the simulator is functioning effectively. The computer program also controls the flow of gases (typically nitrogen and hydrogen) that are introduced into the system. By varying the flow rate and mixture of these gases the coating weight can be controlled and various furnace conditions may be simulated[22].

Steel sections used in the simulator are typically guillotined into panels of dimensions 200mm x 120mm. After rigorous chemical cleaning (using acetone), K type thermocouples are spot welded onto the panel which is subsequently attached to a drive rod (situated within the loading chamber) allowing precision control into each part of the unit. Once secured, the sample is manoeuvered into the infra red heating furnace. Here the sample is heated to ca 400°C before cooling to the designated entry temperature and being submerged into the molten alloy. After dwelling for a required time (hence simulating the line speed of the standard process), the sample is withdrawn through gas knives, which determine the coating weight and the rate at which the coating solidifies, and returns to the loading chamber where it is air cooled to room temperatures.

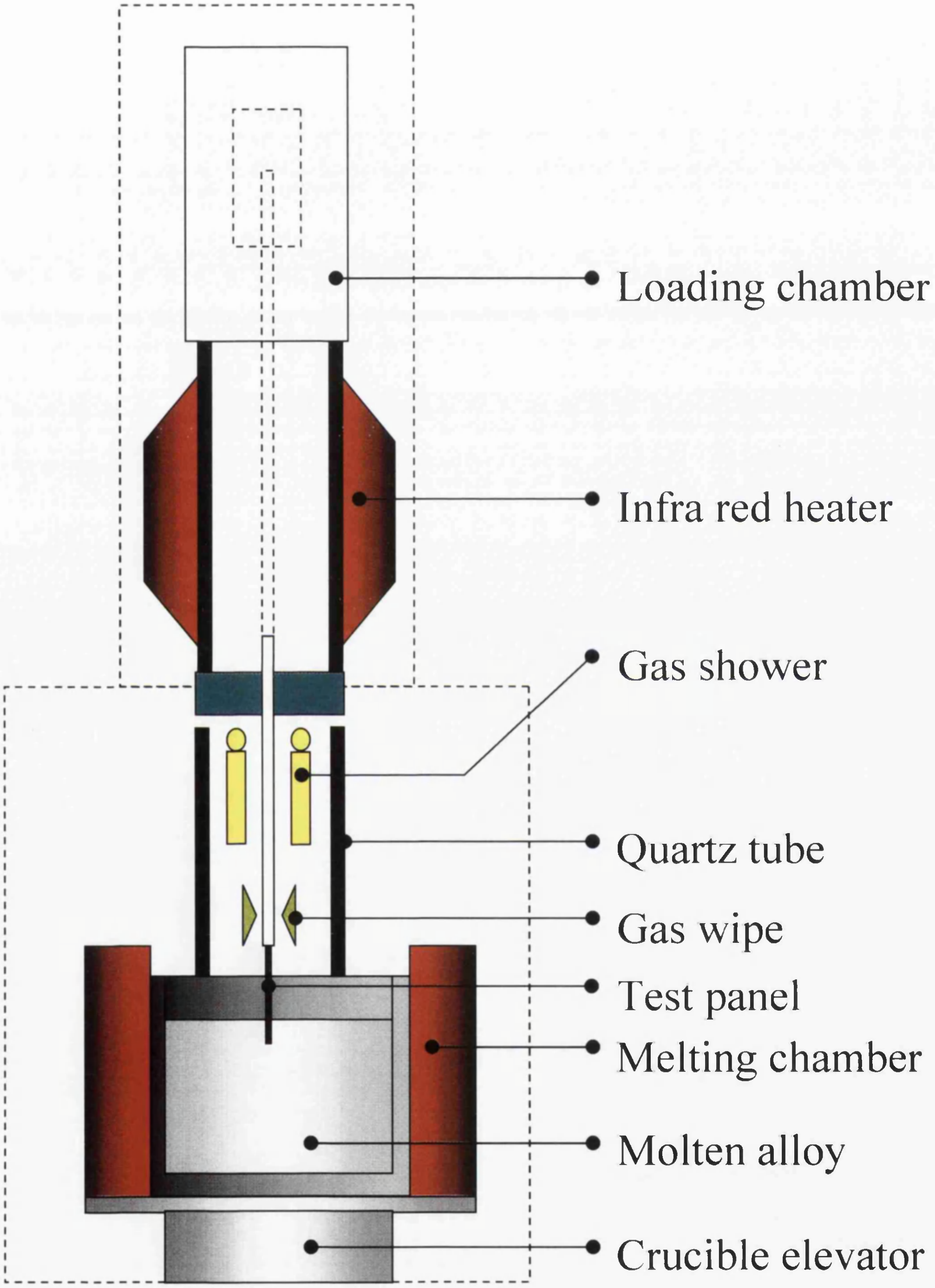

Figure 2.7. Schematic of the processing unit of the hot dip simulator

2.4 Specifications of materials investigated

As previously detailed the major driving force behind this body of research was to determine the relationship between the microstructure and corrosion resistance of Galfan coatings existed. Upon satisfactory completion of the initial drivers, the emphasis of the work progressed into adapting the microstructure to enhance the corrosion protection and hence laying foundations for the best possible product for Corus.

Detailed below are the specifications and production methods for all materials investigated. Materials designated as 'produced by a dedicated line trial' (those for chapters 4 and 5) were produced at Corus Colors, Shotton at the specific request and under supervision of the author. Those materials generated upon the Rhesca Hot dip simulator were processed at the Engineering Centre for Materials and Manufacturing (ECM^2), Corus Strip Products, Port Talbot.

2.4.1 Generic materials

Material	Supplier	Purity
Sodium Chloride (NaCl)	Sigma – Aldrich	99% +
De – ionized water	In-situ	

2.4.2 Materials relevant to specific research

2.4.2.1 Materials relevant to investigations into short term run off prediction

Sample Designation	Organic Coating	Primer	Pre - treatment	Steel gauge	Coating Mass	Comment
G1	PVC Plastisol	Crown	B1303/ P62	0.7mm	255gm^{-2} (~ 20μm)	Unknown processing conditions. i.e. the use (or not of an enhanced cooling rig to solidify coating
G2	PVC Plastisol	Beckers	B1303/ P62	0.7mm	255gm^{-2} (~ 20μm)	Unknown processing conditions. i.e. the use (or not of an enhanced cooling rig to solidify coating
G3	PVC Plastisol	Crown	G768/41	0.7mm	255gm^{-2} (~ 20μm)	Unknown processing conditions. i.e. the use (or not of an enhanced cooling rig to solidify coating
G4	PVC Plastisol	Beckers	G768/41	0.7mm	255gm^{-2} (~ 20μm)	Unknown processing conditions. i.e. the use (or not of an enhanced cooling rig to solidify coating

2.4.2.2 Materials relevant to investigations into the effect of cooling rate and steel gauge

Sample Designation	Organic Coating	Processing conditions	Steel Gauge	Coating Mass	Comment
UG55H	Bare material	Sample rapid cooled at 55% of maximum possible cooling rate	0.67mm	255gm^{-2} (~ 20μm)	Samples produced as part of organized line trial – June 2002
UG80H	Bare material	Sample rapid cooled at 80% of maximum possible cooling rate	0.67mm	255gm^{-2} (~ 20μm)	Samples produced as part of organized line trial – June 2002
UG100H	Bare material	Sample rapid cooled at maximum possible cooling rate	0.67mm	255gm^{-2} (~ 20μm)	Samples produced as part of organized line trial – June 2002
UG55L	Bare material	Sample rapid cooled at 55% of maximum possible cooling rate	0.47mm	255gm^{-2} (~ 20μm)	Samples produced as part of organized line trial – June 2002
UG80L	Bare material	Sample rapid cooled at 80% of maximum possible cooling rate	0.47mm	255gm^{-2} (~ 20μm)	Samples produced as part of organized line trial – June 2002
UG100L	Bare material	Sample rapid cooled at maximum possible cooling rate	0.47mm	255gm^{-2} (~ 20μm)	Samples produced as part of organized line trial – June 2002

2.4.2.3 Materials relevant to the effect of coating weight

Sample Designation	Organic Coating	Processing Conditions	Steel Gauge	Coating Mass	Comment
CT170	Bare Material	All processing conditions remain constant. Gas knives used to reduce coating Mass	0.7mm	170gm^{-2} (~ 15μm)	Samples produced as part of organized line trial – December 2003
CT130	Bare Material	All processing conditions remain constant. Gas knives used to reduce coating Mass	0.7mm	130gm^{-2} (~ 12μm)	Samples produced as part of organized line trial – December 2003
CT100	Bare Material	All processing conditions remain constant. Gas knives used to reduce coating Mass	0.7mm	100gm^{-2} (~ 9μm)	Samples produced as part of organized line trial – December 2003
CT80	Bare Material	All processing conditions remain constant. Gas knives used to reduce coating Mass	0.7mm	80gm^{-2} (~ 7μm)	Samples produced as part of organized line trial – December 2003

2.4.2.4 Materials relevant to investigations of low level Mg additions

Sample Designation	Organic Coating	Processing Conditions	Steel Gauge	Coating Mass	Comment
MGHDS00 4% Al 96% Zn	Bare material	All conditions remain constant for each sample	0.7mm mild steel	255gm^{-2} (~ 20μm)	Samples produced upon Rhesca Hot dip simulator
MGHDS01 4% Al, 0.01% Mg. Remainder Zn	Bare material	All conditions remain constant for each sample	0.7mm mild steel	255gm^{-2} (~ 20μm)	Samples produced upon Rhesca Hot dip simulator
MGHDS02 4% Al, 0.02% Mg. Remainder Zn	Bare material	All conditions remain constant for each sample	0.7mm mild steel	255gm^{-2} (~ 20μm)	Samples produced upon Rhesca Hot dip simulator
MGHDS03 4% Al, 0.03% Mg. Remainder Zn	Bare material	All conditions remain constant for each sample	0.7mm mild steel	255gm^{-2} (~ 20μm)	Samples produced upon Rhesca Hot dip simulator
MGHDS04 4% Al, 0.04% Mg. Remainder Zn	Bare material	All conditions remain constant for each sample	0.7mm mild steel	255gm^{-2} (~ 20μm)	Samples produced upon Rhesca Hot dip simulator
MGHDS05 4% Al, 0.05% Mg. Remainder Zn	Bare material	All conditions remain constant for each sample	0.7mm mild steel	255gm^{-2} (~ 20μm)	Samples produced upon Rhesca Hot dip simulator

Sample Designation	Composition	Produced
MGC00	4.5% Al, remainder Zn	University of wales, Swansea
MGC05	4.5% Al, 0.05% Mg remainder Zn	University of wales, Swansea
MGC1	4.5% Al, 0.1% Mg remainder Zn	University of wales, Swansea

2.4.2.5 Materials relevant to investigations into varying Al level

Sample Designation	Organic Coating	Processing Conditions	Steel Gauge	Coating Mass	Comment
AL4.7	Bare material	All conditions remain constant for each sample	0.7mm mild steel	$90gm^{-2}$ ~ 8μm	Samples produced upon Rhesca Hot dip simulator
Al8.6	Bare material	All conditions remain constant for each sample	0.7mm mild steel	$90gm^{-2}$ ~ 8μm	Samples produced upon Rhesca Hot dip simulator

2.5 References

---

1 H.S. Isaacs and B. Vyas, Electrochemical Corrosion Testing, 3 (1981).

2 H.N. McMurray and D. Worsley: Advances in Chemical Kinetics, (ed. R.G. Compton and G. Hancock), 4, 149. (1997)

[3] H.S. Isaacs: J.Electrochem. *Soc*,138, 722,(1991)

[4] D. Worsley, A. Belghazi and S. M. Powell: Ironmaking and Steelmaking, 26, 387, (1999)

[5] H.S. Isaacs: Corrosion,43, 594,(1987)

[6] I. Sekine, M. Yuasa, K. Tanaka, M. Fuke and L. Silao: Journal of the Japanese Society of Colour Materials,65, 684,(1992)

[7] D. Thierry and F. Zou: Proceedings of the 4th International Conference on Zinc and Zinc Alloy Coated Steel Sheet (GALVATECH '98), 376, (1998)

[8] H.S. Isaacs, A.J. Aldykiewicz, D. Thierry and T.C. Simpson: Corrosion,52, 163,(1996)

[9] F. Zou, C. Barreau, R. Hellouin, D. Quantin and D. Thierry: Materials Science Forum, 289, 83, (1998)

[10] D. Worsley, H.N. McMurray and A. Belghazi: J. Chem. Soc., Chem. Commun, 2369 (1997).

[11] S. M. Powell and D. A. Worsley, British Corrosion Journal, 36, 42 (2001)

[12] S. Bohm, H.N. McMurray, S.M. Powell and D.A. Worsley: Electrochimica Acta, 45, 2165. (2000)

[13] A. Bonnel, F. Dabosi, C. Delouis, M. Dupart, M. Kedam and B. Tribollet: J. Electrochem. Soc.,130, 753, (1983)

14 H.S. Isaacs: Advances in Localised Corrosion, 221,(1988).

[15] D A Worsley and M Challis, British Corrosion Journal, 36, 297, (2001)

[16] M. Challis, T. Heatley and D.A. Worsley, Corrosion and Corrosion Protection – Proceedings of the International Symposium

[17] J.H. Sullivan, H.N. McMurray, I.M Williams and D.A Worsley, Corrosion, NACE, 2003

[18] D. L. Wakeman, *Thesis (Eng.D.)* - University of Wales Swansea, *2003.*

---

[19] S. Price, Studies of the aluminium inhibition layer in galvanneal, Thesis (Eng.D.) - University of Wales Swansea, 1999.

[20] Simon O'Dell, *Thesis (Eng.D.)* - University of Wales Swansea, *2003*

[21] F. Hinterberger, W. Maschek and J. Faderl, Zinc Based Steel Coating Systems: Production and Performance, 281, (1998)

[22] Faulk technical manual

Chapter 3

Short term predictive testing for cut edge corrosion resistance in zinc aluminium alloy galvanised steels

3.0 Introduction

Increasing demand from the users of sheet steel materials for lightweight down-gauged steels are leading to a requirement for more corrosion resistant galvanising chemistries. In particular, organically coated steels (OCS) for construction are now largely based on new zinc galvanising coatings containing *ca.* 4.5% aluminium. As has been described in chapter 1, this coating system demonstrates superior corrosion resistance and better ductility[1] than conventional systems[2] where aluminium is only included at very low levels (ca 0.15%) as a means of preventing iron/zinc intermetallic formation[3]. Painted and scribed panels coated with 4.5% aluminium galvanising layers show superior corrosion resistance[4] generally displaying two to three times the performance of conventional coated galvanised steel sheet containing 0.15% Al.

The increased corrosion resistance of these coatings is also advantageous from an environmental perspective since external exposure will lead to less corrosion and, consequently, less metal ion runoff. Recent studies at Swansea university[5] and by others[6], have highlighted that the Galfan (5%Al) and Galvalume (55%Al) coatings demonstrate far lower levels of zinc metal ion runoff than conventional hot dip, electroplated or annealed hot dip coatings. They therefore present minimal environmental risk as well as improved performance.

Evaluation of the external weathering properties of the Galfan (Zn – 4.5wt% Al) coated steels has been previously reported[5,7]. It is the purpose of this body of work to explore the link between these zinc runoff levels under external weathering conditions and the total zinc loss, determined using the SVET under laboratory conditions, in 24 hours. It is a further aim to ascertain whether these relatively short term measurements can be correlated with organic coating delamination under external weathering since this form of 'cut edge' corrosion is responsible for over half of all commercial failures reported[8].

Table 2.4.2.1 lists the materials used to investigate the above relationships between laboratory and external exposure assessed corrosion behaviour. The samples were obtained from Corus Colors, Shotton, and are archive material from early galfan trials. Consequently the processing parameters and line conditions are unknown. Without such knowledge, it is impossible to elucidate the causes of any microstructural changes. Processing and line conditions can cause dramatic changes to the galfan microstructure as will be discussed in chapters 4, 5 and 6. here though the aim was to relate external exposure data to short term tests.

3.1 Results and Discussion

3.1.1 Microstructural observations

Before describing the microstructures it is prudent to describe the macrostructure. Under low magnification, etched in 1% Nital, a distinct growth pattern is observed with radial growth of the eutectic cells. The growth of a cell is terminated upon impingement with neighbouring cells. The boundaries of the individual cells are defined through the visible change in orientation of the cell structure and the depression surrounding each cell. The depressions are the result of solidification shrinkage and are described elsewhere[9] and in section 1.9.

The microstructure is quantified from determining the following: a.) the volume percentage of primary zinc, b.) the size and number of the primary dendrites, c.) changes in the eutectic spacing and d.) changes in the eutectic cell size.

The chemical compositions for each sample are shown in Table 3.1.

Sample Identity	Al(%)	Mg(%)	Fe(%)
G1	3.46%	0.04%	1.51
G2	3.48%	0.04%	1.65
G3	3.62%	0.01%	1.58
G4	3.43%	0.04%	1.28

Table 3.1 Sample coating composition analysis obtained by acid dissolution & ICPMS analysis

Figure 3.1 a-d shows typical micrographs of each coating at three different depths. At a depth of approximately 3 μm below the coating surface the expected two phase microstructure is present. The primary zinc dendrites (optically white regions) can be seen together with the two phase eutectic. The dendrites typically appear globular with no obvious branching and the eutectic is of rod morphology. At the steel/coating interface, a depth of ~18 μm, there is a clear increase in the volume percentage of the primary phase. The dendrites at this depth are clearly branched and the eutectic microstructures of samples G1, G2 and G4 are of rod morphology, whereas sample G3 displays a mixture of rod and lamellar eutectic.

3.1.2 Changes in the volume percentage of primary zinc

The increase in volume percentage of primary zinc as a function of depth into the coating is shown in figure 3.2. In each of the samples there is a considerable increase of the primary zinc from approximately 10% of the total area close to the air/ coating interface to between 43-55% near to the steel/coating interface. The fact that the majority of the primary zinc is at the interface region infers that nucleation of the zinc crystals is occurring near to the steel substrate.

By consideration of the volume percentages observed as a function of coating depth it is possible to calculate a value for the total volume percentage of primary zinc through the entire coating. These results are shown in figure 3.3. It is clear that the total volume percentage of primary zinc for samples G1 and G2 is almost identical with values of 27.8 % ± 0.2% and 27.6 % ± 0.2% respectively. The volume percentage figure rises to 28.2 % ± 0.2% in G3 and further again in G4 to 30.2 % ± 0.2%.

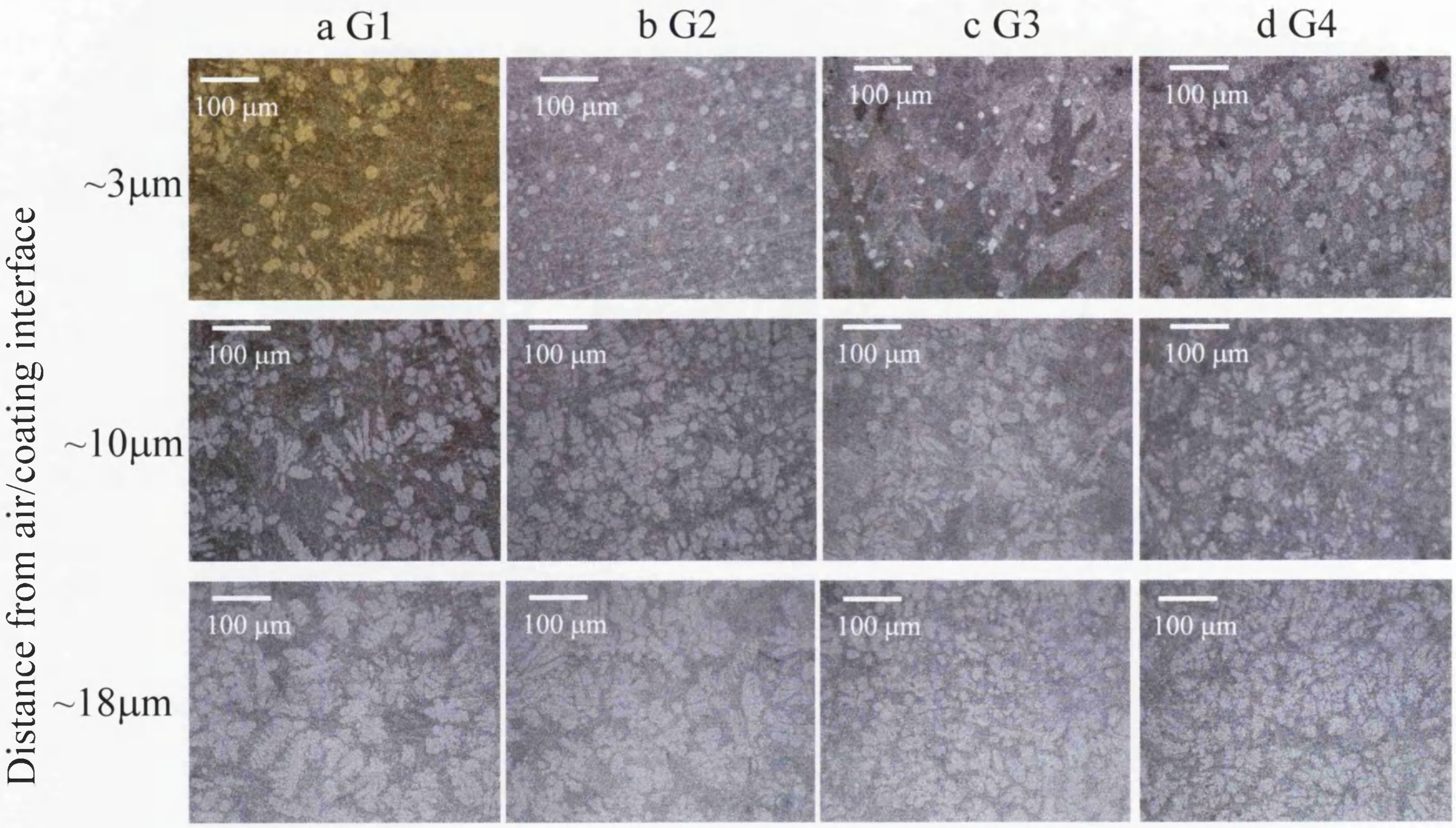

Figure 3.1 Coating microstructures as a function of depth from the air/coating interface

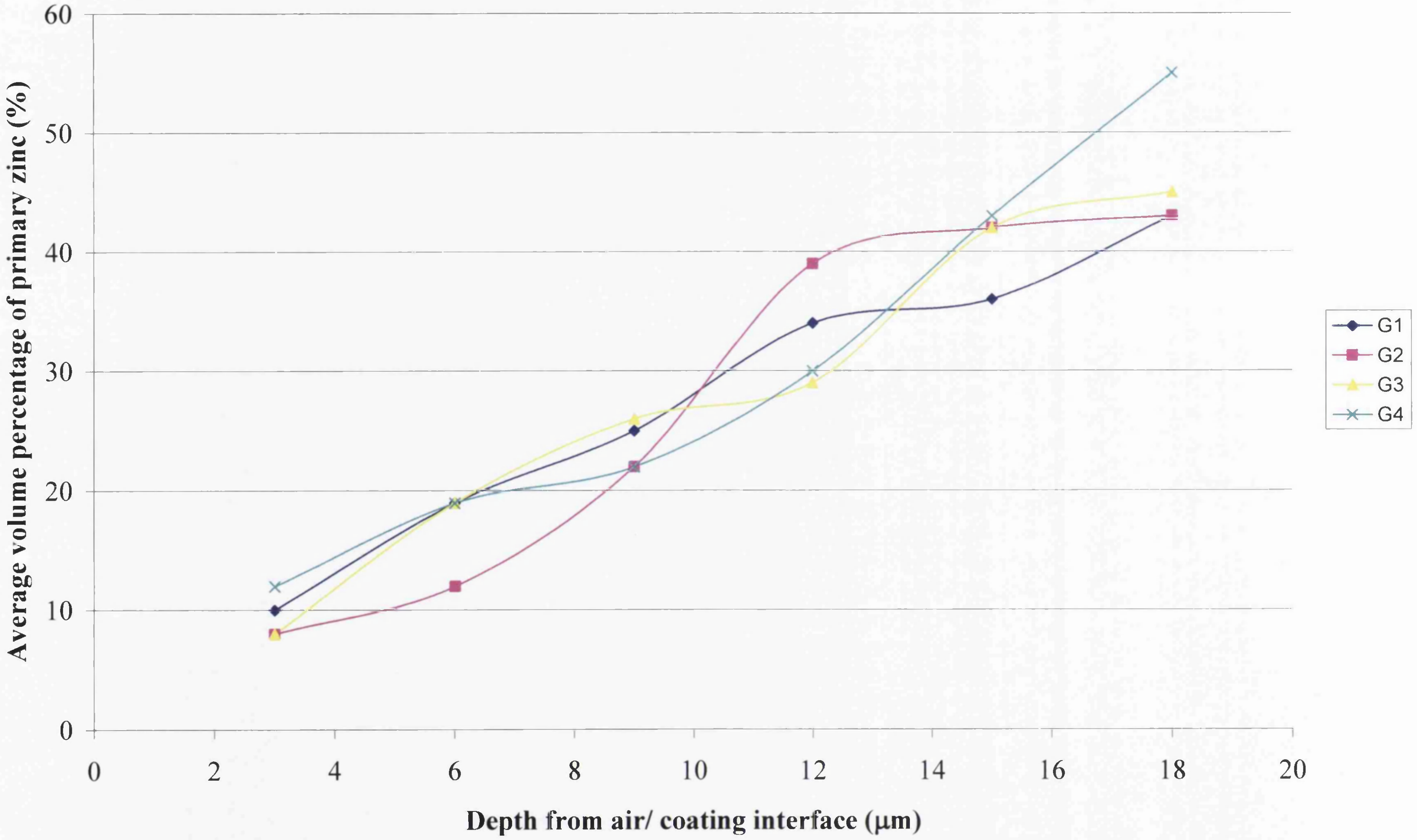

Figure 3.2 Average volume percentage of primary zinc as a function of depth through coating

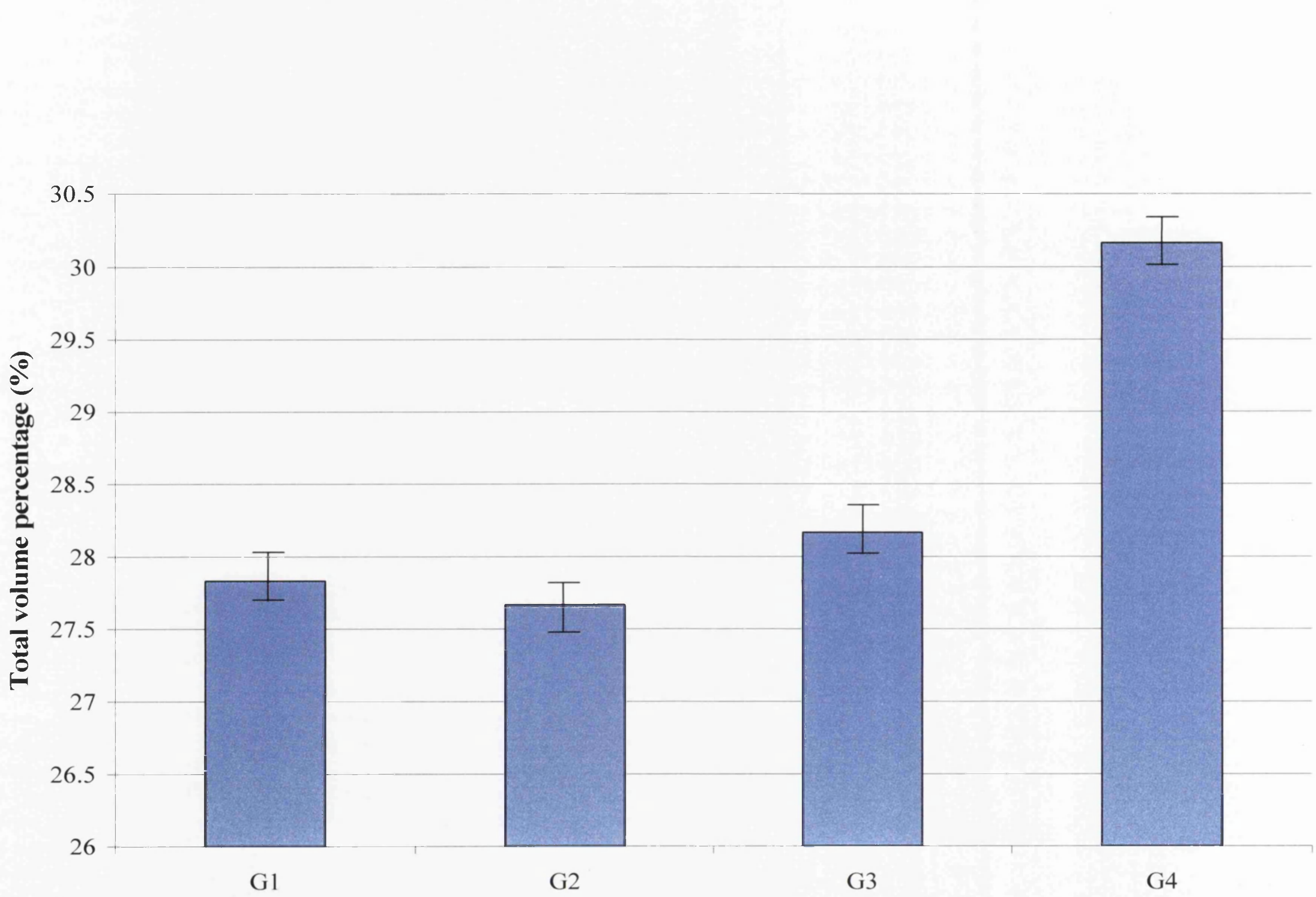

Figure 3.3 Average total volume percentage of primary zinc

3.1.3 Changes in the number and size of the primary zinc dendrites

Figure 3.4 details the number of dendrites per square millimetre recorded near to the steel/ coating interface. It is evident that there is a dramatic difference in this number between the different samples. G1 returns the least number with 650 ± 50 dendrites per mm^2 followed by G2 with 720 ± 50 dendrites per mm^2. Samples G3 and G4 return the highest figures with 914 ± 50 and 1604 ± 50 dendrites respectively. It is clear that one or more of the processing conditions is altering to significantly influence nucleation in this way, but without the relevant information the change in dendrite number cannot be explained.

By dividing the area percentage of primary zinc phase per mm^2 recorded near to the steel/ coating interface of each sample by the corresponding dendrite number per mm^2 an approximate size (area) of the individual dendrites can be calculated. These results are shown in figure 3.5. It is clear from these results that the dendrites in G1 (0.00012 mm^2) are greater in area than those in G2 (0.00011 mm^2), G3 (0.00009 mm^2) and G4 (0.00006 mm^2).

3.1.3 Changes in the eutectic spacing

Figure 3.6 shows the changes in the eutectic spacing (for the rod morphology) recorded close to the steel/ coating interface. Sample G1 has an inter-rod spacing of 8.88 μm ± 0.03 compared to 6.76 μm ± 0.02 in G2. This figure is subsequently reduced to 6.13 μm ± 0.02 in G3 but rises to 7.32 μm ± 0.03 in G4. The eutectic in sample G3 also has an inter-lamellar spacing of 6.16 μm ± 0.02. The appearance of rod eutectic is consistent with data presented later in the thesis following the addition of Mg to the Zn – Al binary system[10]. The mixed morphology within sample G3 (the sample with least Mg, figure 3.1) has also been observed in other research and is detailed in chapter 6.

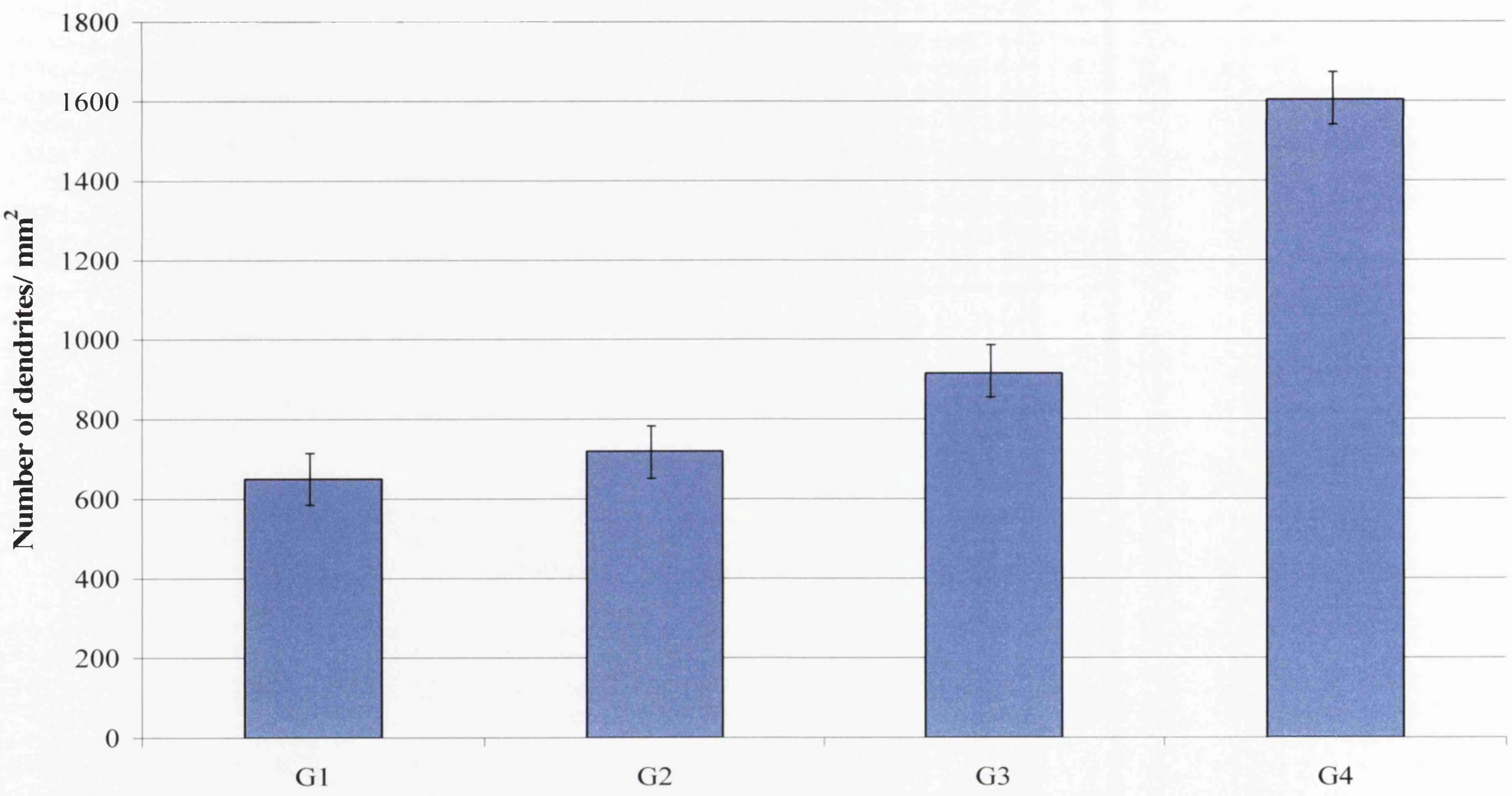

Figure 3.4 Average number of dendrites per mm^2 near to the steel/ coating interface

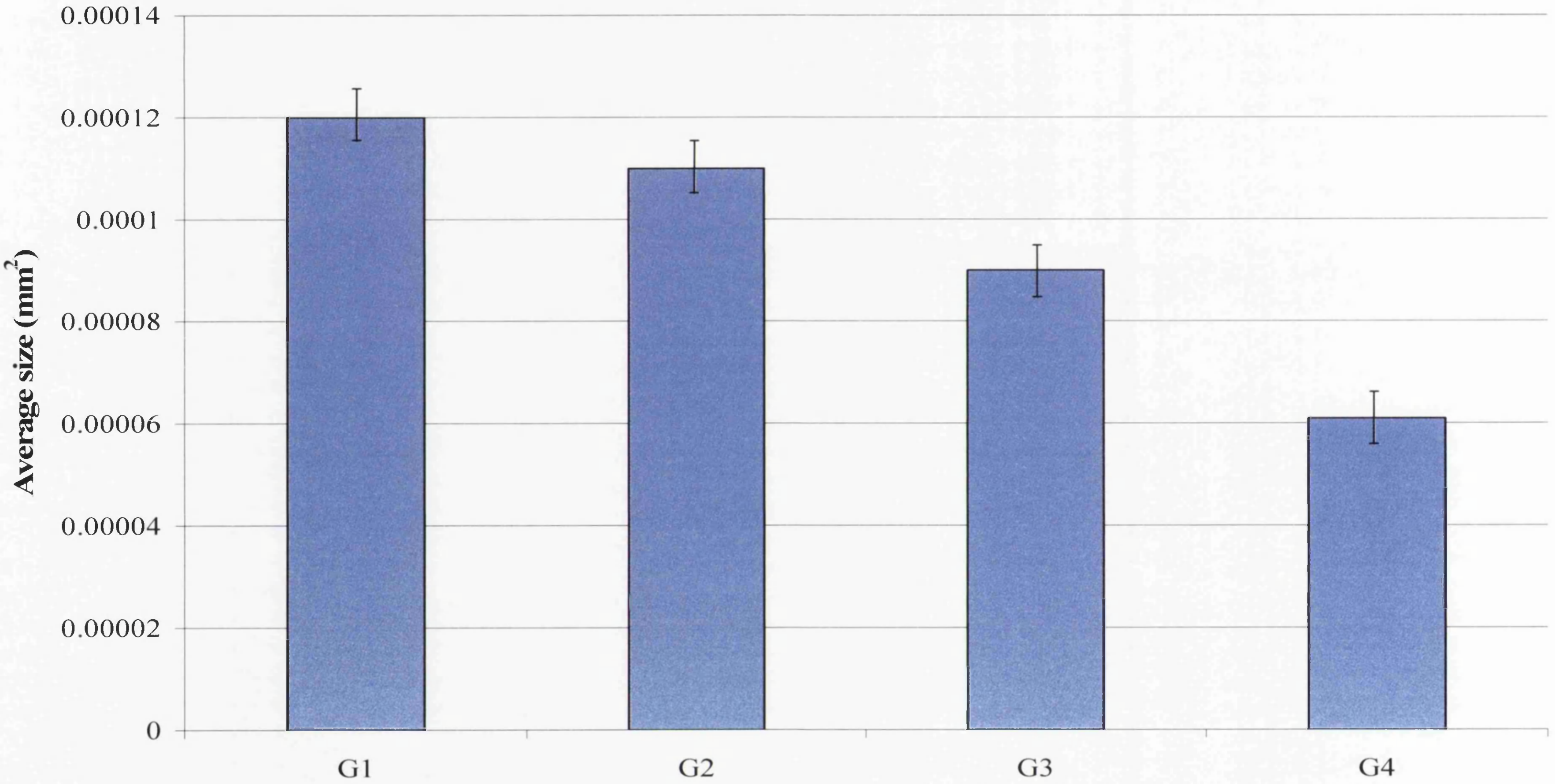

Figure 3.5 Average area of individual dendrites near to the steel/ coating interface

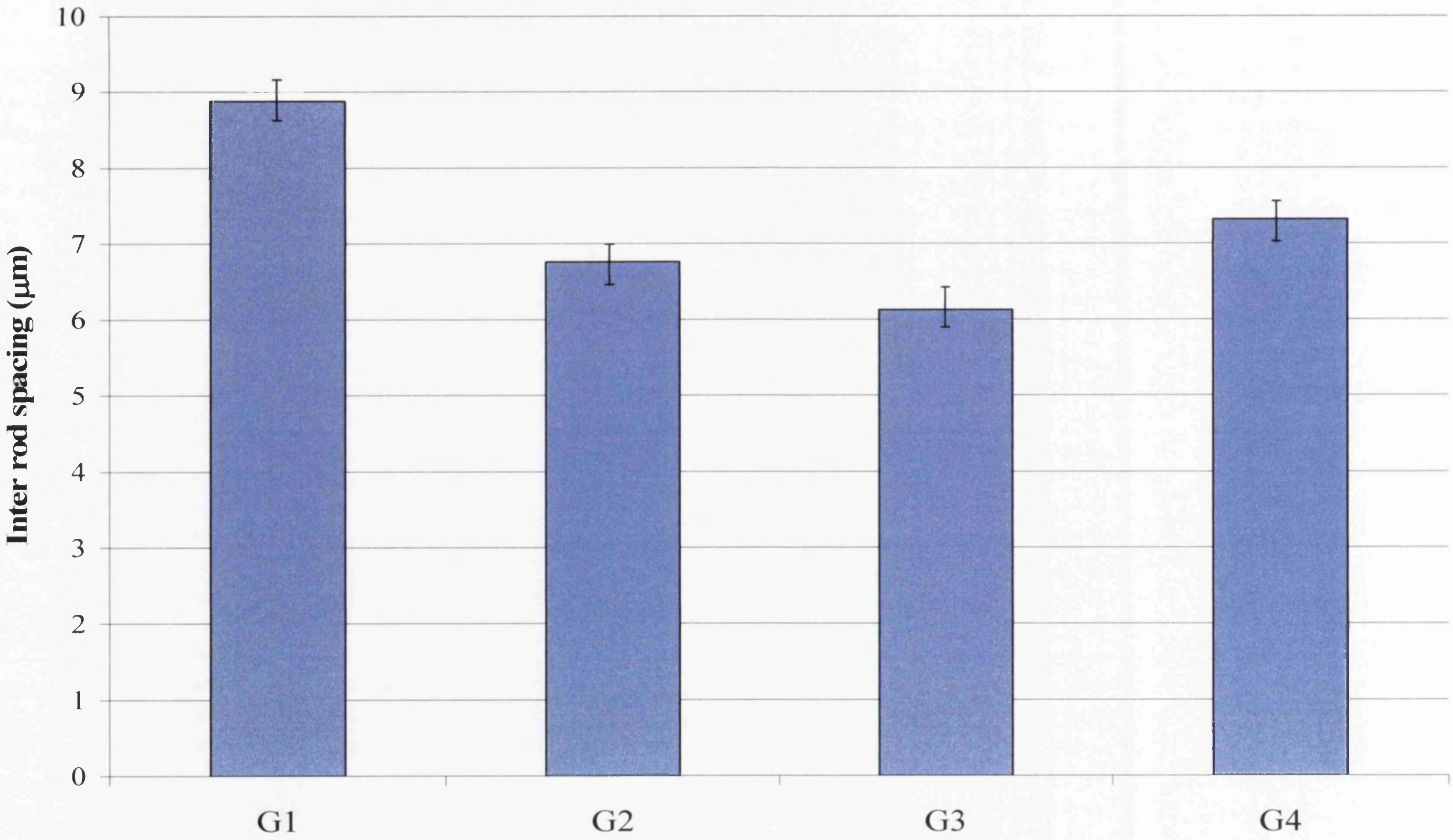

Figure 3.6 Average inter- rod spacing recorded near to the steel/ coating interface

3.1.3 Changes in the eutectic cell size (Spangle size)

Using Dichloromethane, the PVC organic top coating was removed to reveal to galvanised surface. Using the methodology described in section 2.1.2.5 the eutectic cell size was measured. These results are detailed in figure 3.7. Sample G1 has an average cell size of 1.17mm ± 0.05mm which increases to 1.35mm ± 0.05mm in sample G2. Both G3 and G4 have similar cell sizes with 2.62mm ± 0.05mm and 2.6mm ± 0.05mm respectively. Again, since the processing conditions are unknown reasoning for these changes cannot be offered.

3.1.4 Location and intensity of anodic activity along the coating cut edge

Figure 3.8 shows representative SVET iso-current density plots produced whilst scanning the cut edge of the individual samples G1-G4 after 12 hours immersion. The anodic areas (dark colours) are situated on the immediate edges of the cathodic activity (light colours) indicating that the Galfan coating is sacrificially protecting the base steel substrate.

There is an increase in the corrosion activity in particular for samples G3 and G4. Previous work[11,12] has shown that it is the primary zinc phase that will preferentially corrode. From the SVET plots it is possible to convert the current density data (in the plane of scan) into zinc loss data per hour and subsequently into total zinc loss (*tzl*). The results of such a treatment are shown in figure 3.9 and the average of five SVET measurements of *tzl* are compared with the average volume percentage of primary zinc measured in Figure 3.10. There is a broad trend to increasing SVET measured *tzl* as the volume fraction of primary zinc is increased. Figure 3.11 shows the relationship between the number of dendrites per mm^2 and the

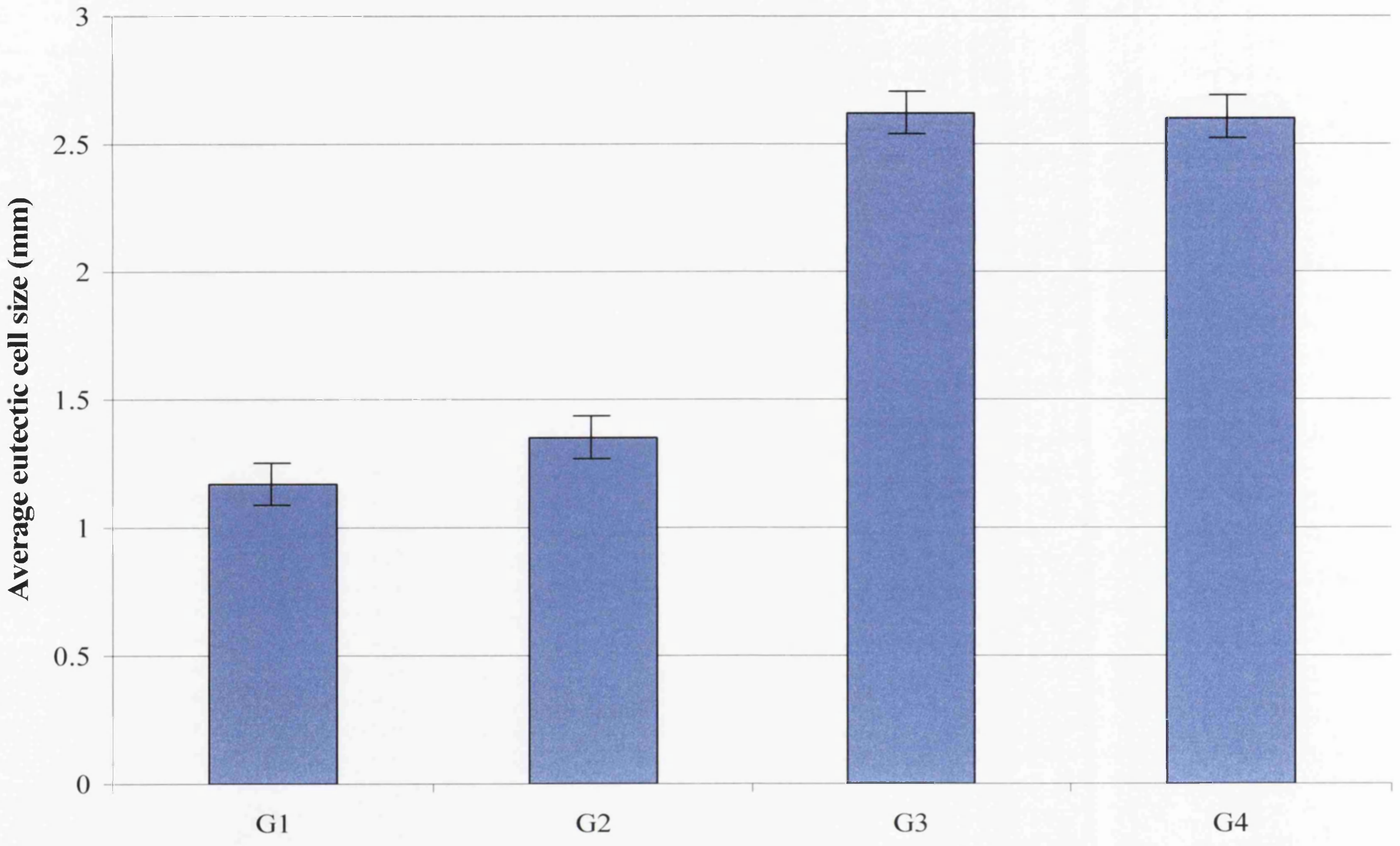

Figure 3.7 Average eutectic cell size recorded at the air/ coating interface

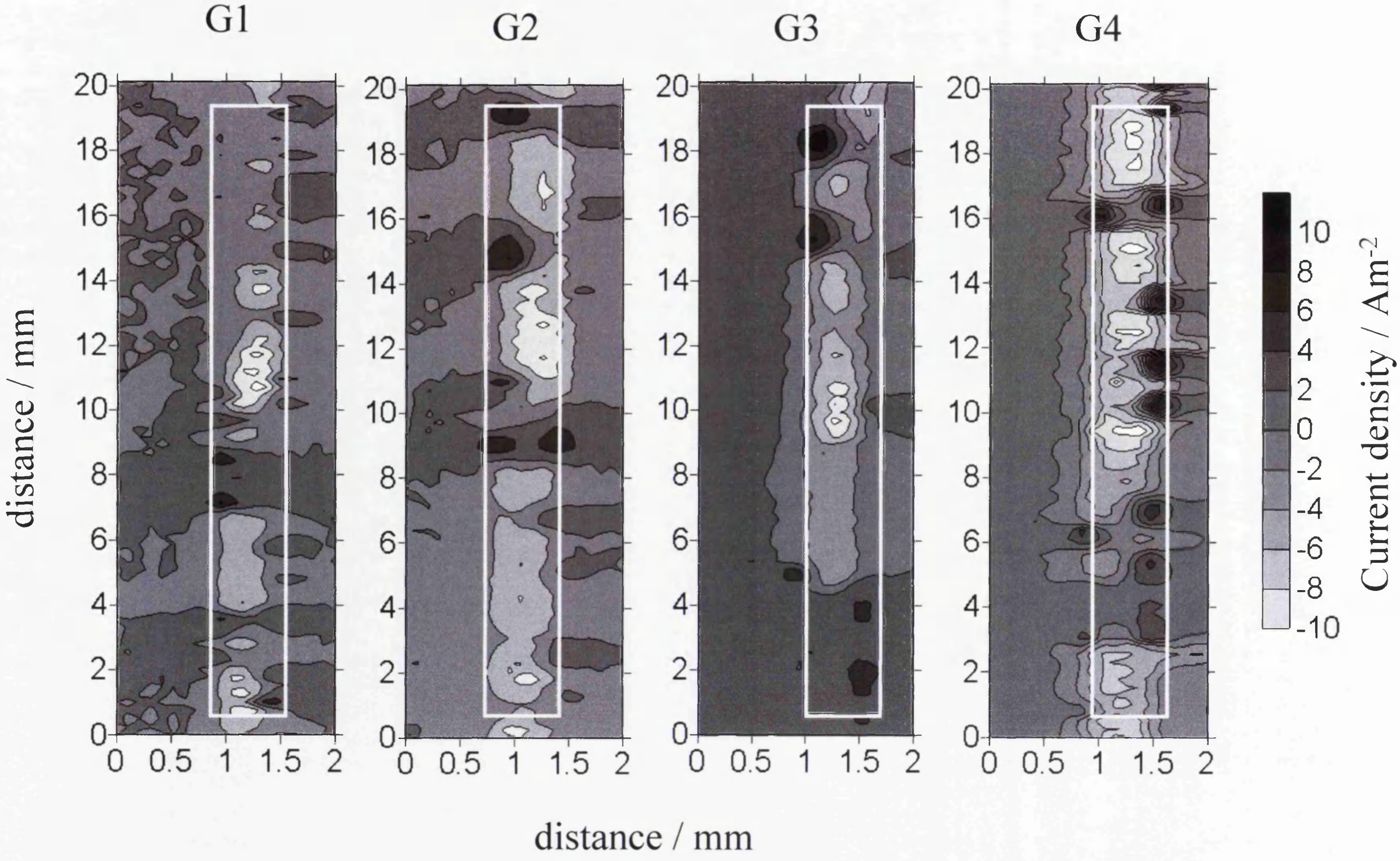

Figure 3.8 Representative Iso- current density maps after 12 hours immersion

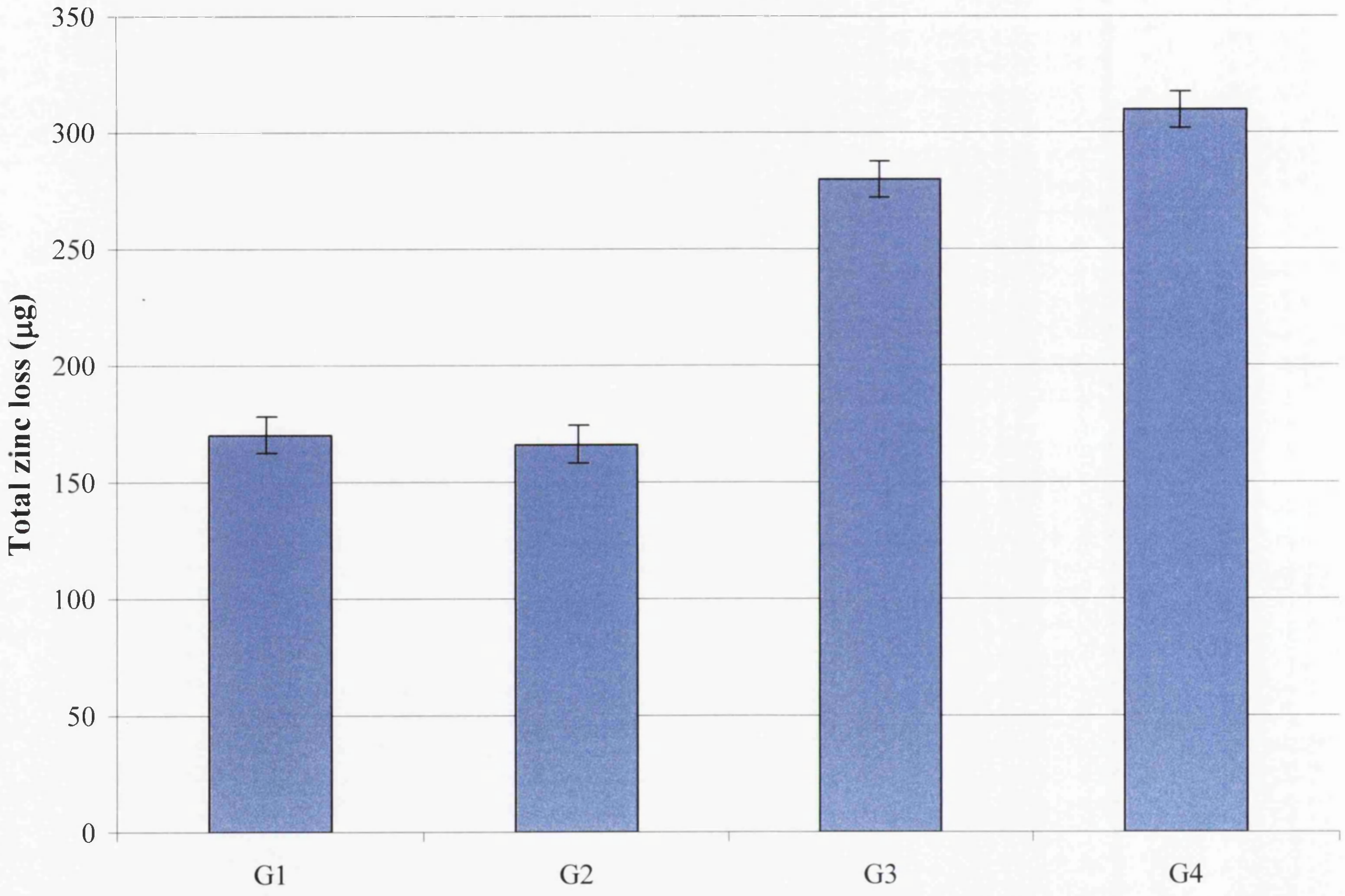

Figure 3.9 Total zinc loss recorded from the sample cut edge

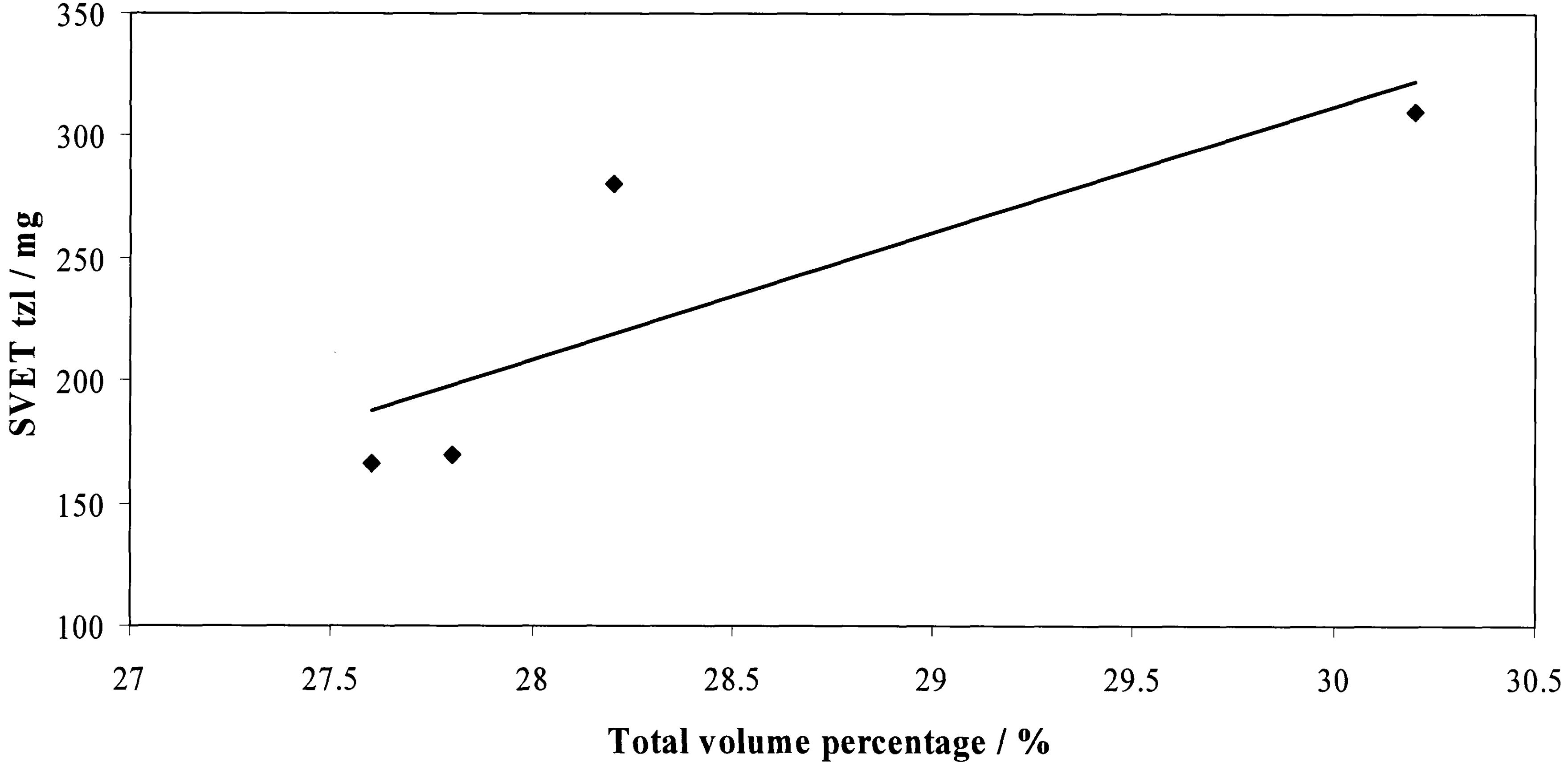

Figure 3.10 Total zinc loss as a function of total volume percentage of primary zinc

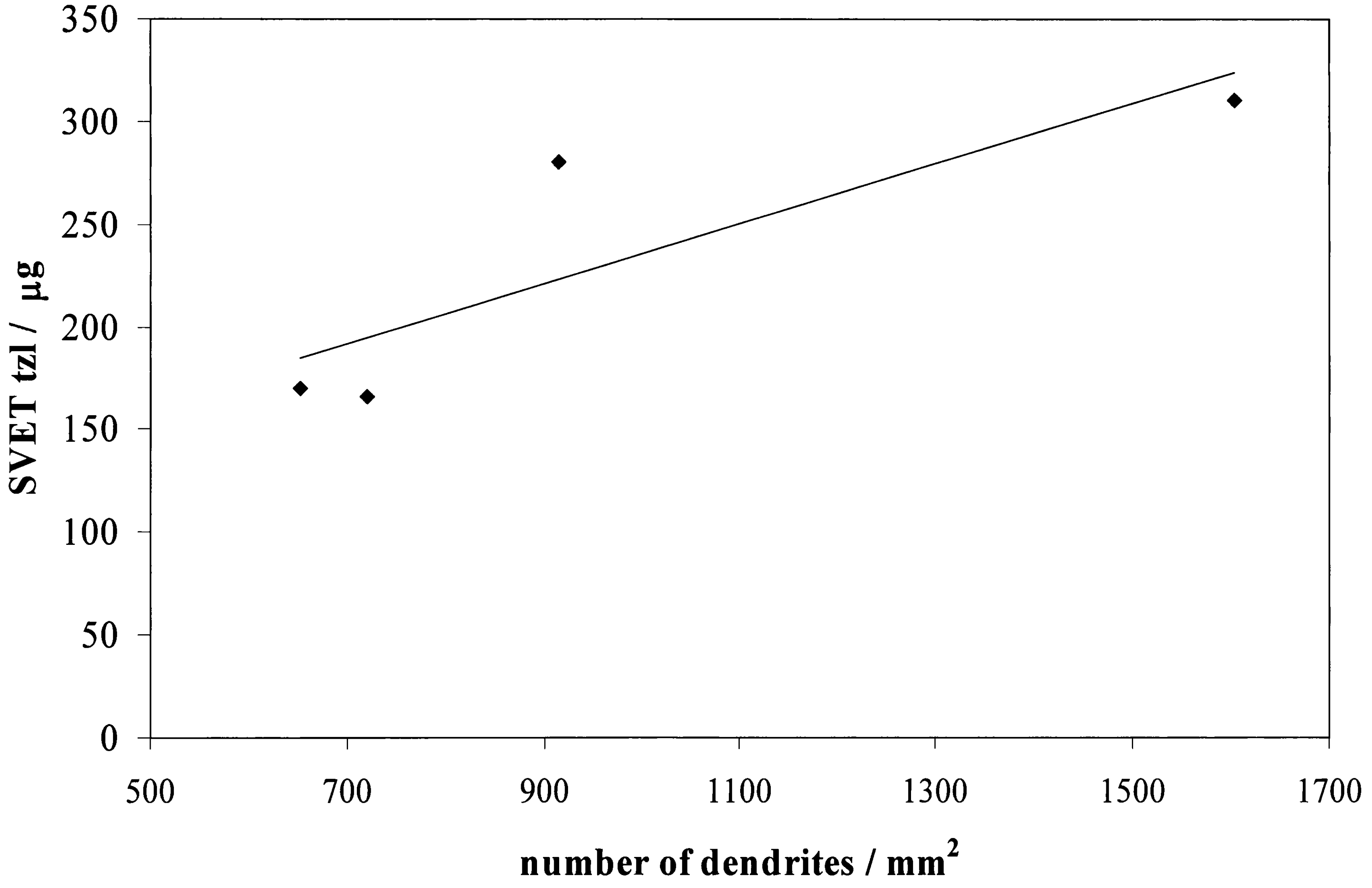

Figure 3.11 Total zinc loss as a function of dendrite number

tzl from the cut edge and from this plot it is also clear that the number of dendrites as well as their overall total volume fraction influences the intensity of anodic activity.

This increase in zinc loss can be related to the individual anode activities as shown in figure 3.12 a and b for samples of G2 and G4 (the least and most active) respectively. Here the individual current densities associated with individual anodes have been plotted as a function of immersion time. All the samples show similar anode plots to this with the majority of anodes active throughout the immersion period. The difference is in the anode currents which are greater for the G4 sample leading to greater zinc loss per anodic event. This is highlighted in Figure 3.13 which represents the sum of anodic activity from each anode as a function of material type. The samples showing greater corrosion resistance have fewer anodes of lower activity. From figure 3.13 it is also possible to calculate the amount of corrosion activity resulting from individual anode corrosion or *tizl*. This data is included in Table 3.2 and it can be seen that the *tzl* and *tizl* values although following a similar trend are not of the same absolute magnitude. Firstly it should be noted that the *tizl* calculation is quite time consuming and data is presented for only one sample of each type here. The major reason for the apparently lower *tizl* value is, however, that this method requires individual anodes to be identified and does not account for non point source corrosion of the zinc or any movement of an anode as material is consumed. Here these issues contribute to *tizl* values typically only one third of *tzl*. Previously we have shown that SVET measured *tzl* and ICPMS measurement of dissolved zinc in the immersion bath agree well over the 24 hour period of the test[5]. Hence the *tzl* method appears superior (and is much more easily performed) than *tizl*. That said, anode lifetime profiles, such as those illustrated in figure 3.12, are useful in determining the persistence of anodic events in one place on the immersed material.

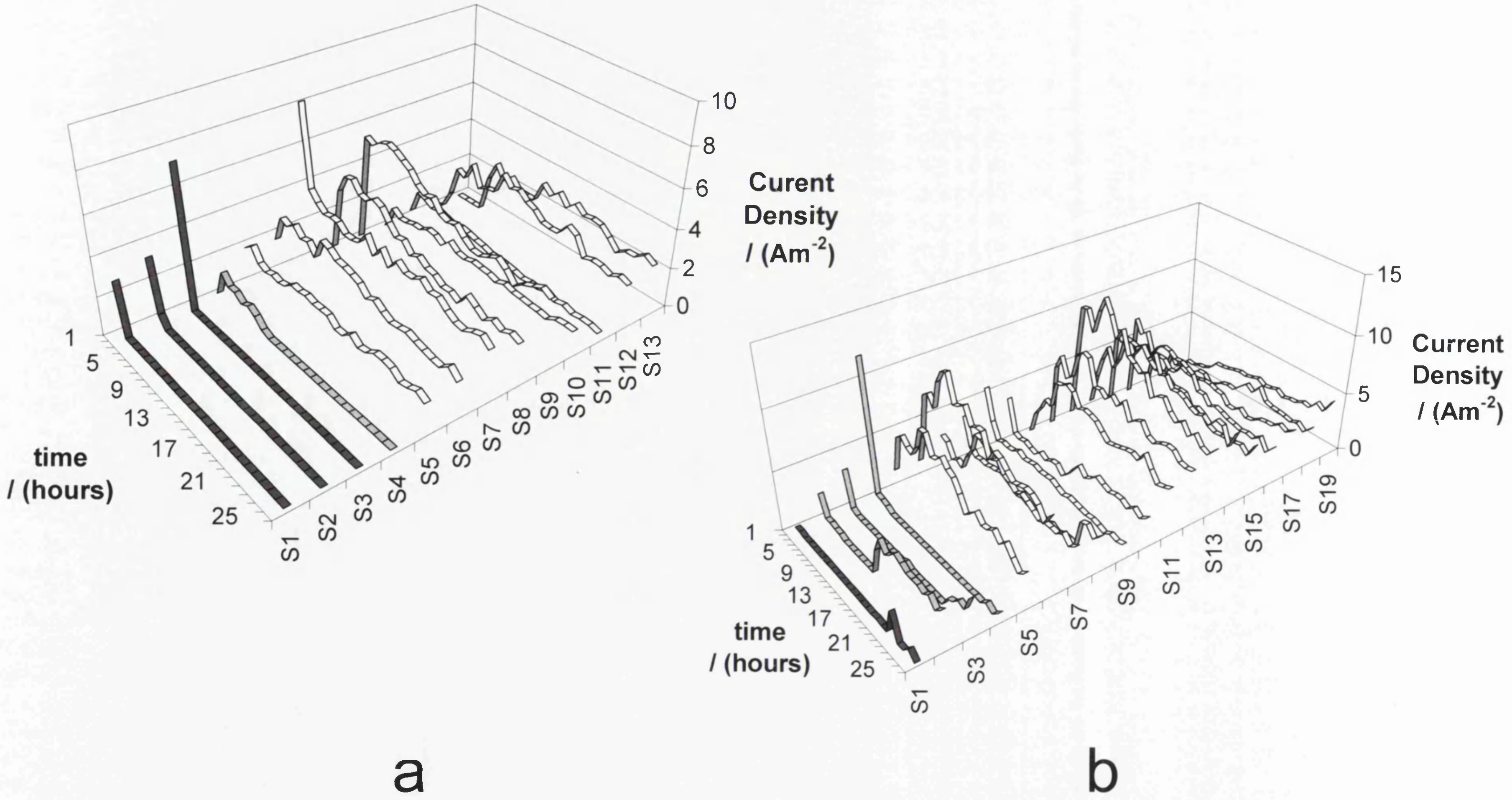

Figure 3.12 Anode intensity as a function of immersion time for samples G2 (a) and G4 (b)

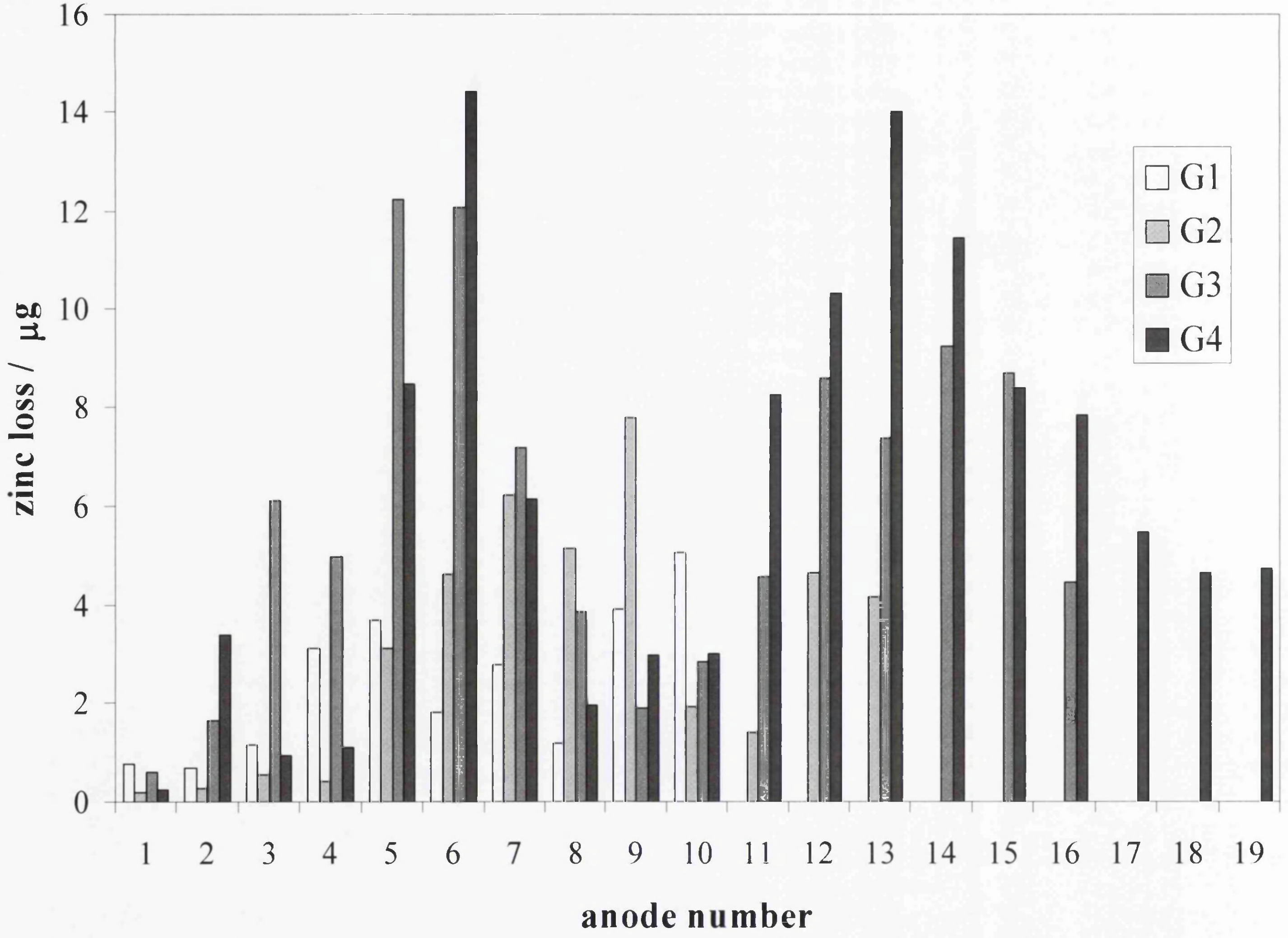

Figure 3.13 Individual zinc loss from individual anodic events

Sample code	SVET tzl/ µg	SVET tizl/ µg
G1	170±10	44
G2	166±10	40
G3	280±10	96
G4	310±10	118

Table 3.2 Comparison of total zinc loss and total individual zinc loss

3.1.5 Comparison of results of external exposure

The four samples were exposed as shown in figure 3.14 for 27 months at the Port Talbot weathering site and the overall zinc runoff (per m of exposed cut edge length) was recorded by measuring the concentration of dissolved zinc in collected runoff water. The data is shown in figure 3.15. Figure 3.16 illustrates the metallic runoff measured at 3, 6 12 and 24 months for the four samples as compared to the total `volume percentage of the primary zinc dendrites. As in the case of the SVET exposure there is again a clear link between the volume fraction of the primary phase and the corrosion resistance, this time measured in external conditions and based on zinc ion runoff. In addition, there is a similar trend in zinc runoff repeated over the exposure period in relation to the number of dendrites per unit area as shown in figure 3.17. This is further re-enforcement that the focus of corrosion activity is the zinc dendritic phase.

The external exposure runoff data has also be compared to the SVET measurements undertaken in 24 hours in the laboratory in 0.1% NaCl. This is presented in figure 3.18 which shows that there is a reasonable relationship between the initial corrosion measurements made using SVET and longer term exposure.

3.1.6 External exposure organic coating delamination

As stated at the outset, one of the most demanding applications of these materials is for construction cladding material which with inherently exposed edges is given performance guarantees of up to 30 years. Hence the last part of this chapter concentrates on comparing 5-year delamination data with both metal ion runoff data obtained from periods between 3 and 24 months.

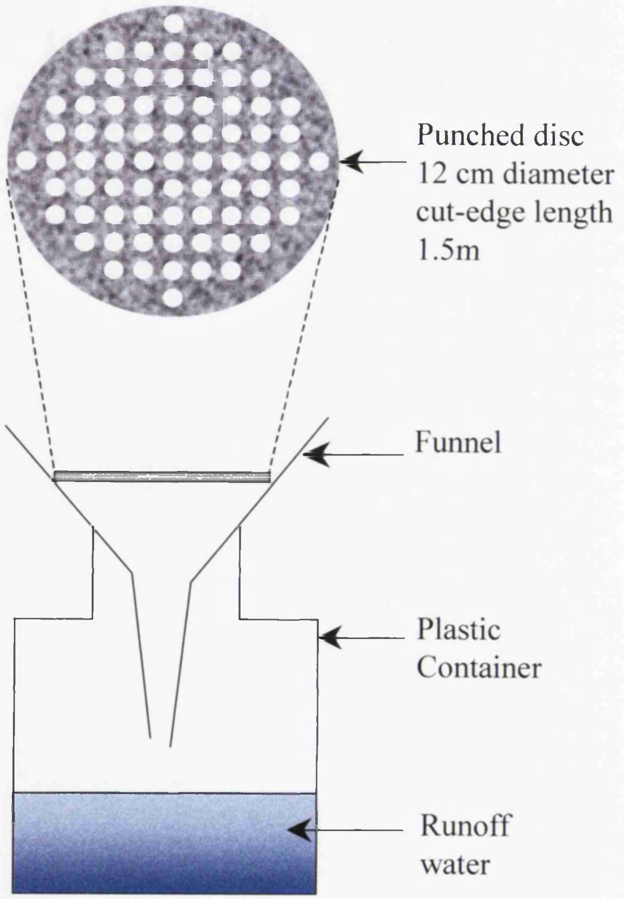

Figure 3.14 Experimental apparatus to collect run off results

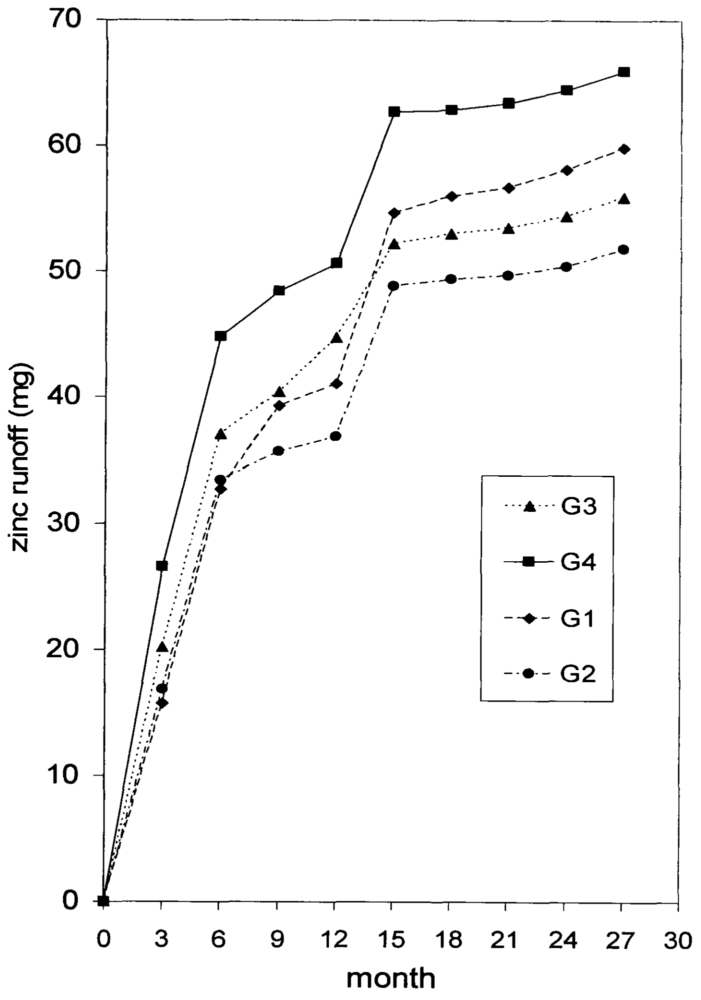

Figure 3.15 Zinc runoff over a 30 month period at Port Talbot, South Wales

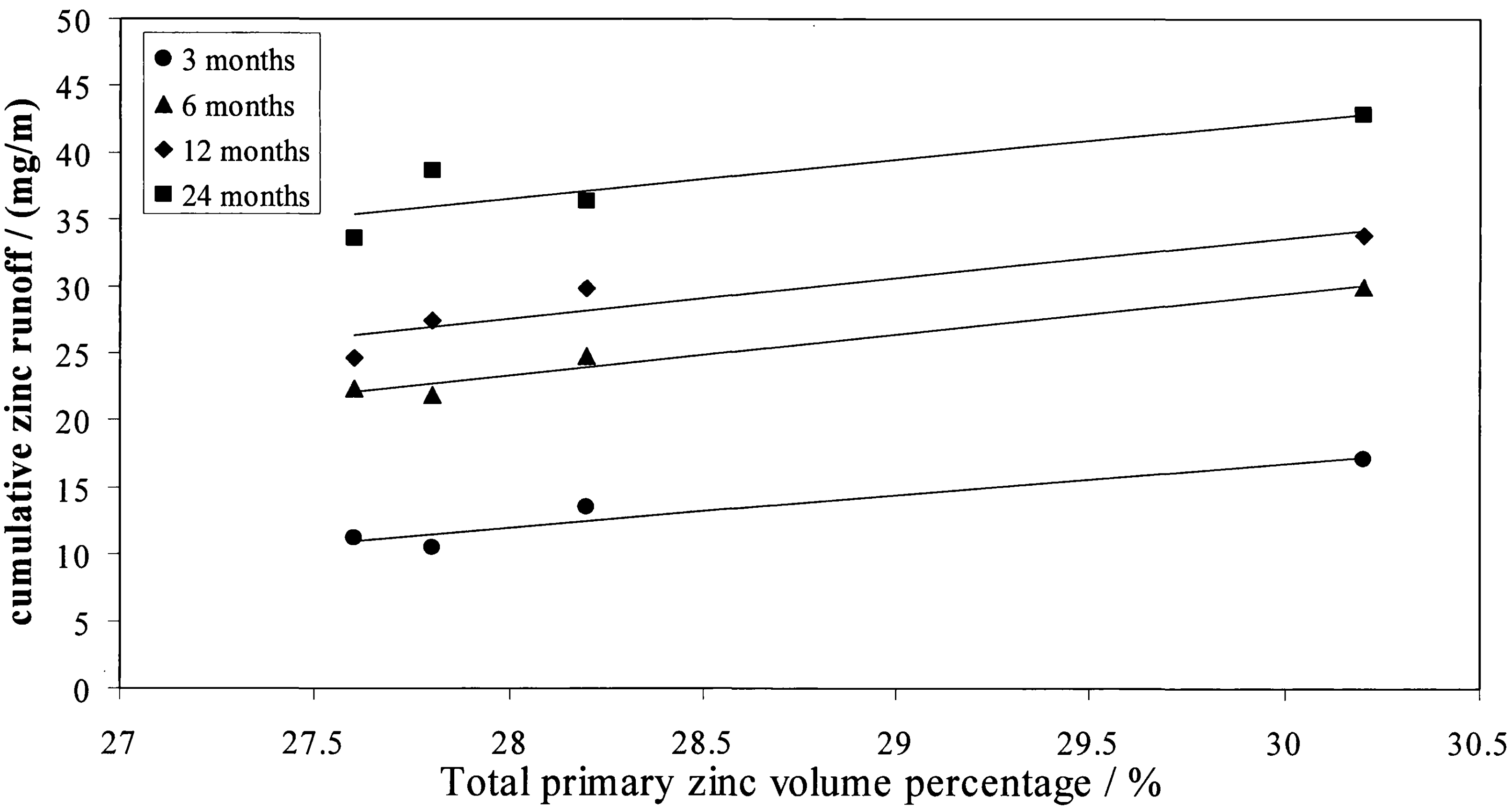

Figure 3.16 cumulative zinc runoff as a function of volume percentage of primary zinc

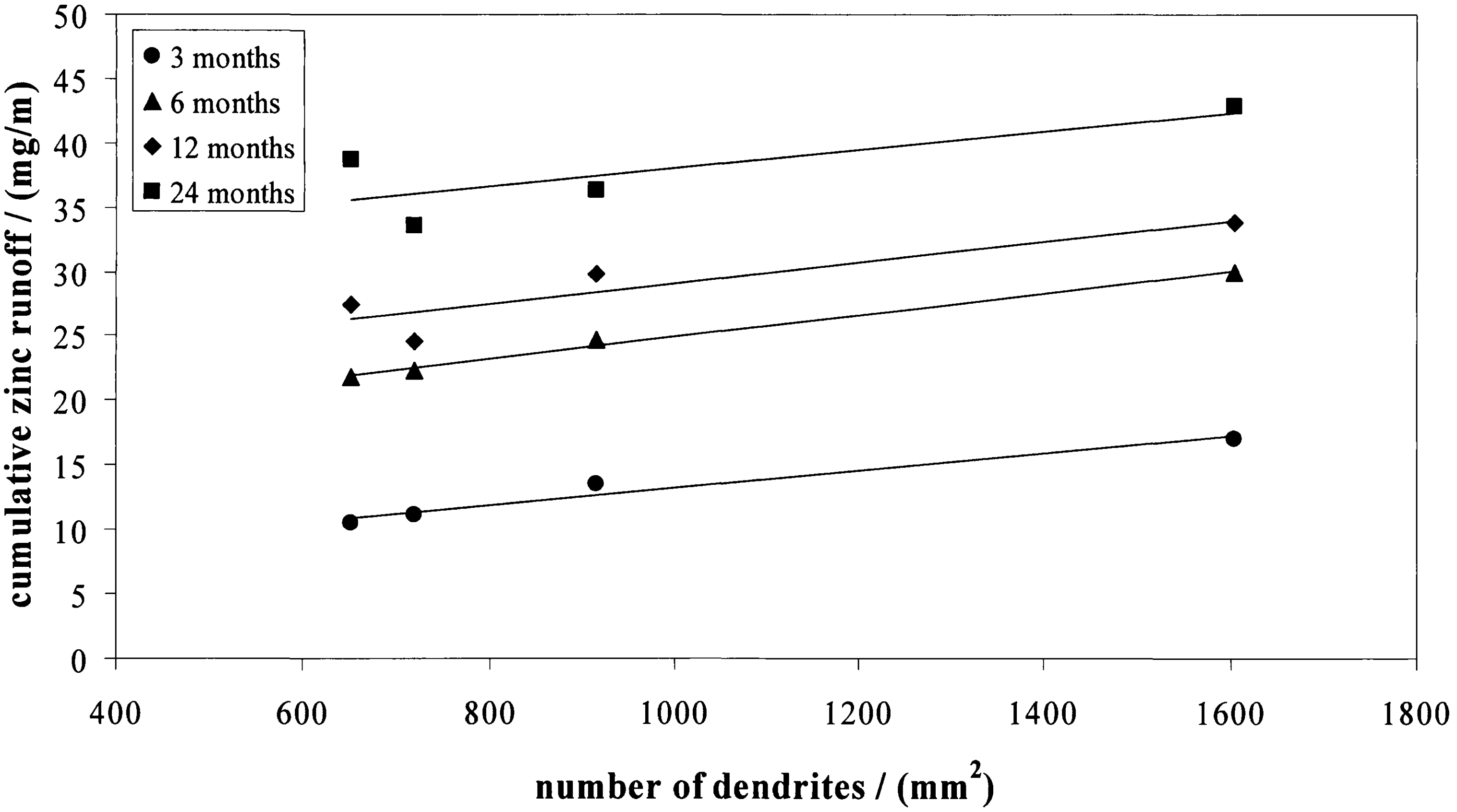

Figure 3.17 Cumulative zinc runoff as a function of dendrite number

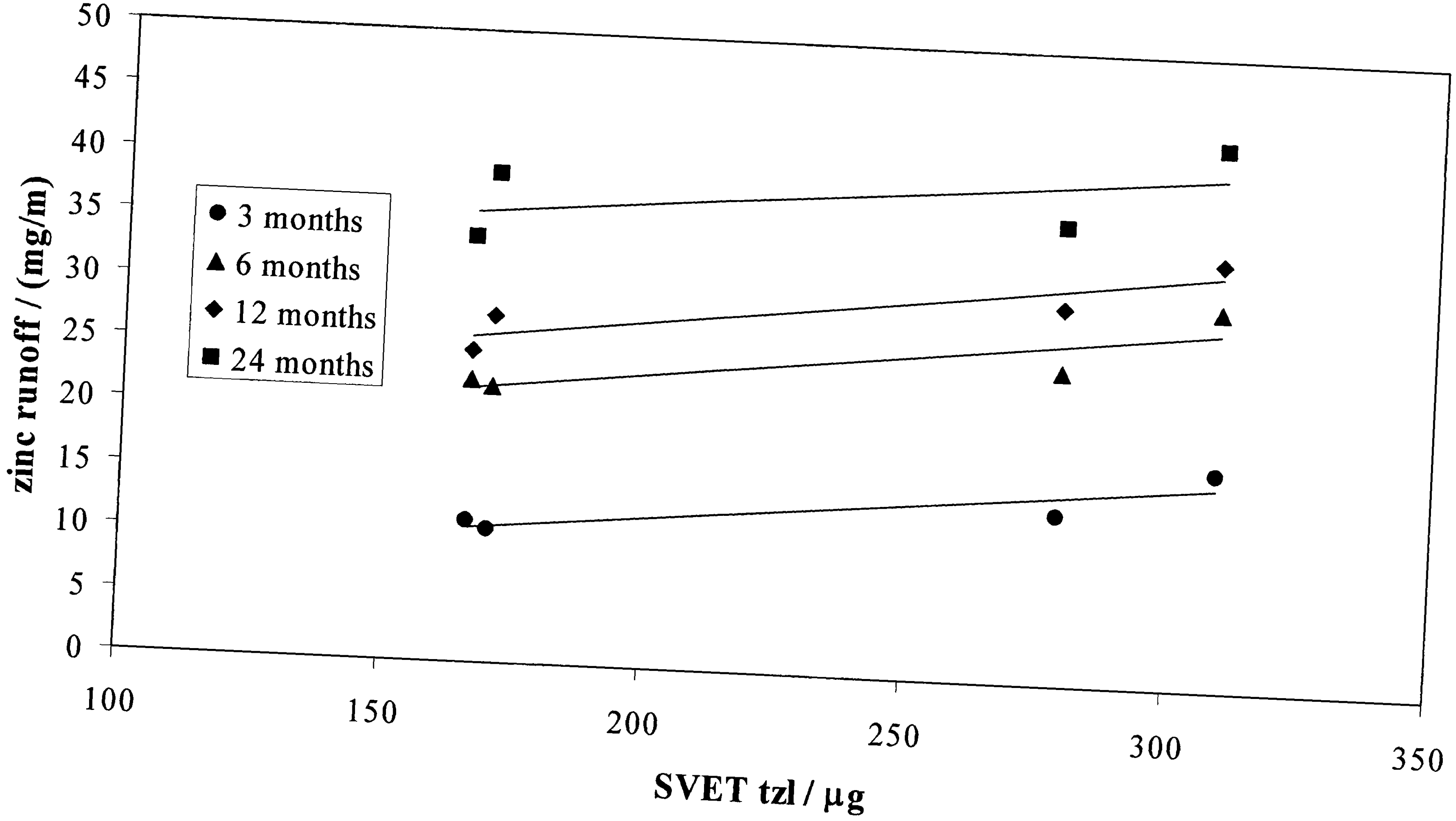

Figure 3.18 Cumulative zinc runoff as a function of SVET *tzl*

Firstly the runoff data from months 3, 6, 12 and 24, illustrated in Figure 3.19, shows a good linear relationship to the observed delamination data recorded over 5 years at the same weathering site. Hence this indicates that this form of exposure method could be used as an accurate and environment sensitive corrosion test. Secondly since there is a reasonable relationship between SVET zinc losses and external runoff (figure 3.18)(both being limited by the volume percentage of primary zinc) it is hardly a surprise that there a reasonable linear relationship between the 5-year delamination data and that of the 24 hour SVET test, as shown in figure 3.20. This latter result is particularly promising in that it demonstrates the ability of SVET to rank the cut edge corrosion resistance of metallic coatings very rapidly indeed. The linear fit is not quite as good as that in figure 20 for runoff measurements, but is none the less quite impressive and illustrates that for the optimisation of this kind of galvanising spelter the SVET is an ideal tool. Where it is likely to be less realistic is in much more benign atmospheres where chloride contamination is lower. In these instances proper design of the exposure condition (rather than simply the use of 0.1%NaCl) should improve the predicted performance ranking offered by the SVET.

3.2 Conclusions

The data presented here has shown that the SVET is a valuable tool for investigating corrosion behaviour of zinc-aluminium alloy galvanising chemistries and can allow mechanistic understanding of the relationship between microstructure and corrosion to be gained. The microstructure of the Galfan coating clearly controls the corrosion performance with corrosion initiating at the primary zinc dendrites leading to increased corrosion with increased volume percentage of primary zinc.

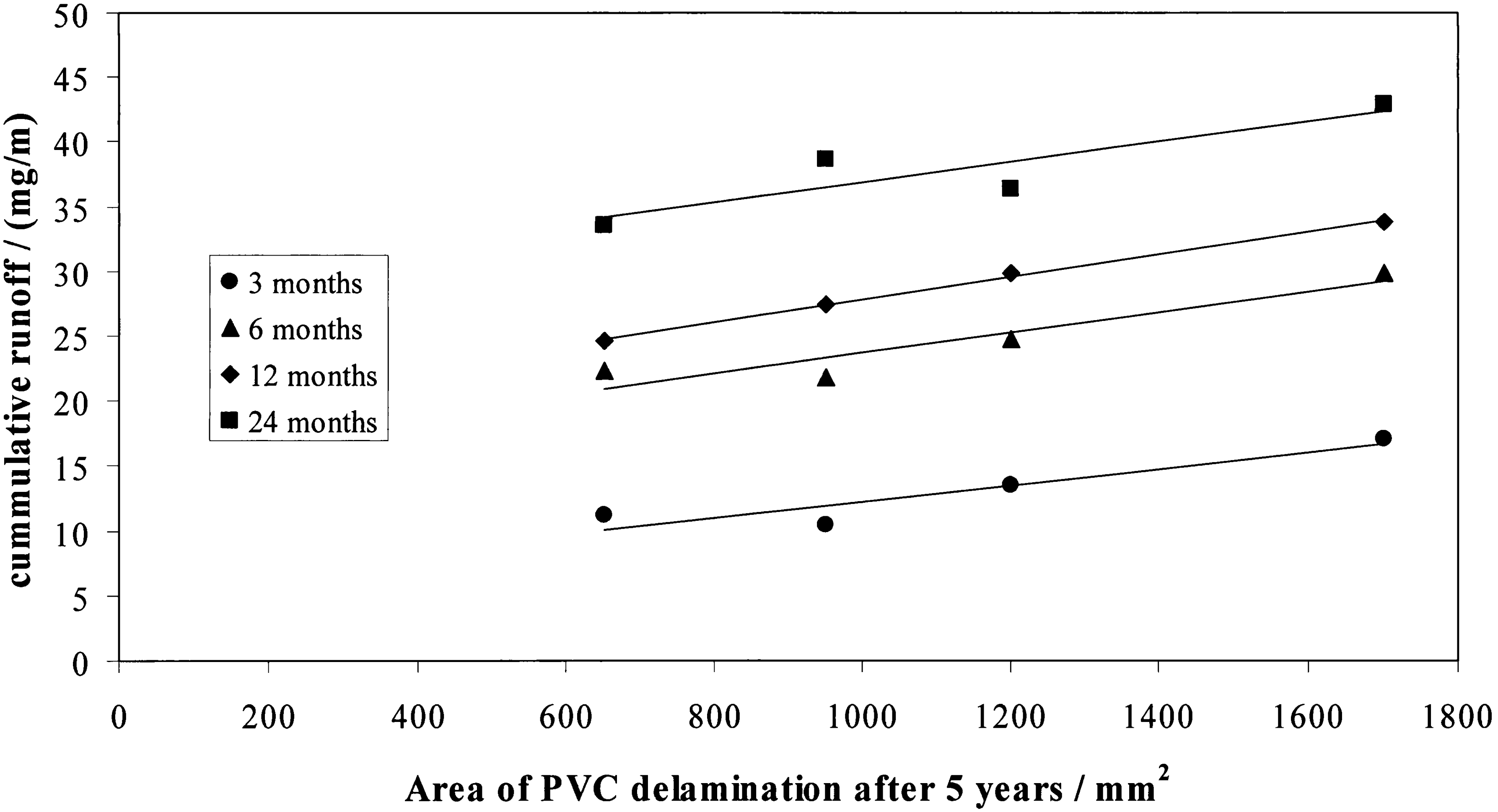

Figure 3.19 Cumulative zinc runoff as a function of area of PVC delamination

UNIVERSITY OF WALES SWANSEA LIBRARY

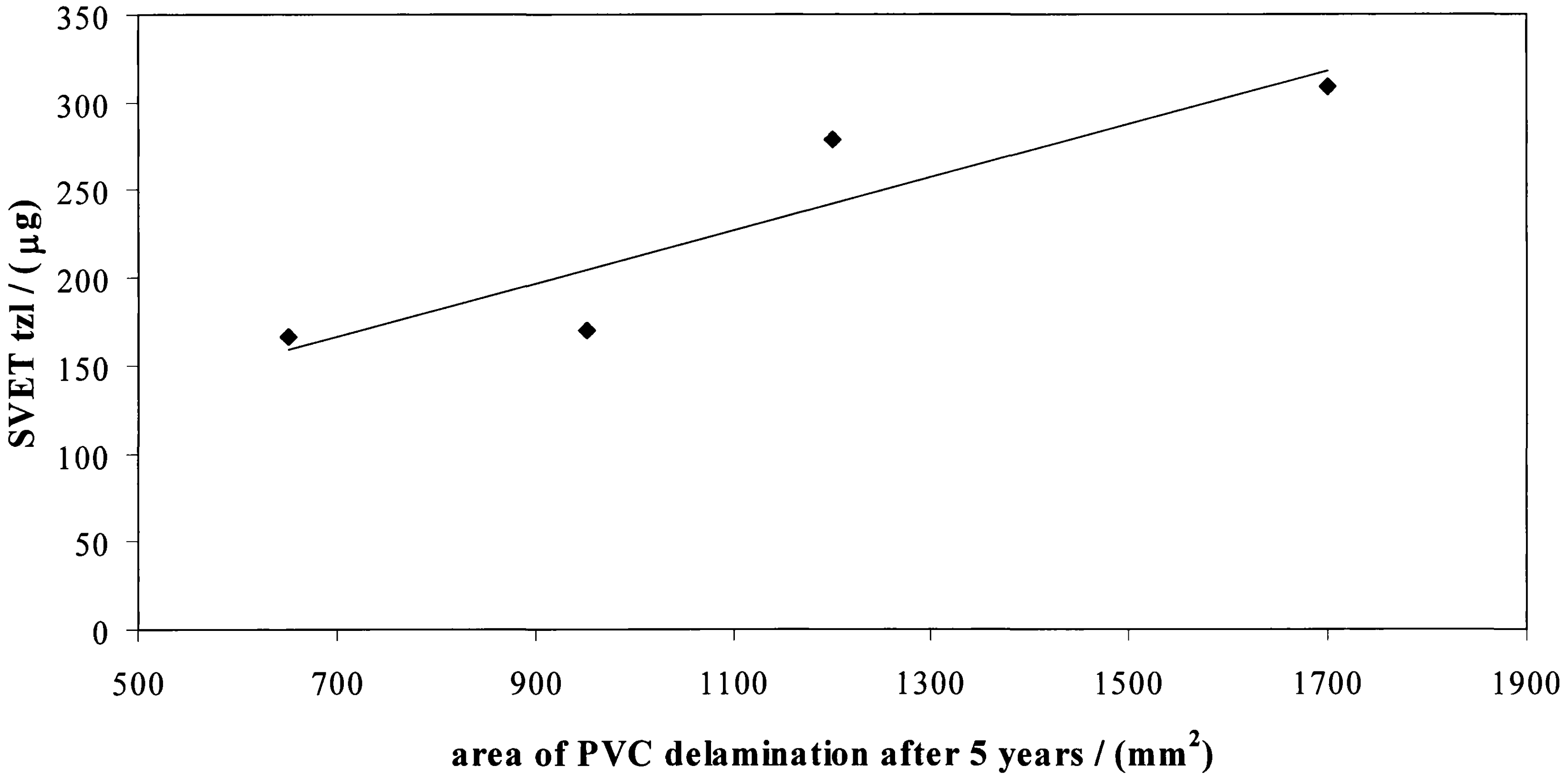

Figure 3.20 SVET *tzl* as a function of area of PVC delamination

The SVET calculated zinc losses made in 24 hours provide an indication of the potential levels of zinc runoff from the Galfan coating exposed in natural weathering experiments. There is a direct correlation between the zinc levels determined by SVET and runoff levels after 3 to 24 months of exposure.

The levels of zinc runoff measured between 3 and 24 months exposure relate directly to the overall performance of the organically coated materials exposed to natural weathering. Indeed, runoff measurements directly relate to the area of the PVC coating delaminated. The runoff test can therefore be used to estimate delamination levels in an environmentally specific atmospheric corrosion test within 3 months of exposure.

The SVET is ideal for coating optimisation giving localised information on corrosion current densities and metal losses as well as total zinc loss value within 24 hours. These measurements are representative of 5 year anti corrosion performance of the organically coated panels. Hence the SVET can reasonably reliable predict coated product performance. Where the SVET fails to deliver is potentially in much more benign environments. Whilst SVET will work tremendously well in dilute solution there are serious issues regarding calibration in these systems since the conductivity of the electrolyte in the plane of vibration can no longer be assumed to be constant.

3.3 References

[1] D. Christian: 'Performance of Prepainted and Unpainted Galfan Test Panels in Corrosive Environments', Proc. Of Eighth Galfan Licencees Meeting, International Lead and Zinc Research Organisation, April 21 (1986)

[2] F. Goodwin: 'Galfan Galvanising Alloy Technology', 2nd Edition, International Lead and Zinc Research Organisation, (1984).

---

[3] I. Suzuki: 'Corrosion-Resistant Coatings Technology', Monticello, NY, Marcel Dekker. (1989)

[4] M. Lamberights, V. Leroy and F. Goodwin, Proceedings of the Third International Zinc Coated Sheet Steel Conference (INTERGALVA), Barcelona, 7, (1991).

[5] J.H. Sullivan and D.A. Worsley, British Corrosion Journal, 37, 282,(2002)

[6] I. Odnevall Wallinder, C. Leygraf, C. Karlen, D.Heijerick and C.R. Janssen, Corrosion Science,43, 809, (2001)

[7] A. Belghazi, S. Bohm, J.H. Sullivan and D.A.Worsley, Corrosion Science,44, 1639, (2002)

[8] P.A. Ryan, R.P. Wolstenholme and D.M. Howell, 'Durability of cladding, a state of the art report'; 1994, London, Thomas Telford.

[9] S.T. Bluni and A.R. Marder, Galvatech '98 conference proceedings,115, Iron and Steel Institute of Japan, Tokyo. (1998)

[10] F.E. Goodwin and J.L. Hostetler, ASM International Materials Congress, 1991.

[11] M. Challis, T. Heatley and D.A. Worsley, Journal of the Institute of Metal Finishing, 79, 16. (2001)

[12] J. Elvins, J.A. Spittle and D.A. Worsley, Corrosion Engineering, Science and Technology,38, 197,(2003)

Chapter 4

Influence of cooling rates on the microstructure and corrosion resistance of Galfan coated steels

4.0. Introduction

As detailed in Chapter 3 the cut edge corrosion performance of Galfan coated steels is irrefutably linked to the amount of pro-eutectic zinc phase contained within the coating. Earlier research[1,2] in the same field has also shown a direct correlation between changes in the microstructure (relating to the pro-eutectic phase) and subsequent variations in cut edge corrosion performance. This section of work investigates the effect of modifying the cooling rate (i.e. the solidification rate) of the coating during production, and also details changes occurring as a result of the variation in gauge of the base steel substrate upon the microstructure, the cut edge corrosion and the surface corrosion performance. Previous studies[3, 4] have discussed changes in the microstructure due to enhanced cooling but have not related these observed changes to the corrosion performance.

Table 2.4.2.2 lists the materials used to investigate cooling rates and steel gauge on coating performance. Each sample set was produced during a line trial at Corus Colors, Shotton, in the summer of 2002. The trial was organized in such a way as to ensure that each group of samples was generated as close to each other as possible (in terms of time) allowing confidence in the fact that the bath conditions remained constant. A 'Spooner Fast Cooler' cooling rig was employed to alter the cooling regime, via changes in high volume, low pressure air, used to solidify the galvanized coating. Three A4 size panels were removed from the centre of each coil enabling the comparisons to be made. A film was used to seal the samples from the atmosphere and prevent damage during transportation. The samples were subsequently treated as described in section 2.1.

4.1 Results and Discussion

4.1.1. Microstructural Observations

The microstructures were quantified on the basis of the following: a.) the volume percentage of primary zinc, b.) the size and number of the primary dendrites, c.) changes in the eutectic spacing and d.) Changes in the eutectic cell size.

Figure 4.1 details the microstructures of samples UG55H – UG100H and likewise in figure 4.2 showing the microstructures of UG55L – UG100L. In each case the depth shown is the depth through the coating from the air/ coating interface. Comparisons are made at 2μm, 10 μm and 18 μm from the air/ coating interface. In each case the optically white regions are the primary zinc solid solution crystals (containing ~1% Al) and these are encased in a Zn – Al lamellar eutectic matrix. The primary zinc dendrites exhibit growth along the close packed directions $<11\bar{2}0>$, which is typical for HCP structures. Initially obvious, when comparing the slow cooled (UG55H and UG55L) and the fast cooled (UG100H and UG100L) samples is that the dendrites within the fast cooled samples are considerably smaller and more numerous.

4.1.2. Effects of metallic coating cooling rate and steel gauge upon the volume percentage of the primary zinc

Figure 4.3 shows the average volume percentage (in each case, a mean from three regions within a single 20mm *x* 10mm sample) of the primary zinc dendrites as a function of depth from the air/ coating interface. These results show that as the steel/ coating interface is approached (i.e. at a depth of approximately 18 μm) the volume percentage of primary zinc increases. For UG55H the increase is from ~4%, 2 μm below the air/ coating interface to ~ 43% near to the steel/ coating interface. Similar

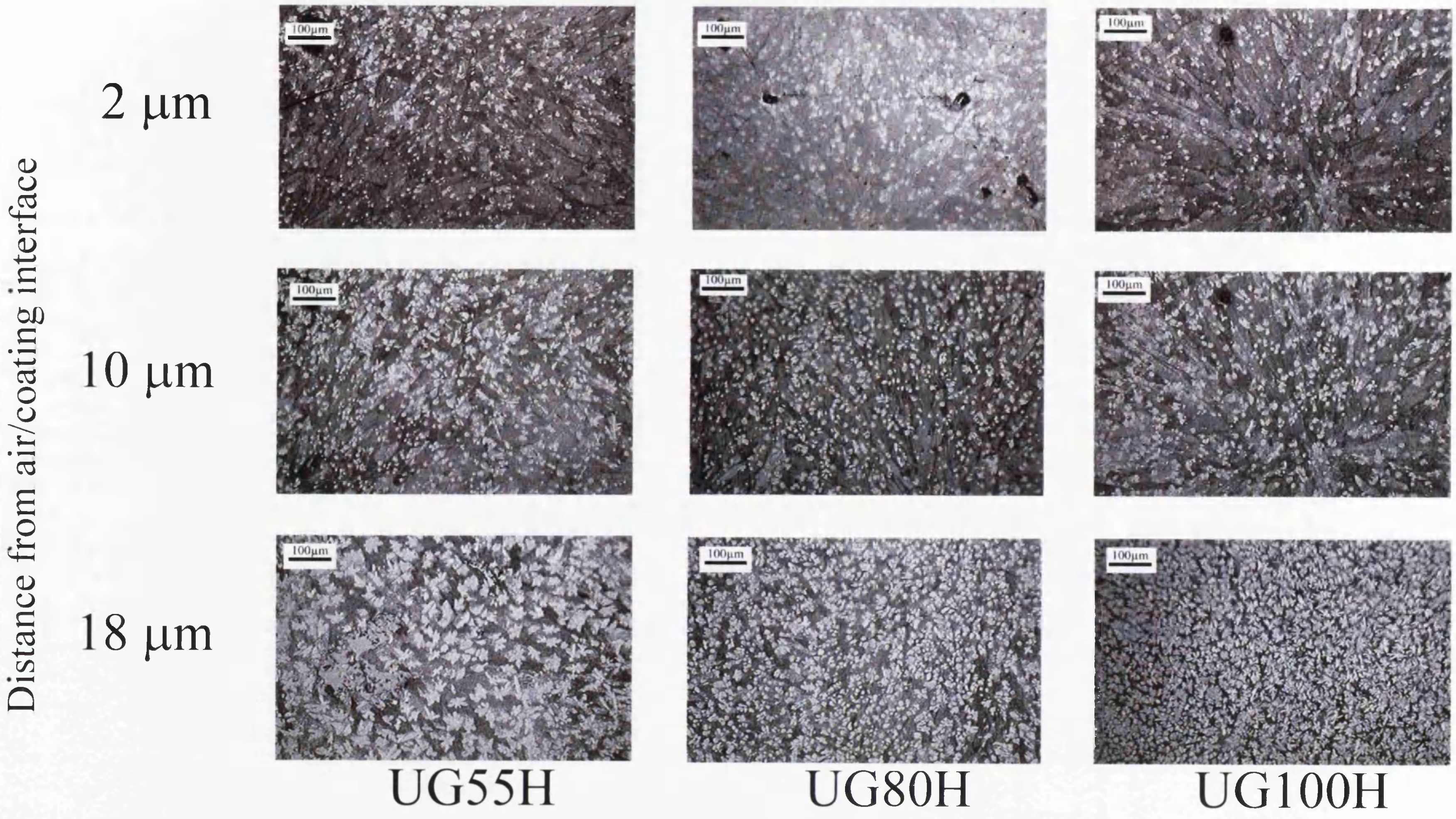

Figure 4.1. Through coating microstructures of heavy gauge samples

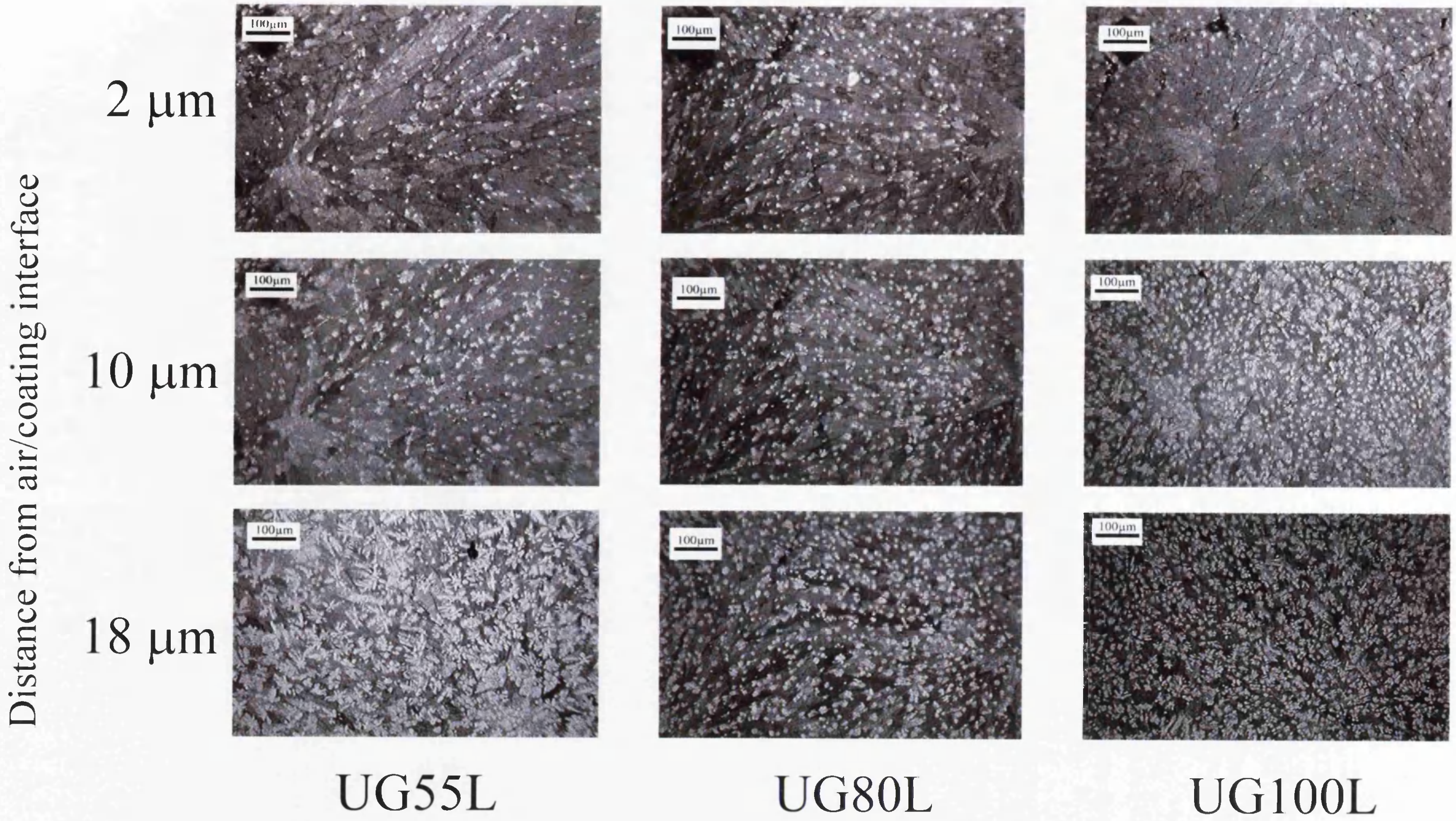

Figure 4.2. Through coating microstructures of light gauge samples

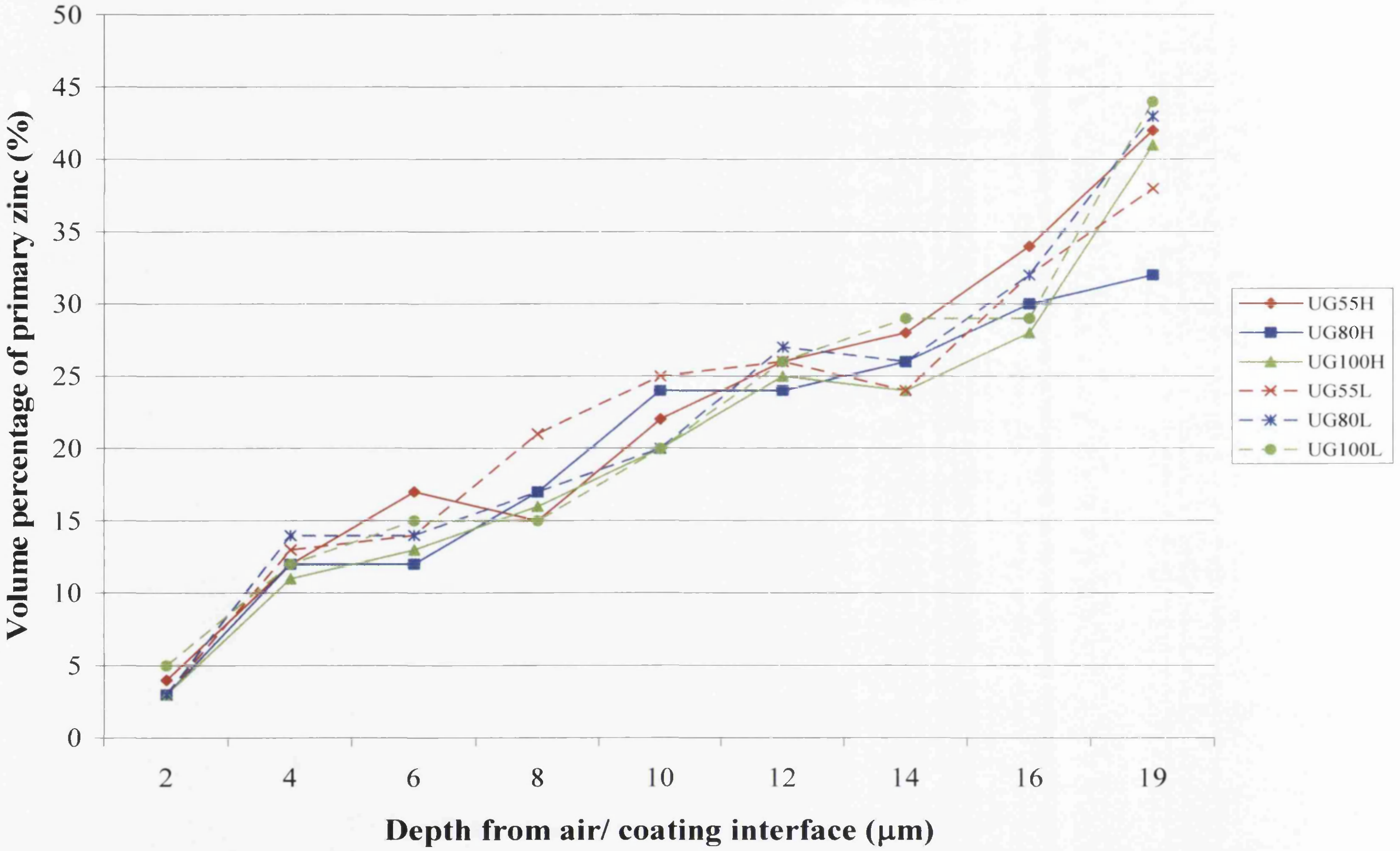

Figure 4.3. Average volume percentage of primary zinc as a function of depth through coating

results are obtained for each cooling rate and both steel gauges. The distribution of the primary zinc through the coating in this manner has been previously observed[4]. Since the majority of the primary phase is in close proximity to the steel/ coating interface it is assumed that the nucleation of this phase is occurring near to the base steel. This observation is again in agreement with previous researchers[4].

By taking the mean average of the primary zinc volume percentages at the defined depths, an approximate total volume percentage of primary zinc in each coating can be calculated (section 2.1.2.1). These results are shown in figure 4.4 for all samples. It can be seen that for each sample the total volume percentage of primary zinc remains at 20% ± 2%. The fact that the individual totals remain constant (within experimental error) leads to the conclusion that the quantity of primary zinc present, in this circumstance, has not been altered by either the variation in cooling rate of the sample or the variation in base steel thickness. Table 4.1 details the chemistry each of the coatings. As previously described (section 1.11) variations in the Al content within each coating will have a direct influence upon the volume percentage of the primary phase. However, in this study the Al content within each coating remains constant at 4.20% ± 0.06% (see table 4.1). Hence any changes observed in the cut edge corrosion performance will be largely independent of the total volume percentage of the primary zinc in the coating.

4.1.3. Effects of metallic coating cooling rate and steel gauge upon the size and number of the primary zinc dendrites

Since it is believed that nucleation of the primary zinc dendrites is occurring near to the steel substrate, the number and size (area) of dendrites was calculated as close to the steel/ coating interface as possible. The results for the number of dendrites

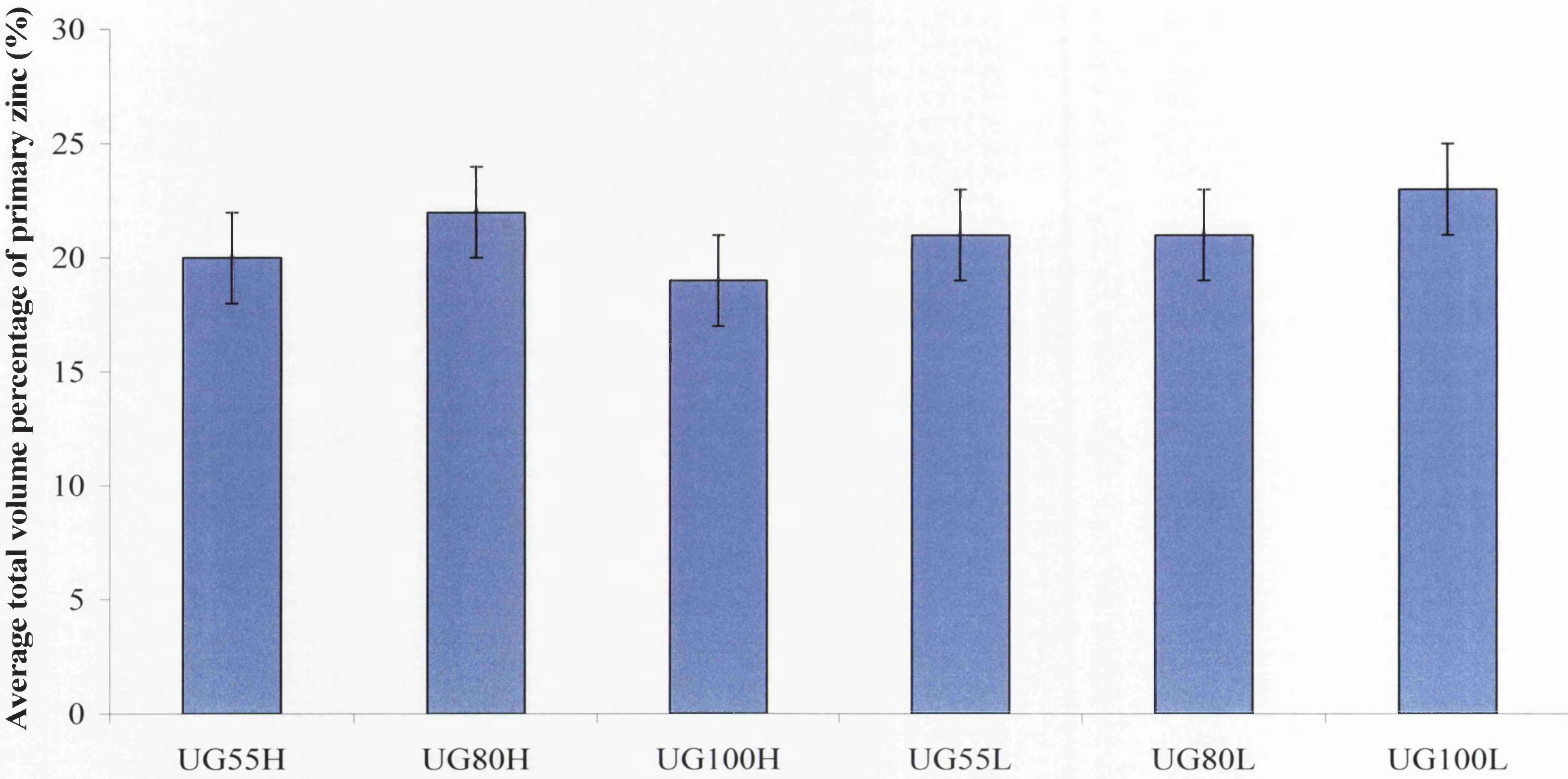

Figure 4.4. Average total volume percentage of primary zinc

Sample	**%Al**	**%Fe**	**%Mg**	**%Pb**	**%Sb**	**%La**	**%Ce**
UG55H	4.22	0.33	<0.01	0.01	<0.01	<0.01	<0.01
UG80H	4.22	0.34	<0.01	0.01	<0.01	<0.01	<0.01
UG100H	4.15	0.34	<0.01	0.01	<0.01	<0.01	<0.01
UG55L	4.15	0.24	<0.01	0.01	<0.01	<0.01	<0.01
UG80L	4.22	0.33	<0.01	0.01	<0.01	<0.01	<0.01
UG100L	4.26	0.34	<0.01	0.01	<0.01	<0.01	<0.01

Table 4.1. Sample coating chemistries obtained using ICPMS analysis

per square mm are shown in figure 4.5. It is obvious that the number of dendrites per unit area dramatically increases with cooling rate. UG55H contains approximately 1877 ± 75 dendrites per square millimeter with this figure raised to 2575 ± 103 and 3008 ± 120 in samples UG80H and UG100H respectively. Likewise in sample UG55L has 1473 ± 60 dendrites per mm^2 with UG80L having 2343 ± 95 and UG100L containing the greatest number at 2891 ± 115. Comparisons of samples of like conditions on the cooling rig for the two steel gauges reveal that there are more dendrites per mm^2 in each of the heavy gauge samples than in the light gauge samples.

The results show that the employment of a cooling rig providing different cooling regimes will dramatically change the Galfan microstructure. The increase in cooling rate generates a greater undercooling, resulting in the observed microstructural changes. It follows that from equation 1.19[5] (section 1.7) the increased undercooling serves to reduce the free energy barrier to nucleation and also to reduce the critical radius for a nucleus. Hence as the cooling rate is increased the dendrites become more numerous. The increase in number of primary dendrites observed when comparing samples of like conditions on the cooling rig at the two steel gauges is difficult to quantify. The difficulty in inferring any mechanistic change as a function of gauge is that there was no information on the individual strip surface characteristics. In other words, whilst gauge might be responsible for the changes observed (the different strip gauges will contain differences in residual heat), the effect of surface roughness also could not be ruled out.

Figure 4.6 details the average area of the individual dendrites at the steel/ coating interface. In agreement with previous observations (section 4.1.1) it is evident that the dendrite size is reducing with increasing cooling rate. The average dendrite size for UG55H was 50 μm^2 reducing to 13 μm^2 and 11 μm^2 in samples UG80H and

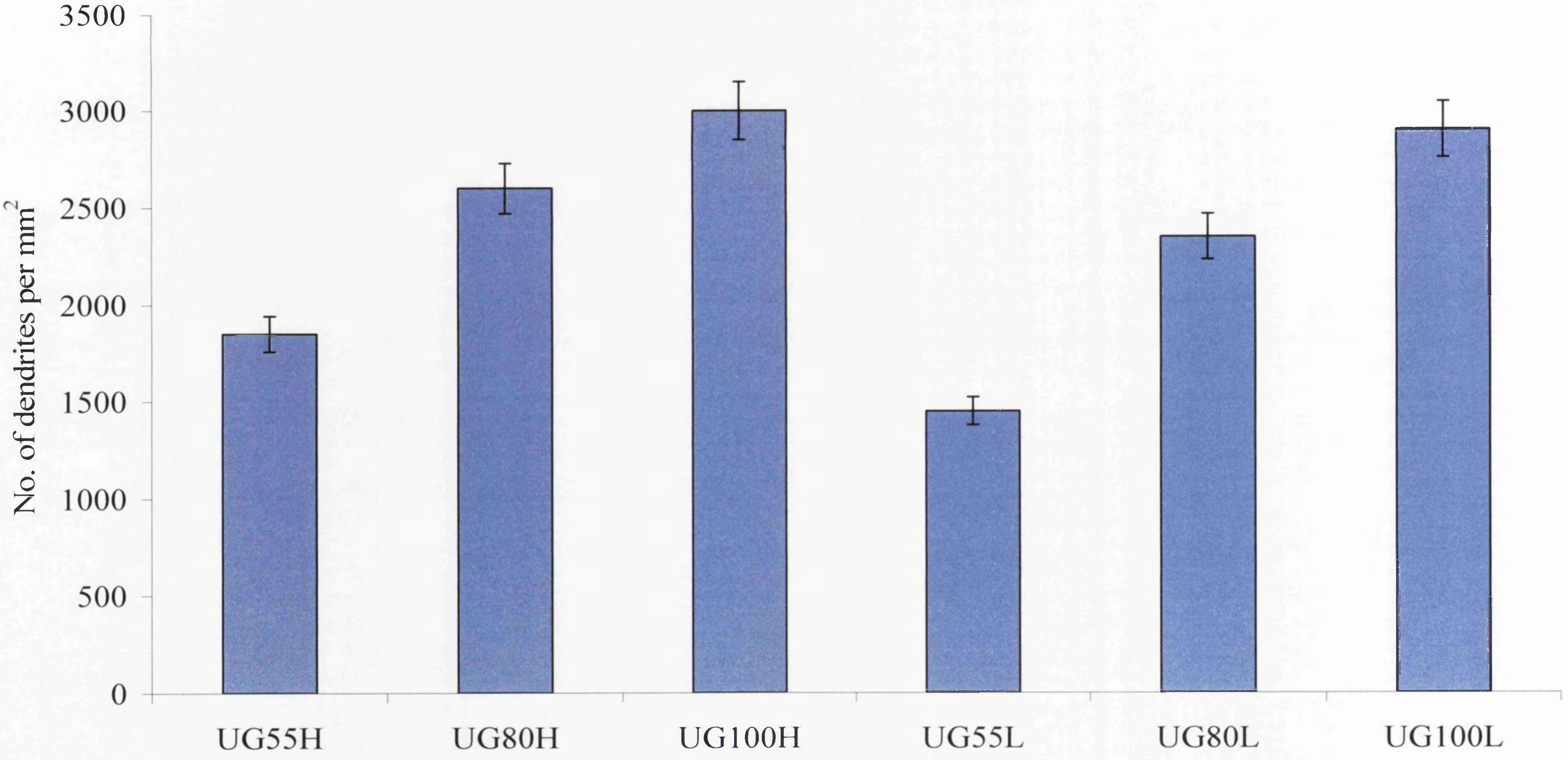

Figure 4.5. Average number of dendrites per mm^2 at the steel – coating interface

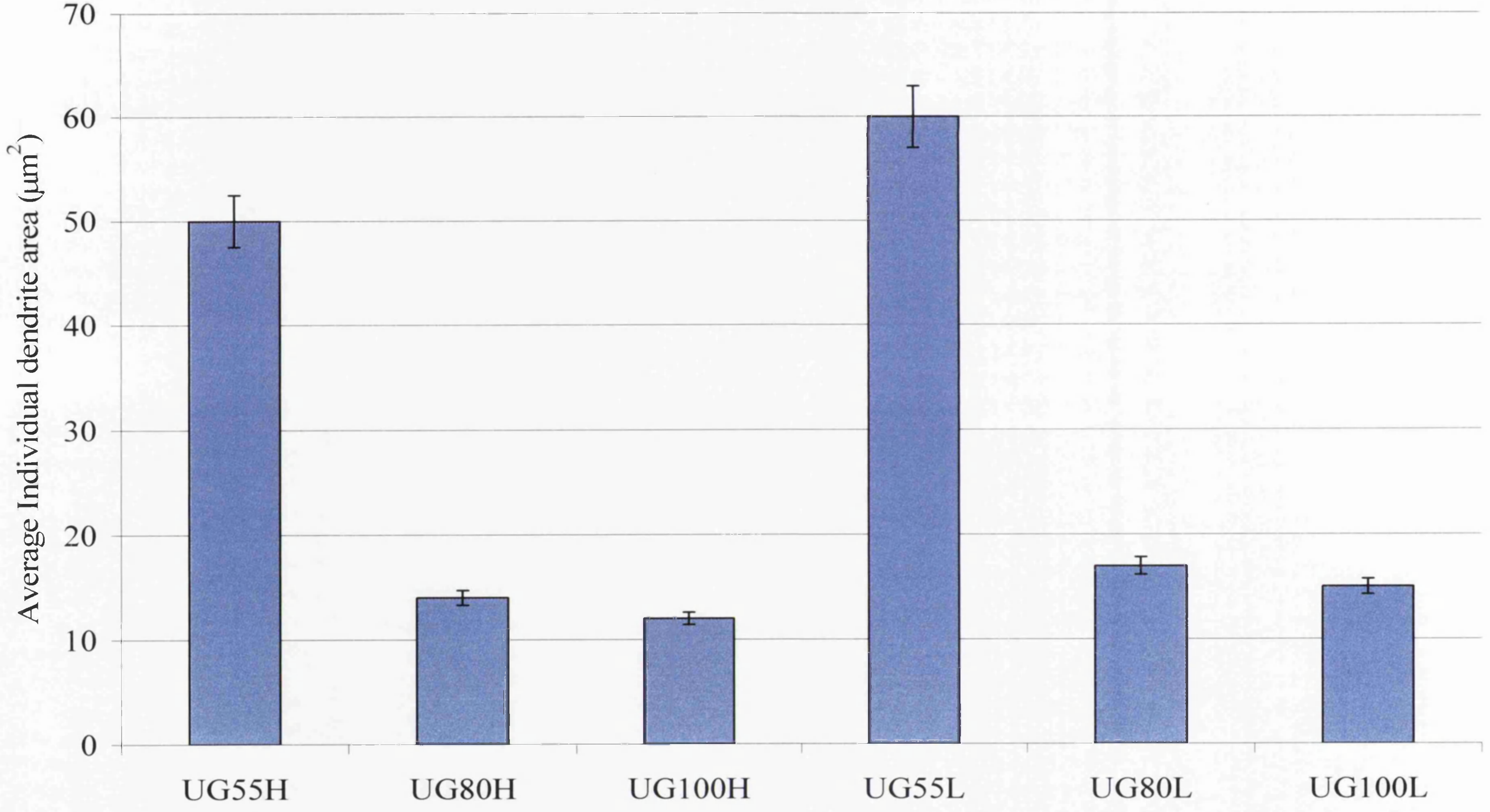

Figure 4.6. Average individual dendrite area

UG100H respectively. Again this trend is observed with the light steel gauges showing a reduction in area from 60 μm^2 (UG55L) to 15 μm^2 (UG100L). When comparing the dendrite areas at like conditions on the cooling rig for the two gauges it becomes apparent that the average dendrite size in the light steel gauge is greater than those in the heavier gauge.

The reduction in dendrite size with increasing cooling rate is not surprising. It follows that since the total volume percentage of primary zinc remains constant, the increased nucleation of the primary phase in the fast cooled samples must consequently reduce the size of the individual crystals.

The increase in size of the primary crystals on the light steel gauge is consistent with the changes observed in dendrite number detailed previously. Again, as the total volume percentage remains constant between samples the increased nucleation for the heavy gauge samples will generate smaller dendrites than those of the lighter gauge material.

4.1.4. Effects of metallic coating cooling rate and steel gauge upon the eutectic inter-lamellar spacing

Recorded close to the steel/ coating interface figure 4.7 shows example images of the eutectic microstructures. Changes in the inter-lamellar spacing (λ) were measured as detailed in section 2.1.2.4. These results are shown in figure 4.8. It is evident that as the cooling rate is increased the inter-lamellar spacing is decreased. For the heavy gauge materials the inter-lamellar spacing changes from 1.37μm ± 0.05μm in UG55H to 0.33μm ± 0.05μm in UG100H. Likewise UG55L has a spacing of 0.93μm ± 0.05μm which is reduced to 0.65μm ± 0.05μm in UG100L. The inter-

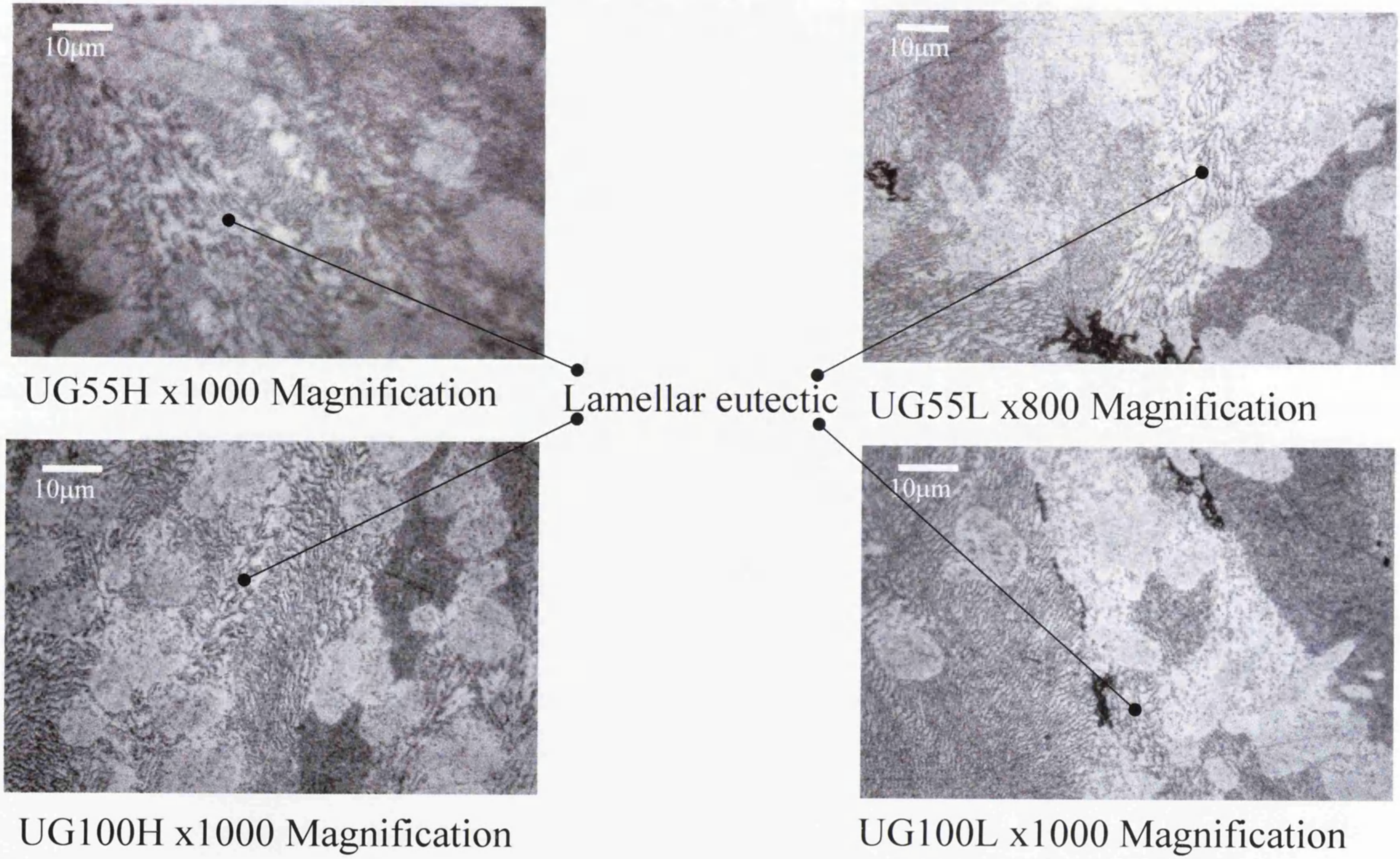

UG55H x1000 Magnification

UG55L x800 Magnification

UG100H x1000 Magnification

UG100L x1000 Magnification

Figure 4.7. Eutectic microstructures of samples UG100H, UG55H, UG100L and UG55L recorded near to the steel / coating interface

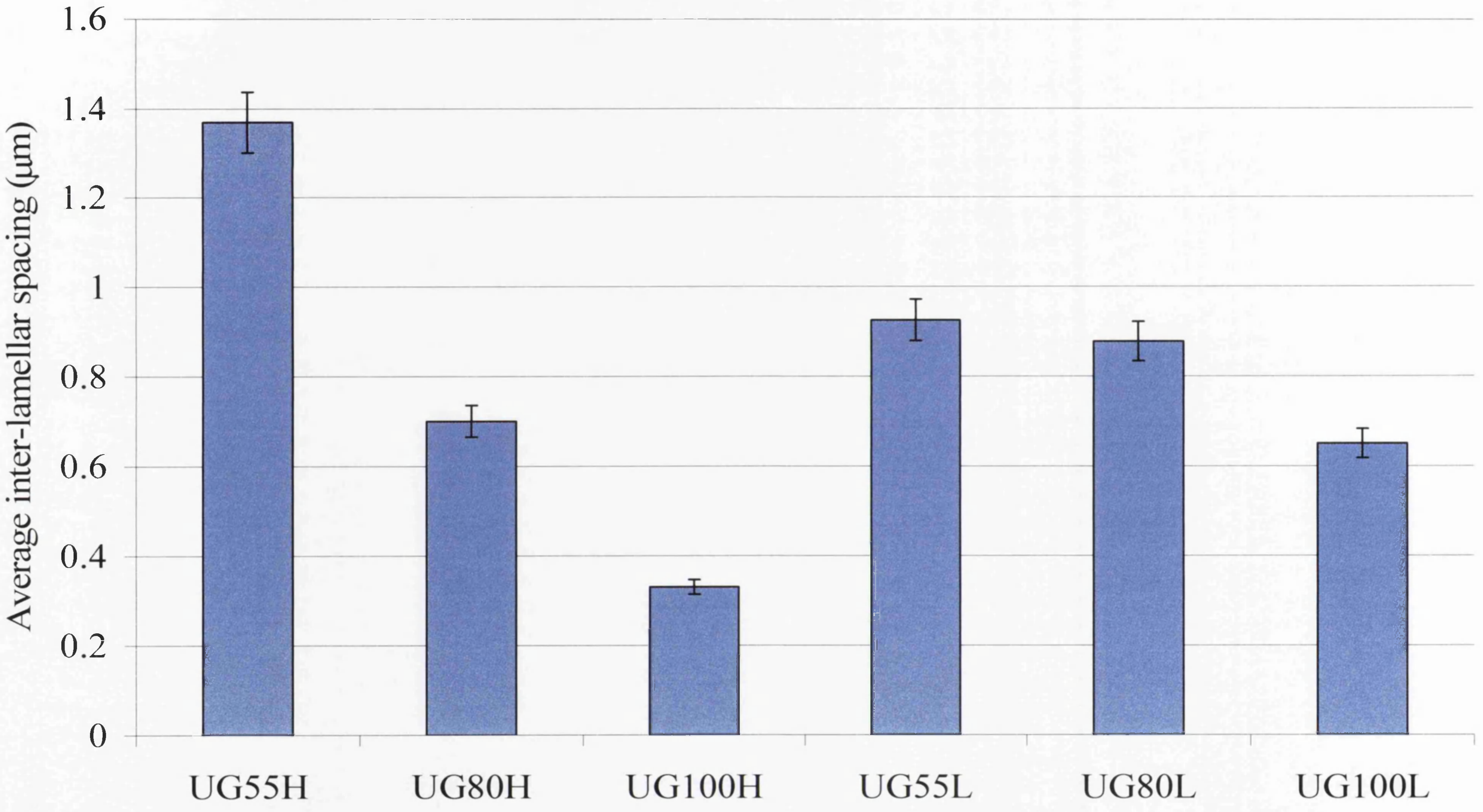

Figure 4.8. Average inter lamellar spacing recorded near to the steel/ coating interface

lamellar spacing has been shown to be related to growth velocity (v) by $\lambda v^{1/2} = \text{constant}$ [6]. Hence, as the cooling rate increases (consequently increasing the growth velocity) the inter-lamellar spacing is reduced. The distance through which the diffusion of B atoms to the β lamellae depends upon the time available which in turn depends upon the cooling rate. Hence, rapid cooling reduces the available time leading to a finer microstructure.

4.1.5. Effects of metallic coating cooling rate and steel gauge upon the eutectic cell size

The observed microscopic changes in the coating structure are also matched by macroscopic changes in the eutectic cell sizes apparent on the surface of the galvanised material. The cells grow radially from a central nucleation point (probably located near to the steel/ coating interface) and cease growth upon impingement with neighbouring cells. Solidification shrinkage occurs at the boundaries of the cells due to volume changes between the liquid and solid states. The size of the eutectic cells was also measured using surface images processed through image enhancing software and the summary of this measurement is presented in Figure 4.9. The average eutectic cell size (recorded as detailed in section 2.x) for sample UG55L is 2.09mm ± 0.21mm. As the cooling rate is increased this figure is reduced to 1.28mm ± 0.13mm for sample UG80L and 1.07mm ± 0.11mm for sample UG100L. Likewise a similar trend is observed for the heavy gauge samples with a reduction in size from 1.87mm ± 0.18mm in sample UG55H to 0.89mm ± 0.09mm in sample UG100H. It is clear from the data presented in Figure 4.9 that the microscopic changes in dendrite numbers are matched by macroscopic changes in the surface appearance and eutectic cell sizes, the faster cooling rates leading to smaller eutectic cells and an increasing length of the

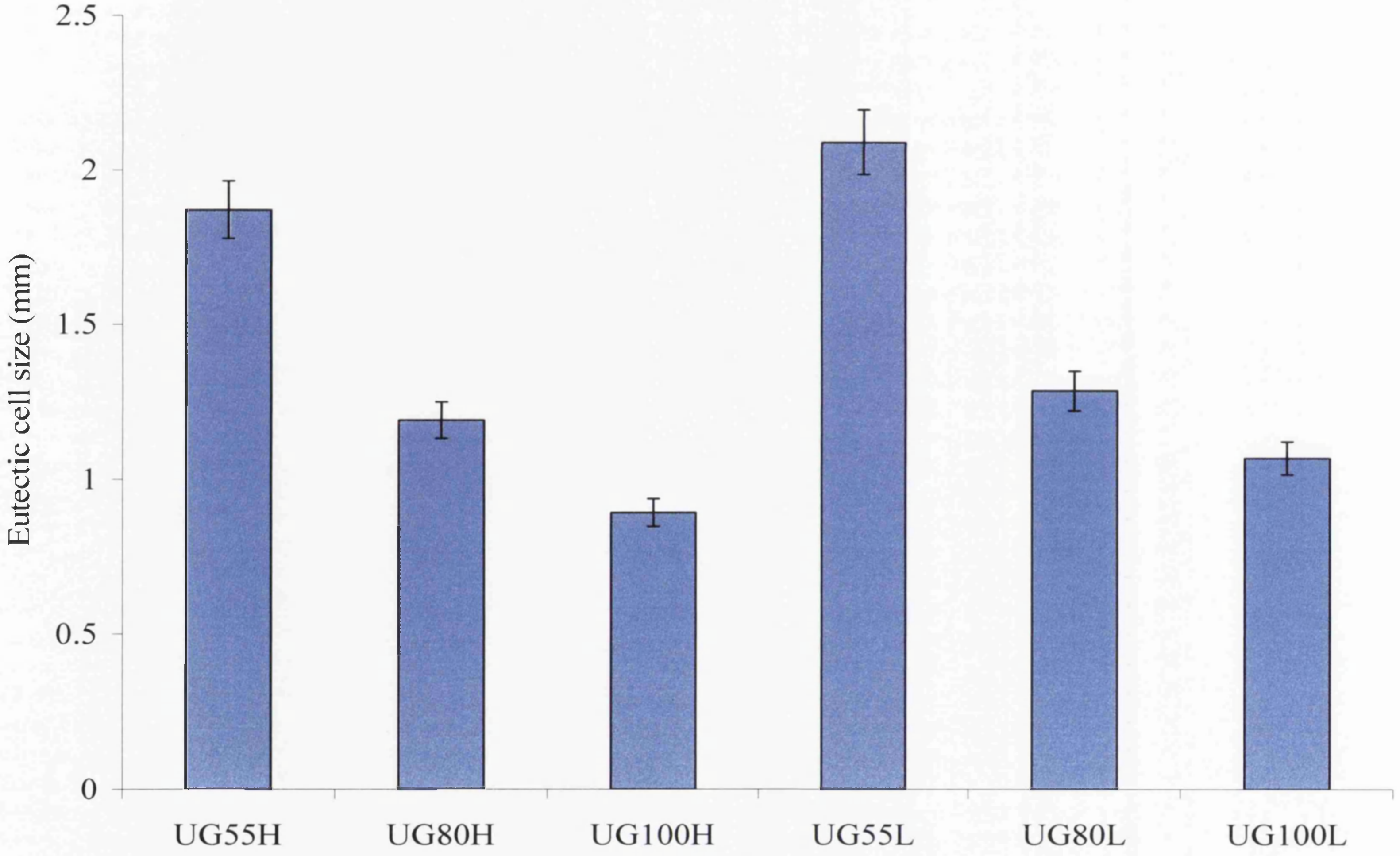

Figure 4.9. Average eutectic cell size recorded near to the air/ coating interface

depressed cell boundary on the surface of the galvanised material. The increased cooling rate increases undercooling and consequently leads to a greater number of nucleation events. Hence there are a greater number of smaller sized cells when compared with the slow cooled specimens.

4.1.6. Location and intensity of anodic sites along the sample cut edges

Figures 4.10 and 4.11 show representative SVET iso-current contour plots obtained by scanning the cut edge of UG55H, UG80H and UG100H samples after 12 hours immersion in 5% aqueous NaCl. The plots show anodic area (dark) located on the galvanising layers and cathodic activity (light) located on the steel. Initial inspection of the current density scales in Figure 4.10 indicates that the rate of corrosion is influenced by the microstructural changes induced by altering the cooling rate. There are significantly higher corrosion current densities occurring upon the slower cooled specimen and this trend was found to be repeated for the light gauge materials.

Previous work has shown that immersion of zinc aluminium alloy galvanising coatings lead to preferential corrosion of the zinc dendritic phases[1]. Figure 4.12 shows a micrograph of a typical cut edge directly after the end of an experiment. The corrosion products have been removed using ultrasound and the sample has not been chemically etched. This image confirms that the primary dendrites have been corroded preferentially to any other component of the coating or steel substrate.

The SVET data provides an excellent visual representation of the corrosion occurring over the 24-hour immersion period used. In order to quantify the corrosion process, the SVET data was then subject to further analysis to probe total corrosion activity and individual anode activity.

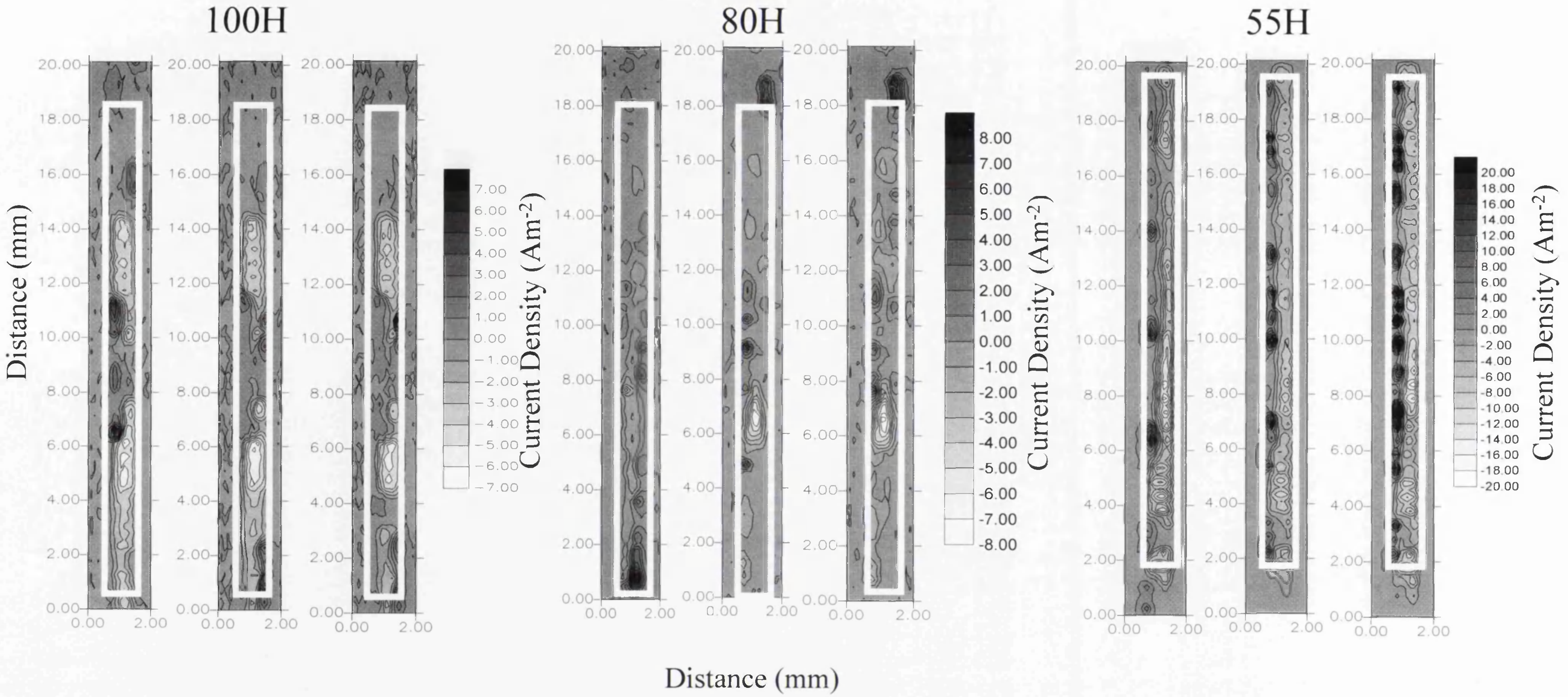

Figure 4.10. SVET Iso-Current maps showing Anodic (dark) and Cathodic (light) regions at 0, 12 and 24 hours for samples 100H, 80H and 55H

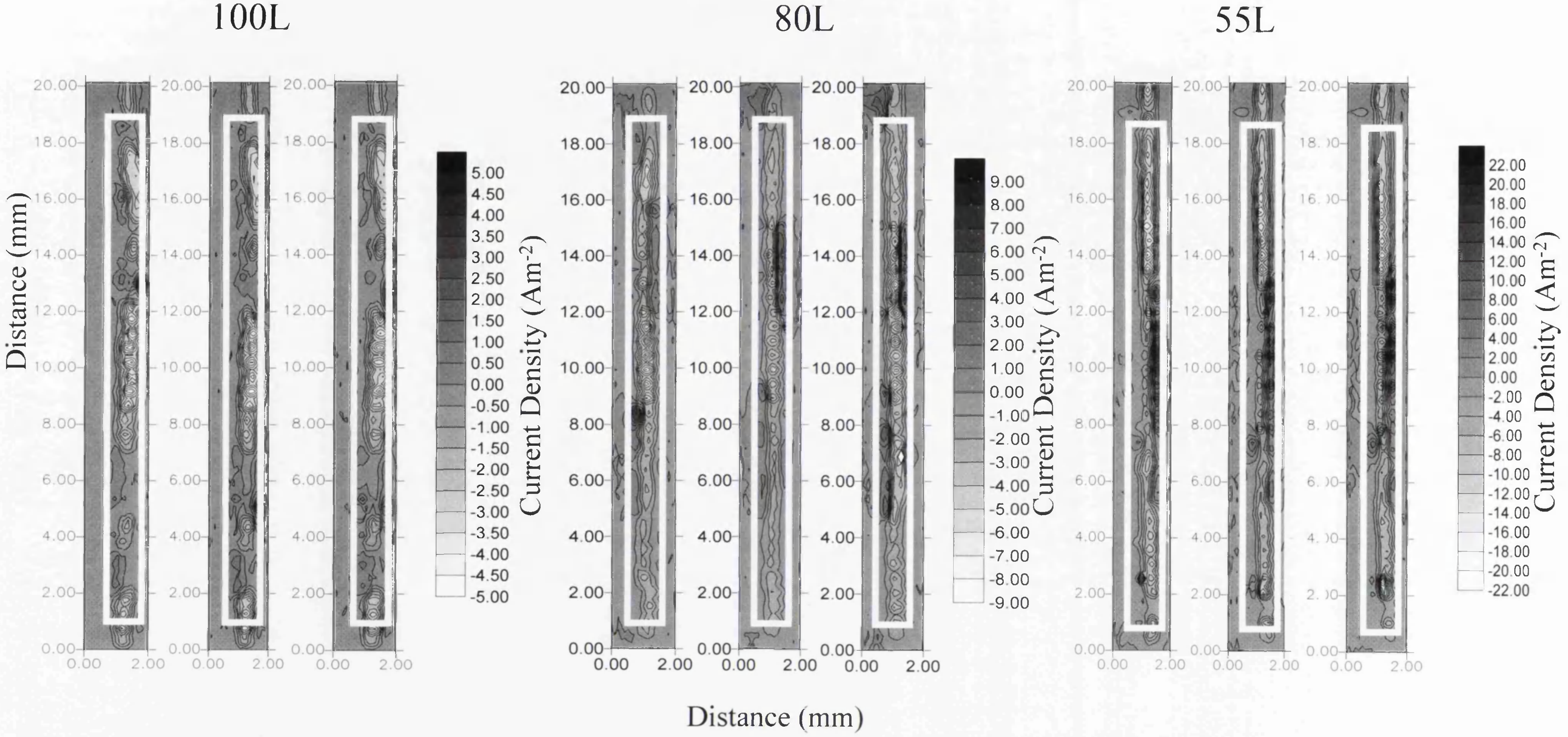

Figure 4.11. SVET Iso-Current maps showing Anodic (dark) and Cathodic (light) regions at 0, 12 and 24 hours for samples 100L, 80L and 55L

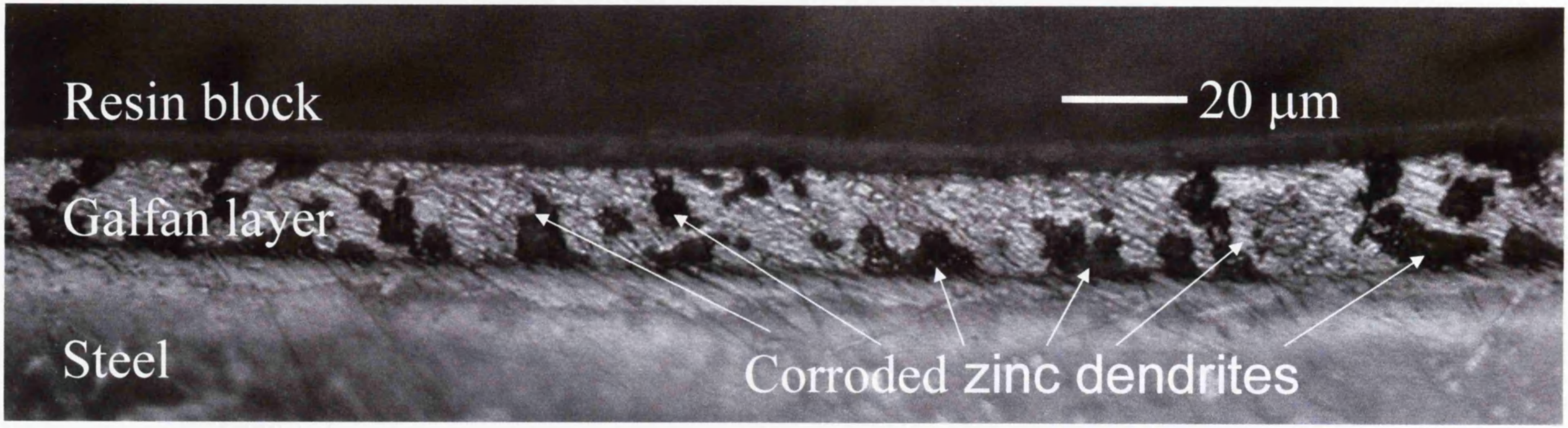

Figure 4.12. Micrograph showing preferential corrosion upon primary zinc

4.1.7. Effects of metallic coating cooling rate on total zinc loss and anode lifetimes along the cut edge

The SVET records signals proportional to the normal component of current density in the plane of scan. The data from a single SVET iso-current contour map can be integrated over the sample area to provide a measure of the ionic current emitted for that particular scan. The simplifying assumption made has been that from scan to scan the current remains constant. By the use of Faraday's law the current data can been converted into a zinc loss over the one-hour period. Summation of the individual, hourly scan, zinc losses yields a total zinc loss (*tzl*) over the 24 hour immersion period. Such a treatment is shown in Figure 4.13, which represents the average *tzl* for 5 individual samples of each of the six coating types. This is a reliable measurement of zinc loss as has been recently demonstrated for a wide range of galvanized steel samples immersed in 5% NaCl[7].

By comparing the *tzl* values in Figure 4.13 it is clear that in both gauges of materials the increasing cooling rate decreases the level of corrosion activity. Thus, the critical factor in determining the corrosion activity on the 4.5% Al zinc galvanising coating is not necessarily the volume percentage (which remains constant) or number of primary zinc dendrites (which increases) but is rather their physical size. This is more clearly shown in Figure 4.14, which compares the dendrite weight with the *tzl* value measured using SVET for the two gauges of material. In this plot the weight of individual dendrites has been calculated from a knowledge of the total volume percentage (figure 4.4), the coating thickness (~19.2 μm) and the number of dendrites per square mm (figure 4.5). The plot in Figure 4.14 illustrates the link between increasing corrosion intensity and the weight of the dendrites in the coating

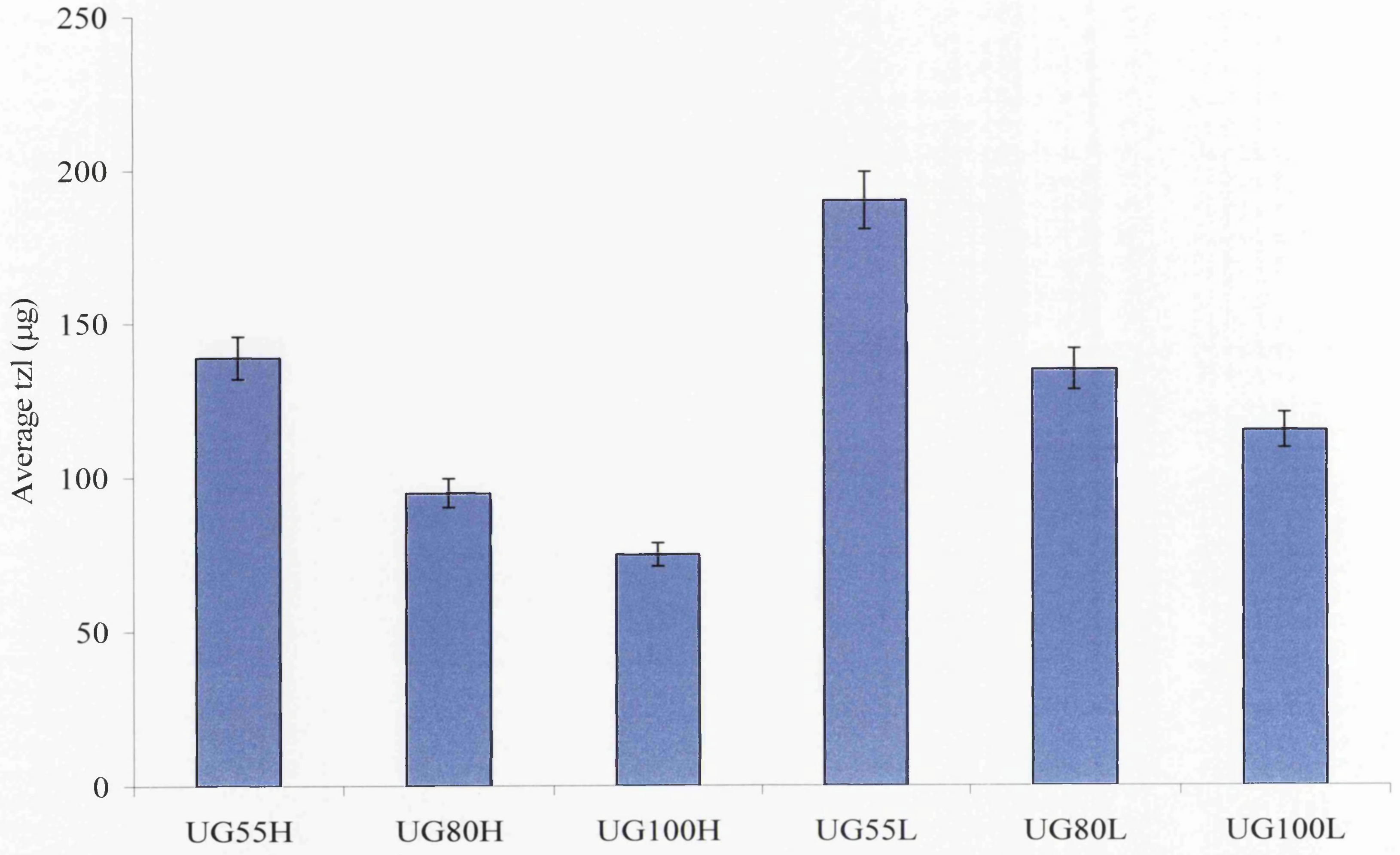

Figure 4.13. Average total zinc loss from exposed cut edges during 24 hour SVET experiment

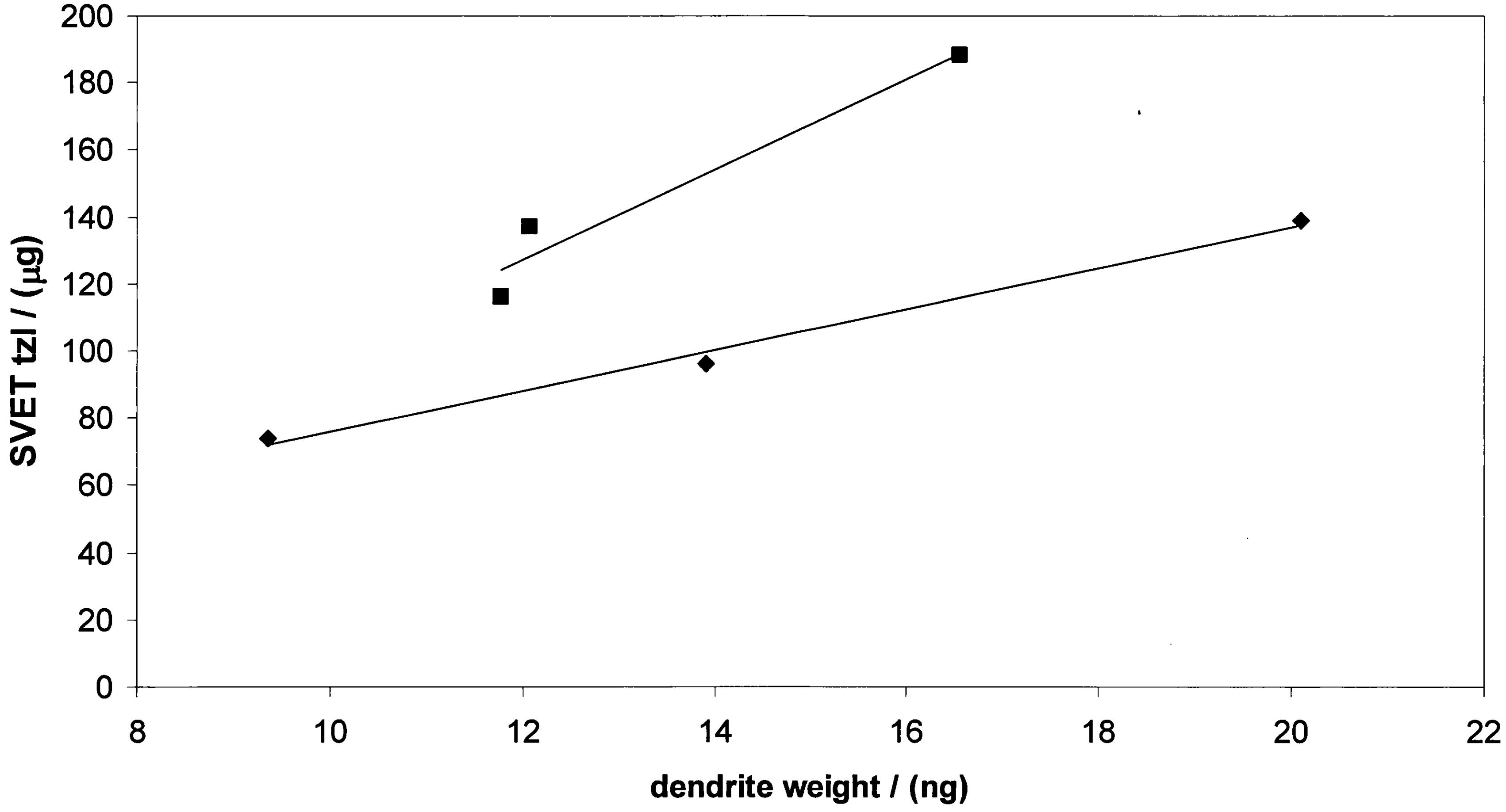

Figure 4.14. Recorded SVET *tzl* as a function of average dendrite weight

(when the volume fraction is constant at least). What is rather surprising is that the zinc loss from the light gauge material is the greatest again suggesting that the surface condition of the heavy gauge strip may have been different potentially leading to greater nucleation.

To determine what the nature of the anodic events is on the metallic coating we have subjected the SVET data to further scrutiny. Individual anodes were identified over the 24-hour exposure period and their temporal evolution profile plotted for the UG55H and UG100H samples. The data for this analysis for typical scans is shown in Figures 4.15 (a) and (b) for the UG55H and UG100H samples respectively. The data shown represents the number of active anodes and their corrosion current densities as a function of time. In order to simplify the analysis it is assumed that each of these anodes is a point current source. This is a reasonable assumption since, on this substrate, corrosion is localised and the *whm* values measured were typically <0.22mm suggesting that the anodes resembled closely our point source calibration cell. Inspection of the data reveals that for the UG55H sample the anodes are not only more intense but display greater lifetimes as compared to those for the UG100H samples. Indeed twelve anodes are persistent (with lifetimes 18-24 hours) throughout the exposure compared to only seven for the UG100H sample. Hence the larger primary zinc dendrites in the UG55H sample are more prone to localised corrosive attack and reduce the overall corrosion resistance of the galvanising coating towards cut edge corrosion. The difference between individual anode zinc losses for the UG55H and UG100H sample is shown in Figure 4.16. This re-enforces the fact that whilst for edge corrosion the number of anodes is similar their relative activity is quite different with the larger dendrites present in the UG55H samples leading to elevated levels of zinc loss from the coating. One point of interest

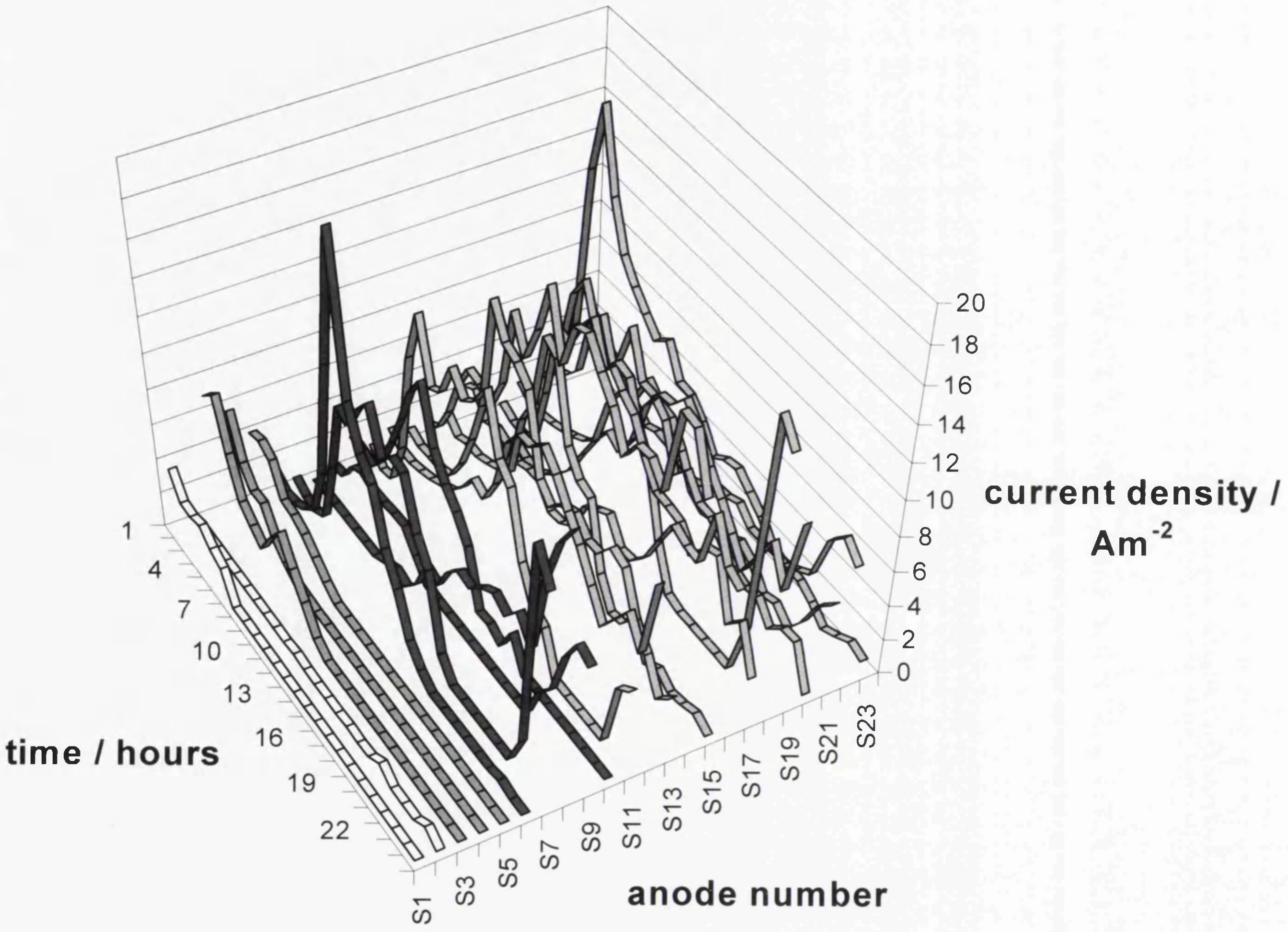

Figure 4.15a. Anode lifetimes as a function of immersion time for sample UG55H

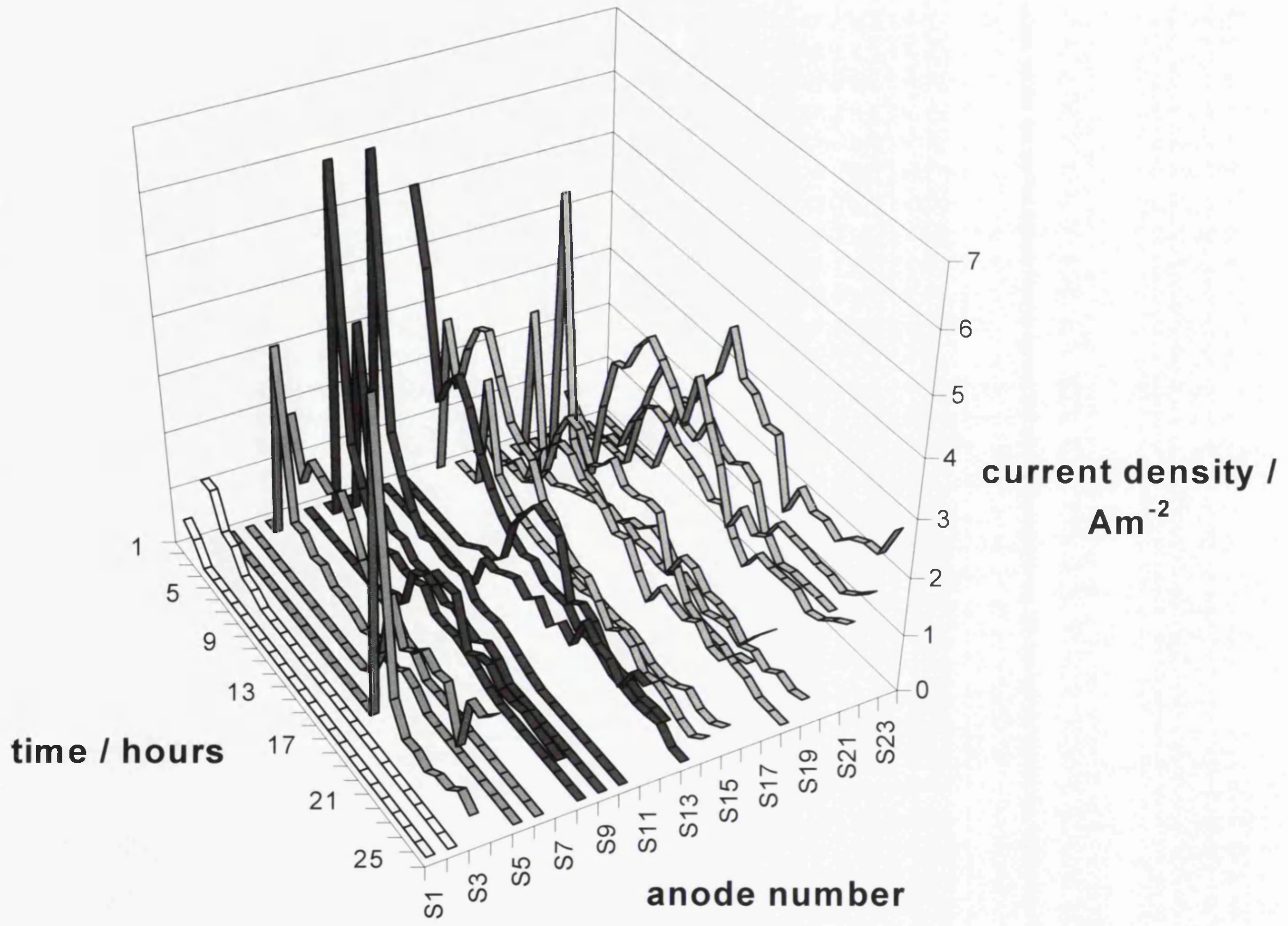

Figure 4.15b. Anode lifetimes as a function of immersion time for sample UG100H

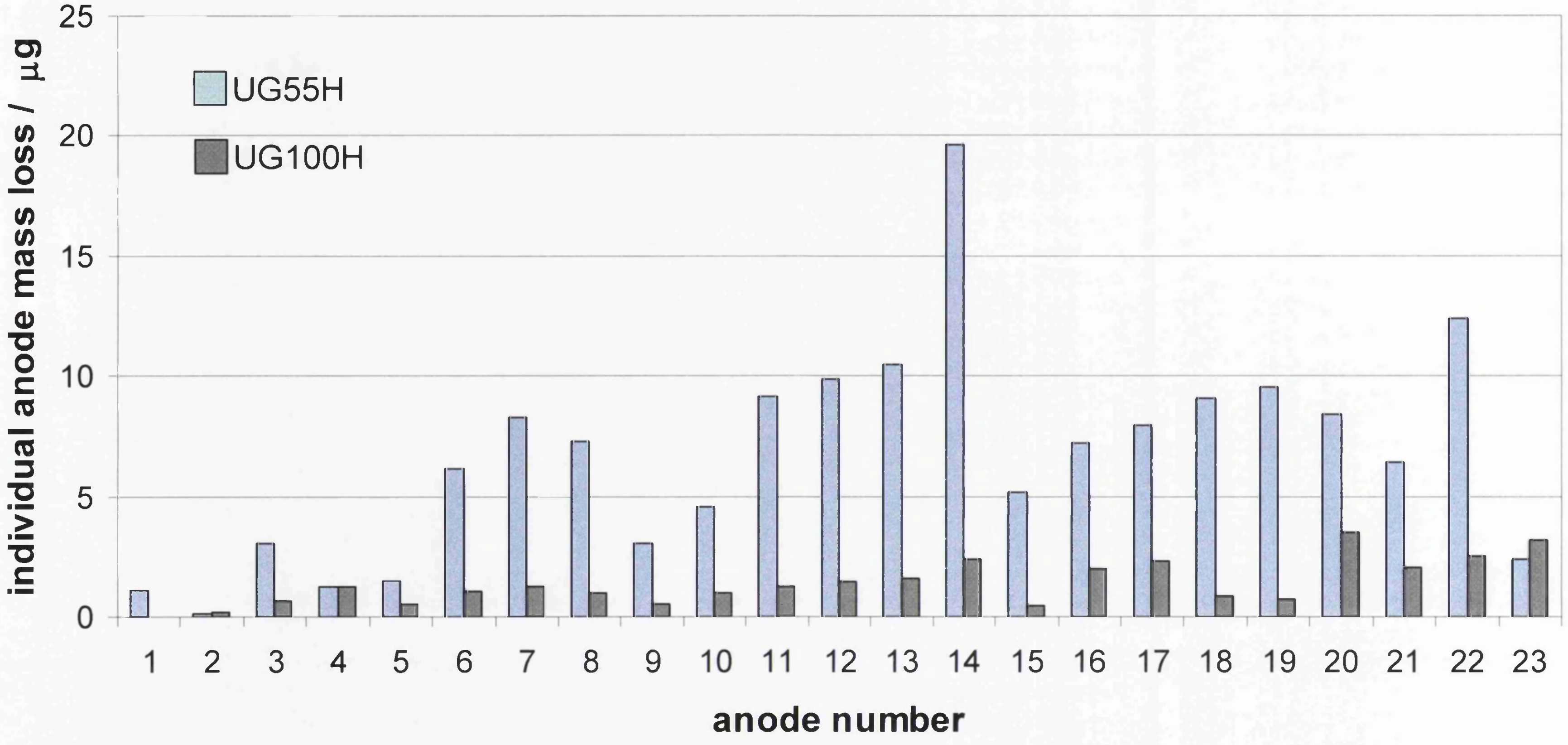

Figure 4.16. Comparison of individual anode zinc losses for samples UG55H and UG100H

is that the SVET measurement of individual anode zinc losses allows the number of dendrites removed per anodic event to be calculated. For the UG55H sample the average zinc loss per anode from Figure 4.16 is 6.7 μg and the dendrite weight is 20 ng which means that each anodic event consumes some 335 dendrites. For the 100 H this falls to 155 dendrites (since the anodic events are on average responsible for 1.4μg zinc loss and the dendrites weigh 9 ng).

4.1.8 Location and intensity of anodic sites across the Galfan surface.

Typical SVET iso-current contour maps are shown in Figure 4.17 for the UG55H and UG100H samples. These SVET maps were recorded after 12 hours immersion in 5% NaCl and show two key features. Firstly the intensity of the corrosion activity is approximately two fold higher in the fastest cooled (UG100H) sample and secondly that the number of active anodes in any single scan on the sample surface is actually higher for the UG55H sample. The increase in corrosion activity is in marked contrast to the decreasing corrosion intensity as a function of cooling rate displayed in Figures 4.11 and 4.15 for cut edge corrosion. In all samples exposed to surface corrosion anodes appeared in the depressed regions i.e. the eutectic cell grain boundaries. The same trend was also observed for the light gauge panels and further quantification of the SVET data was undertaken as detailed below.

4.1.9 Effect of metallic coating cooling rate and gauge on total zinc loss and anodic lifetimes

As previously stated it is possible to calculate the zinc loss (*tzl*) occurring upon the surface from the SVET iso-current contour maps using Faraday's law. Figure 4.18 is

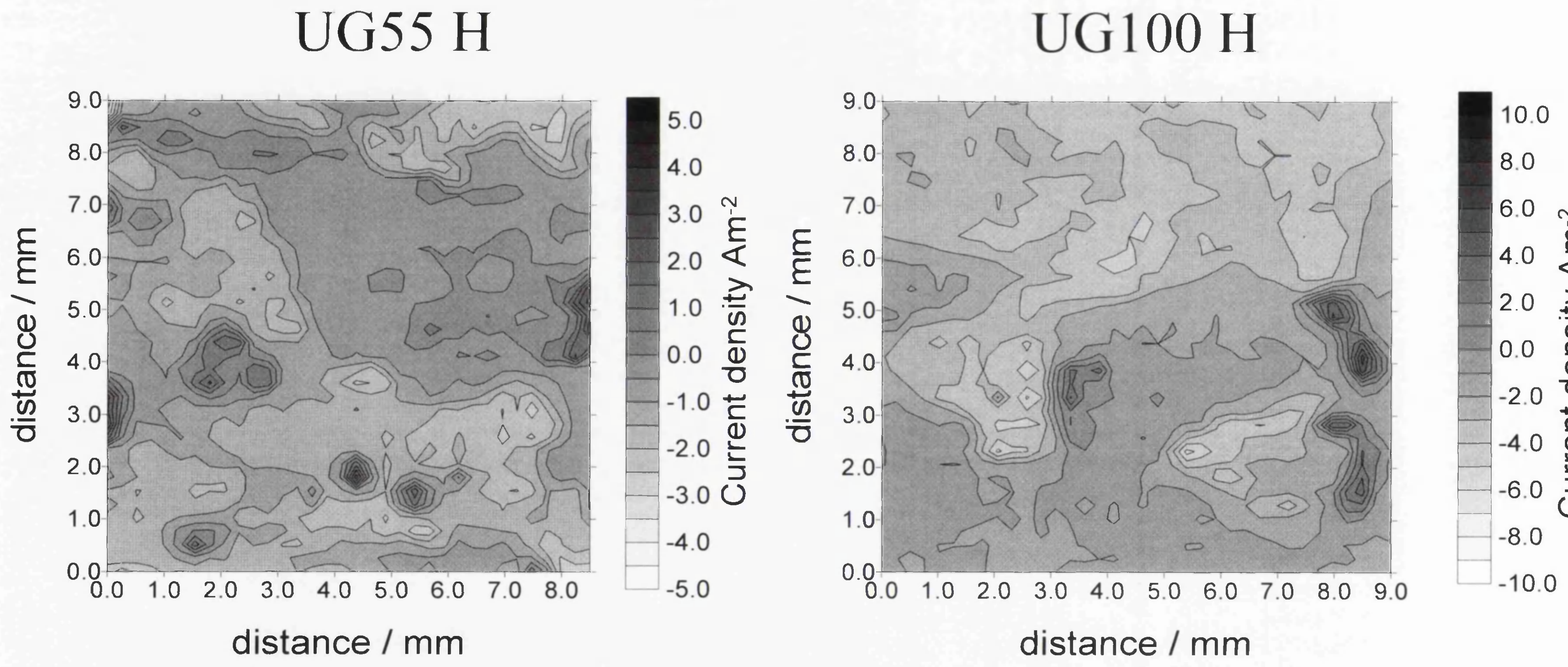

Figure 4.17. Representative iso –current maps for samples UG55H and UG100H

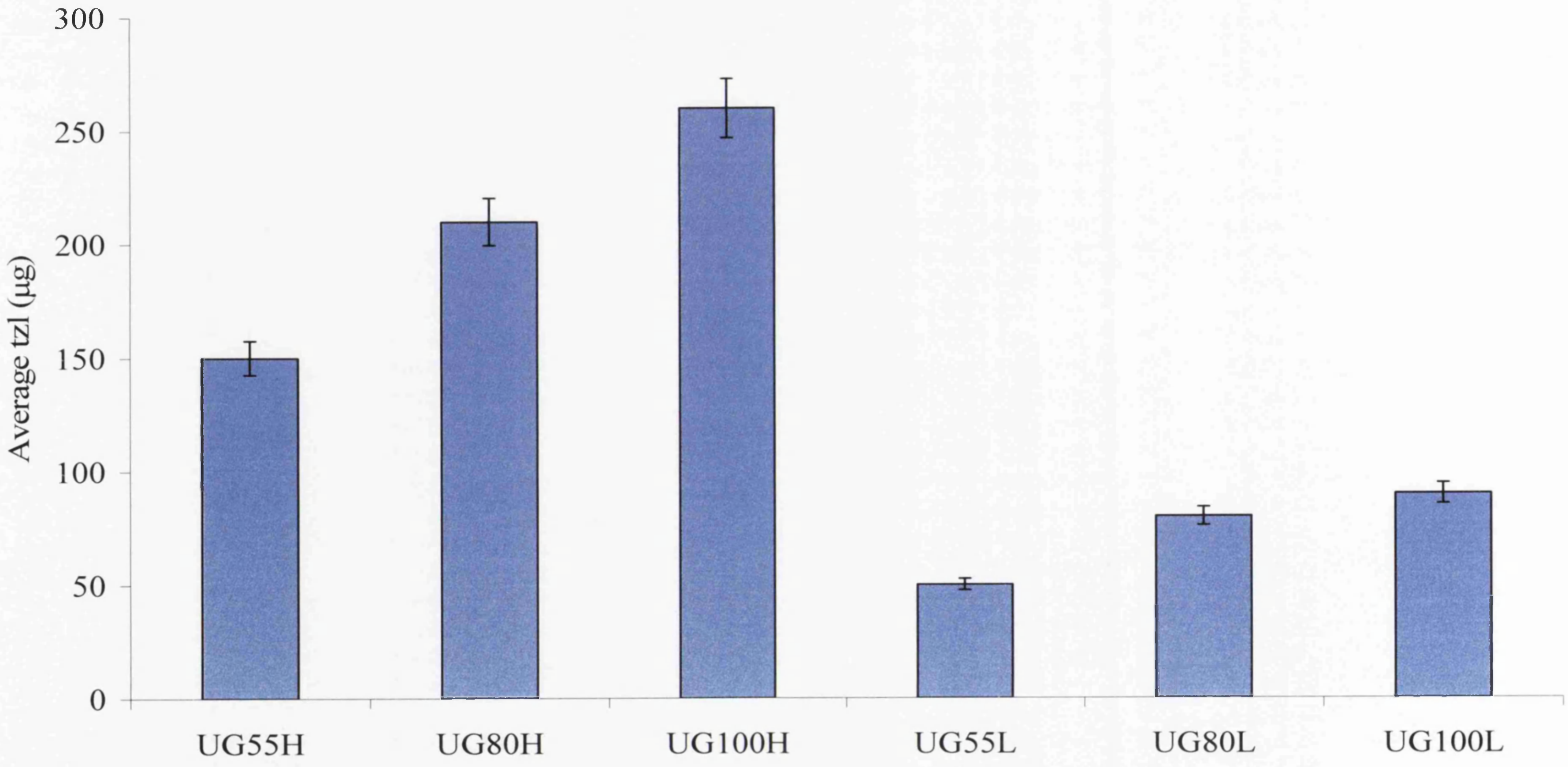

Figure 4.18. Average total zinc loss from exposed surfaces during 24 hour SVET experiment

an illustration of the effect that cooling rate and gauge have on the *tzl* values measured from the surfaces of the galvanised materials as a function of the cooling rate. Within the cooling rate subsets, there is a reduction in zinc loss as the cooling rate is decreased. This result holds for both of the steel gauges. The results in Figure 4.18 also show a reduced amount of zinc loss occurring upon surfaces of the light gauge samples. Interestingly this compares with increased zinc loss for the cut edge samples on the light gauge substrate again re-enforcing the link between microstructure and corrosion resistance. Once again, it is difficult to provide a direct reasoning for the change in microstructure between the two gauges since little is know about the surface characteristics of the two coils.

Repeated scanning using the SVET showed that the anodes active throughout the exposure period were located at triple points and eutectic cell grain boundaries. The increase in corrosive attack upon the faster cooled samples also indicates that the differing corrosion performance is a result of the changes in solidification at the surface. As described earlier, the increase in cooling rate leads to a reduction in the eutectic cell size (and consequently a change in the visual appearance). The reduction in cell size corresponds with an increase in the unit length of the depressed grain boundaries. The depressed region is a site for dendrite arms to penetrate the surface and act as sites for the initiation of corrosion. Hence the increasing corrosion activity in the fast cooled samples (UG100L and UG100H) is due to the increasing eutectic cell boundary length and the potential for initiation of corrosion at surface zinc dendrite arms in these locations.

Upon examining the temporal evolution of anodic activity at specific sites some interesting observations can be made using the SVET data. In terms of the number of active anodes present over the 24-hour exposure period the faster cooled samples display greater total active anodes. In addition, the faster cooled materials display higher anode intensities but in general anodic lifetimes are short. By contrast the slower cooled samples show anodes that are much more persistent but less intense. This is summarized in Figures 19 (a) and (b) where anode lifetimes for surface corrosion of the UG55H and UG100H samples are compared.

Individual anode zinc losses are compared in Figure 4.20. These values are obtained by summation of the current emerging from anodes shown in Figures 4.19 (a) and (b). This data highlights not only the increasing anode numbers in the faster cooled samples but also that individual anode zinc losses are on average higher for the UG100H sample (0.92 μg as compared to 0.51 μg). The individual anode mass losses from the cut edge corrosion data shown in Figure 4.16 show that each anode in the case of cut edge corrosion removes on average 6.7 μg and 1.3 μg respectively for the UG55H and UG100H samples. Comparison with the dendritic sizes (0.02 μg for UG55H and 0.01μg for UG100H) allows the estimation of the numbers of dendrites completely removed per anodic event. For surface corrosion this is therefore 25 and 92 respectively for UG55H and UG100H. The fact that each anodic event consumes more than one dendrite is not surprising since there is dendritic interconnection in the coating.

Figure 4.21 is a useful comparison of the two methods used in this work to evaluate zinc losses. The solid line is obtained by summing individual anode currents and the dashed line by integration of all current densities. In cases where anodic events are not point sources one would expect a reduction in the individual anode zinc losses as compared to the integration method. The two methods in this instance agree reasonably well as is shown in Figure 4.21 indicating that the corrosion is highly localized and focused on the anodes identified in Figures 19 (a) and (b).

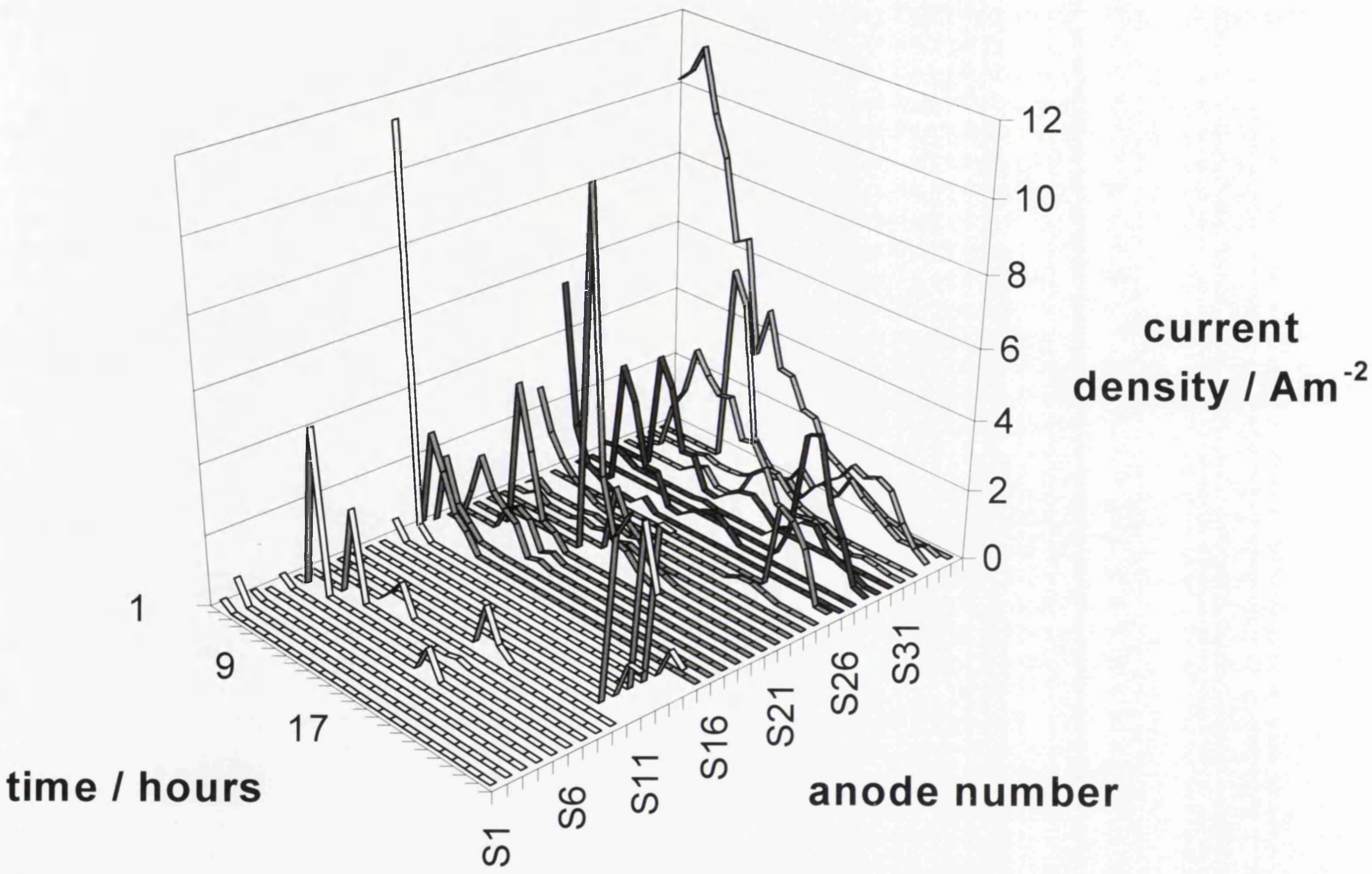

Figure 4.19a. Anode lifetimes as a function of immersion time for sample UG55H

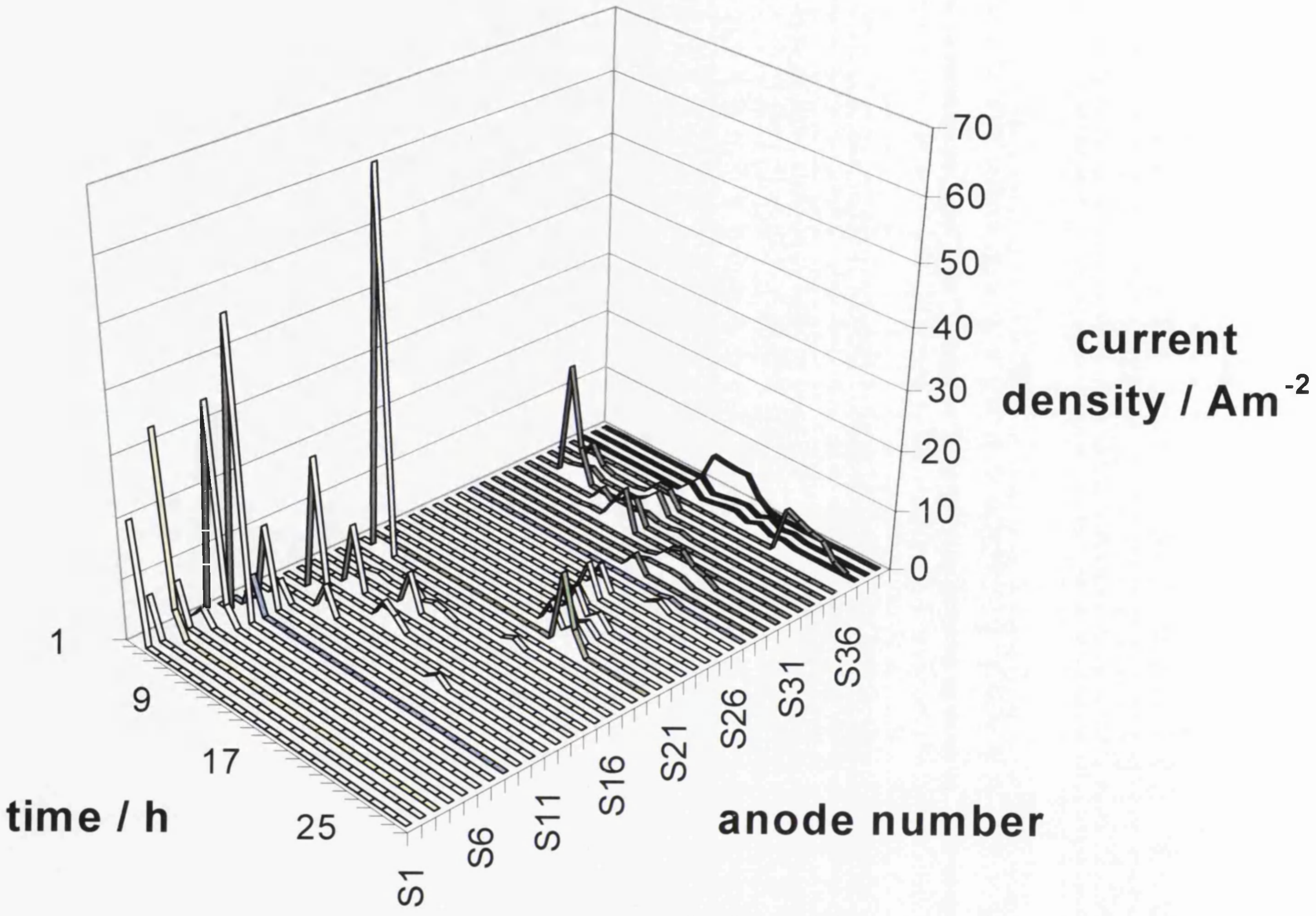

Figure 4.19b. Anode lifetimes as a function of immersion time for sample UG100H

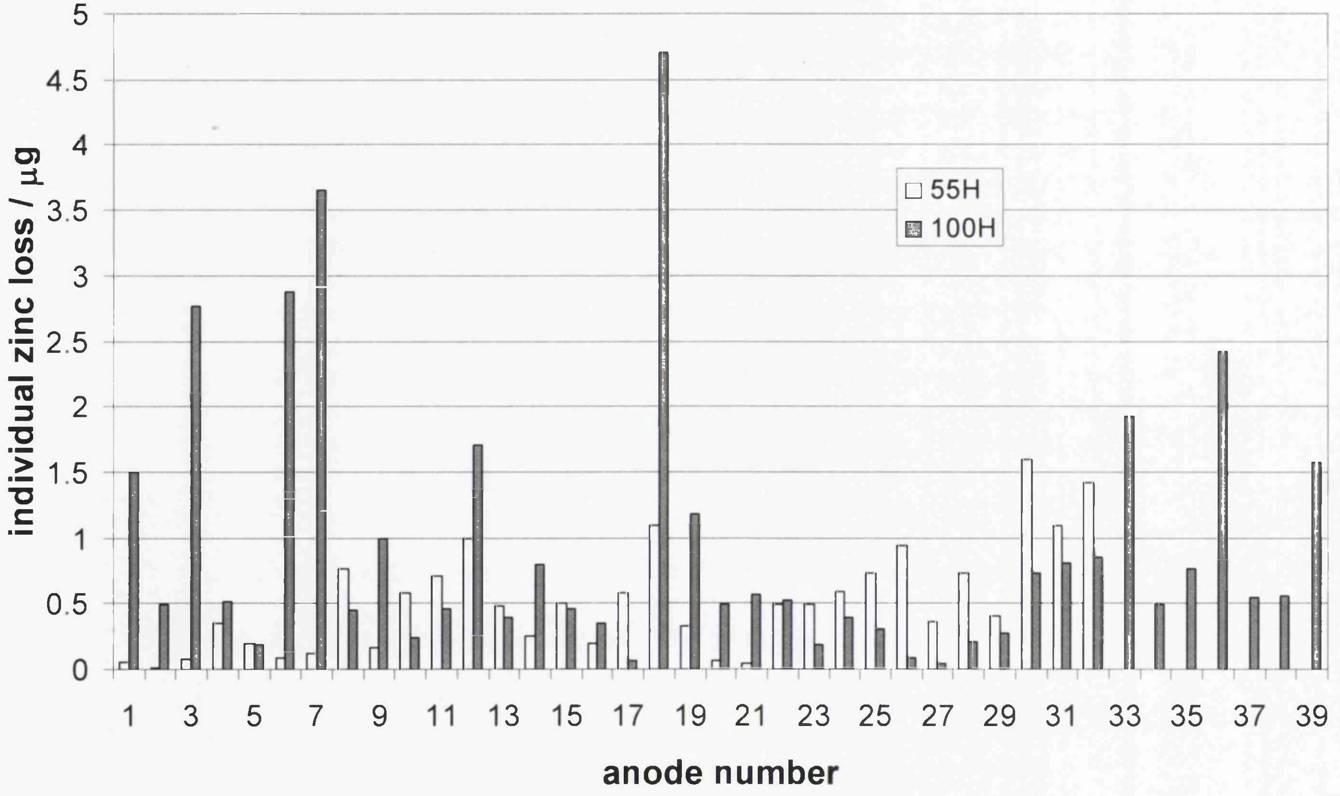

Figure 4.20. Comparison of individual anode zinc losses for samples US55H and UG100H

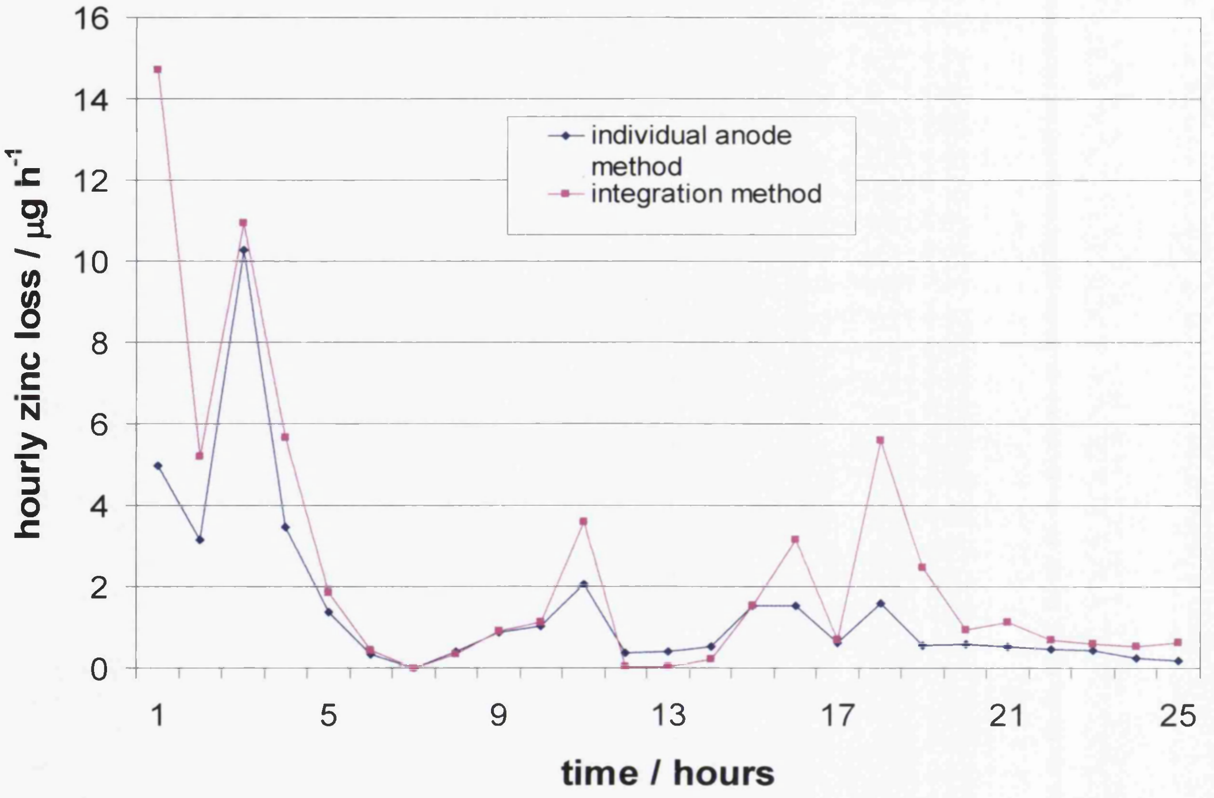

Figure 4.21. Comparison of methodology of calculating zinc loss

The link between the surface and edge corrosion resistance as determined using SVET and eutectic cell size alterations, indicative of microstructural changes, is shown in Figure 4.22, from which it can be seen that overall for the two gauges there is a good correlation between surface and edge corrosion resistance and the sizes of eutectic cells. This is again an important point since it enables the line operator to be able to adjudge corrosion resistance of such materials on the basis of an on line visual inspection which can therefore be used as a guide for corrosion activity during the changes in processing parameters that accompany any production run.

4.2 Conclusions

The combined use of microstructural analysis and advanced localized corrosion measurements using SVET has highlighted the link between coating microstructure and corrosion resistance and also the critical difference between corrosion measurements made on the surface of OCS and at their cut edges. The trends for cut edge and surface corrosion resistances determined are different, but both are a result of changes borne from processing parameters altering the microstructure. Increasing the cooling rate leads to a large number of smaller primary zinc dendrites as a result of greater nucleation. However, the volume percentage of this dendritic phase remains constant, within experimental error. The increased cooling rate also produces a finer lamella eutectic, as a result of rapid growth, which at very high cooling rates forces a change in eutectic morphology to include some rod structures. The increasing nucleation also leads to a reduction in the surface eutectic cell size upon faster cooling, leading to an increased length of cell boundary per unit area of coating.

The smaller number of large dendrites in the slower cooled samples directly influence cut edge corrosion. The dendrites are preferentially corroded and the

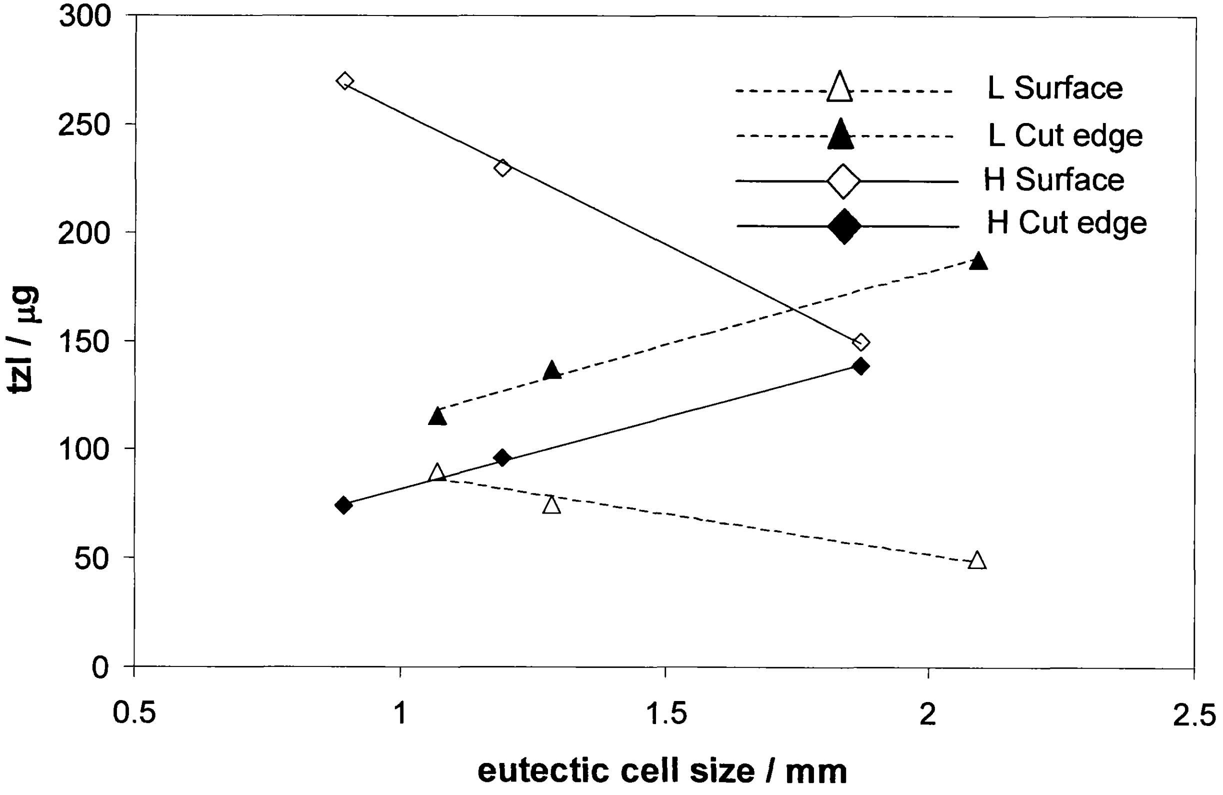

Figure 4.22. Recorded zinc losses as a function of eutectic cell size

lifetime and intensity of the anodes are greater, consequently resulting in a greater amount of zinc loss.

The increase in length of depressed boundaries per unit area due to the reduced eutectic cell size at higher cooling rates leads to a greater amount of surface corrosion. The combination of increasing eutectic cell boundary and increasing dendritic penetration in the boundary region contribute elevated surface corrosion. These microstructural changes in the surface of the material lead to the formation of larger numbers of short lived high intensity anodes.

In summary, in the evaluation of new zinc aluminium alloy galvanising chemistries and processing conditions it is important to consider both surface and edge corrosion and the precise way in which the localisation and intensity of corrosion is influenced by microstructural changes. The combination of SVET with conventional microscopic techniques is a powerful technique in this regard.

4.3 References

---

[1] D A Worsley and M Challis, British Corrosion Journal, 36, 297, (2001)

[2] A.F. Skerazi: Proceedings of the 14th International Galvanising Conference, Munich Germany, (Zinc Development Association), 51(1986)

[3] P.A.Porot, N.Venthan, R.D. Jones and J.A. Spittle, Metallography, 20, 181, (1987)

[4] F. Hinterberger, W. Maschek and J. Faderl, Zinc Based Steel Coating Systems: Production and Performance, 281, (1998)

[5] D.A. Porter and K.E. Easterling, Phase transformations in metals and alloys, Chapman and Hall, second edition.

[6] H.Y. Liu and H. Jones, Acta Metallurgica et Materialia, , 40, 2003(1992)

[7] J.H. Sullivan and D.A. Worsley, British Corrosion Journal, 37, 282. (2002)

Chapter 5

Influence of coating weight on the microstructure and corrosion resistance of Galfan coated steels

5.0 Introduction

Increasing demand for improved performance, reduced cost materials has lead to a re-evaluation of the performance criteria of many organically coated steel systems. In a drive to reduce the production costs whilst retaining corrosion performance, (producing a more cost effective product with increased profitability) some of the processing parameters and coating dimensions considered to be 'set in stone' have been assessed to deduce whether they are actually the optimum conditions providing the most functional and cost effective product.

One of the more obvious coating dimensions to investigate is the coating weight of the galvanized metallic coating i.e. its thickness. The galvanized coating provides valuable protection for the base steel substrate against corrosion, however it would be easy to 'super size' this layer producing a coating that although providing excellent corrosion protection, is ultimately wasting a galvanising material and consequently reducing the profitability to the manufacturer.

To assess the importance of the coating weight of Galfan a line trial was initiated through Corus Colors, Shotton during December 2003. Using a single steel gauge of 0.7mm, and keeping a constant setting on the cooling rig, samples were produced by down gauging the metallic coating from a standard[1] 255gm^{-2} coating (typically 20μm thick, an industrial standard for this coating[2]) to a lowest weight of 80gm^{-2} (typically 7μm in thickness). This reduction in coating weight was achieved using high velocity, low pressure gas knives which are situated at a height of 0.9m above the galvanizing bath.

Material dimensions, specifications and coating compositions are detailed in section 2.4.2.3 For each experimental trial the samples were examined in the dipped condition and had not been pre-treated or organically coated prior to testing. The metallic coating thickness's were verified using a calibrated microscope and the results of this analysis are detailed in figure 5.1. Each of the samples was subjected to corrosion testing using the SVET as detailed in Chapter 2.

5.1 Results and Discussion

5.1.1. Microstructural Observations

The microstructure is to be quantified through a measure of the following: a.) the volume percentage of primary zinc, b.) the size and number of the primary dendrites, c.) changes in the eutectic type and spacing and d.) changes in the eutectic cell size.

Figures 5.2 and 5.3 detail the through coating microstructures of samples CT80, CT100, CT130 and CT170. In each case the depth shown is relative to the depth through the coating from the air/ coating interface. In each case the optically white regions are the primary zinc solid solution dendrites and these are encased in the Zn – Al eutectic matrix which varies in morphology (wholly rod, or a mixture of rod and lamellar) depending upon the sample. Residue of the mounting process can be seen on the images close to the air/ coating interface. The primary zinc dendrites exhibit growth along the close packed directions $<11\bar{2}0>$, which is typical for HCP structures. Initial comparison of the images shows there is little change in all the samples between the number and size of the primary dendrites close to the steel/ coating interface. However, comparing the images 1-2μm below the air/ coating interface it is apparent that the volume percentage of primary zinc visible is greater in sample CT80 when compared with that of sample CT170 at this coating depth.

Sample Code	Coating weight (gm^{-2})	Coating thickness (μm)
CT80	$80gm^{-2}$	$\sim 7\mu m$
CT100	$100gm^{-2}$	$\sim 9\mu m$
CT130	$130gm^{-2}$	$\sim 12\mu m$
CT170	$170gm^{-2}$	$\sim 15\mu m$

Figure 5.1. Sample coating weights and associated coating thicknesses

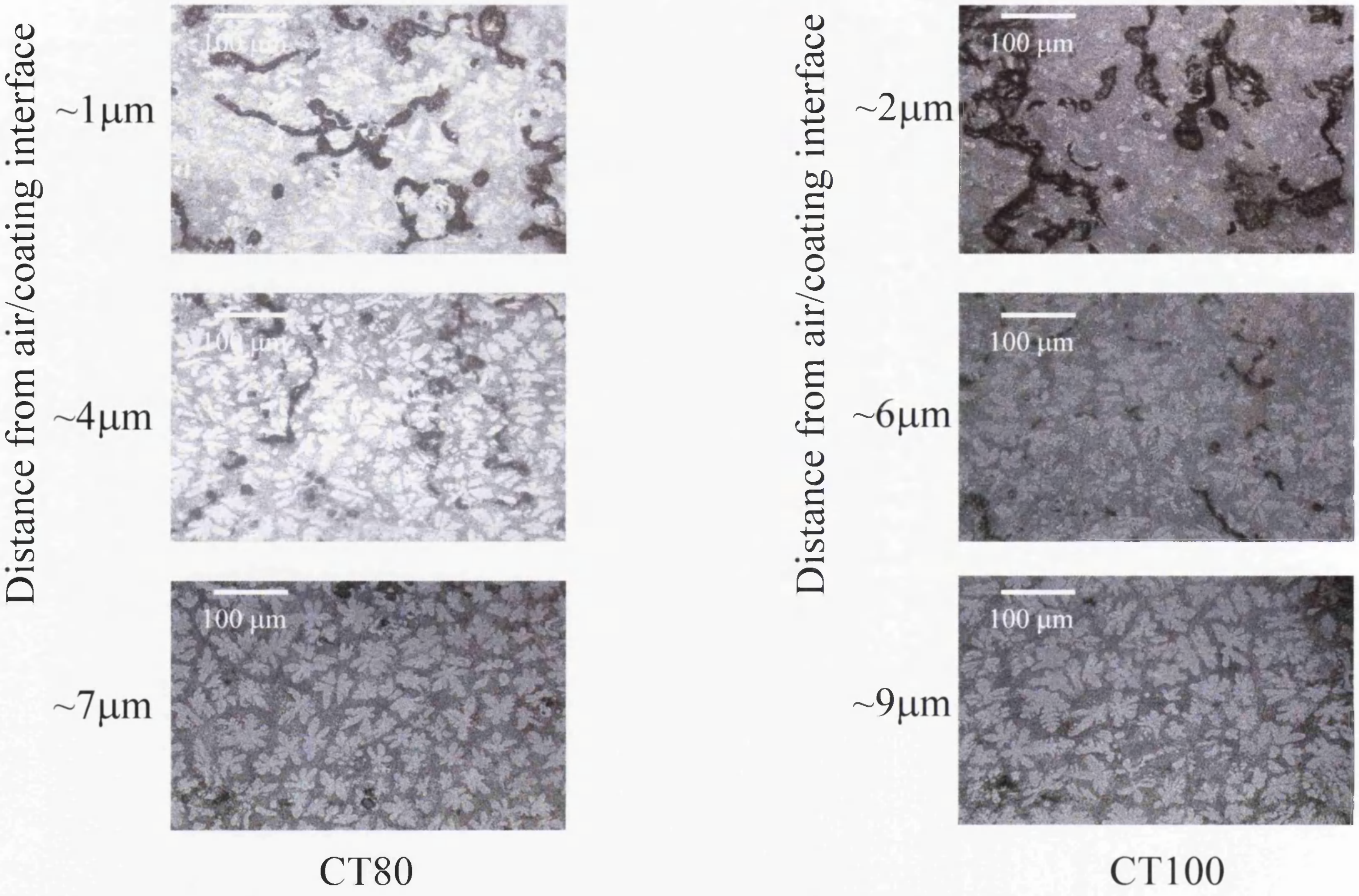

Figure 5.2 Coating microstructures as a function of depth from the air/coating interface

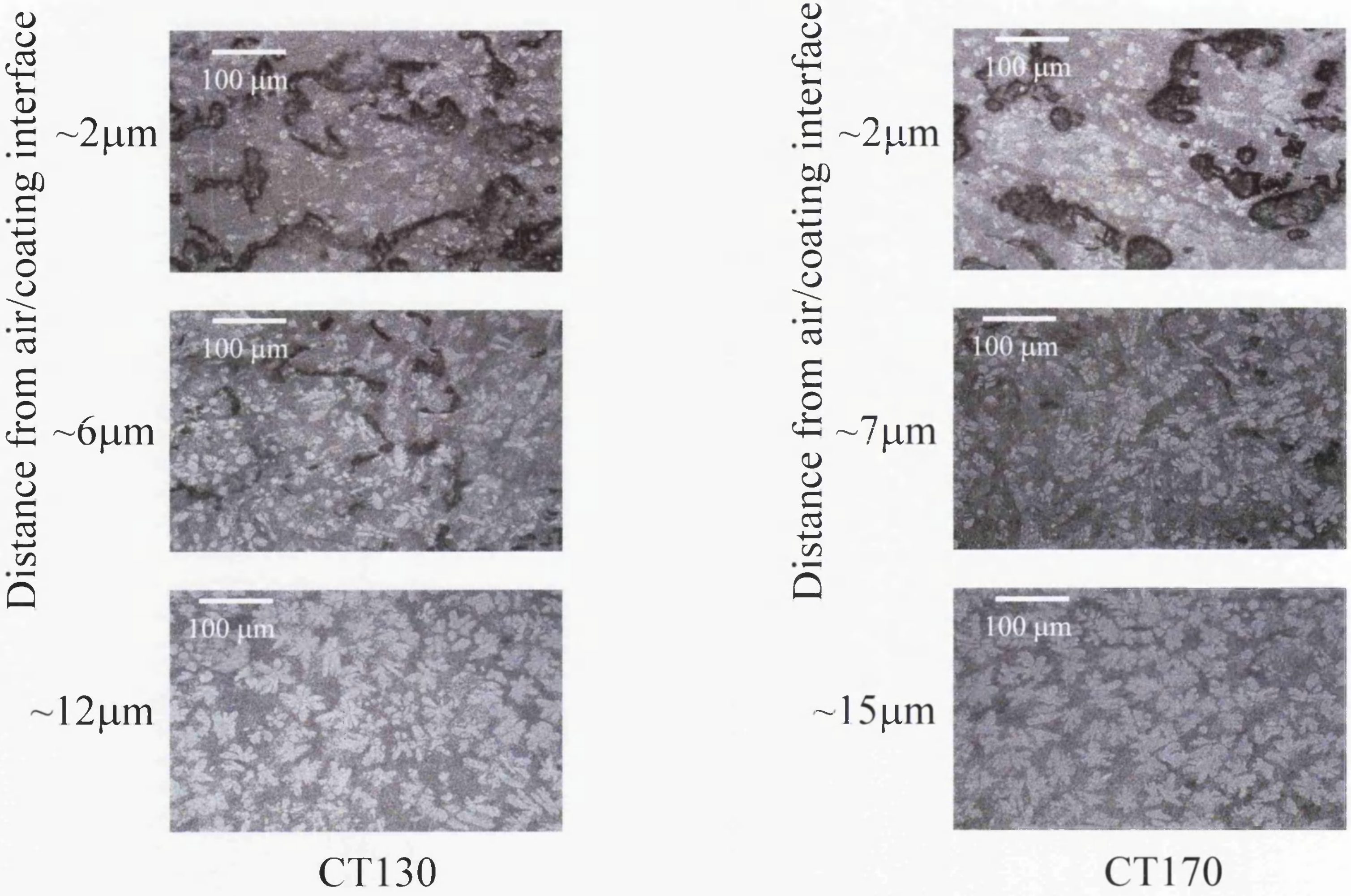

Figure 5.3 Coating microstructures as a function of depth from the air/coating interface

5.1.2. Effects of Galfan coating weight upon the volume percentage of the primary zinc

Figure 5.4 shows the average volume percentage (in each case, a mean average from three regions at each depth within a single 20mm *x* 10mm sample) of the primary zinc dendrites as a function of distance from the steel/ coating interface. From figure 5.4 (sample CT80) it can be seen that at a distance ~1µm below the air/coating interface the average volume percentage of primary zinc is ~28%. This figure increases as the steel/ coating interface is approached, ultimately to a value of ~46% close to the steel/ coating interface. The trend is observed in each of the samples with the volume percentage in sample CT100 (air/ coating interface to steel/ coating interface) rising from ~15% to ~46%, in CT130 (figure 5.4) from ~12% to ~48% and CT170 from ~8% to ~47%. Again, as previously stated, the increased volume percentage of primary zinc near to the steel/ coating interface infers that the nucleation of the primary phase is occurring near to the base steel substrate.

By taking the mean average of the primary zinc volume percentages at the defined depths, an approximate total volume percentage of primary zinc in each coating can be calculated (see section 2.1.2.1). This result is shown in figure 5.5. From this chart it can be observed that the total volume percentage of primary zinc is reduced as the coating weight increased. Sample CT80 has an average total volume percentage of 37%± 1.8%. This figure is reduced to 32%± 1.6% in sample CT100 and further to 29%± 1.4% and 26%± 1.3% in samples CT130 and CT170 respectively. In this instance, the observed increase in the total volume percentage of primary zinc is not a result of a change in the evolution of the primary phase but a direct consequence of the distribution of the primary zinc dendrites through the coating and changes brought about by the wiping action of the gas knives. Figures 5.6.(a-c) show a schematic of the Galfan microstructure with different coating weights which have

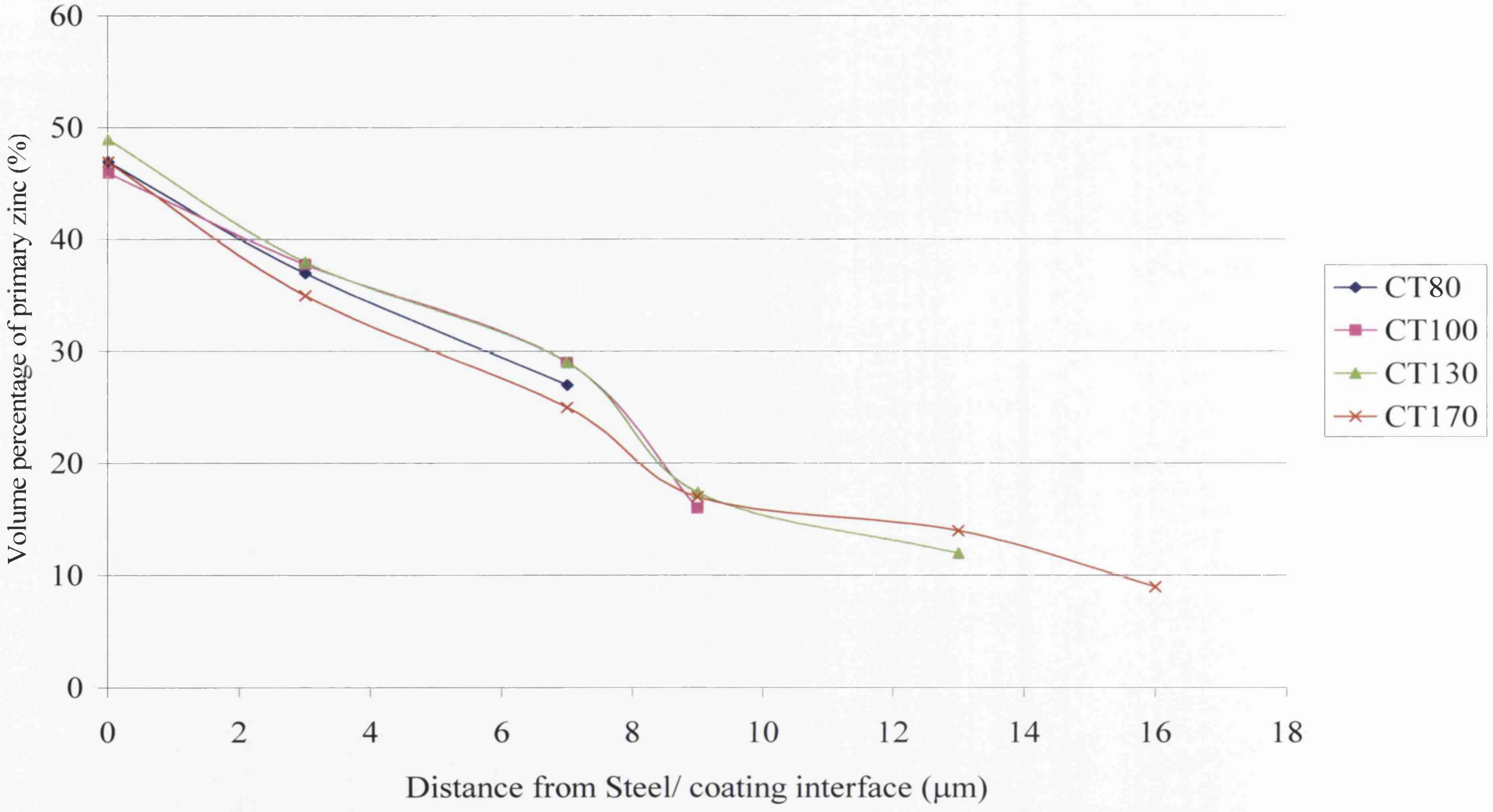

Figure 5.4 Average volume percentage of primary zinc as a function of depth through coating

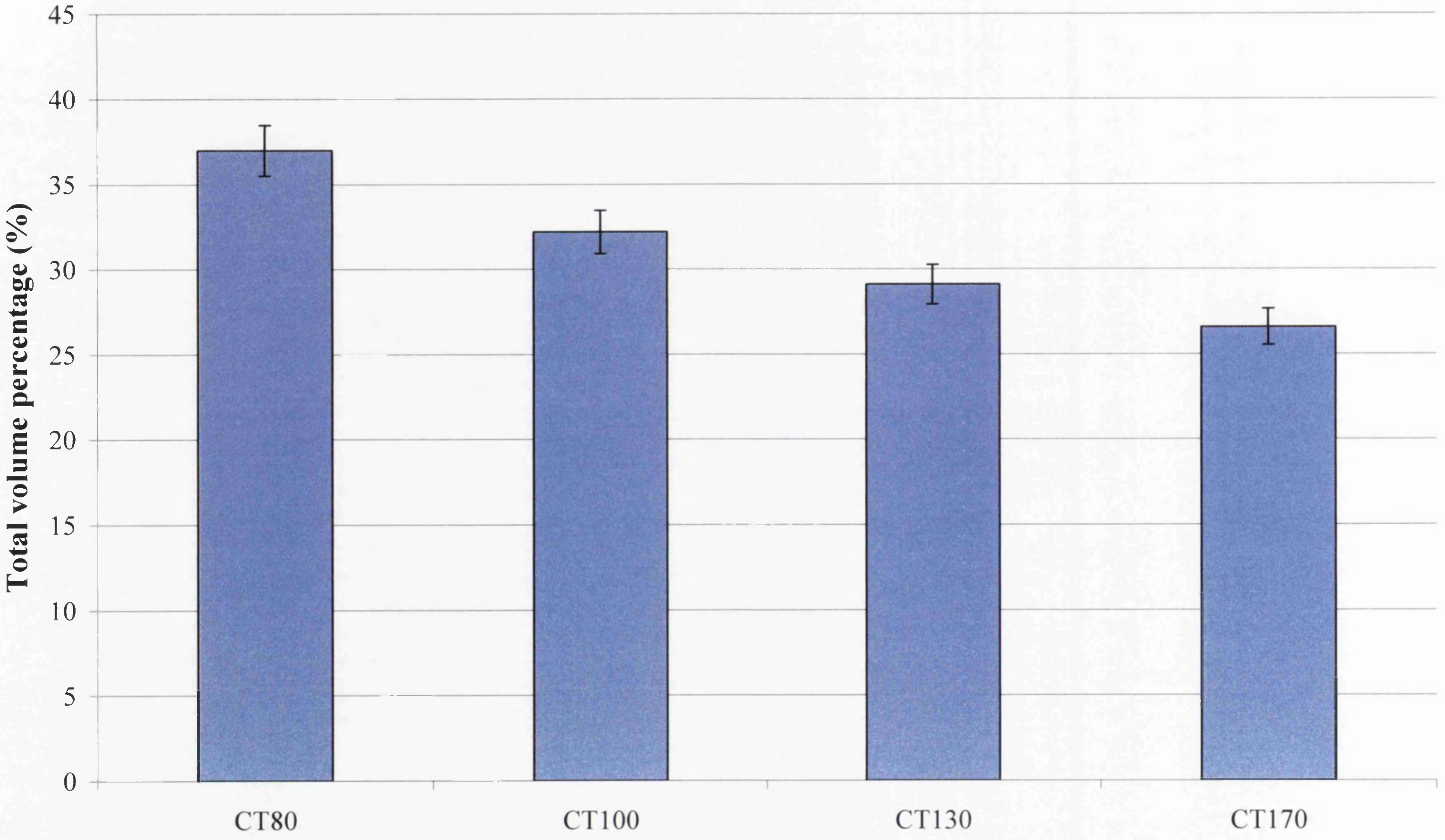

Figure 5.5. The average total volume percentage of primary zinc

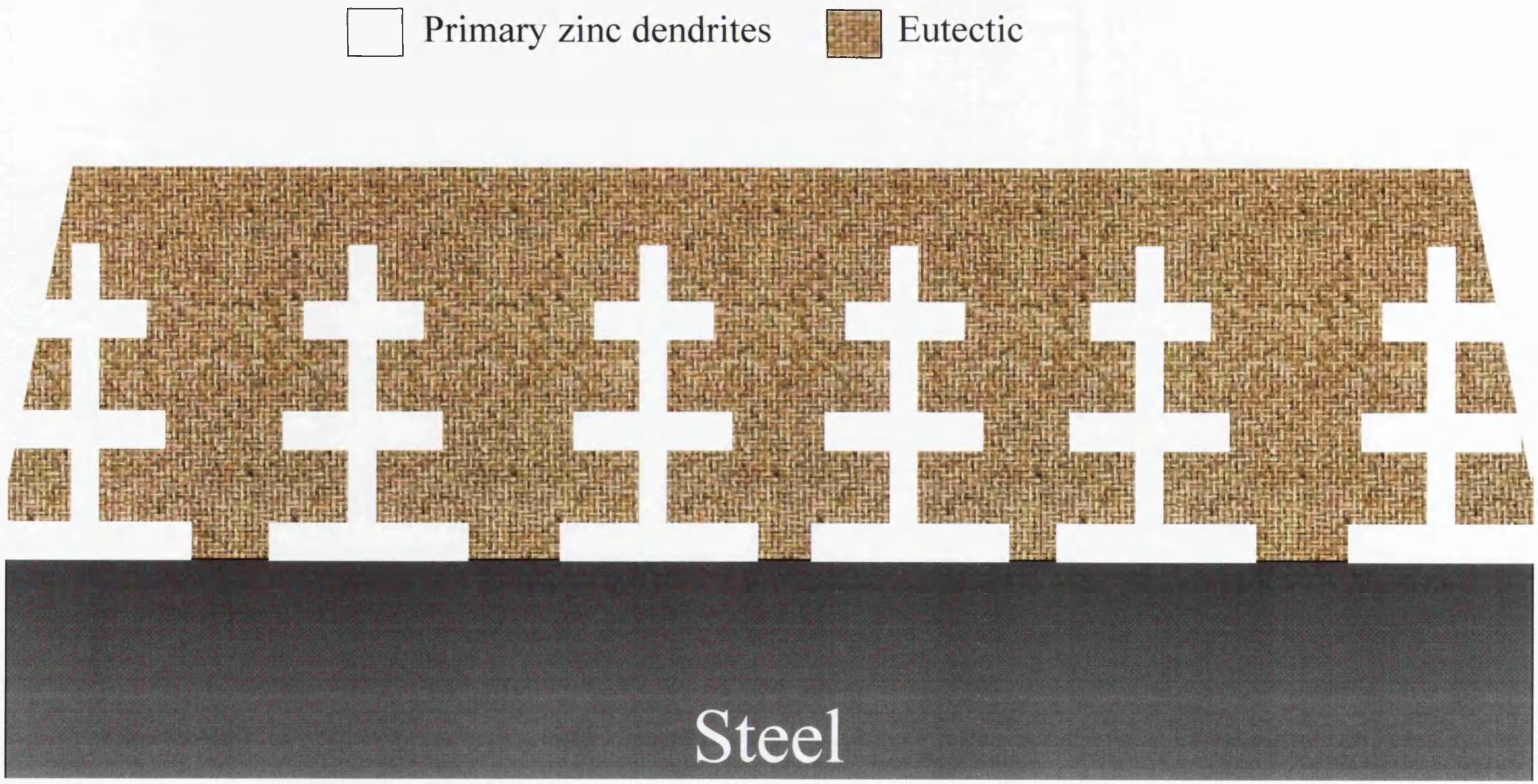

Figure 5.6 (a) Schematic of galfan coating (255gm^{-2}) laterally sectioned

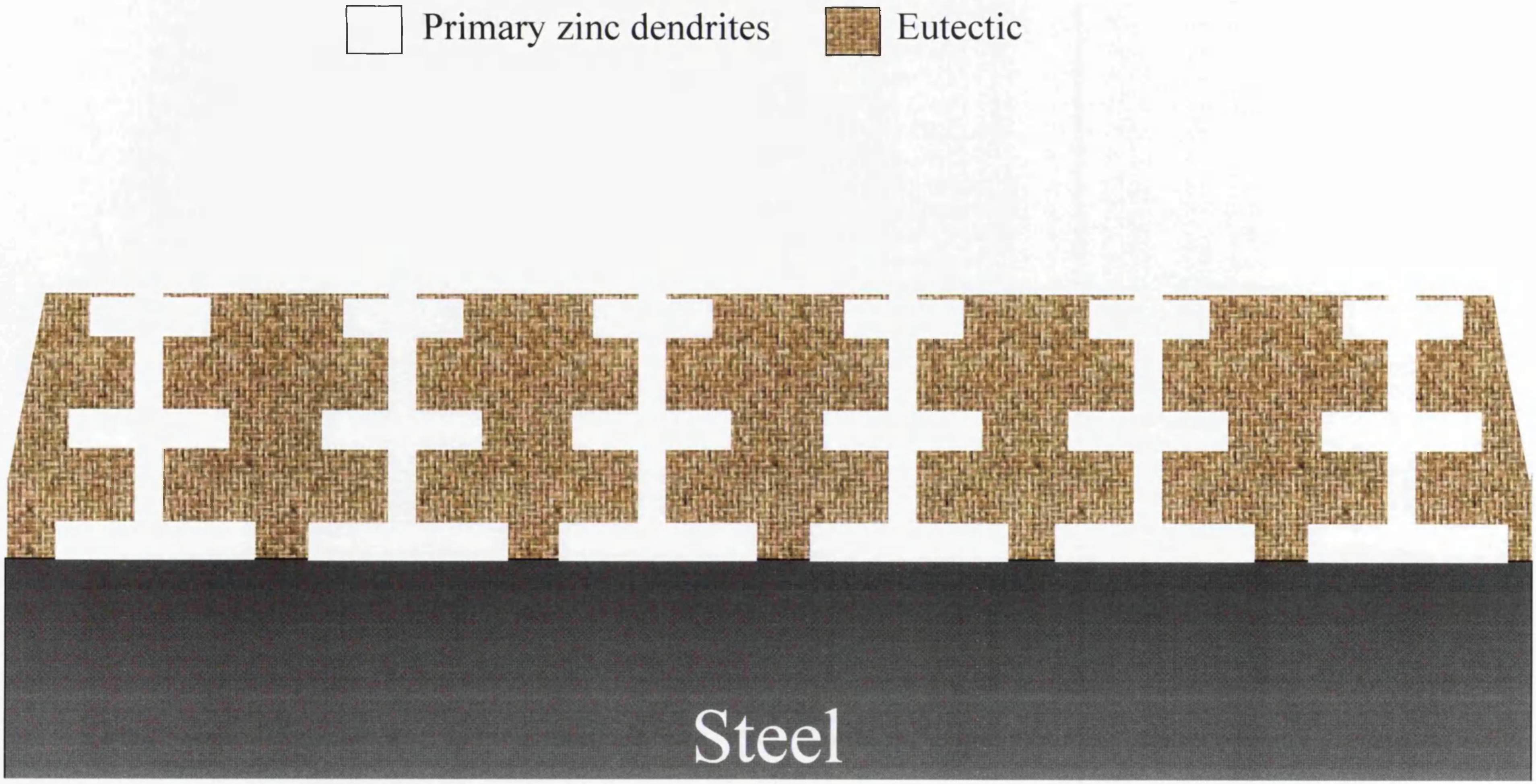

Figure 5.6 (b) Schematic of galfan coating (170gm^{-2}) laterally sectioned

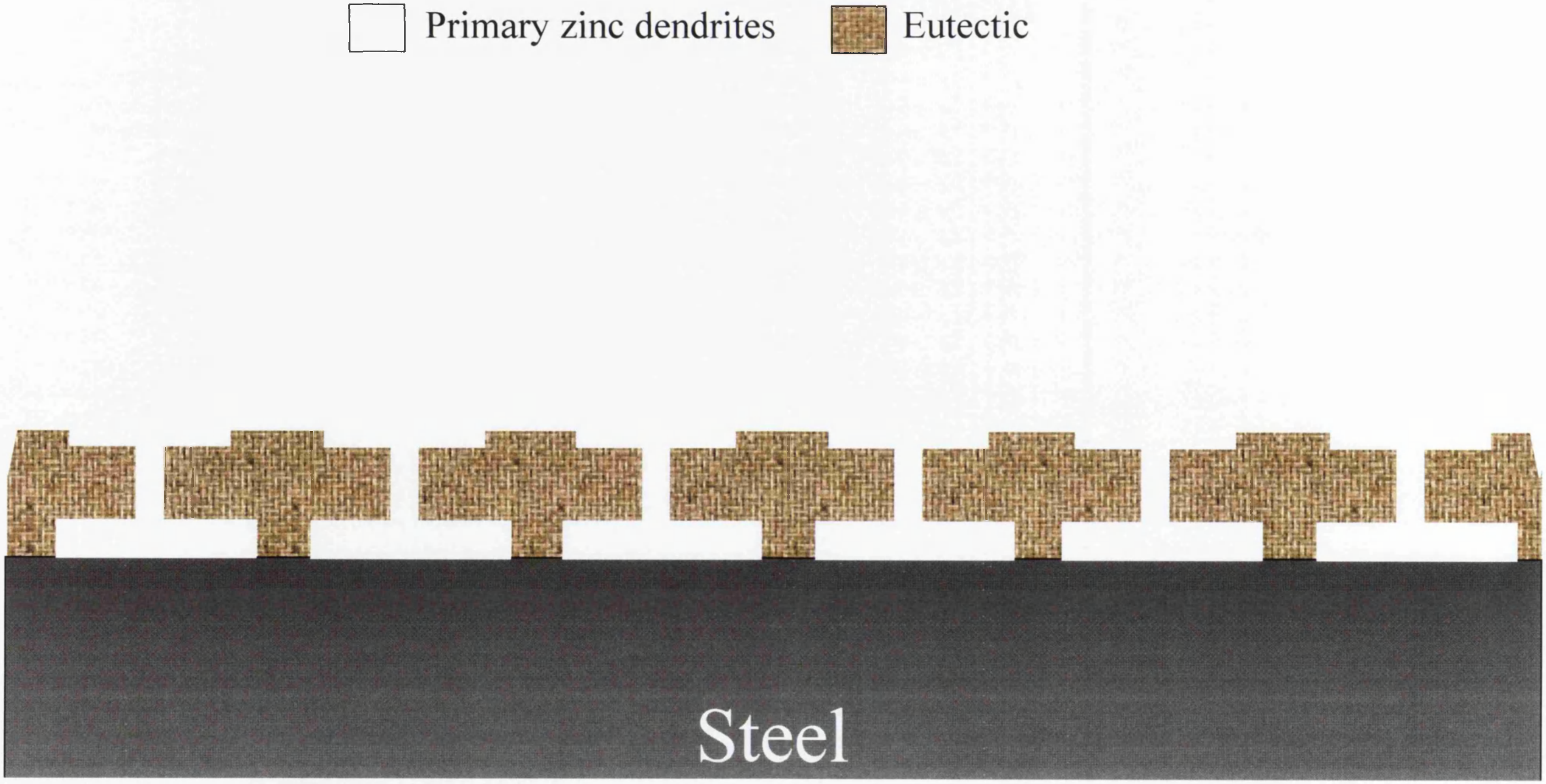

Figure 5.6 (c) Schematic of galfan coating ($80gm^{-2}$) laterally sectioned

been laterally sectioned. This diagram assumes the nucleation of the primary phase upon the base steel substrate and follows trends observed in figure 5.4 where by the volume percentage of primary zinc decreases from the steel/ coating interface to the air/ coating interface. Overall the volume percentage of primary zinc in the coating is greater with lower coating thickness but this is a reflection of the removal of the Al rich liquid via the action of the gas knives. Indeed the observation is further confirmed through comparisons of the volume percentage readings at incremental depths close to the steel/ coating interface (figure 5.7). This data shows that the values of the volume percentage of the primary phase are almost identical for each sample within a distance of 5µm from the steel/ coating interface. Hence the primary zinc forms as a solid phase equally for all coating weights but at the lower coating weights have successively higher amounts of Al rich liquid removed.

5.1.3. Effects of Galfan coating weight upon the number and size of the primary zinc dendrites

Figures 5.2 and 5.3 detail the microstructures of each sample at the steel/ coating interface. Since it is believed that nucleation is occurring near to the steel substrate, the number and size (area) of dendrites was calculated as close to the steel/ coating interface as possible. The results for the number of dendrites per square mm are shown in figure 5.8. What is initially apparent from the data is that with experimental error (±5%) the number of dendrites per square mm remains constant. Sample CT80 has an average of 1250±62. In samples CT100, CT130 and CT170 the dendrite numbers are 1316±65, 1166±58 and 1208±60 respectively.

Continuing with the assumption that the nucleation of the primary phase is occurring near to the steel substrate, the size (area) of the dendrites has been

	Average volume percentage primary zinc (%)			
Depth above steel/coating interface	CT80	CT100	CT130	CT170
~5μm	27%	29%	29%	25%
~2μm	37%	38%	38%	35%
~0μm	47%	46%	49%	47%

Figure 5.7 The average volume percentage of primary zinc near to the steel/ coating interface

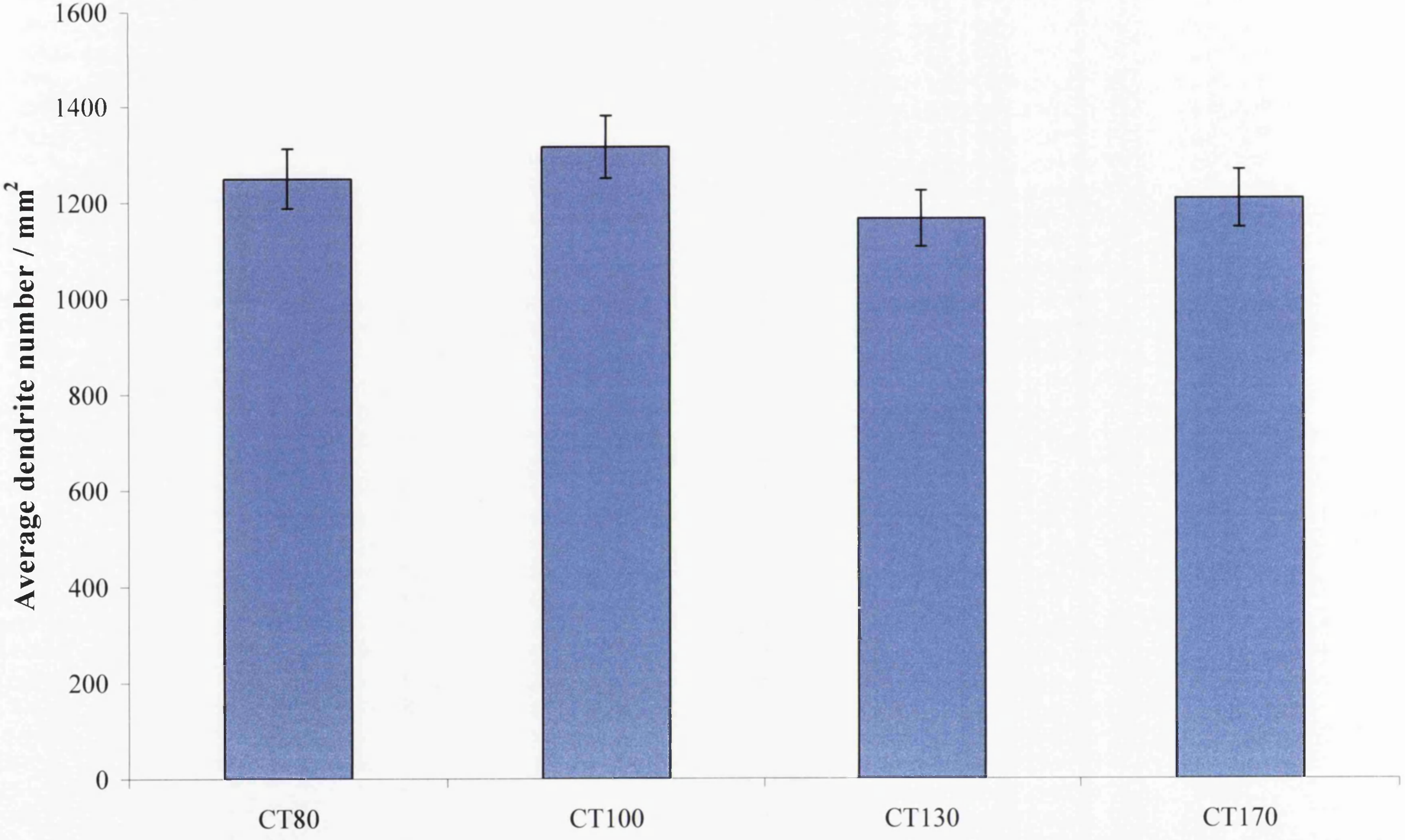

Figure 5.8 Average number of dendrites per mm^2 near to the steel/ coating interface

calculated close to the steel/ coating interface. As previously described (section 2.1.2.3) the area of an individual dendrite is obtained by dividing the total area (mm^2) of the primary zinc at the steel/ coating interface by the associated number of dendrites within that unit area. Figure 5.5 clearly shows that the volume percentage of the primary material (recorded close to the steel/ coating interface) remains constant for all samples at 47% ± 2%. Since the dendrite number also remains constant it is of little surprise that the size of the dendrites remains the same for each sample as shown in figure 5.9. For sample CT80 the average dendrite size is $0.32\mu m^2 \pm 0.02\ \mu m^2$. This figure remains constant (within experimental error) for samples CT100, CT130 and CT170 returning average dendrite sizes of $0.29\mu m^2 \pm 0.02\ \mu m^2$, $0.35\mu m^2 \pm 0.02\ \mu m^2$ and $0.33\mu m^2 \pm 0.02\ \mu m^2$ respectively.

The consistency in the number of dendrites per square millimetre and their physical size is a somewhat surprising result. Addressing the situation logically, it would be assumed that under identical line conditions a thinner coating would solidify more rapidly than one which is thicker and that the gas knives would directly influence this cooling rate. Previous studies[3,4] and investigations in chapter 4 have shown that the cooling rate will directly influence the nucleation of the primary phase. These present results (number and size of dendrites) indicate that there is no change in the nucleation of the primary phase which might imply that there are no changes in the applied cooling rate. Hence, it would seem logical to assume that the nucleation of the primary phase is occurring before passing through the gas knives. Based on this assumption, the nucleation conditions are identical for each sample and hence there is little change in the dendrite size or number. Therefore it would seem possible that the nucleation of the primary phase β crystals occurs at some point between exiting the galvanizing bath and the gas knives. Hence, once the coating passes through the air

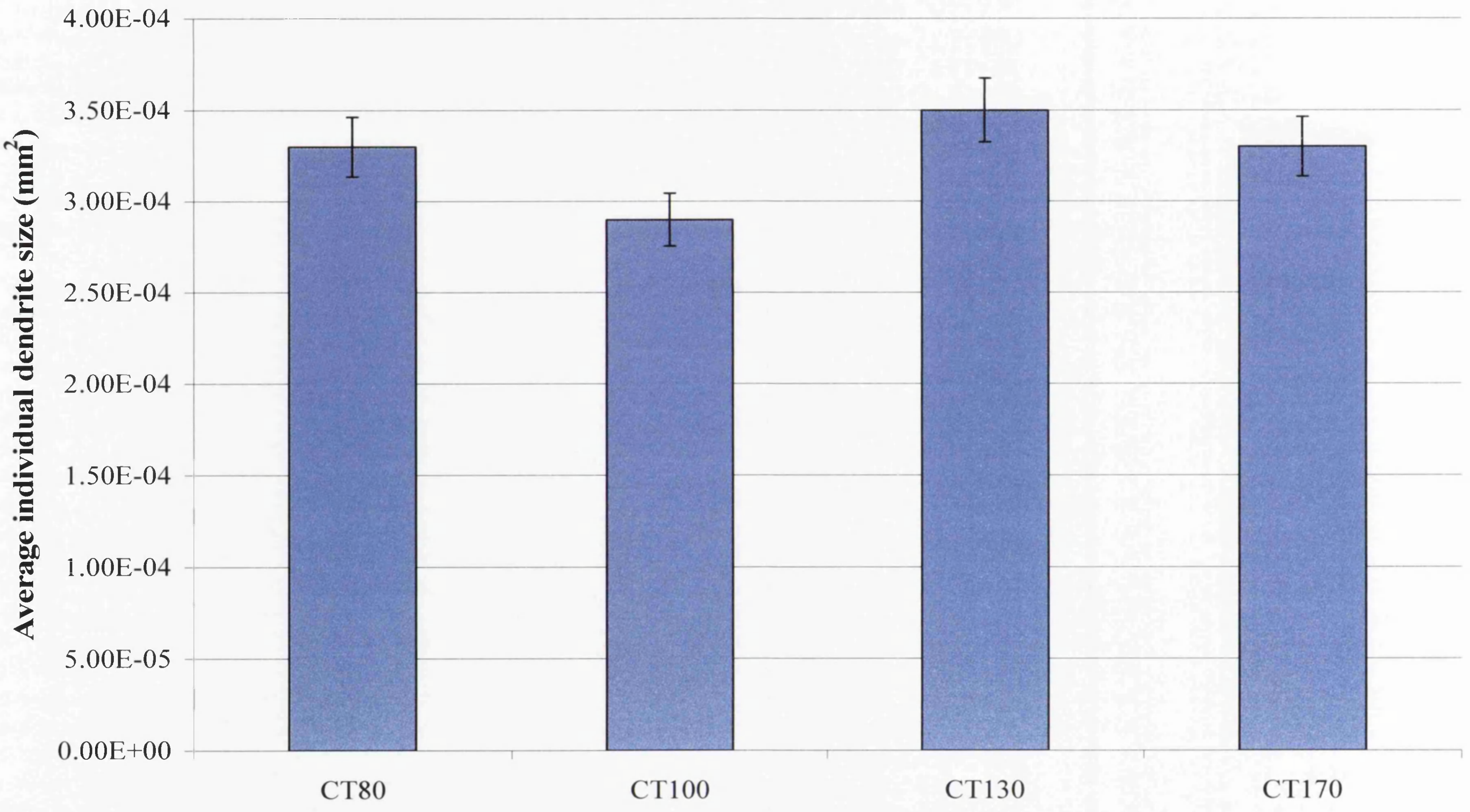

Figure 5.9 Average dendrite size (area) near to the steel/ coating interface

knives they can have no effect upon the number of dendrites present within the coating under the particular conditions of this trial.

5.1.4. Effects of Galfan coating weight upon the eutectic cell size (Spangle size)

As previously described (section 2.1.2.5) the eutectic cell size is measured through digitally enhanced linear analysis. The results for the measurement of the eutectic cell size (measured upon as received surface) are shown in figure 5.10. It is clear from this figure that although there is a slight trend to a reduction in cell size as the coating weight is reduced (a result which would agree with the increased cooling rate theory), the change is very small and contained well within experimental error. The average cell size for sample CT170 was 1.30mm ± 0.1mm. For sample CT130 the corresponding result was 1.24mm ± 0.06mm changing to 1.22mm ± 0.1mm and 1.20mm ± 0.1mm for samples CT100 and CT80 respectively. It is not possible to determine whether the slight reduction in size is a real phenomenon. Hence the only clear conclusion from these results is that the size of the eutectic cells (in this circumstance) does not dramatically vary with reduction in the coating weight. This would again imply that the eutectic cells are nucleated well below the cooling rig position.

5.1.5. Effects of Galfan coating weight upon the eutectic spacing

Recorded close to the steel/ coating interface figure 5.11 shows images of the eutectic microstructures. Changes in the inter-lamellar and inter-rod spacing were recorded as detailed in section 2.x. These results are shown in figure 5.12. It is evident from the microstructures that in the cases of samples CT100, CT130 and CT170 the

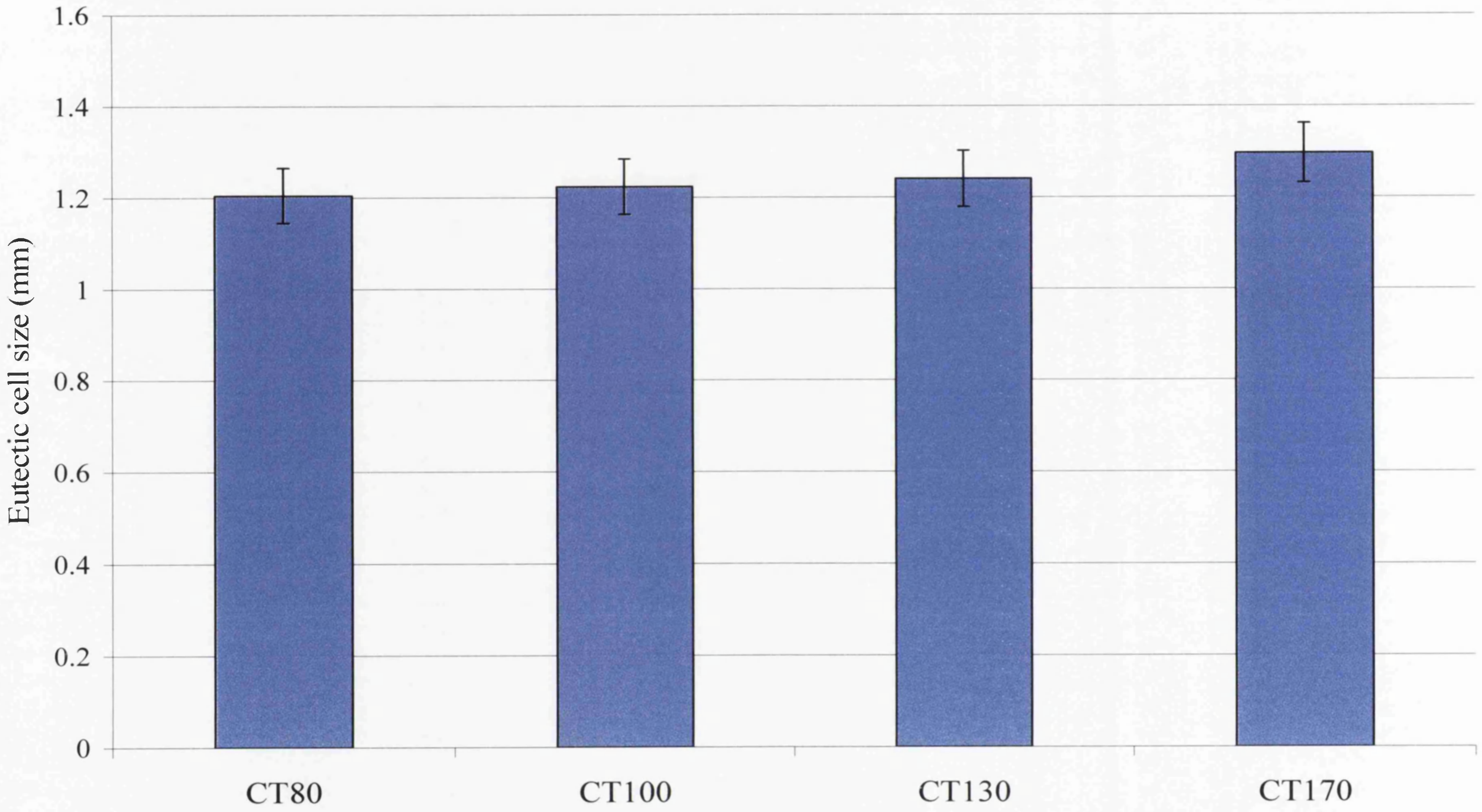

Figure 5.10 Average eutectic cell size (spangle size) at the air/ coating interface

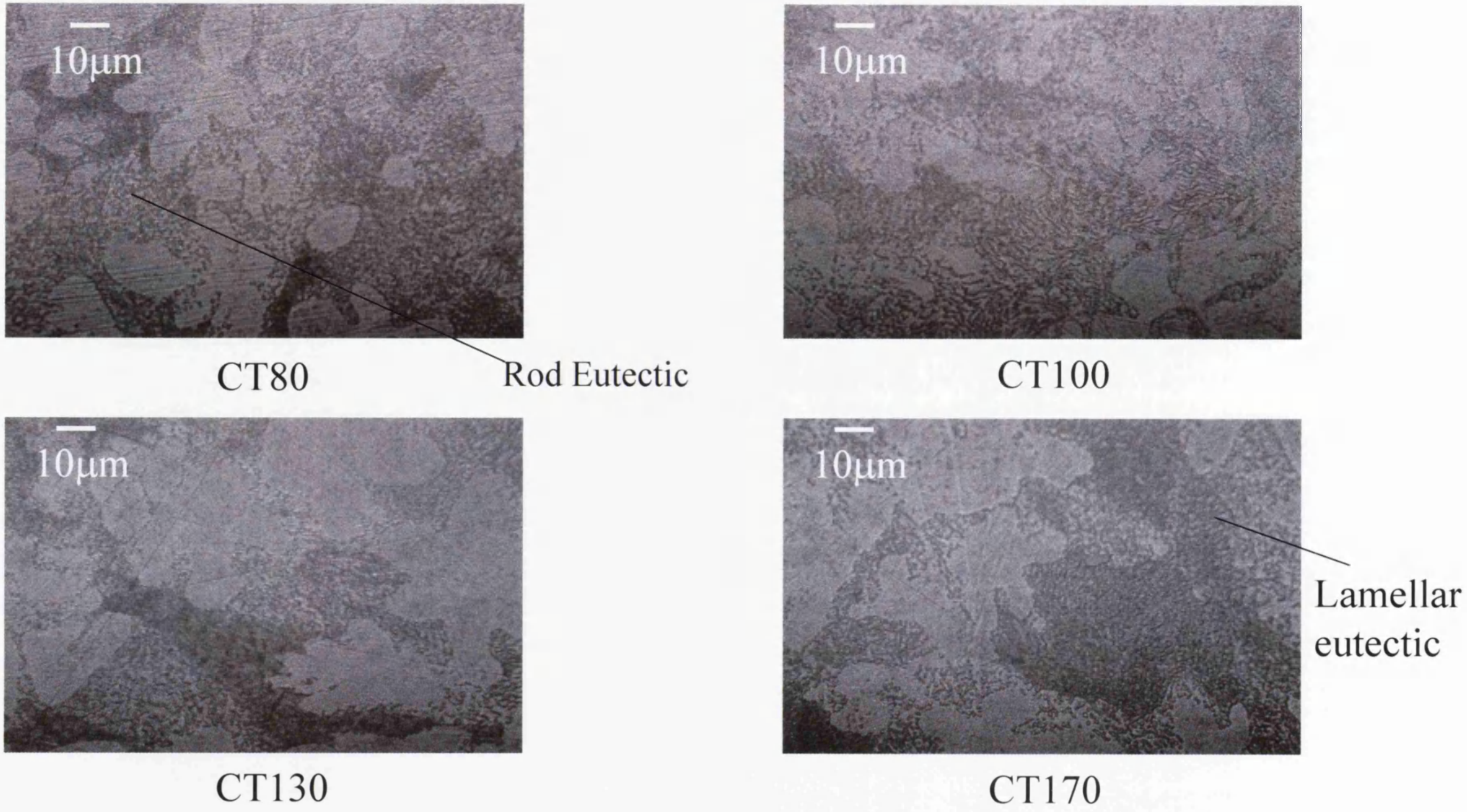

CT80

CT100

CT130

CT170

Figure 5.11. Typical eutectic microstructures recorded at the steel/coating interface (*X*800)

Sample	Inter-lamellar spacing (μm)	Inter-rod spacing (μm)
CT80		6.2 ±0.3
CT100	5.3 ±0.3	6.3 ±0.3
CT130	5.9 ±0.3	6.5 ±0.3
CT170	6.4 ±0.3	7.7 ±0.4

Figure 5.12 Average inter-lamella and inter- rod spacing recorded near to steel/ coating interface

microstructure is of a mixed morphology displaying both lamellar and rod structures. In the case of CT80 the structure shown is wholly rod. Figure 5.12 shows that there is a reduction in the inter-lamellar and inter-rod spacing as the sample coating weight is reduced. CT170 has an inter-lamellar spacing of 6.4 μm ± 0.3 μm with a corresponding inter-rod spacing of 7.7 μm ± 0.4 μm. These spacings are reduced to 5.9 μm ± 0.3 μm (inter-lamellar) and 6.5 μm ± 0.3 μm (inter-rod) in sample CT130 and again to 5.3 μm ± 0.3 μm (inter-lamellar) and 6.3 μm ± 0.3 μm (inter-rod) in sample CT100. Finally in sample CT80, the structure is of wholly rod morphology and has an average inter-rod spacing of 6.2 μm ± 0.3 μm.

The refinement of the eutectic structure appears to be in agreement with the proposed theory for solidification as described in section 5.1.2. It was postulated that the reduced coating weight samples will solidify quicker then those of higher coating weight. As seen in chapter 4 the increased cooling rate when solidifying the eutectic structure leads to a finer eutectic spacing and also a change in morphology from a lamellar structure to a mixed lamellar and rod structure. Considering the changes seen in the eutectic microstructures of these samples, the results are consistent with the changes previously observed (chapter 4) and one may assume that the growth of the eutectic portion of the thinner coating (CT80) occurred more rapidly than the corresponding portion of the thicker coating (CT170).

5.2.1 Location and intensity of anodic sites along the cut edge

Figures 5.13(a) and 5.13(b) show typical current density maps generated whilst scanning the cut edges of samples CT80, CT100, CT130 and CT170. Each map shows representative scans from 0, 12 and 24 hours from a single experiment of test

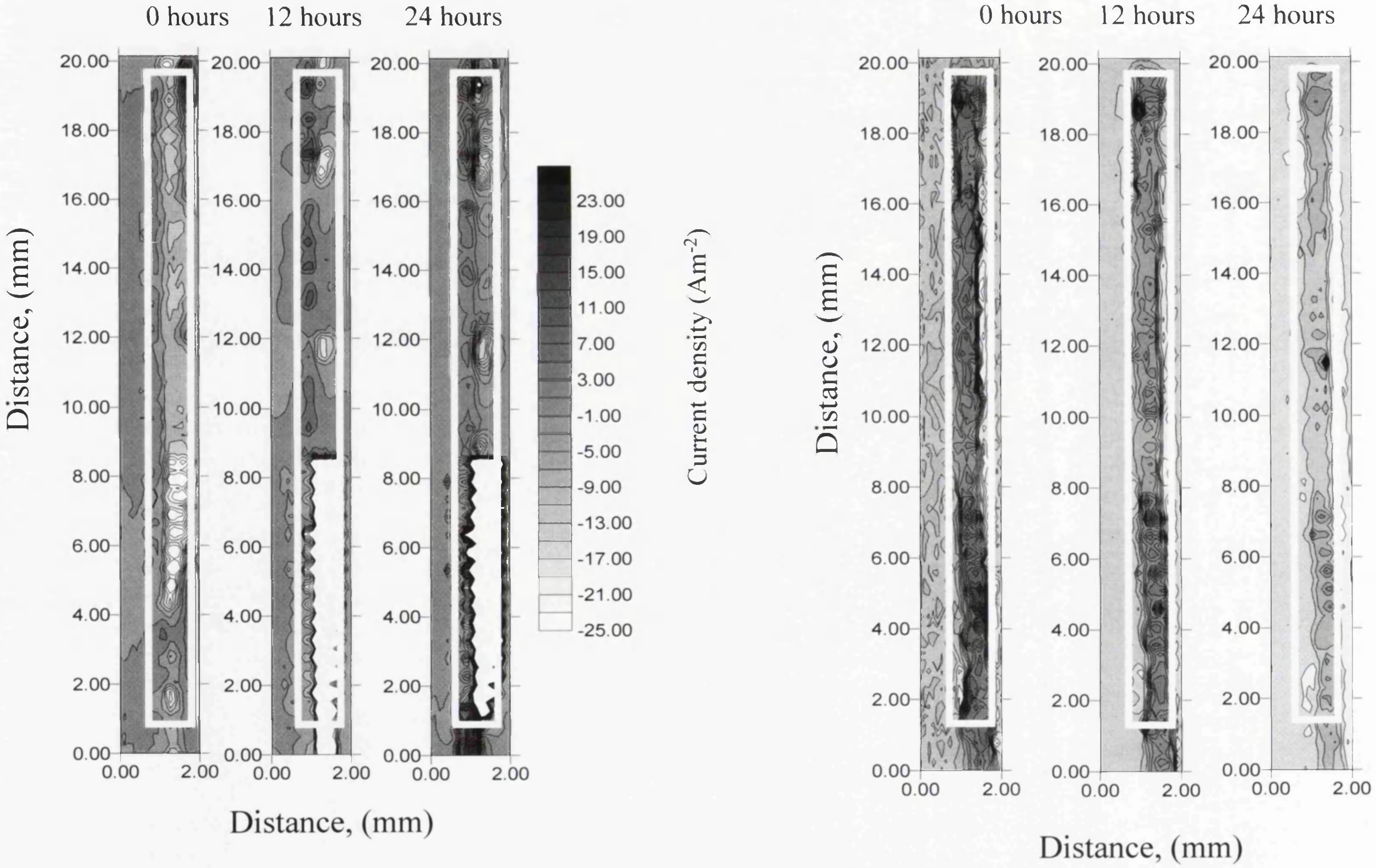

Figure 5.13 (a) Representative iso – current density cut edge maps for cut edge samples CT80 and CT100

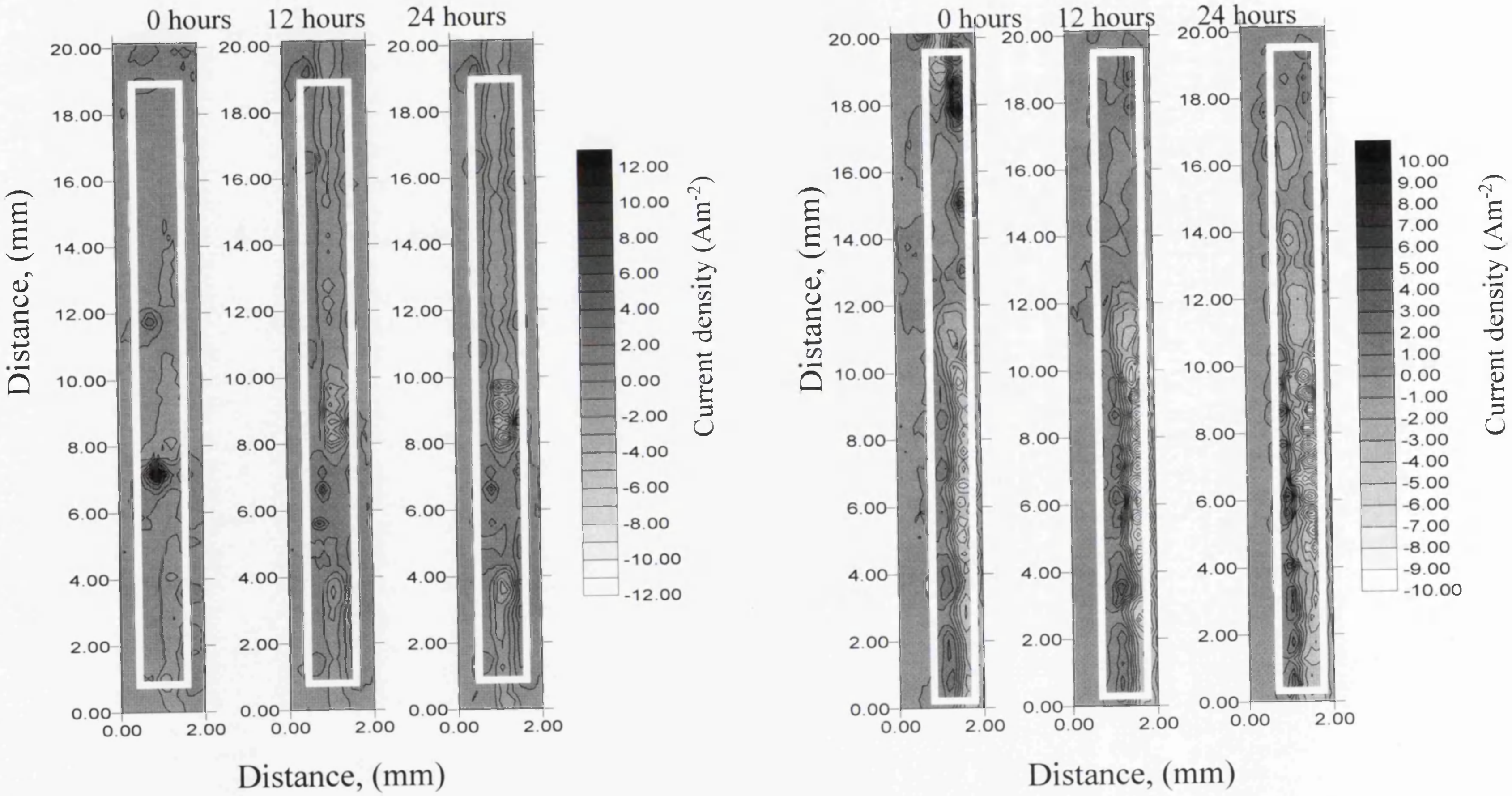

Figure 5.13 (b) Representative iso – current density maps for cut edge samples CT130 and CT170

period 24 hours. The SVET scanned each sample hourly during the test period. The dark regions on the iso- current maps represent anodic activity (metal dissolution) and the lighter regions represent cathodic activity (oxygen reduction). The proximity of the anodic activity, at the edges of the cathodic activity, indicates that the galvanising layer is corroding anodically and protecting the base steel substrate from such attack. As seen in previous chapters, the point anodes displayed on these maps are indicative of the isolation of the primary zinc phase within the eutectic matrix and add weight to the argument that it is this phase which will preferentially corrode.

The intensity of the corrosion varies with the applied coating weight. Sample CT80 has a current density value of $23Am^{-2}$. This figure is reduced in samples CT100 and CT130 to $15Am^{-2}$ and $12Am^{-2}$ respectively with CT170 having the lowest intensity of $10Am^{-2}$. Considering that the only parameter altering within this body of work is the coating weight, these results would imply that this will have a significant effect upon the corrosion performance of the coating. Indeed, the greater loss of zinc from the thinner coating is most likely to be due to microstructural change and increasing volume percentage of primary zinc.

5.2.2. The influence of coating weight upon the zinc loss and anode lifetimes

Detailed analysis of the data provided by SVET experimentation allows the calculation of zinc losses occurring during corrosion activity. Figure 5.14 details the mean average total zinc loss (*tzl*) calculated from three individual experiments from each of the sample sets. From the data it is clear that as the coating weight is reduced the level of recorded zinc loss will also be reduced. The recorded zinc loss for sample CT80 is 475μg ± 19 μg, this is reduced to 376μg ± 15 μg and 224μg ± 9 μg for samples CT100 and CT130. CT170 has the lowest *tzl* with an average value of 192μg

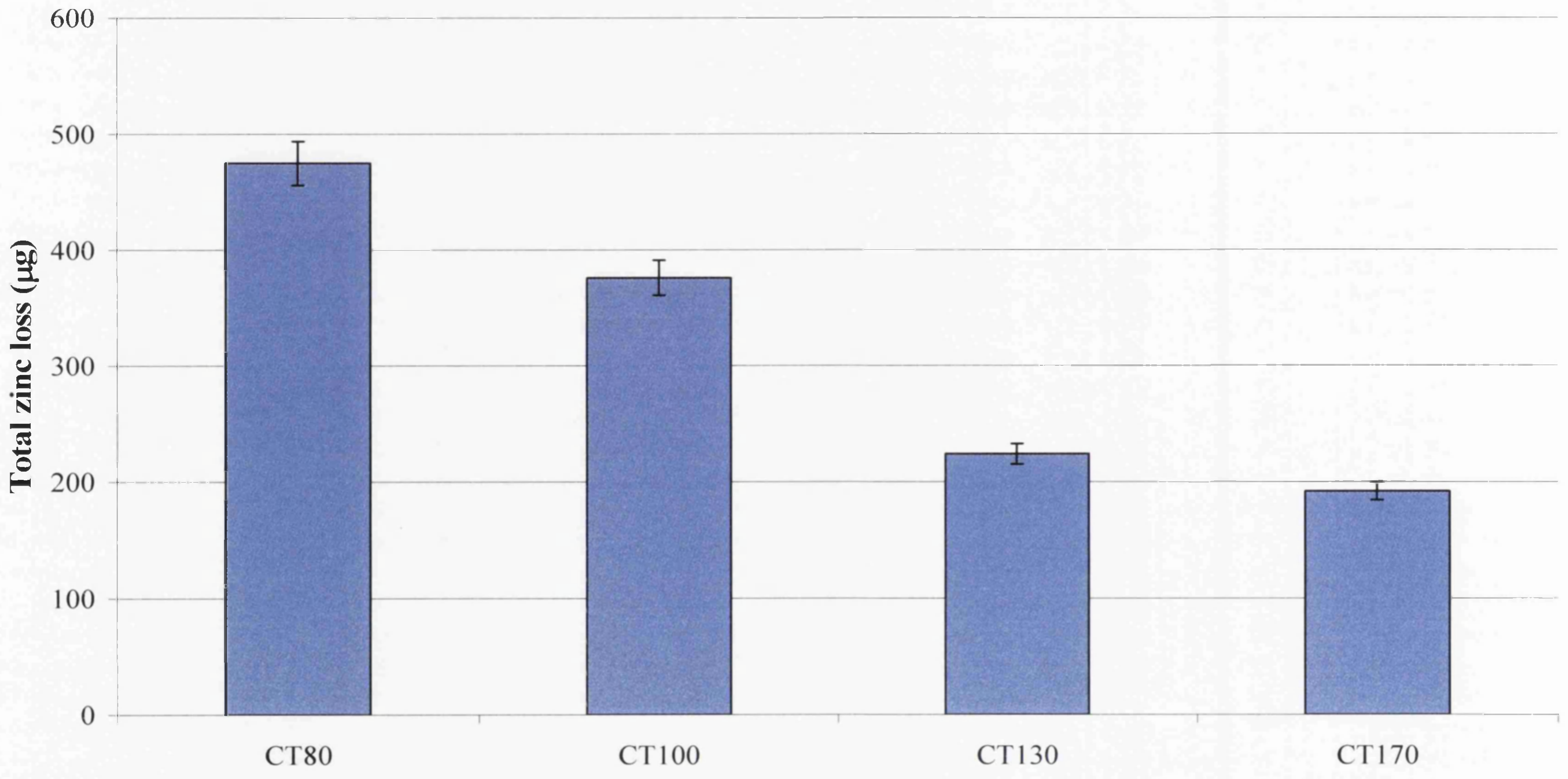

Figure 5.14 The average total zinc loss recorded across the sample cut edge

± 8 μg. This reduction in zinc loss is in good agreement with the reduction in corrosion current densities shown in the SVET maps of figure 5.13.

The recorded zinc loss as a function of relative volume percentage of primary zinc is shown in figure 5.15. It is clear from figure 5.15 that the increase in recorded zinc loss is almost linear with the increase in the volume percentage of primary zinc. A correlation co-efficient (R^2) of 0.9608 confirms this relationship, however it should be tempered with the recognition that these are only 4 data points.

Figure 5.16 shows a comparison of hourly zinc losses from a single experiment from samples CT80 and CT170. Initial inspection of the data shows is the greater zinc loss at each hour from sample CT80 indicating that the corrosion activity is always higher throughout the experimental period. In both cases the initial corrosion levels are significantly higher than those towards the latter part of the testing. For CT80 initial recorded zinc loss is $42\mu gh^{-1}$ and the corresponding figure for CT170 is $18\mu gh^{-1}$. These figures reduce to $21\mu gh^{-1}$ and $7\mu gh^{-1}$ for CT80 and CT170 respectively. This reduction in activity reaffirms previous data[5] in so much that the corrosion activity occurring along the Galfan cut edge is reduced over time.

In figure 5.17 the anode lifetimes and intensities are shown as a function of experimental time for samples CT80 and CT170. Due to the more complex nature of these results the charts are from a single experiment and not an average of all experiments undertaken. In both cases there are 15 long life anodes (18-24 hour lifetime) but the intensity of the anodes is far greater in CT80 with anodes peaking at $20Am^{-2}$ as opposed to $8Am^{-2}$ in sample CT170. It is also the case that the majority of the anodes in CT80 are consistently more intense (of higher current density) than those in CT170 giving rise to the higher recorded zinc losses The individual zinc loss (*tizl*) from each anode is plotted for samples CT80 and CT170 in figure 5.18.

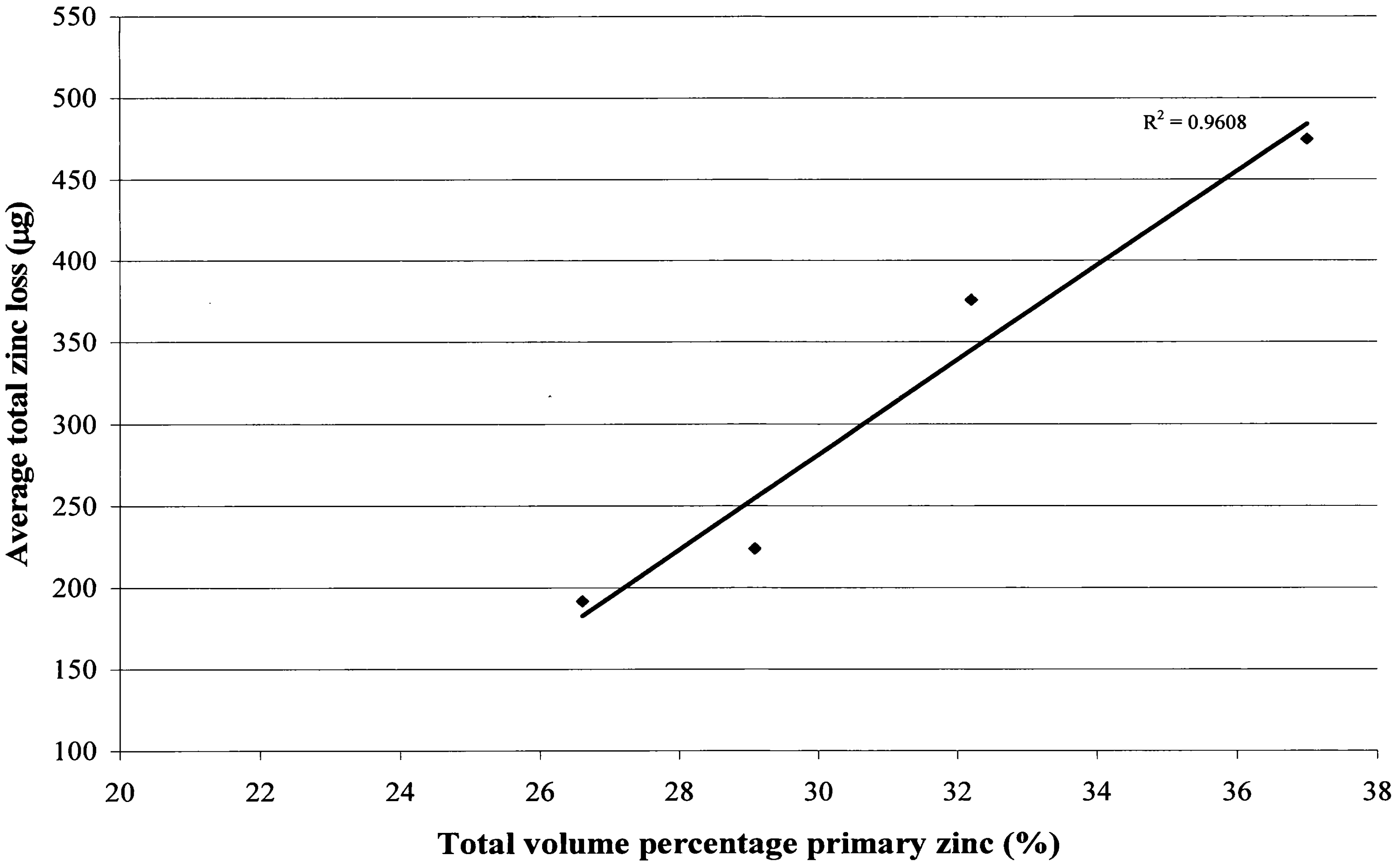

Figure 5.15 Total volume percentage of primary zinc as a function of zinc loss

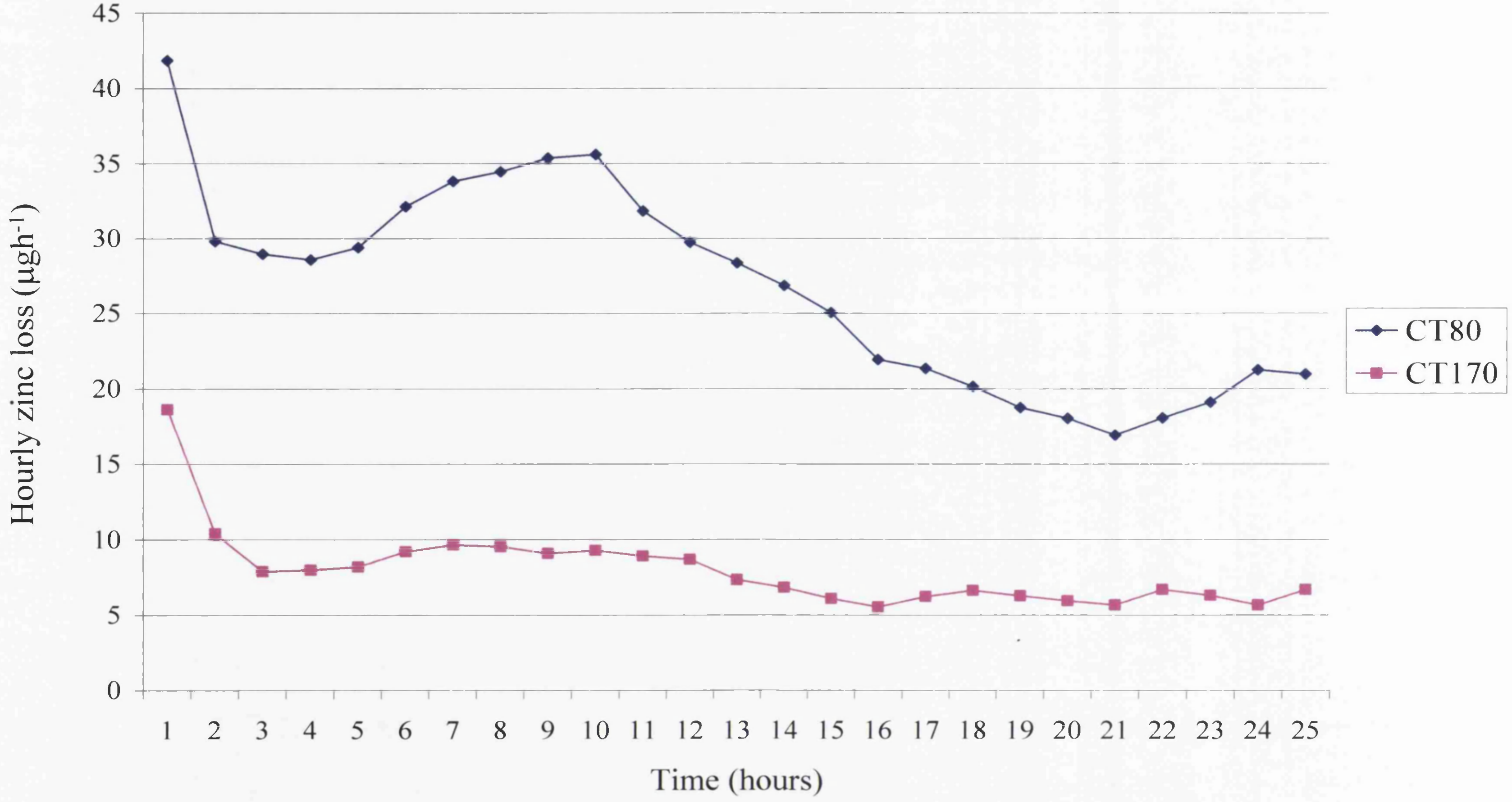

Figure 5.16 Hourly zinc losses from cut edges of samples CT80 and CT170

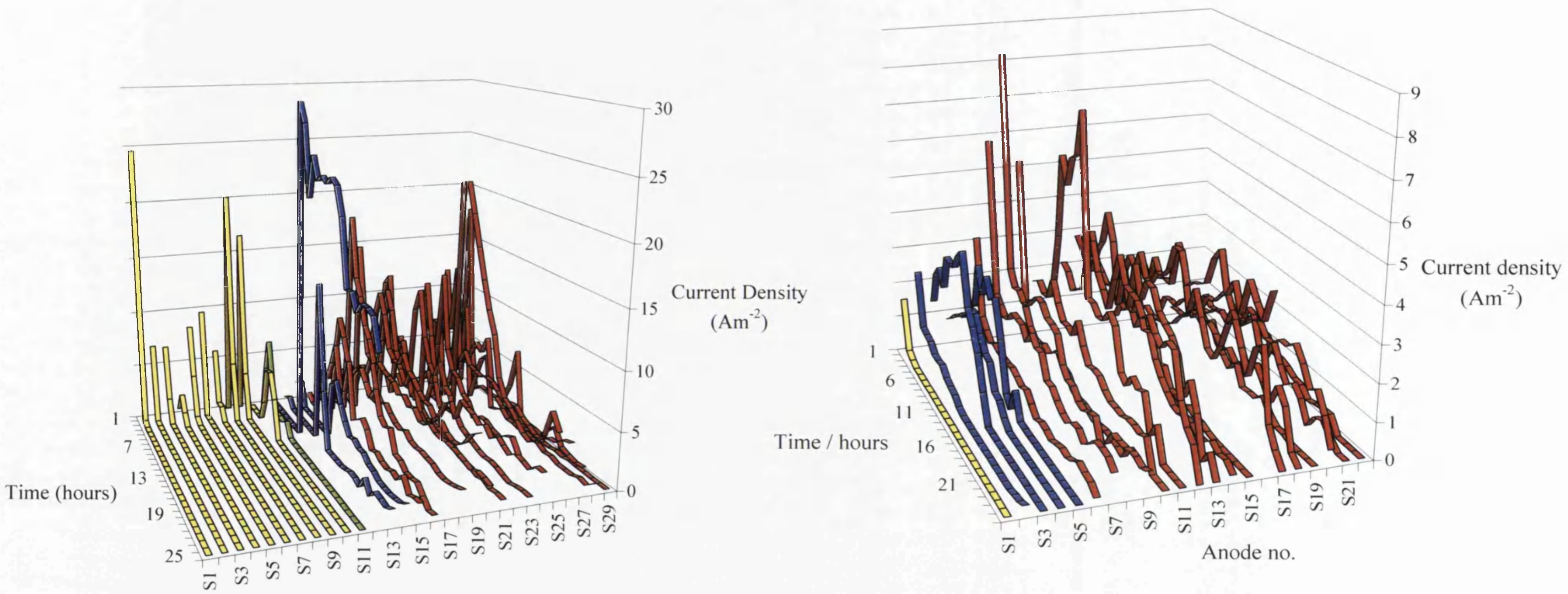

Figure 5.17 Anodic activity as a function of immersion time for samples CT80 (left) and CT170 (right) along the cut edge

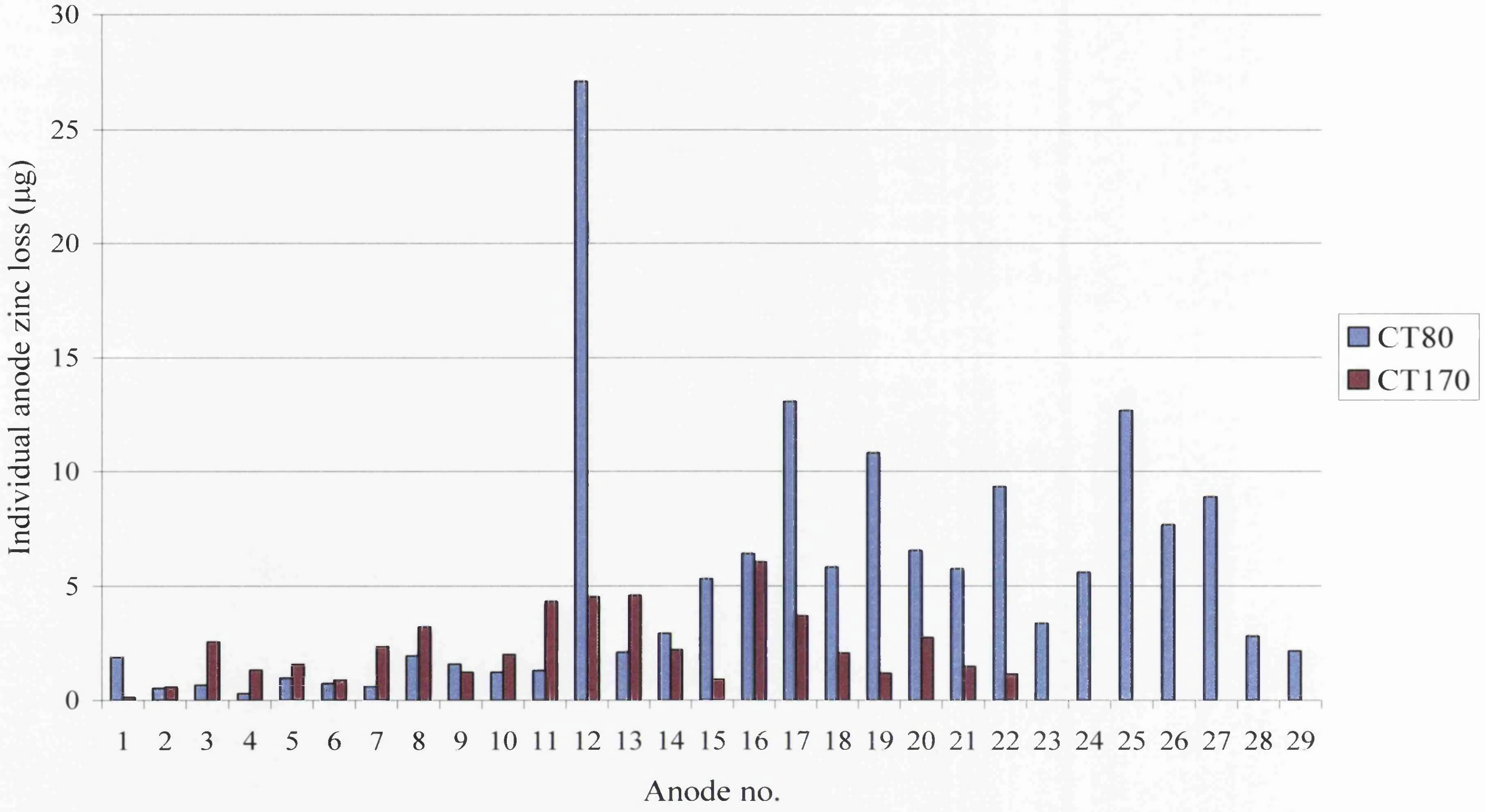

Figure 5.18 Comparison of individual anode zinc losses along the cut edge

The microstructural analysis revealed that although the relative volume percentage of primary zinc was increasing, the actual amount of this phase in the coating was reduced due to the coating thickness reduction. Hence the zinc loss figures detailed within this section are somewhat surprising. It is believed that this phenomenon is brought about via the changes in volume percentage of the eutectic phase. The majority of the cathodic activity is focused upon the steel substrate, however, if this alone controlled the reactivity then zinc loss would be uniform for all coatings. Therefore some cathodic activity will occur on the galvanizing layer. The eutectic is Al rich compared to the primary zinc and it is known that Al is a very poor cathodic material, due to the formation of an oxide layer upon its surface. Therefore altering the amounts of eutectic within the coating changes the driving force for the cathodic processes occurring on the coating. As the mechanical wiping action of the gas knives reduces the coating weight (increasing the relative volume percentage of primary phase) the relative volume percentage of the eutectic is decreased. Therefore with a larger amount of the eutectic present, the cathodic reaction will be subdued and the rate of corrosion reduced. Therefore, even though a greater physical volume of zinc is present within the thicker coatings, the rate at which it is corroded away is significantly reduced. Consequently, in the thinner coatings there is (relatively) less of the eutectic phase and so the cathodic reaction is increased (compared to coatings of greater coating weight) corroding greater amounts of primary zinc during the experimental period. This phenomenon has been noted previously[6] with the original researchers from ILZRO noting that the time to red rust was significantly increased when the volume percentage of the primary phase was reduced. It would be interesting to measure the oxygen reduction kinetics on the galvanizing layers using the rotating disc electrode technique, but unfortunately due to time constraints this was not possible.

5.3 Location and intensity of anodic sites across the surface

Representative current density maps for samples CT80 and CT170 are shown in figure 5.19. The maps were generated for each sample after immersion in aerated 5% NaCl after 12 hours and show significant changes in the corrosion behaviour. As previously, the anodic activity is shown in dark colours and the cathodic activity in light colours. Initially it is clear when comparing the intensity scales that the corrosion occurring upon sample CT80 ($27Am^{-2}$) is far greater than that upon CT170 ($8Am^{-2}$). This would indicate that the zinc losses will also be significantly greater. It can also be observed that although there are a greater number of anodes occurring on CT170 the dominant anodes upon CT80 are far more intense. The focused corrosive activity displayed on both surfaces is different to that observed in other work in preceding chapters. Previously it has been observed that the anodic activity is highly localised within the depressed boundaries of the eutectic cells. In this instance the anodic activity appears as point anodes focused upon various regions.

5.4 Influence of coating weight upon the anode lifetimes and associated zinc loss

As previously shown it is possible to estimate zinc losses occurring during corrosion. Figure 5.20 details the mean average zinc loss from three individual experiments for each sample group. An increase in zinc loss is shown when the coating weight is reduced. The average *tzl* for sample CT170 is 127μg ± 5 μg. This

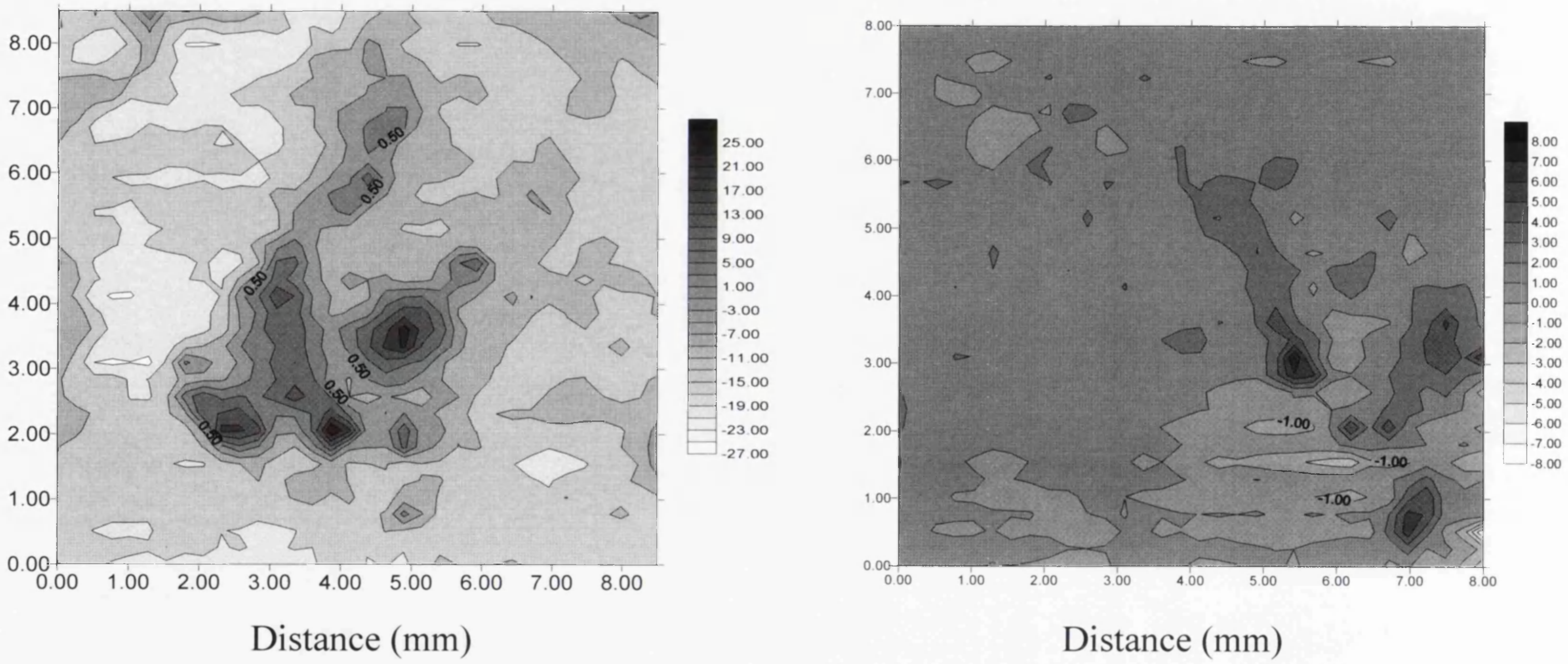

Figure 5.19 Representative iso – current cut edge maps for samples CT80 and CT170

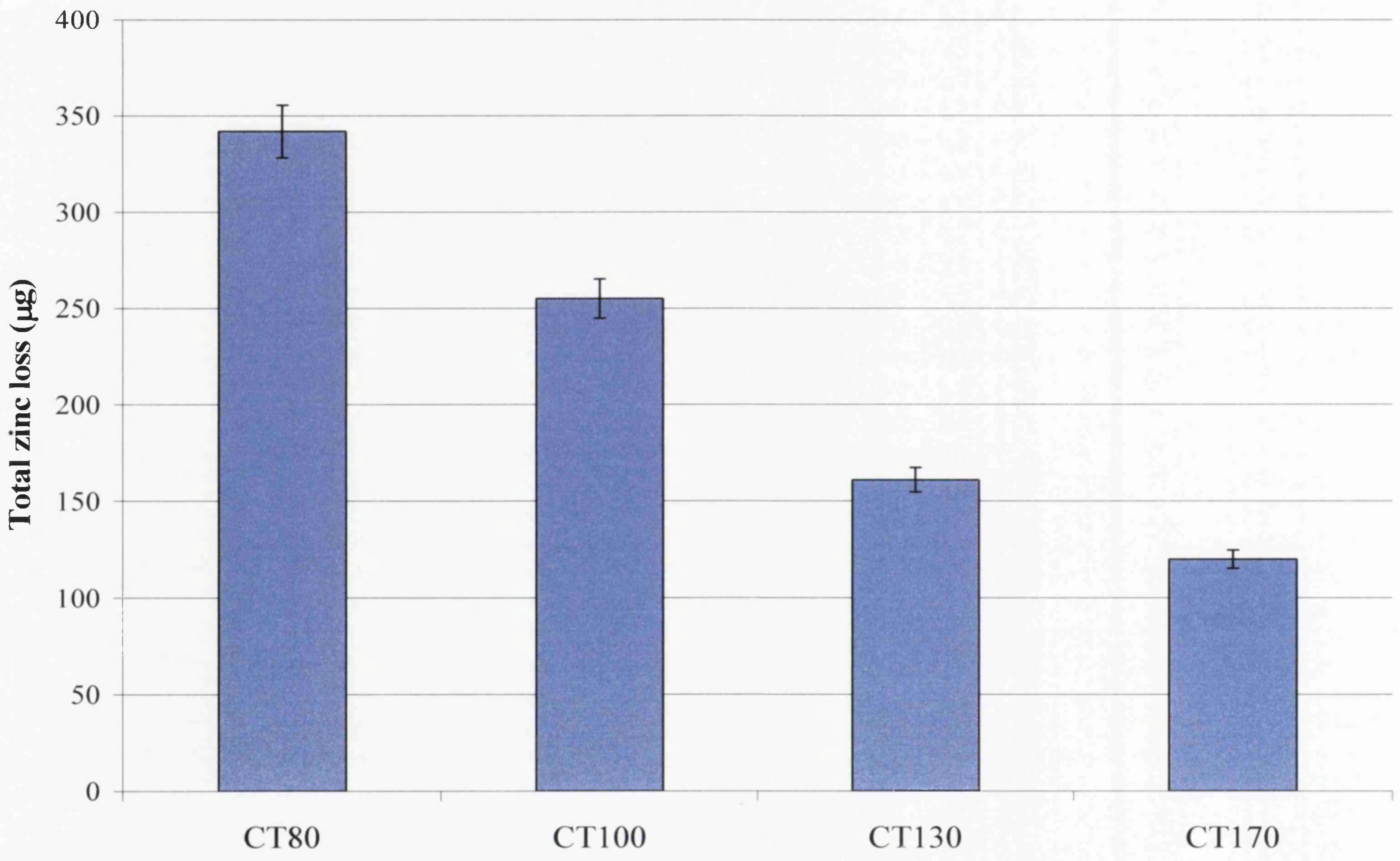

Figure 5.20 The mean average total zinc loss recorded across the sample surface

increases to 158μg ± 6 μg in sample CT130 and further to 255μg ± 10 μg in CT100. The highest average recording was 343μg ± 13 μg from sample CT80.

Figure 5.21 shows the intensity and lifetime of the anodes on CT80 and CT170 whilst figure 5.22 shows the associated zinc loss of each anode. In both CT80 and CT170 there are very few long life anodes (2 in CT80 and 3 in CT170) but there are a significant number of anodes of lifetimes 12-18 hours in each. CT80 displays a greater intensity of corrosive activity which is observed peaking at $26Am^{-2}$ compared to $8Am^{-2}$ in CT170. The effects of this increase in current density is shown in figure 5.22 where the zinc loss contribution of individual anodes is shown. Each of the anodes in CT80 contributes a far greater zinc loss to the overall total than any of the anodes in CT170. Hence the overall zinc loss of CT80 is far greater than CT170 even though there are fewer detected anodes.

Interestingly, when the volume percentage of primary zinc at the air/ coating interface is plotted as a function of *tzl* as shown in figure 5.23, another broadly linear relationship ($R^2 = 0.9429$) is produced. Herein lies the explanation for the focused anodes observed on the iso-current maps and the increased corrosion upon CT80. The wiping action of the gas knives has been schematically illustrated in figure 5.6 (a,b and c). For a standard $255gm^{-2}$ coating, the only primary zinc breaching the surface appears within the depressed boundaries. Hence the corrosive activity is focused within these regions. Figure 5.6 (b) details the schematic for CT170 where it is then evident that the primary zinc dendrites will breach the surface all across the eutectic cells. Therefore, instead of the corrosive activity being focused entirely within the boundaries, it will be focused upon the dendrites breaching the surface. As the coating weight is reduced the amount of primary zinc visible at the surface increases. The reasoning for this is again evident in figure 5.6 (c) with the majority of the primary

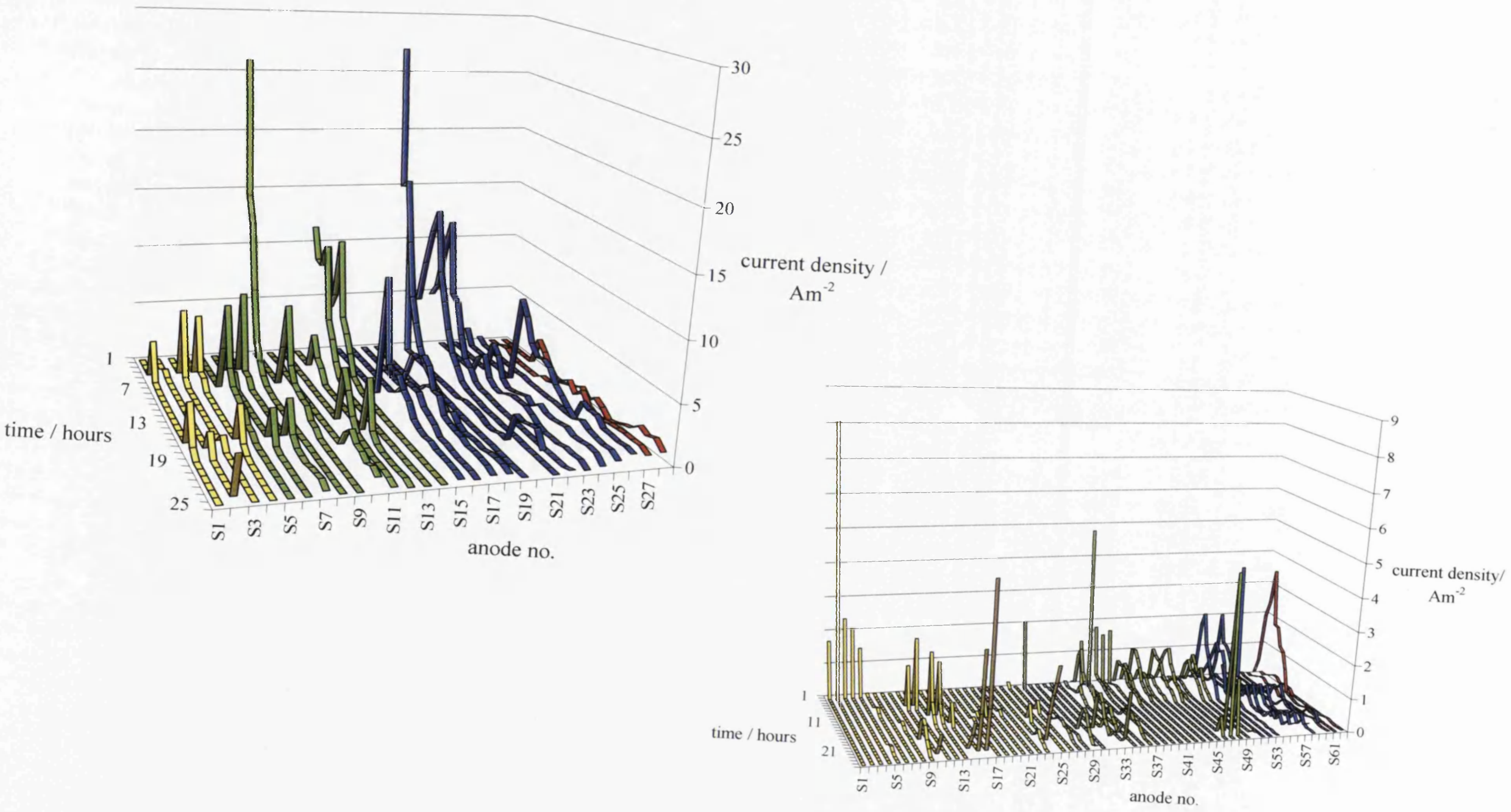

Figure 5.21 Anodic activity as a function of immersion time for samples CT80 (left) and CT170 (right) across the surface

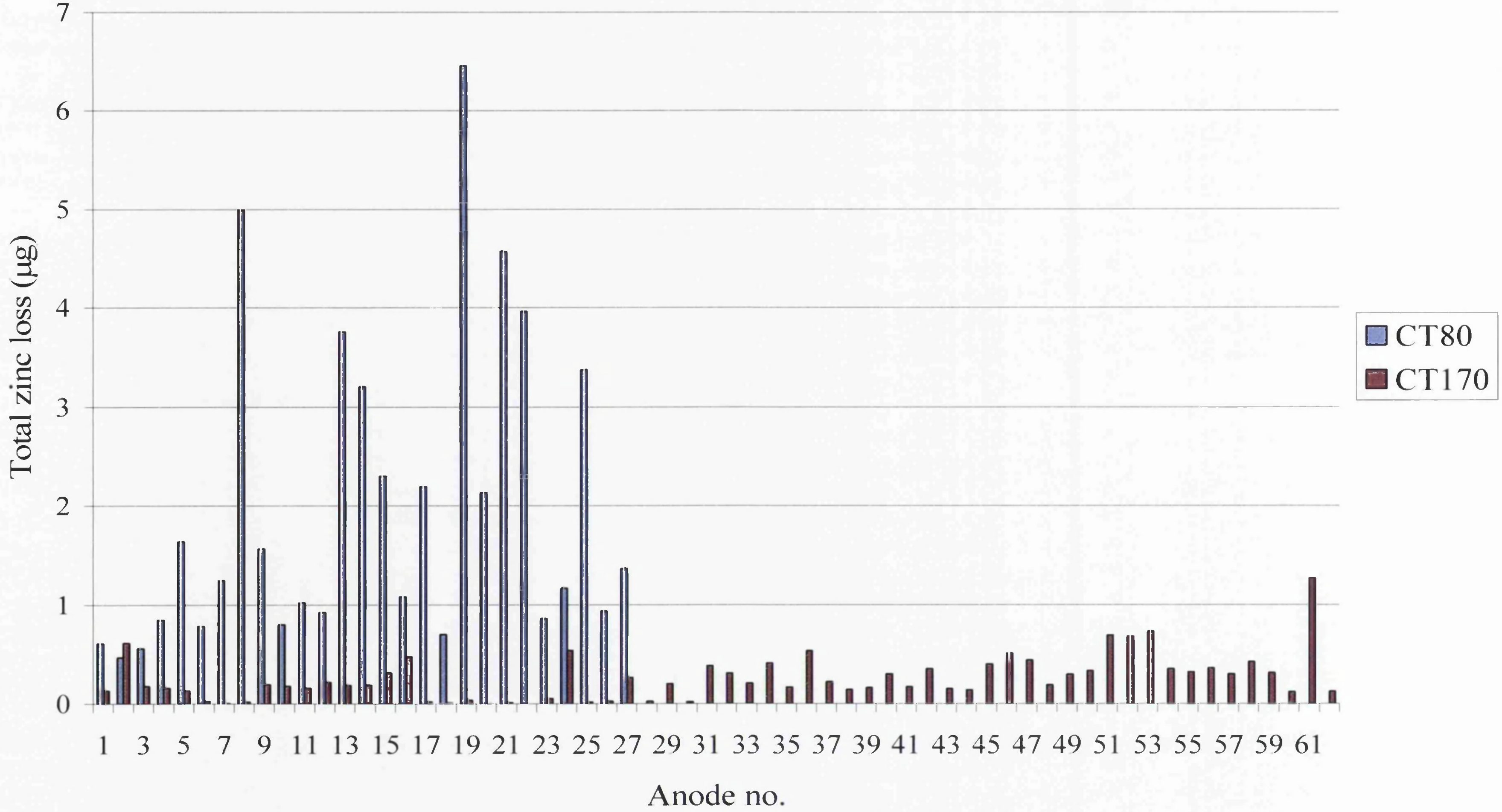

Figure 5.22 Comparison of individual anode zinc losses across the surface

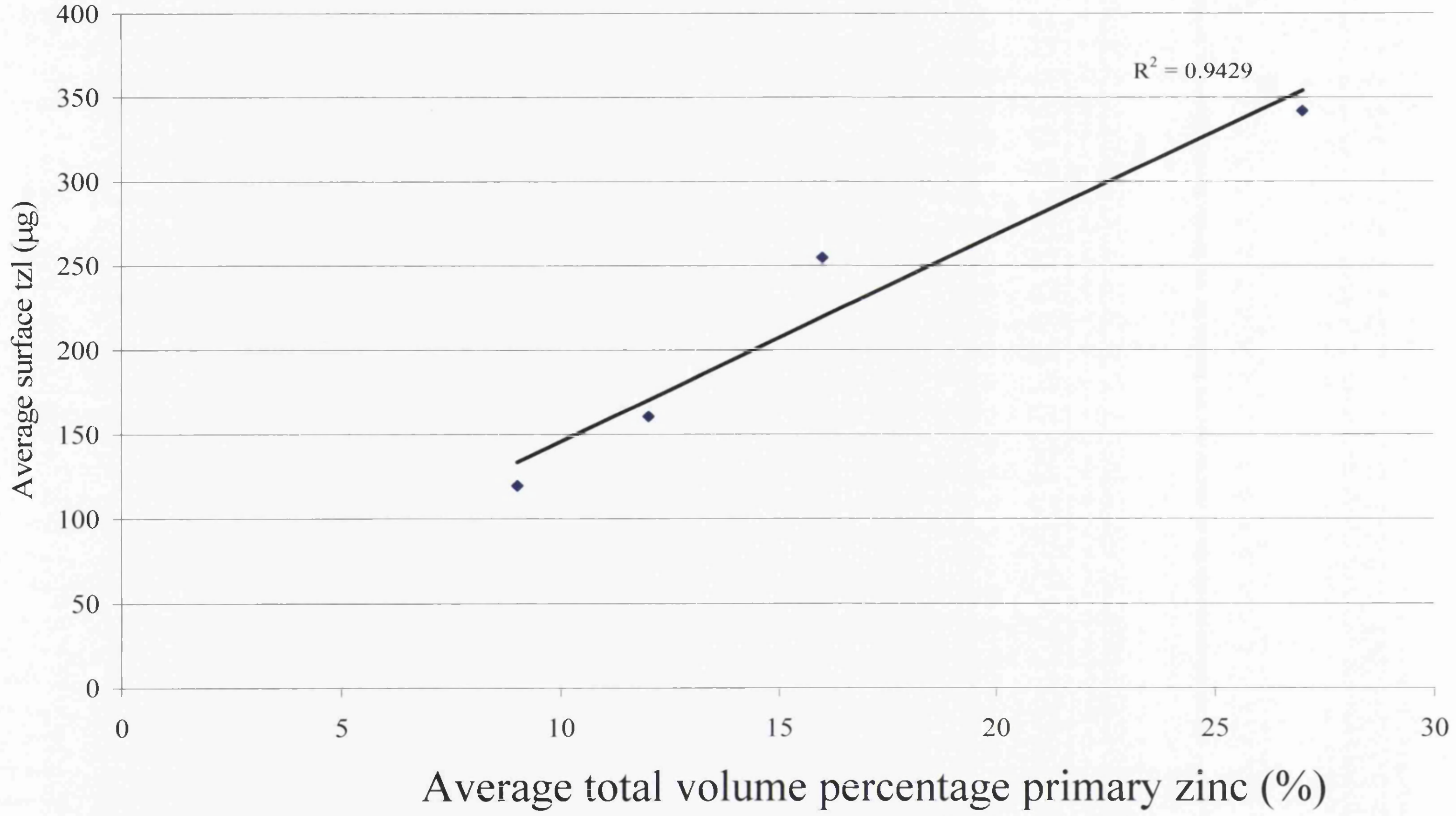

Figure 5.23 Total volume percentage of primary zinc at the air/ coating interface as a function of zinc loss

zinc phase being contained within the area close to the steel/ coating interface. The increase in visible primary zinc can also been seen from the microstructures detailed within figures 5.2 and 5.3. As the amount of visible primary zinc increases, there will be a subsequent reduction in the volume percentage of eutectic visible. As explained previously the reduction in the volume percentage of the eutectic will allow an increase in the intensity of corrosion. Hence, the increase in recorded zinc loss is observed due to increased cathodic activity. Since the number of dendrites per mm^2 remains constant (figure 5.8) it may be expected that the number of anodes in CT80 and CT170 would be the same. It is believed that this is probably the case, but the high intensity of corrosion occurring upon the CT80 surface is masking a lot of low intensity activity making it appear that there are less anodic events than actually there are.

5.5. Conclusions

The results show that the reduction of the coating weight of a Zn- Al Galfan coating will have a dramatic effect on both the microstructure and the corrosion resistance.

In this particular trial the gas wiping knives did not appear to affect the nucleation of the primary zinc dendrites since their size and number is fixed indicating that the nucleation occurs prior to the coating reaching the knives. Since the volume percentage of primary zinc increases the increased wiping is removing Al rich liquid. The eutectic undergoes a transition to the rod microstructure at the thinner coating weights and a finer eutectic spacing. The number of dendrites per mm^2 remains the same (within experimental error) for each sample. This indicates that there is little change in the conditions affecting the nucleation of this phase, again leading to the conclusion that nucleation occurred between exiting the galvanising bath and prior to entering the air knife zone. Along with no change in the dendrite number, the dendrite size (area) recorded close to the steel/ coating interface remained the same (within experimental error) for each sample.

Eutectic cell size is the same in all samples indicating cells are nucleated below the cooling rig. The final microstructural changes induced via the reduction in coating weight are the eutectic morphology and spacing. For samples CT170, CT130 and CT100 a mixed morphology of lamellar and rod eutectic is observed. For sample CT80 the coating is entirely rod eutectic. Coupled with this change a slight refinement in inter-lamellar and inter-rod spacing occurs from CT170 down to CT80.

Using the SVET it has been shown that the relative increase in the volume percentage of primary phase causes an increase in the corrosion rates. Both along the cut edge and at the surface of the galvanised samples an increase in corrosion is observed due to the change in volume percentages of the primary and eutectic phases. As the volume percentage of the primary phase increases there is a consequent reduction in the amount of eutectic. Hence by reducing the eutectic volume percentage, which appears to be the phase limiting the cathodic activity and keeping the corrosion rate, the corrosion rate is increasing consequently leading to the higher zinc losses observed.

From these studies it has been shown that a reduction in coating weight is detrimental to the corrosion performance along the cut edge and across the surface.

5.6 References

---

[1] D. Reynolds, Corus. *Private Communication*

[2] F. Goodwin: 'Galfan Galvanising Alloy Technology', 2nd Edition, ILZRO, (1984).

[3] P.A.Porot, N.Venthan, R.D. Jones and J.A. Spittle, *Metallography*, 20, 181, (1987)

[4] F. Hinterberger, W. Maschek and J. Faderl, Zinc Based Steel Coating Systems: Production and Performance, 281, (1998)

[5] M. Challis, Thesis (Eng.D.) - University of Wales Swansea, (2002).

[6] D. Christian, Proc. Of Eighth Galfan Licencees Meeting, International Lead and Zinc Research Organisation (ILZRO), April 21 (1986)

Chapter 6

The influence of Mg on the microstructure and corrosion resistance of Galfan coatings

6.0 Introduction

Throughout the development of Galfan the intrinsic phase transformation characteristics of the binary alloy[1] have been manipulated to alter the coating microstructure. As with altering various processing parameters[2,3], the addition of trace elements can have a significant effect upon microstructural evolution and ultimately the corrosion performance of the coating[4,5].

Within this body of work, the effect of the addition of Magnesium (Mg) to the Zn – Al binary alloy is investigated from two different view points. Initially the effects of magnesium additions from 0% to 0.1wt% (at 0.05wt% intervals) on the structure of small conical castings are examined and, secondly, trace additions (0.01wt% - 0.05wt%, at 0.01% intervals) are studied for typical Galfan galvanised coatings produced upon the Rhesca hot dip simulator.

Typical specifications for each sample can be viewed in table 2.4.2.4 for the simulated coatings and for the conical castings.

6.1 Results and Discussion

6.1.1 The effect of Mg additions upon the microstructure of the castings

The conical castings were produced at the University of Wales Swansea and the samples description are shown in section 2.4.2.4. Each casting was sectioned transversely into six equally sized pieces. Three sections were chosen (as shown in figure 6.1) to give a detailed visualisation of the evolution of the microstructure near to the top, close to the centre and the base of the casting. The individual sections were examined across the width of the casting at positions near to the edge, the centre of the casting and at a half radius distance. Example micrographs from each of these regions are shown in figure 6.2.

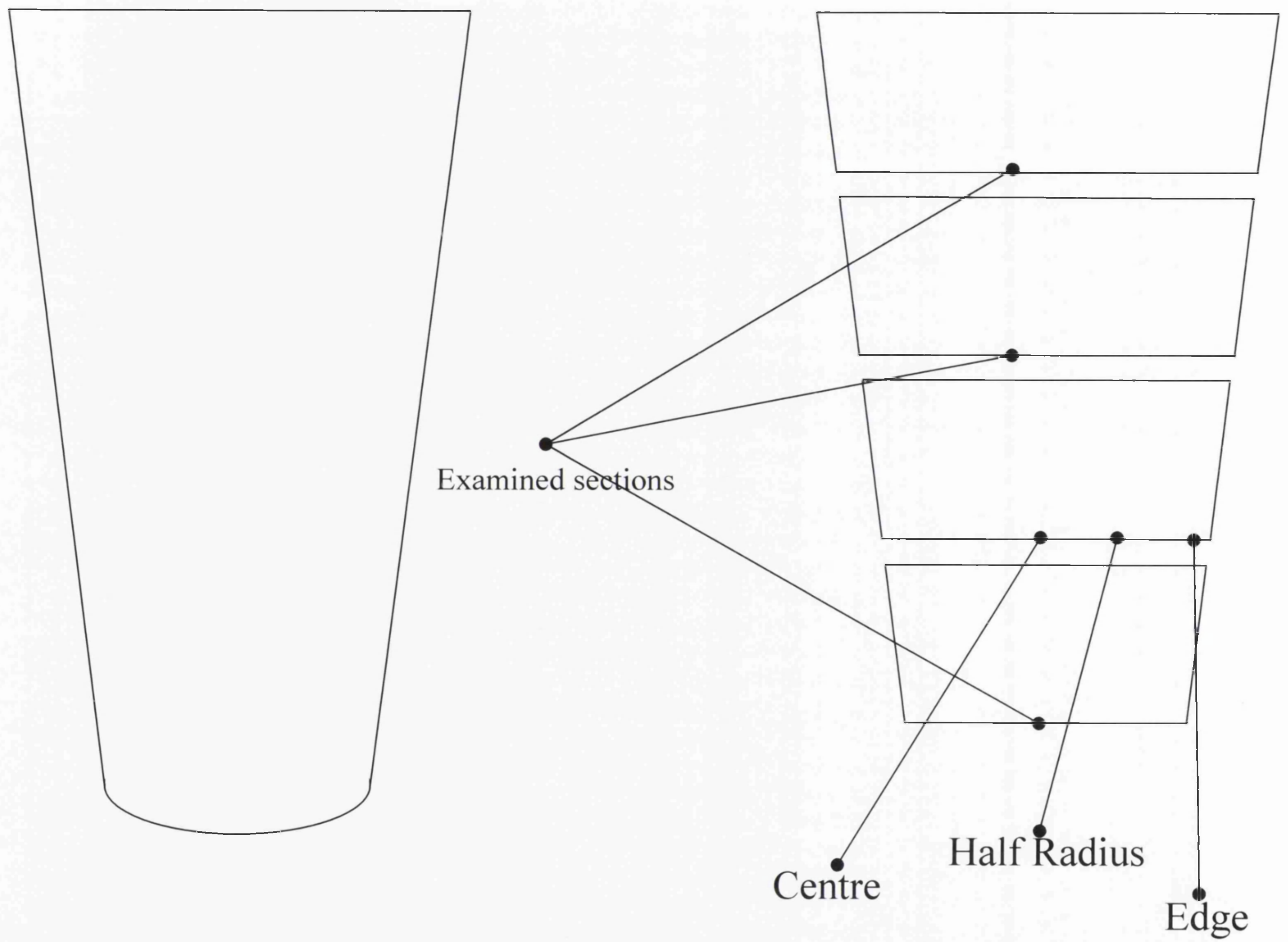

Figure 6.1. Examined sections of conical castings

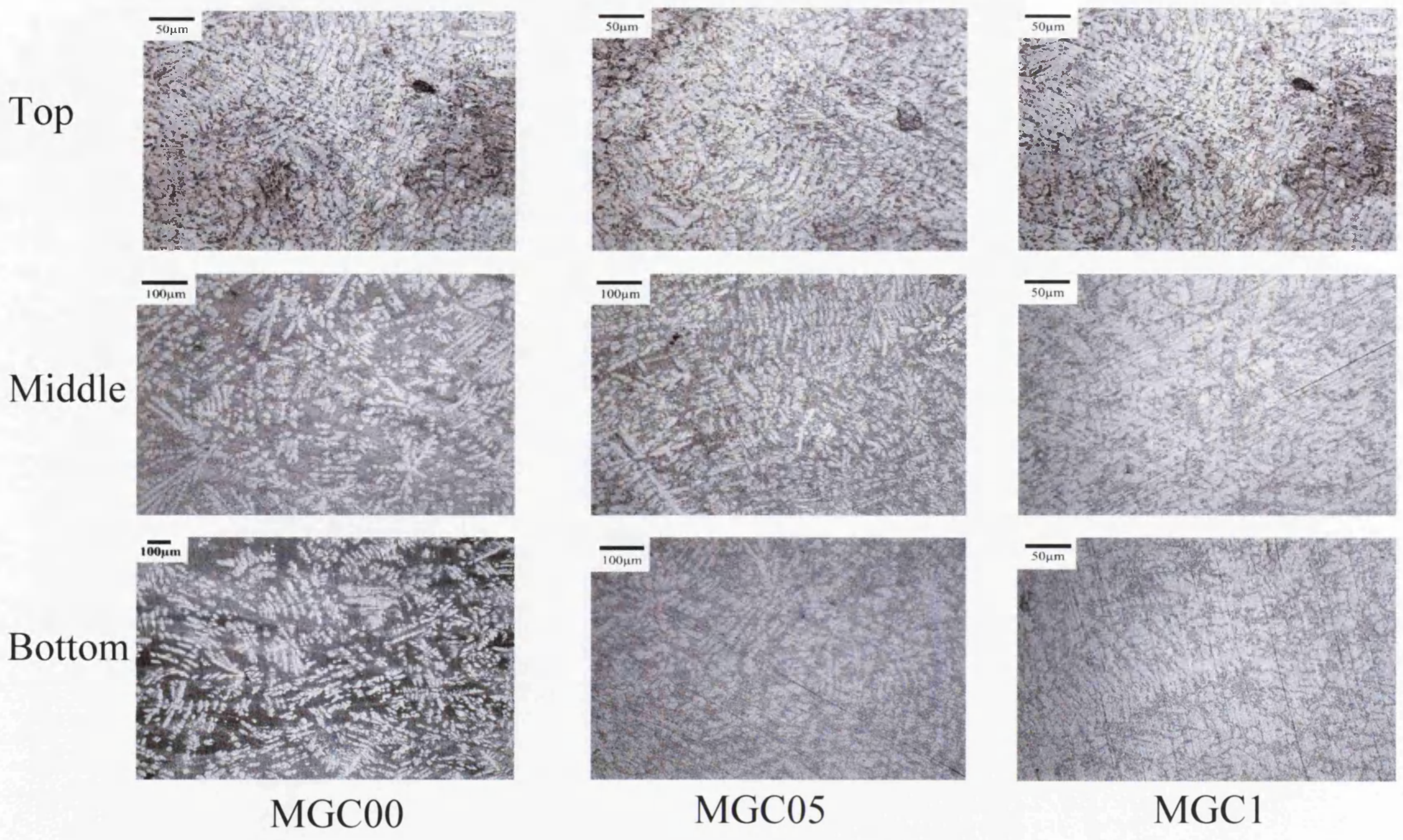

Figure 6.2.a Typical micrographs for each sample at the casting edge

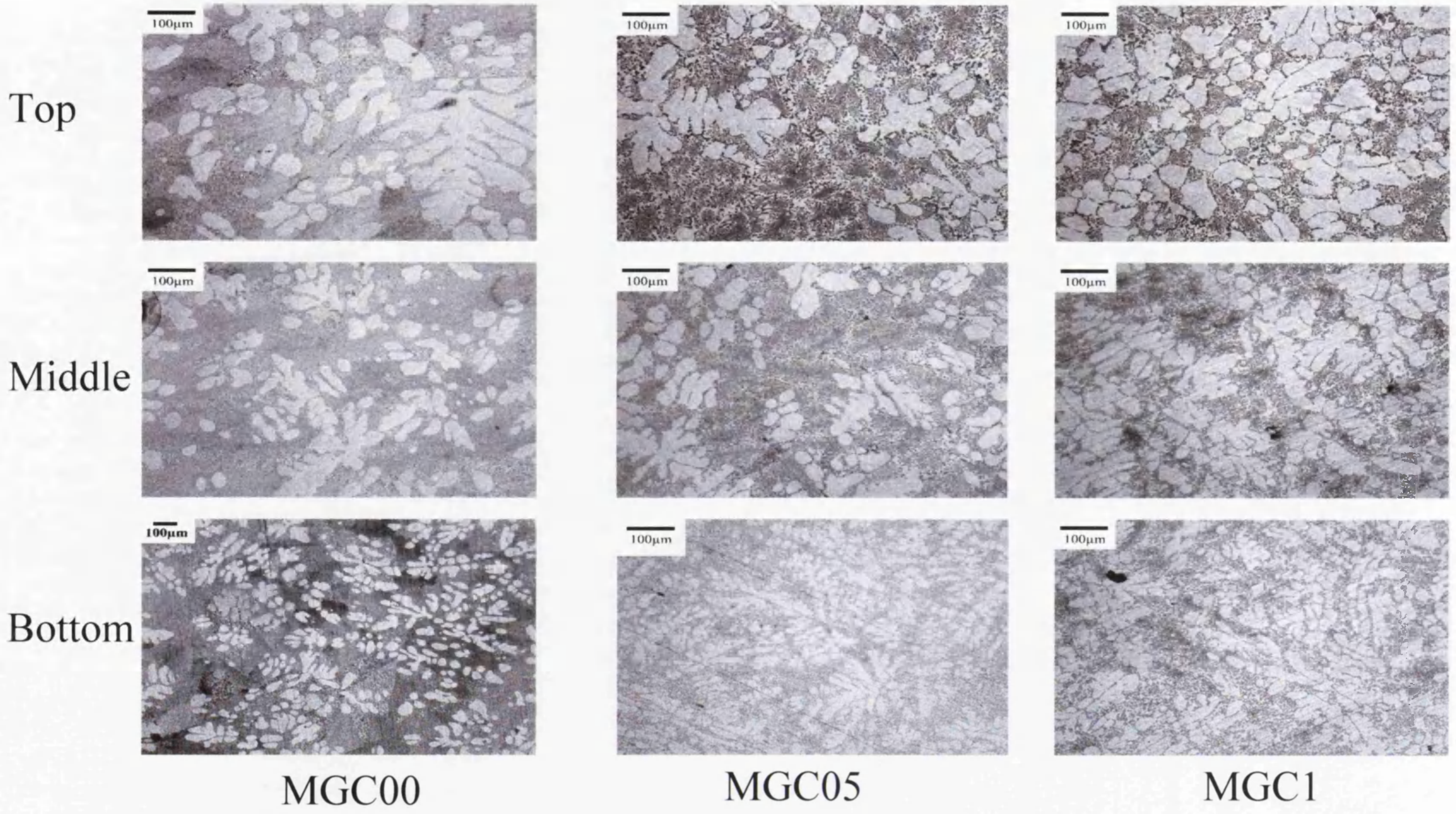

Figure 6.2.b Typical micrographs for each sample at the casting centre

The galvanized coated samples were produced using the hot dip simulator as described in section 2.3. In each case, coupons were guillotined from the centre of the coated panel and the coating thickness was determined using visual techniques. The coating thicknesses are detailed in table 2.4.2.4 and are deemed to be sufficiently similar enough to allow comparisons to be made between the different samples. Typical microstructures recorded close to the steel / coating interface are shown in figure 6.3. The optically white regions are primary zinc solid solution crystals which are encased within the Zn – Al eutectic matrix. The branching of dendrite arms exhibits growth along the $<11\bar{2}0>$ directions, the typically observed crystallographic growth directions for the HCP zinc phase. Closer observation of the structures reveals that the morphology of the eutectic undergoes a change from wholly lamellar to wholly rod with the addition of the ternary element.

The microstructures were characterized for both castings and coatings via changes in: a.) Volume percentage of primary zinc, b.) the size and number of primary zinc dendrites and c.) eutectic morphology and spacing.

6.1.2. Effect of Mg on volume percentage of the primary zinc rich phase

Table 6.1 details the average volume percentages of the primary zinc solid solution (Zn) crystals at the previously defined regions within the castings. Further to this, figures 6.4 and 6.5 provide a graphical summary of the average volume percentage of primary zinc solid solution crystals, for each chosen depth, at the casting edge and centre.

From table 6.1 it can be seen that at like positions (e.g. for each sample at the base of the casting) there is a significant increase in the volume percentage of the primary phase with increase in Mg. At the base of sample MGC00 the average

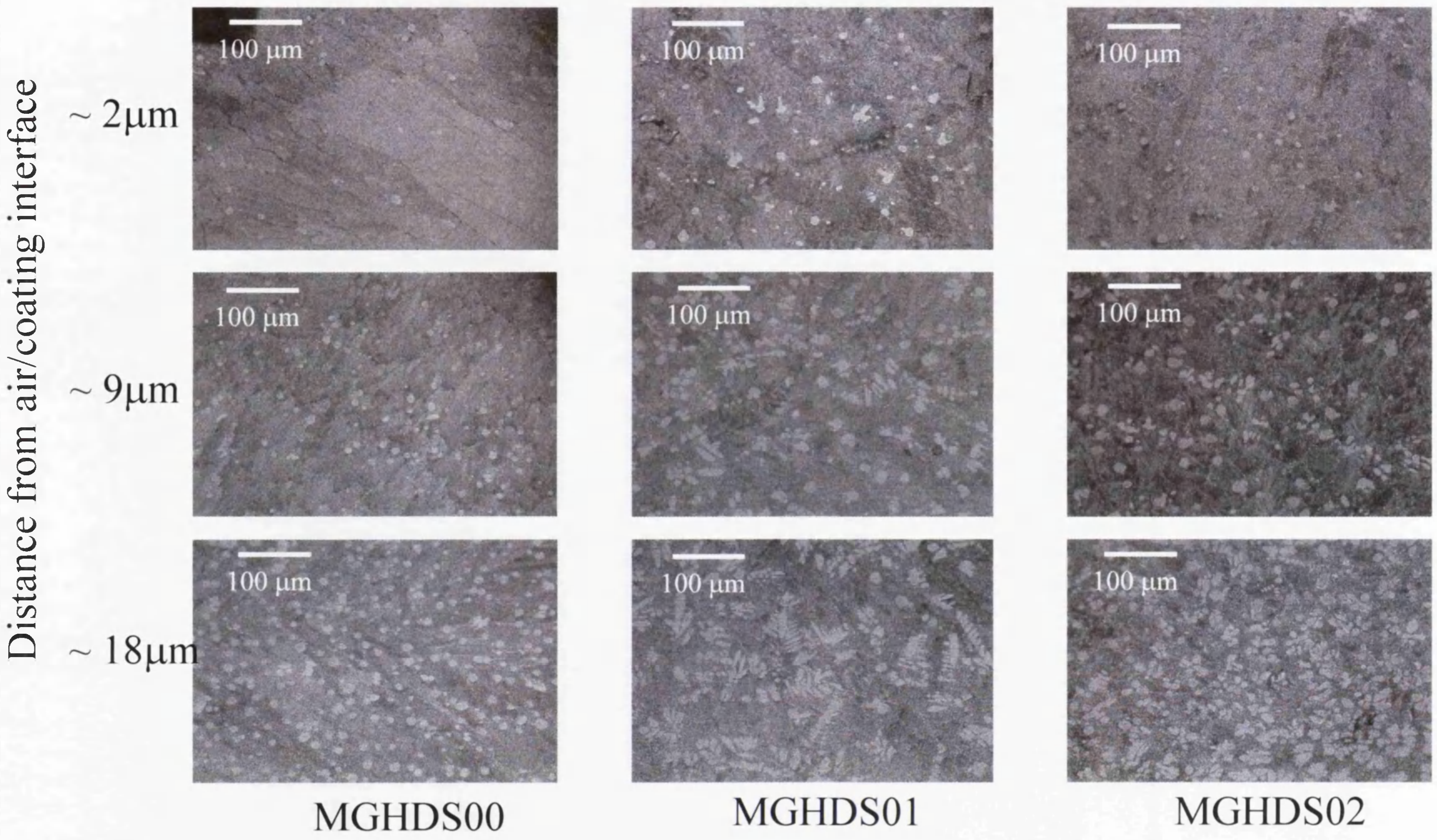

Figure 6.3.a Examined sections of galvanised coatings

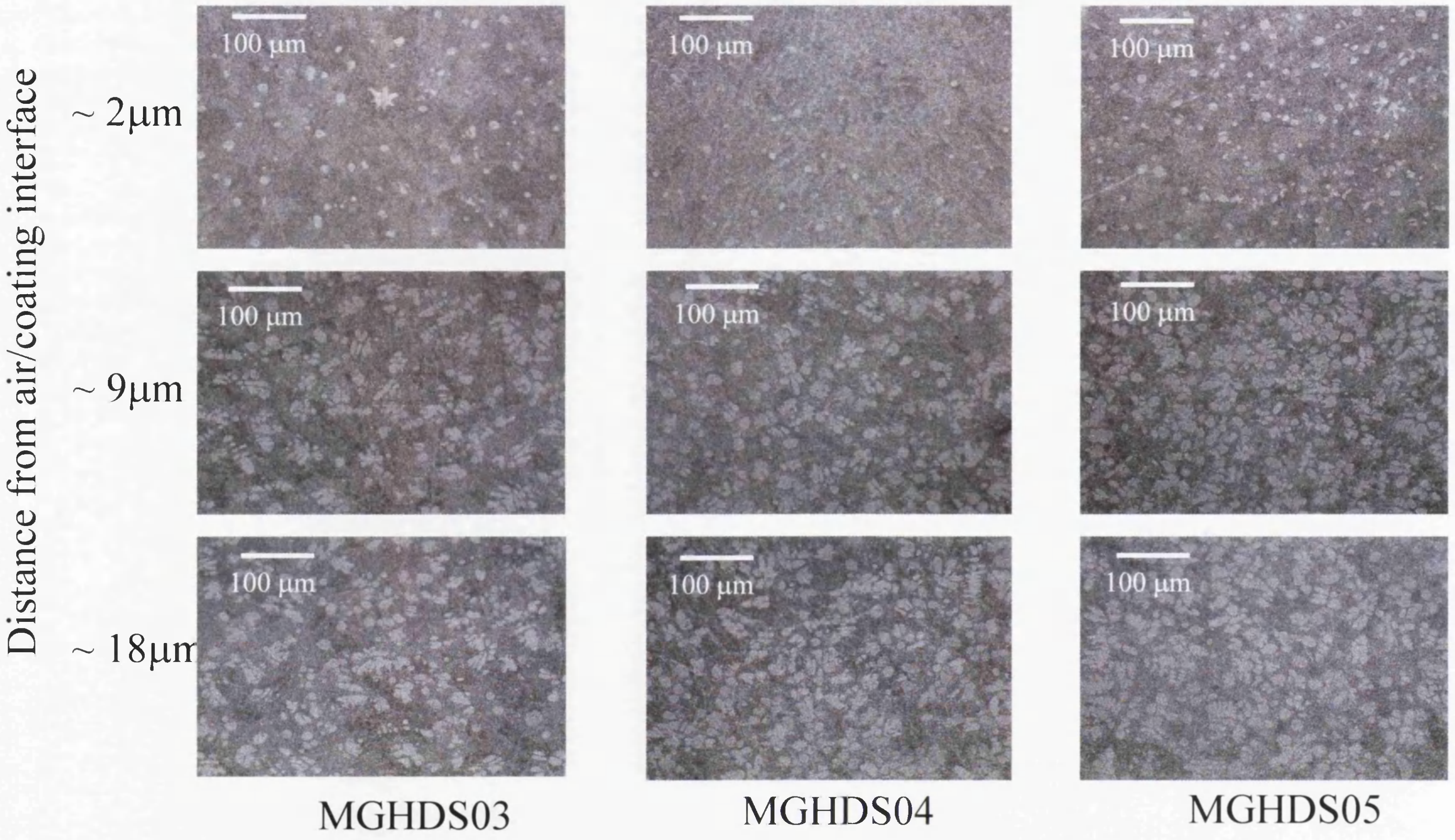

Figure 6.3.b Examined sections of galvanised coatings

Mg composition	Edge	Half Radius	Centre	Average Volume Percentage	Total Average Volume Percentage
MGC00 Bottom	29.3% ± 0.5%	32.3% ± 0.5%	31.7% ± 0.5%	31.1% ± 0.5%	
MGC00 Middle	32.5% ± 0.5%	32.1% ± 0.5%	38.2% ± 0.5%	34.3% ± 0.5%	
MGC00 Top	32.5% ± 0.5%	31.8% ± 0.5%	27.6% ± 0.5%	30.6% ± 0.5%	32.0%± 0.5%
MGC05 Bottom	42.4% ± 0.5%	41.0% ± 0.5%	36.4% ± 0.5%	39.9% ± 0.5%	
MGC05 Middle	41.9% ± 0.5%	39.2% ± 0.5%	35.0% ± 0.5%	38.7% ± 0.5%	
MGC05 Top	46.4% ± 0.5%	44.2% ± 0.5%	31.5% ± 0.5%	40.7% ± 0.5%	39.8%± 0.5%
MGC1 Bottom	54.3% ± 0.5%	52.6% ± 0.5%	48.6% ± 0.5%	51.8% ± 0.5%	
MGC1 Middle	54.1% ± 0.5%	37.1% ± 0.5%	42.4% ± 0.5%	44.5% ± 0.5%	
MGC1 Top	53.3% ± 0.5%	44.2% ± 0.5%	48.4% ± 0.5%	48.6% ± 0.5%	48.3%± 0.5%

Table 6.1 Volume percentages of primary zinc throughout casting

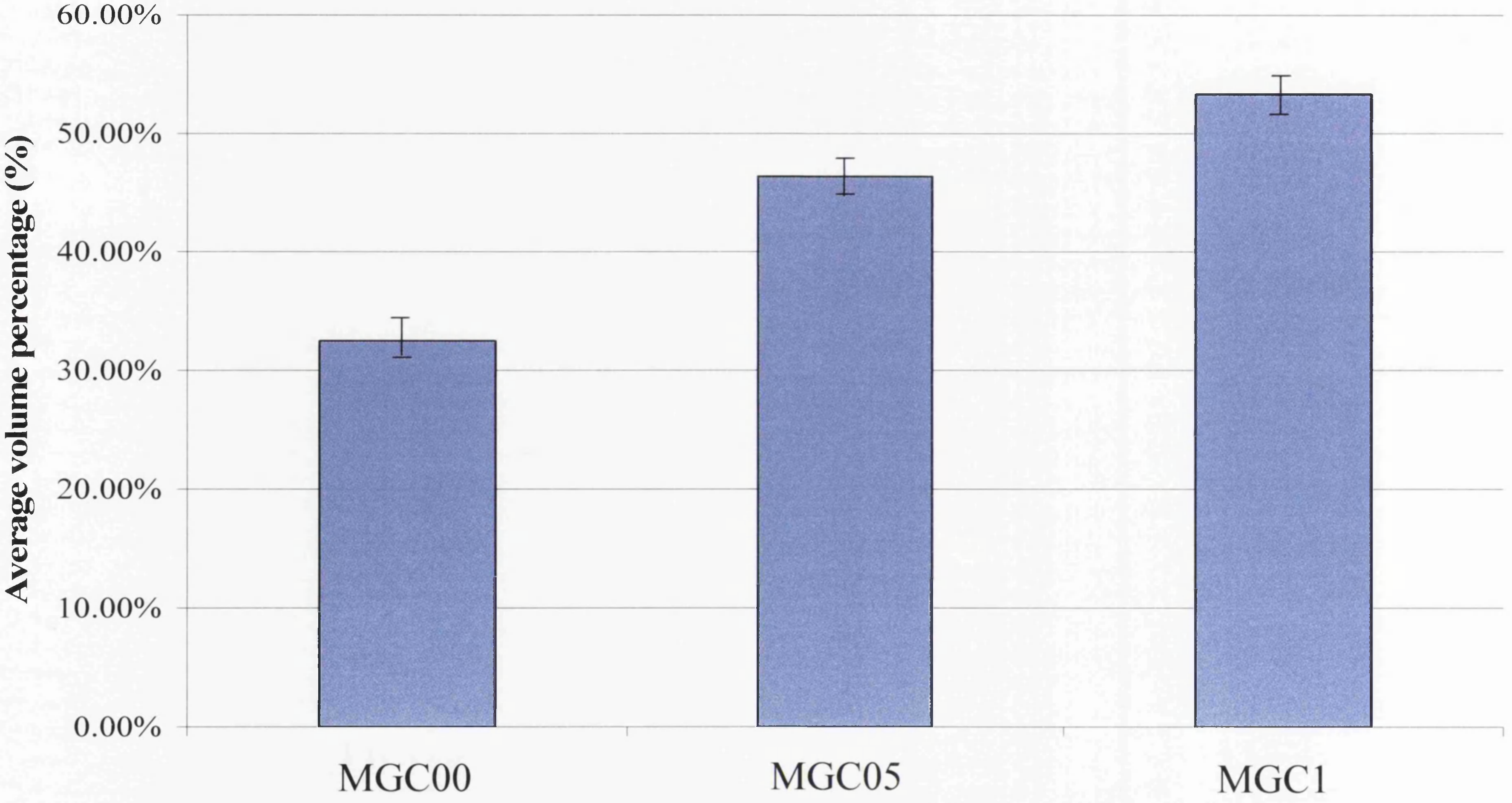

Figure 6.4 Average volume percentages of the primary zinc phase at the casting edge

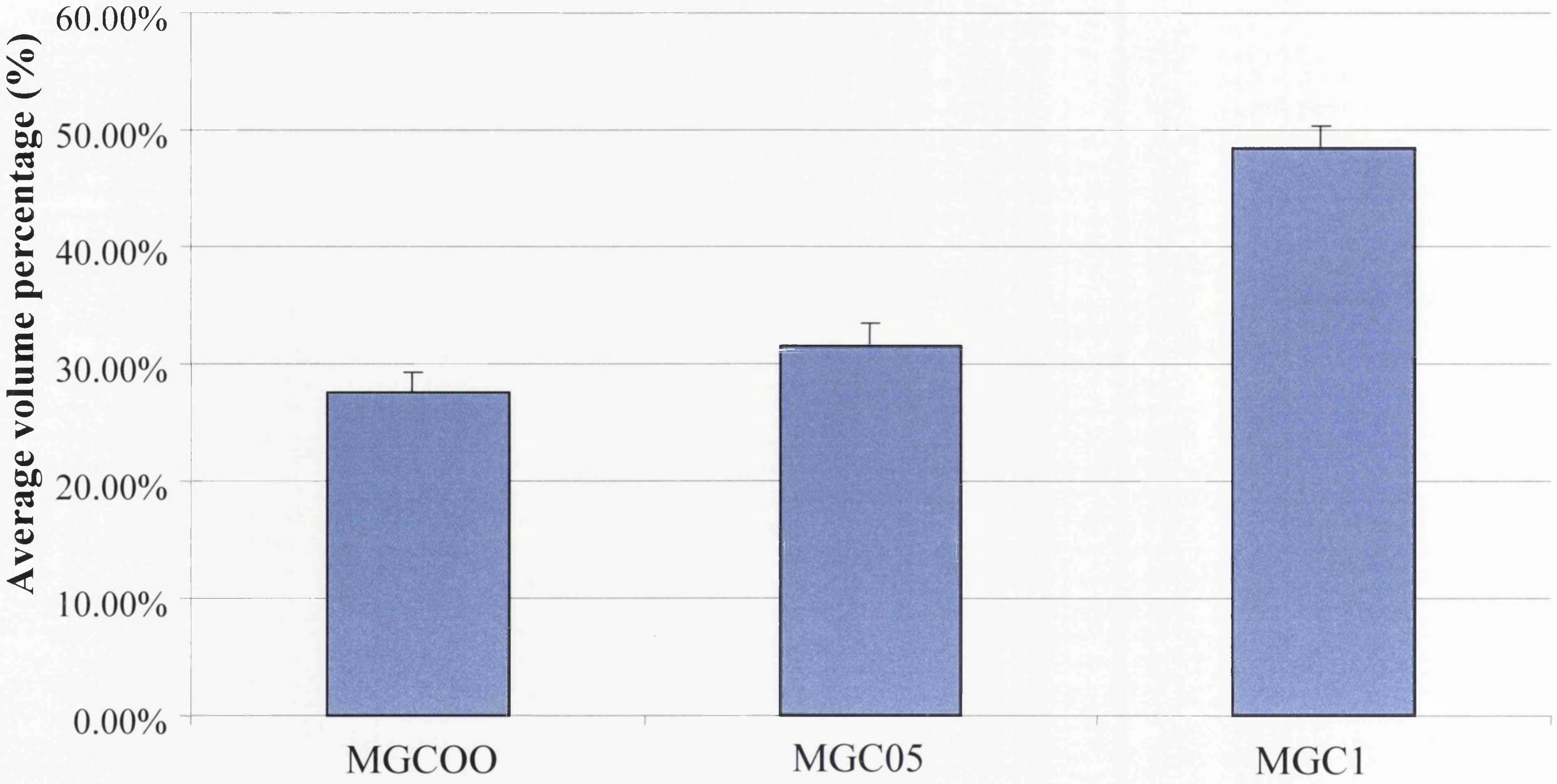

Figure 6.5 Average volume percentages of the primary zinc phase at the casting centre

volume percentage (calculated from the mean average of edge, half radius and centre results) of the primary phase is 31.1% ±0.5%. In samples MGC05 and MGC1 this value has risen to 39.9%±0.5% and 51.8%±0.5% respectively. Similar trends are observed at the centre and again at the top of the casting, in each case with a greater volume percentage of primary zinc being observed with increasing Mg content. Figure 6.6 shows the total average volume percentage of solid solution primary zinc crystals within each casting (average of top, middle and bottom values). Sample MGC00 has an average total volume percentage of 32%± 0.5%. 0.05wt% additions of Mg cause this figure to increase by 7% to 39.8% ±0.5% in sample MGC05 and by a further 9% to 48.3% ±0.5% in sample MGC1. Since all other processing conditions are held constant it would appear that the Mg is having a marked effect upon the volume percentage of the primary zinc phase.

Figure 6.7 details the change in volume percentage as a function of depth from the air/ coating interface for the simulated galvanised coatings. It is clear from these results that the greatest amount of primary zinc is situated at the base of the coating near to the steel/coating interface. With the highest percentage of the primary phase located within this region it would indicate that the nucleation of the primary phase is occurring on or very close to the base steel substrate (as seen in previous chapters). Each sample displays a similar trend with the volume percentage values of MGHDS00 increasing from ~ 0.6% at the surface through to ~12% at the steel/coating interface. Drawing a comparison with sample MGHDS03, the volume percentage at the surface is ~ 7% and at the steel/coating interface the value rises to ~25%. At the maximum level of Mg addition (MGHDS05) the volume percentage at the respective positions within the coating changes from ~ 8.17% at the surface to ~33% at the steel/coating interface. Interestingly, with each increase in Mg level the volume

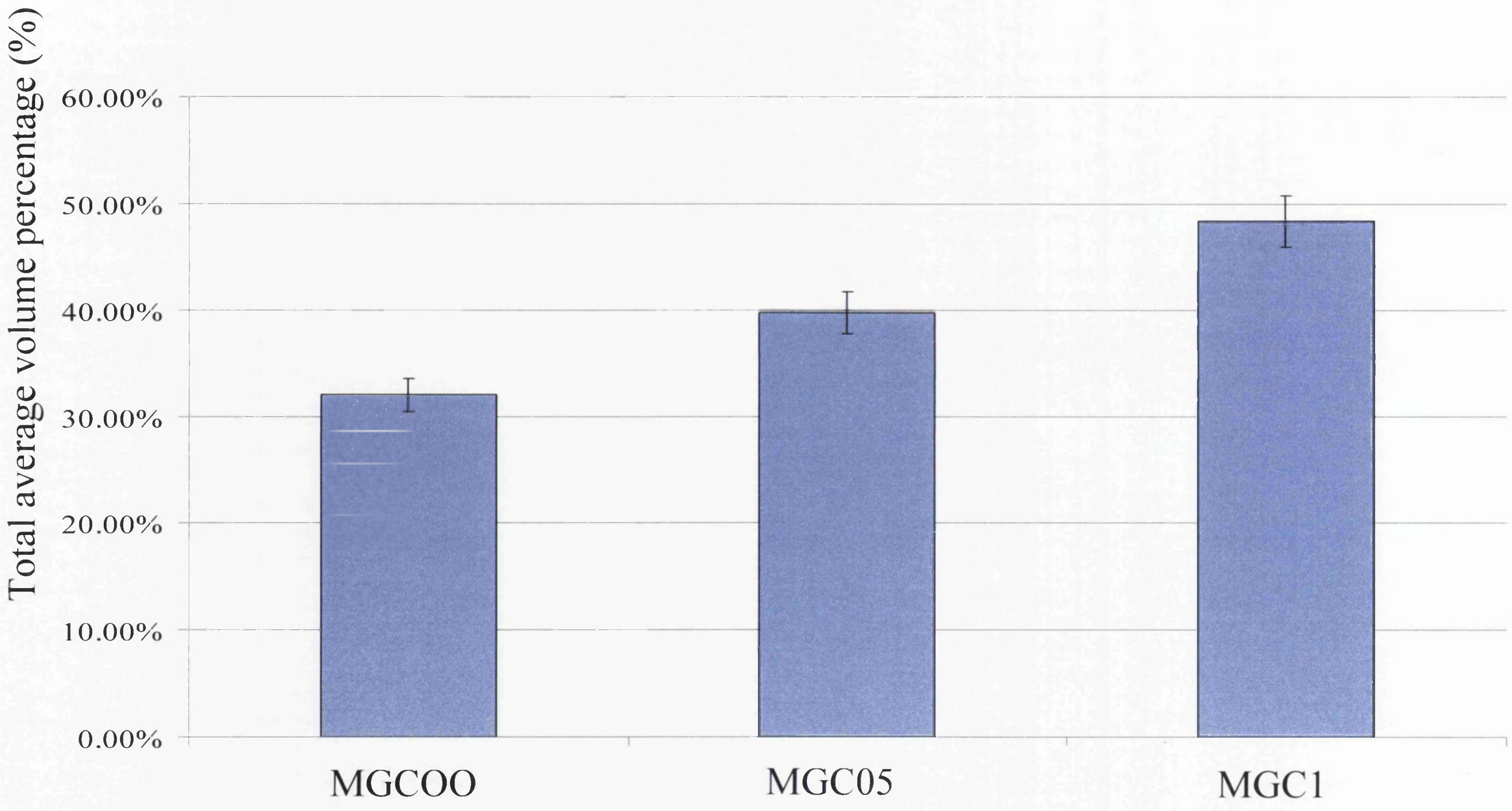

Figure 6.6. Total average volume percentage of primary zinc dendrites

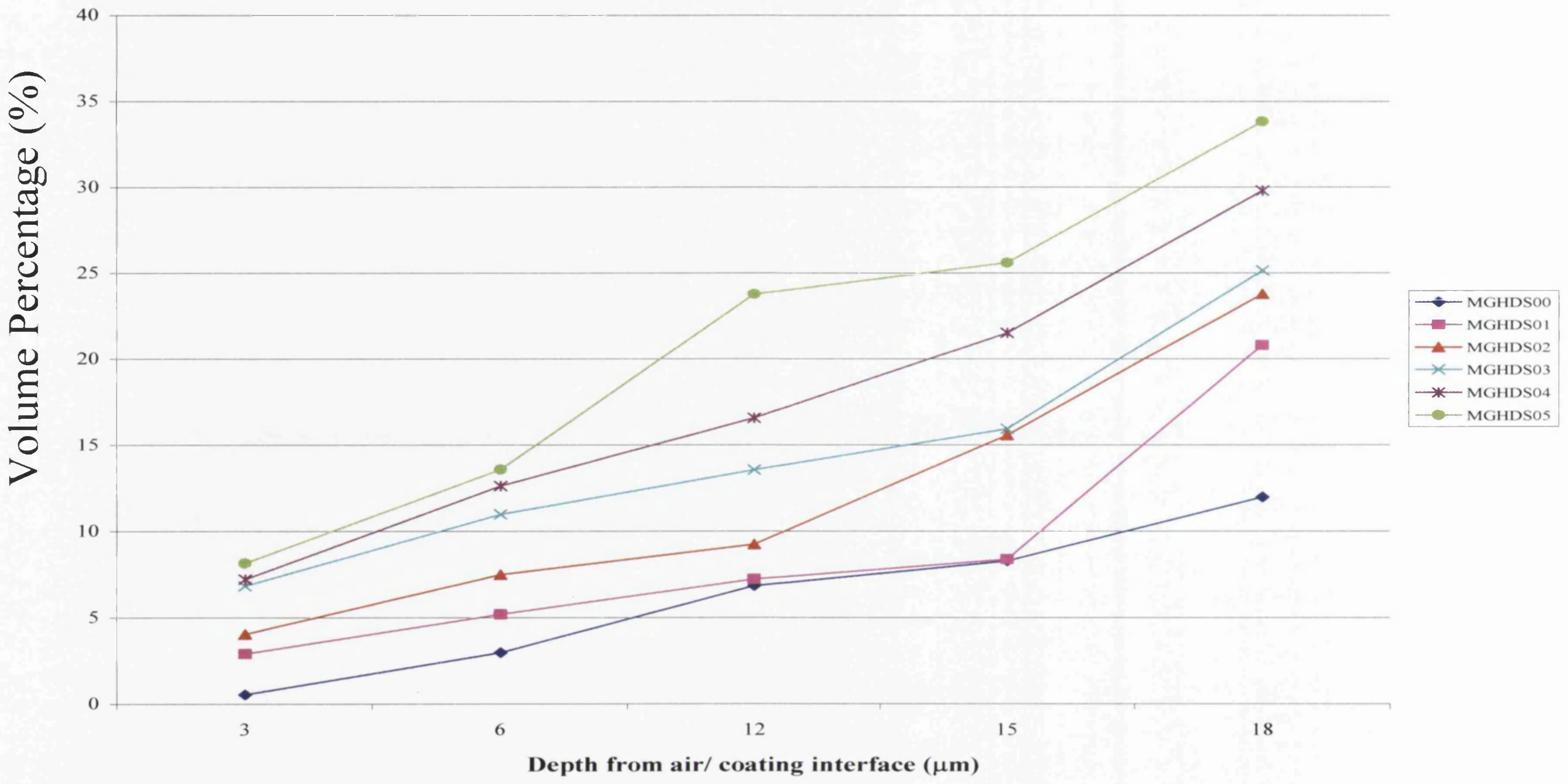

Fig.6.7. Volume percentage of primary Zinc as a function of depth for HDS simulated coatings

percentage at like positions increases. At the surface, the volume percentage of primary zinc in MGHDS00 is ~0.6%, increasing to ~7% for MGHDS03 and finally ~8% for MGHDS05. This trend is consistent at each depth with the samples containing higher Mg additions having a greater volume percentage. Likewise, values at the steel/ coating interface increase from ~12% (MGHDS00) through to ~33% (MGHDS05). By taking an average of the values at all depths, in each coating an approximate volume percentage of primary zinc within the coating can be generated (see section 2.1.2.1). These results are shown in figure 6.8. From this chart it can be observed that as the level of Mg is increased there is a distinct increase in the volume percentage of the primary phase. For sample MGHDS00 the volume percentage is ~6%. This value increases to ~14.5% in MGHDS03 and at the maximum Mg level the average volume percentage has increased to ~21%. Since all processing conditions were fixed it is clear that the addition of Mg is having a similar effect to that observed in the conical castings. Further analysis shows that, within experimental error, each addition of 0.01wt% Mg increases the average volume percentage by ~ 3%. For example, the addition of 0.01wt% Mg to the binary alloy increases the volume percentage from 6.148% to 8.924%. A further addition of Mg increases the value to 12.05%. The strikingly consistent change further supports the assumption that it is indeed the Mg altering the volume percentage.

In both the castings and the simulated galvanized coatings the results show that with the increasing amount of Mg the volume percentage of the pro eutectic zinc solid solution phase is increasing. This result is in agreement with previous published work[6] in which the area occupied by the primary (Zn) phase was shown to increase from 23% to 70% with a 0.1% addition of Mg for a continuous coating hot dip galvanizing bath.

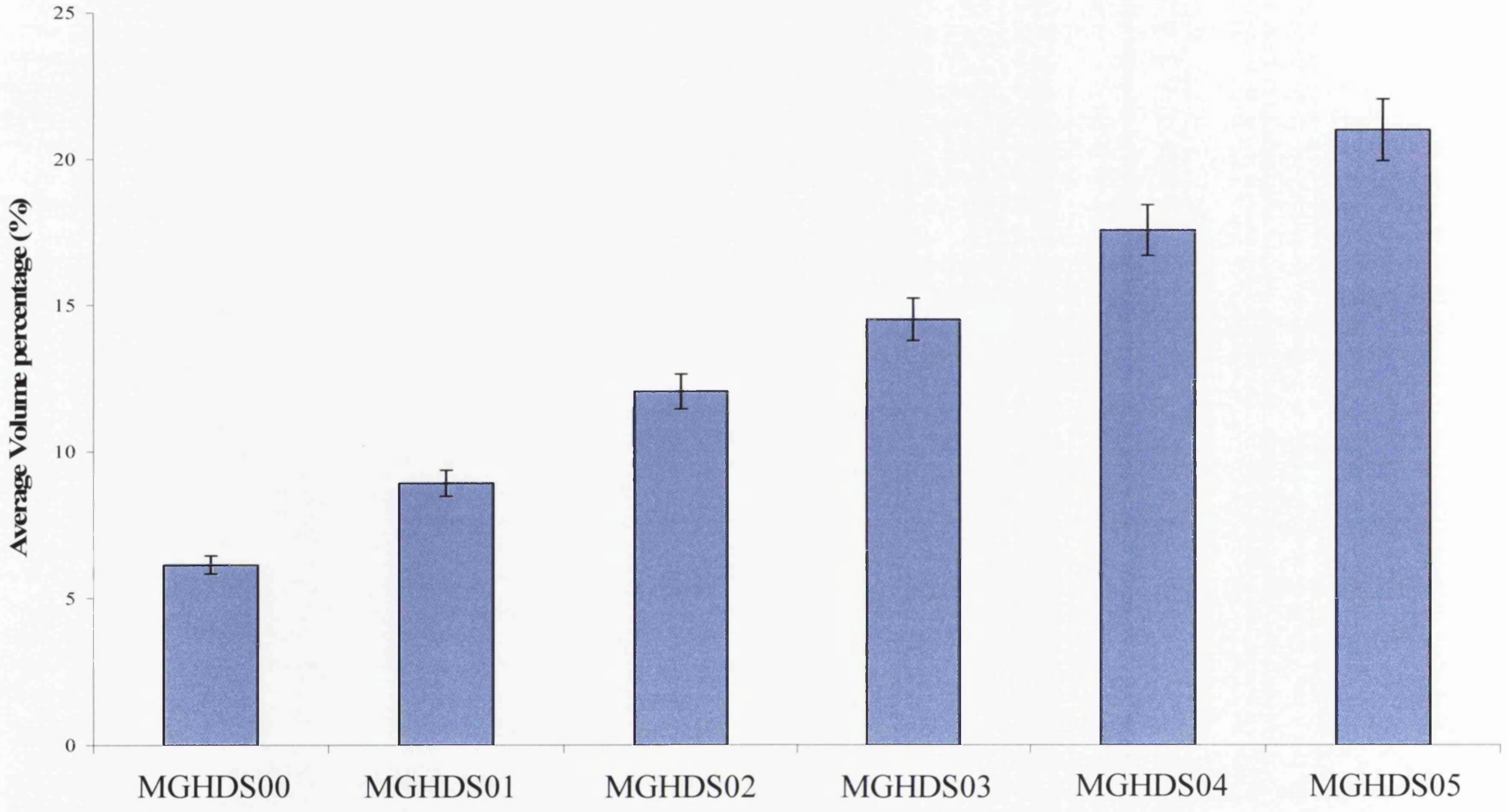

Fig.6.8. Average volume percentage of primary zinc in the galvanised coatings

To elucidate the mechanism for this change in the volume percentage of primary zinc it is appropriate to gather and compare all of the available data. For a simple binary alloy it is possible to calculate the percentage of each phase present for equilibrium conditions from the equilibrium phase diagram (shown for Zn – Al in fig 1.7) using the lever rule. Varying the Al content significantly changes the volume percentage of the primary phase present in the final microstructure. Decreasing the proportion of Al within the alloy beyond the eutectic point (variations between 95% and 98.85% Zinc, at the defined eutectic temperature, 382°C) will significantly increase the volume percentage of the primary zinc solid solution phase. Table 2.4.2.4 details the coating chemistry for each of the simulated galvanised samples. It can be seen that the Al content remains fairly consistent at 4.05% ± 0.04%. This slight change in Al content is not great enough to bring about any significant change in volume percentage of primary zinc.

The cooling rate has also been shown to have a significant effect upon the microstructural evolution of alloys in certain eutectic systems. Chill modification[7] has been used to modify and subsequently improve the microstructures of small Al – Si castings. Increasing the cooling rate increases the volume percentage of the primary Al phase in hypoeutectic alloys. However, in each of the present studies of the castings and galvanised samples, the rate of solidification remained unchanged. Each casting was produced, in the University of Wales, Swansea foundry, during the same morning. The molten alloy was poured from an identical holding temperature for each casting and subsequently left to air cool until solid. As such, no significant changes in the cooling rate could occur. The production conditions for the simulated coatings remained identical. All panels were processed using the same strictly defined parameters and consequently the cooling rate for each sample would have been almost identical. Hence the increase in volume percentage in each experiment cannot be attributed to changes in cooling rate.

The modification of Al- Si alloys can be brought about via two methods; firstly through the chill modification mentioned previously and secondly, and more effectively, through the addition of a ternary element (Na or Sr). It has been long accepted[8, 9,10] that the trace addition of a modifying element to specific binary eutectic systems will bring about a depression in the eutectic arrest temperature and a displacement of the eutectic composition. As previously described (section 1.5) the eutectic temperature, under equilibrium conditions, is the unique temperature at which the eutectic reaction occurs transforming remaining molten liquid into the two phase eutectic microstructure. Under non equilibrium conditions this temperature varies slightly but remains close to the defined temperature. The work of Crosley and Mondolfo[11] has best shown that the addition of Na to the Al- Si alloy will depress the eutectic temperature. Thermal analysis revealed a eutectic depression of some 10° C under slow cooling conditions.

Hence it is believed that the addition of Mg to the Zn – Al alloy is causing a depression in the eutectic temperature and a displacement of the eutectic composition to a higher Al level thus leading to an increase in the volume percentage of the primary zinc solid solution phase. The increase is brought about due to an extended freezing range allowing an increase in precipitation of the primary phase and growth over an extended time period. Since the eutectic temperature is now lower and the eutectic composition is displaced to a higher Al level, it is possible for a greater amount of the primary phase to be formed as discrete dendrites prior to the eutectic reaction. The almost linear increase in the volume percentage is consistent with previous research[10] detailing that the depression in eutectic temperature is proportional to the amount of the modifying element added.

6.1.3. Effect of Mg on size and number of primary zinc dendrites

6.1.3.1 Conical Castings

The number of dendrites per square mm has been calculated at each of the previously mentioned positions within the casting, using methodology described in section 2.1.2.2. The results are shown in table 6.2. It can be seen that at like positions the number of dendrites per mm^2 increases respectively in samples MGC00, MGC05 and MGC1. At the bottom edge of the casting the dendrite number increases from 253 per mm^2 (MGC00) up to 1123 per mm^2 (MGC1). These numbers increase at the top of the casting to 1986 per mm^2 and 2640 per mm^2 for samples MGC00 and MGC1 respectively. An increase in dendrite number is observed at each depth through the casting with the sequential addition of Mg. Interestingly, similar trends in the distribution of the dendrites through the casting are observed when comparisons are drawn between the base, centre and top of the three castings. At the edge of the casting, closest to the mould wall, the number of dendrites per square millimetre in each individual case is far higher than close to the centre. Also, at this position, the number of dendrites at the top of the casting is significantly higher (1986 per mm^2 in sample MGC00) than at the bottom of the casting (250 per mm^2). However this trend is reversed through the centre of the casting where the dendrite number is greater at the bottom of the casting (150 per mm^2) than at the top (62 per mm^2). This trend reversal was observed in all three samples, along with the sequential increase in dendrite numbers at the like positions. It is thought that the observed trend reversal is induced as a result of the pouring and initial freezing conditions. Upon pouring, the

Sample	Position	Dendrites/ mm^2	Dendrites/ mm^2
		Edge	Centre
MGC0	Top	1986	62
	Middle	874	76
	Bottom	253	150
MGC05	Top	2247	120
	Middle	1480	165
	Bottom	999	270
MGC1	Top	2640	159
	Middle	1627	197
	Bottom	1123	312

Table 6.2. Dendrite number per square mm within the casting

molten alloy entering the mould will begin to solidify and equiaxed Zn crystals will form in the liquid. Flow will be induced via the continued pouring action, and will transport already nucleated primary crystals from the base of the mould to the top of the casting. Since nucleation will continue as liquid rises up the cold walls of the mould the subsequent number of dendrites at the casting top edge will be a sum of the recently nucleated dendrites plus those transported via fluid flow. Hence at the casting edges the observed number of dendrites per square mm is greater at the top than at the bottom. Once pouring is complete the dendrites within the central mould region are able to settle naturally within the casting under the action of gravity which will lead to an increased number of dendrites at the casting bottom. The overall increase in number of dendrites as Mg increases is obviously due to enhanced nucleation, possibly the result of an increase in nucleant substrates e.g. MgO.

The size of the dendrites varies through the radius of the casting. At the edge of the casting the dendrites are small and numerous, at the centre of the casting the reduction in number of dendrites leads to a greater size of individual crystals. This is a result of rapid cooling at the mould walls. Heat is more quickly removed from the solidifying casting at the edges due to rapid conduction through the graphite crucible. This rapid cooling promotes nucleation of an increased number of dendrites at the edges.

6.1.3.2 Simulated Coatings

For the simulated galvanized samples the average size and number of primary dendrites has been recorded as close as possible to the steel / coating interface. Figure 6.9 shows the number of dendrites per mm^2 at the steel coating interface for each sample. Again an obvious trend is apparent such that as the level of Mg increases the

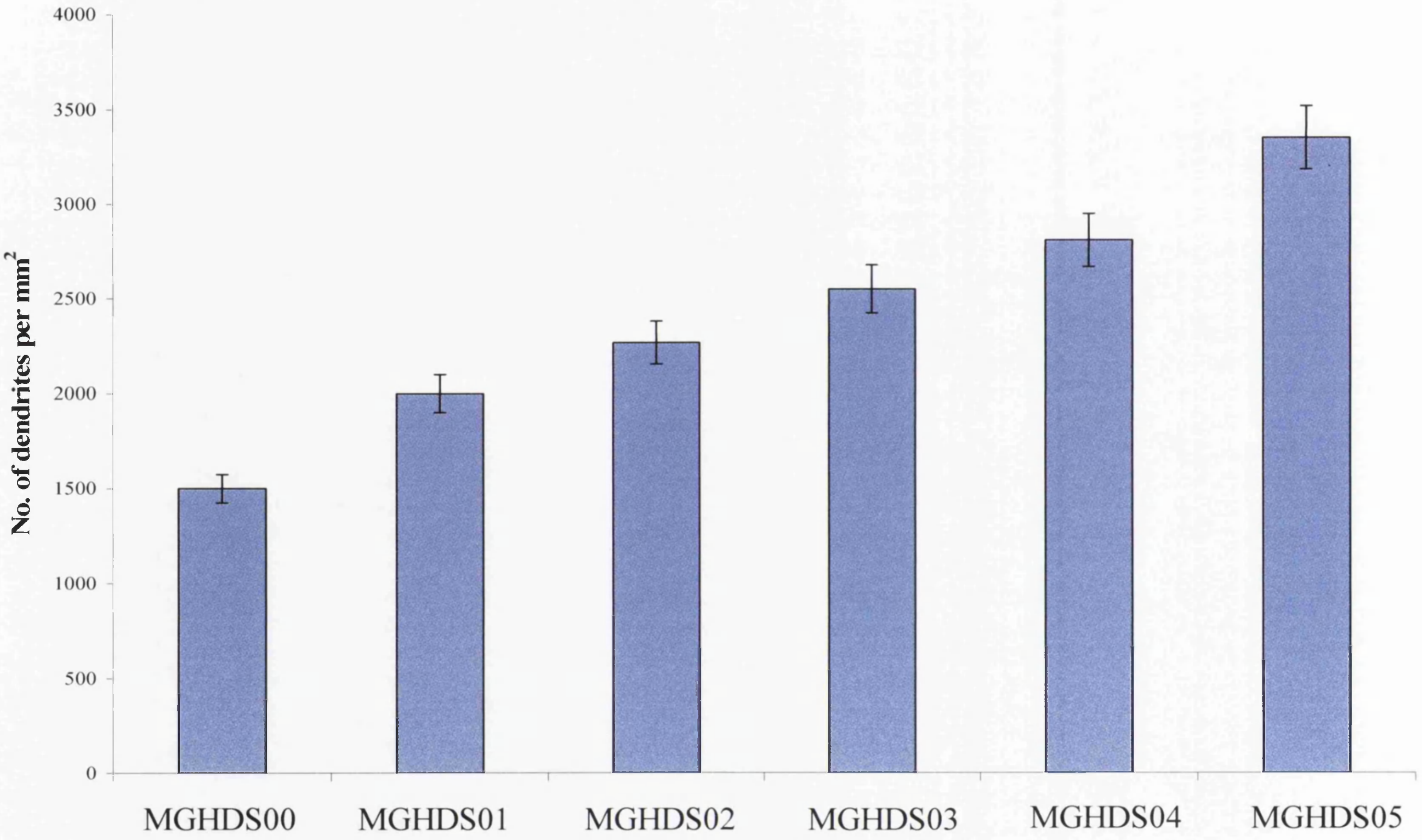

Figure 6.9. Average number of dendrites per mm^2 recorded at the steel- coating interface

number of dendrites is increased. Sample MGHDS00 has ~1499 ± 75 dendrites per mm^2, this increases to ~2548 ± 127 with sample MGHDS03 and finally ~3348 ± 167 for MGHDS05. Again, since all other process parameters were held constant the increased number of dendrites appears to be a result of enhanced nucleation provided by the addition of Mg.

Figure 6.10 shows that after the addition of Mg the size (area) of the individual dendrites remains constant within experimental error. Initially the size of the dendrites (sample MGHDS00) is $0.667mm^2$ increasing to an average value of $\sim 0.86mm^2$ for each of the other samples. The similarity in dendrite size can be explained due to the fact that the increase in volume percentage of the primary phase and also the increase in number of nucleation events are similar for each addition of Mg. Hence the ratio of primary phase to nucleation events is similar and there is little change in dendrite size. The similarity in ratios can be seen when plotting the volume fraction as a function of dendrite number (figure 6.11.). Here the direct linearity is obvious with the correlation factor, R^2 returning a value of 0.9948.

In both the castings and the galvanized samples there is an increase in the number of primary zinc crystals as a result of the addition of Mg. It is believed that this increase is caused by one of, or a combination of, the following two reasons. Clearly, the greater number of crystals is due to an increased number of nucleation events in the initial stages of solidification. Firstly it is possible that, due to the affinity between the Magnesium and Oxygen, magnesium oxide (MgO) is forming. These particles may be acting as nucleation centres promoting the larger number of crystals formed. It follows that as the amount of Mg is increased there will be a greater chance of MgO forming and consequently a greater number of nucleation events. Secondly, since the Mg additions cause a depression in the eutectic

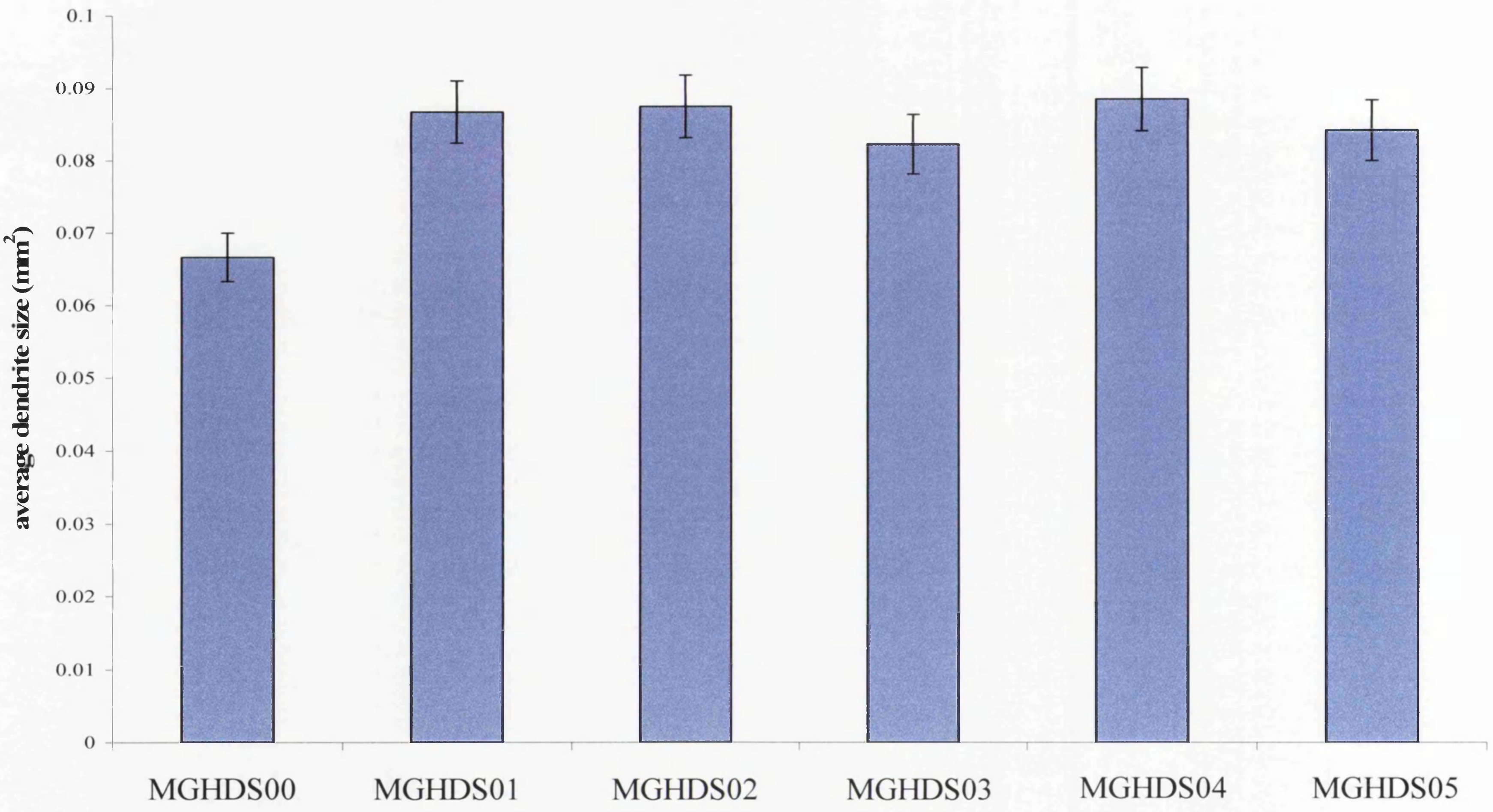

Figure 6.10. Average area of each primary zinc dendrite

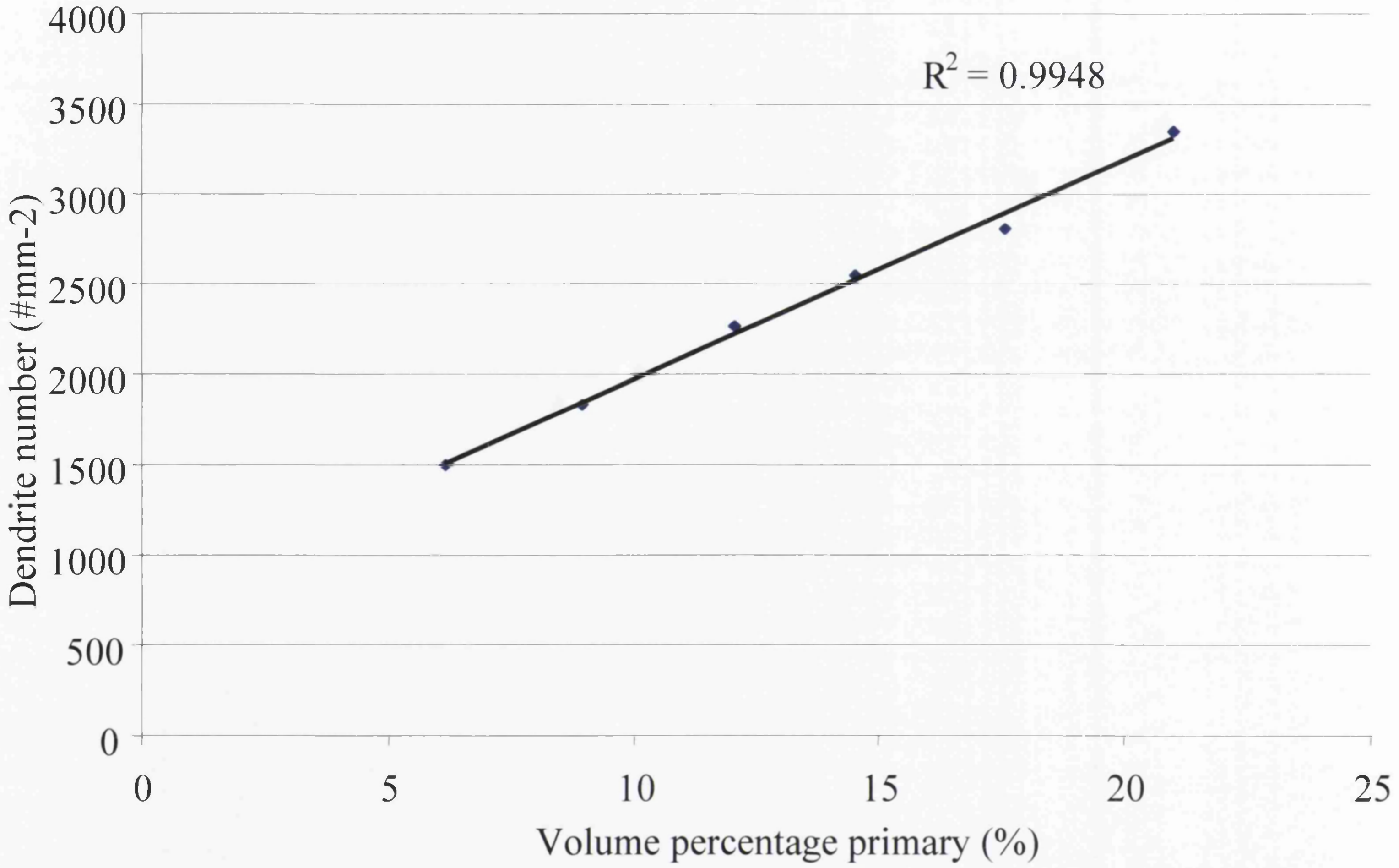

Figure 6.11. Average volume percentage as a function of dendrite number

temperature, the temperature range over which nucleation of primary zinc dendrites can occur is increased. The greater number of nucleation events results from equation 1.19 and which shows that, with the subsequent increase in undercooling, the critical radius, r*, required to form a stable nucleus is reduced and also the free energy barriers to nucleation is also reduced.

6.1.4. Effect of Mg on morphology and spacing of eutectic

Figure 6.12 details the eutectic structure of each sample. As previously stated the addition of Mg forces a change in morphology from a wholly lamellar eutectic (MGHDS00), to a mixed morphology (MGHDS01, MGHDS02) and finally a wholly rod eutectic (MGHDS03, MGHDS04 & MGHDS05). For each sample the inter-lamella spacing and/or the inter-rod spacing (which ever was relevant) was recorded as described in section 2.1.2.4. The results are tabulated in table 6.3. What is apparent from this data is a refinement of the eutectic structure with increasing Mg. The structures containing lamellar eutectic (MGHDS00, MGHDS01 and MGHDS02) show a reduction in inter-lamellar spacing from 6.7μm ± 0.1 μm (MGHDS00) to 5.2 μm ± 0.1 μm (MGHDS01) and finally 4.0 μm ± 0.1 μm (MGHDS02). The change is also apparent with the rod eutectics with the inter-rod spacing reducing from 6.7 μm ± 0.1 μm (MGHDS01) to 5.1 μm ± 0.1 μm (MGHDS05).

The change in the eutectic morphology coupled with the increase in volume percentage of the primary zinc phase leads to the conclusion that Mg additions are significantly modifying the Galfan microstructure. The associated refinement of the eutectic is also consistent[7,9] with this conclusion. However the reasoning for the eutectic change is not fully understood as it is possible that one of two mechanisms are forcing the transformation. The first possibility is associated with the change in

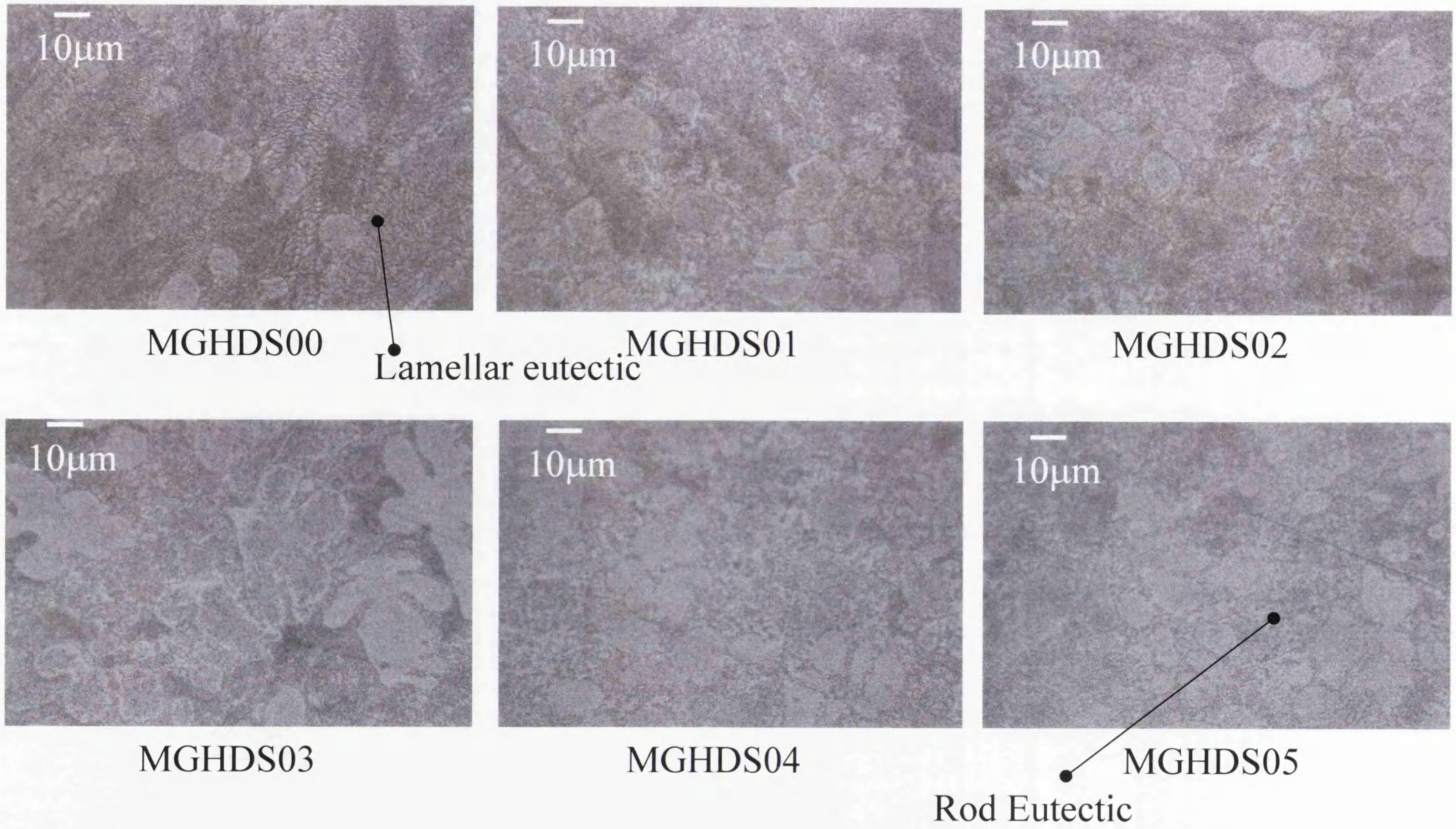

Figure 6.12. Typical eutectic microstructures recorded at the steel/coating interface (*X*1000)

Sample	lamella (µm)	rod (µm)
MGHDS00	6.7 ± 0.1	
MGHDS01	5.1 ± 0.1	6.6 ± 0.1
MGHDS02	4.0 ± 0.1	6.5 ± 0.1
MGHDS03		5.7 ± 0.1
MGHDS04		5.2 ± 0.1
MGHDS05		5.1 ± 0.1

Table 6.3. Average inter-lamellar and inter- rod spacing

eutectic spacing. It has been found for Al-Si alloys that as the eutectic temperature falls the volume percentage of eutectic falls and the percentage of Al rich phase in the eutectic increases. The eutectic spacing then becomes finer. The change in eutectic morphology is due to the inter facial energies are more favourable for rod formation than lamellar. Secondly Mg additions are believed to affect the surface tension of the liquid alloy. Thall and Chalmers[8] concluded that in Al– Si alloys it is possible that a small amount of modifying agent (in Al- Si the agent is Na) is able to reduce the surface energy of the growing two phase structure. The result of this reduction is to increase the interfacial angle between the coupled phases which leads to the suppression of growth of one of the phases and hence a change in the local structure. The work of Thall and Chalmers is supported by research conducted by a series of Russian researchers. Reviewed by Korol'kov[12] the influence of a few surface active additions upon the surface tension of Al, Zn and Mg is discussed. From this work it is clear that the addition of Sb, Mg, Li, Bi and Pb reduce the surface tension of the base Al metal. Likewise, additions of Sb, Li, Bi and Pb also reduce the surface tension of the base Zn metal. Research into the effect of Mg on Zn is not reported. However, it can be reasoned that it is likely that Mg will reduce the surface tension of Zn since the 'surface active effect' appears to be a result of considerably different atomic volumes, which is the case with these two elements. Hence the addition of increasing amounts of Mg is responsible for the change of the eutectic structure from a lamellar morphology to a rod structure.

6.1.5. Effect of Mg on surface eutectic cell size

The eutectic cell size was determined using linear analysis as described in section 2.1.2.5. The recorded results are detailed in table 6.4. Consistent with the

Sample	cell size (mm)
MGHDS00	2.35 ±0.01
MGHDS01	2.28 ±0.01
MGHDS02	2.16 ±0.01
MGHDS03	2.10 ±0.01
MGHDS04	2.02 ±0.01
MGHDS05	1.98 ±0.01

Table 6.4. Average eutectic cell size

depression of the eutectic temperature, the eutectic cell size is reduced with increasing additions of Mg. Sample MGHDS00 has an average cell size of 2.35mm ± 0.01mm reducing to 2.10mm ± 0.01mm in sample MGHDS03 and finally 1.98mm ± 0.01mm in sample MGHDS05.

The reduction in size of the eutectic cells is associated with a small increase in the number of nucleation events brought about via the addition of Mg. The nucleation of each cell is a discrete event followed by radial growth of the cell away from the central nucleation point[13]. The growth continues until impingement with an adjacent growing cell occurs.

Close inspection of the eutectic cells near to the steel/ coating interface has revealed tiny cubic particles at the centres of several of the cells. A typical particle is shown in figure 6.13. The particles have been analysed using EDX techniques to reveal the chemical composition. What is clear from the results is that the particle is composed almost entirely of Fe and Al. The proportions indicate that this is a Fe_2Al_5 particle. Previous work researching bath chemistries[14] has shown that Fe_2Al_5 is the chemical makeup of top dross (Fe_2Al_5 particles being less dense than the melt float to the top of the bath). A great number of such particles have been seen within the simulated samples, and they always appear at precisely the centres of eutectic cells. Therefore it would seem possible that these Fe_2Al_5 particles are acting as nucleation sites for the two phase eutectic.

6.1.6. Corrosion occurring on the casting surfaces

Since similar microstructural changes were occurring in both the castings and the galvanising coatings it was deemed beneficial to contrast changes occurring in the corrosion behaviour. SVET was used to measure the corrosion activity within a $5mm^2$

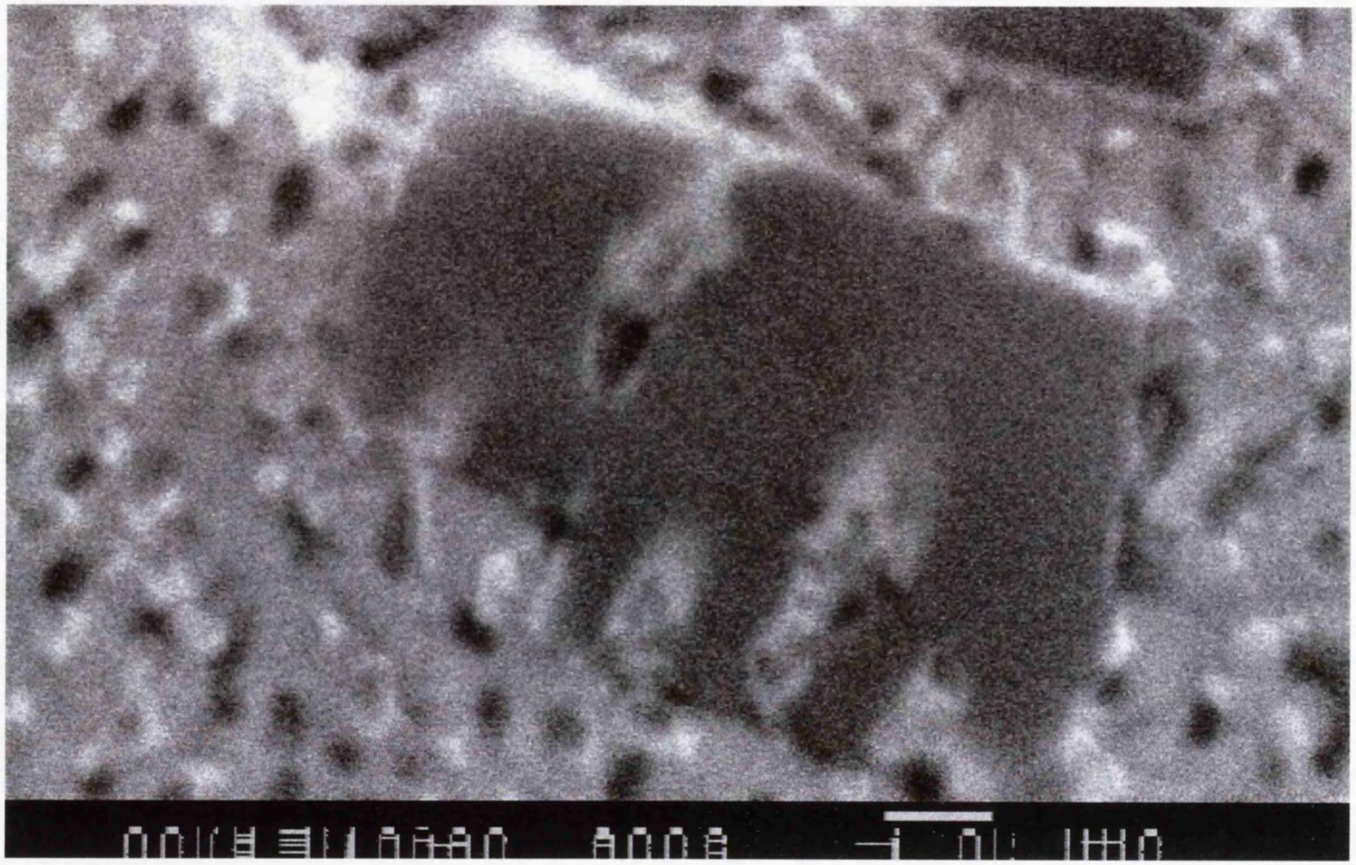

Figure 6.13. Typical Fe_2Al_5 particle in the centre of a eutectic cell

area at the centre and close to the edge of the casting. Figure 6.14 details the mean average zinc losses from three experiments at each relevant region. MGC0 shows the lowest recorded zinc loss at both the edge (210μg) and centre (170μg) of the casting. As the Mg content is increased there is an observed increase in the zinc loss at both the edge (230μg) and centre (250μg) of sample MGC05 and a further increase to 310μg (edge) and 350μg (centre) of sample MGC1. It follows that since the volume percentage of the primary zinc is increasing due to the Mg addition, the zinc loss will also increase as it is this phase on which corrosion is focused. Further evidence of the influence of the primary phase upon corrosion appears when comparing results from the edge and centre. In each case the recorded zinc loss at the edge of the casting is higher than the corresponding figure from the centre. When observing the change in volume percentage (figures 6.4 and 6.5) it is apparent that the volume percentage is greatest, in each circumstance, at the casting edge. Figures 6.15, 6.16 and 6.17 detail the increase in zinc loss as a function of volume percentage of primary zinc at the edge, centre and an overall mean average. Whilst there are only three data points it is difficult to ascertain whether this is a true linear relationship but it does appear that, as in previous chapters, zinc volume percentage controls *tzl.*

6.1.7 Location and intensity of anodic sites

Figures 6.18 and 6.19 detail the SVET current density maps generated whilst scanning the cut edges of samples MGHDS00 - MGHDS05. The plots show representative scans after 0, 12 and 24 hours of immersion in 5% NaCl. The anodic sites (areas of metal dissolution, dark colouration) in each sample set are located proximal to the cathodic activity (areas of oxygen reduction, light coloured regions) indicating that the galvanized coating is sacrificially protecting the base steel substrate. The point

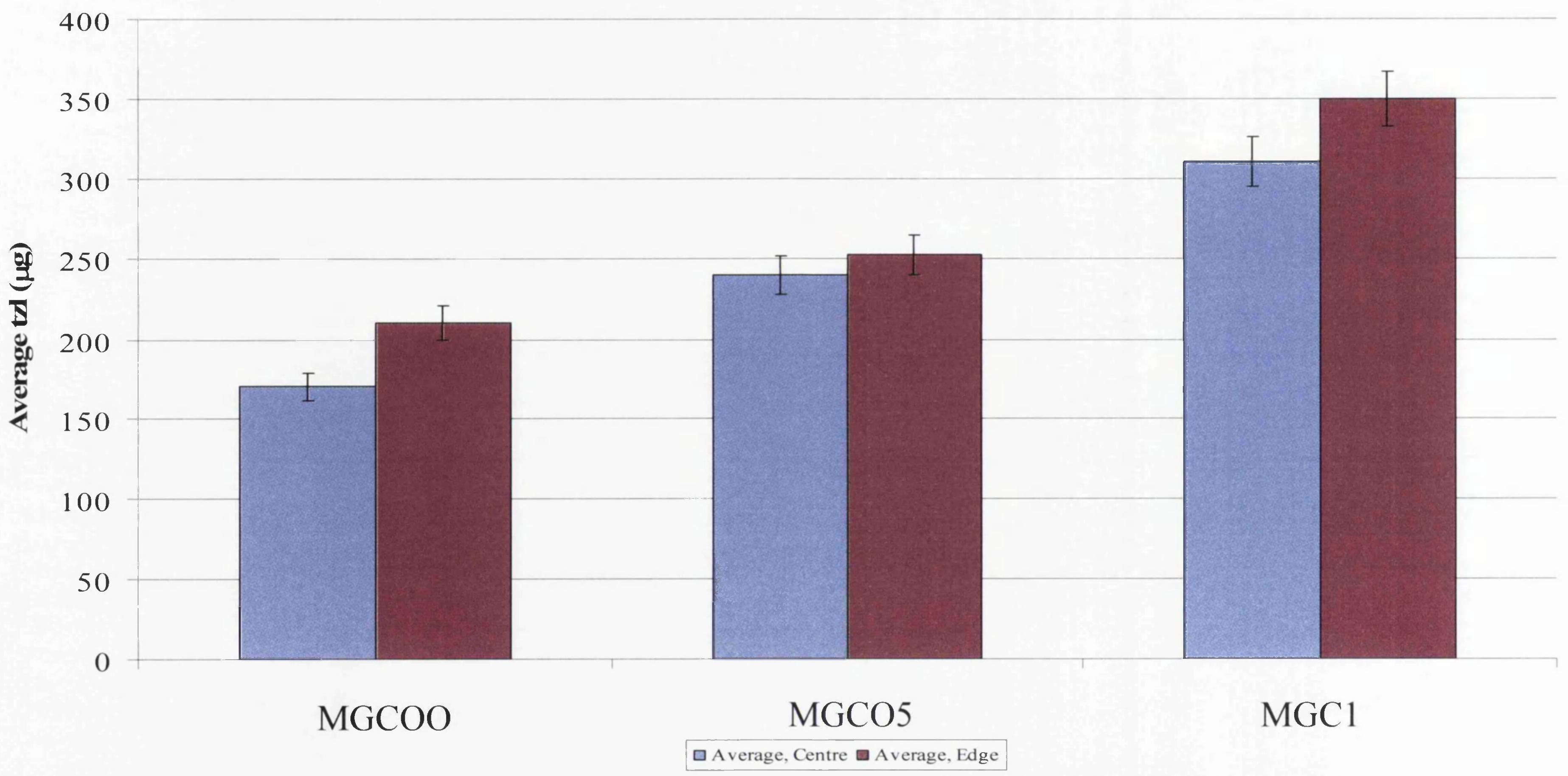

Figure 6.14. Average *tzl* recorded from conical castings

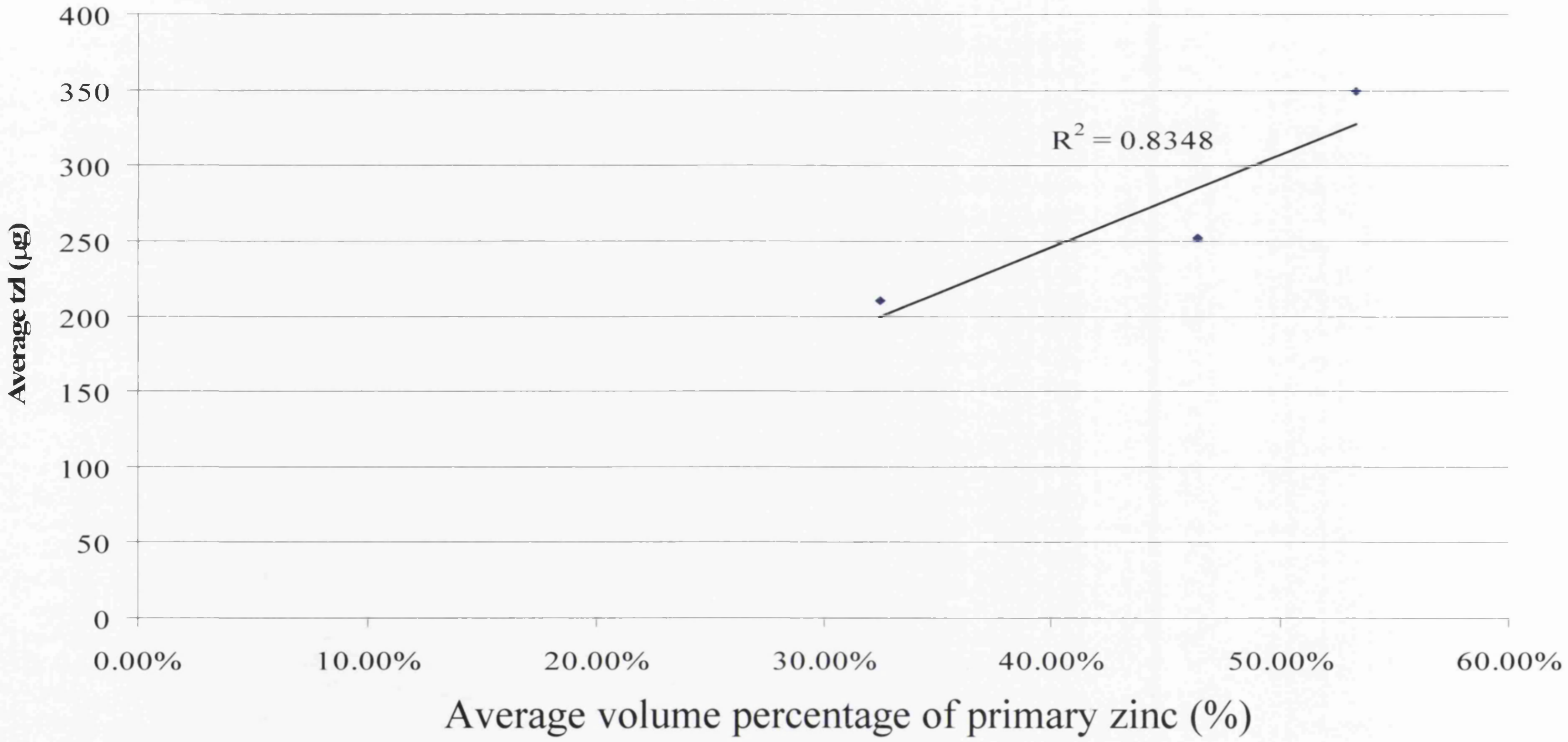

Figure 6.15. Average *tzl* as a function of volume percentage of primary zinc at the casting edge

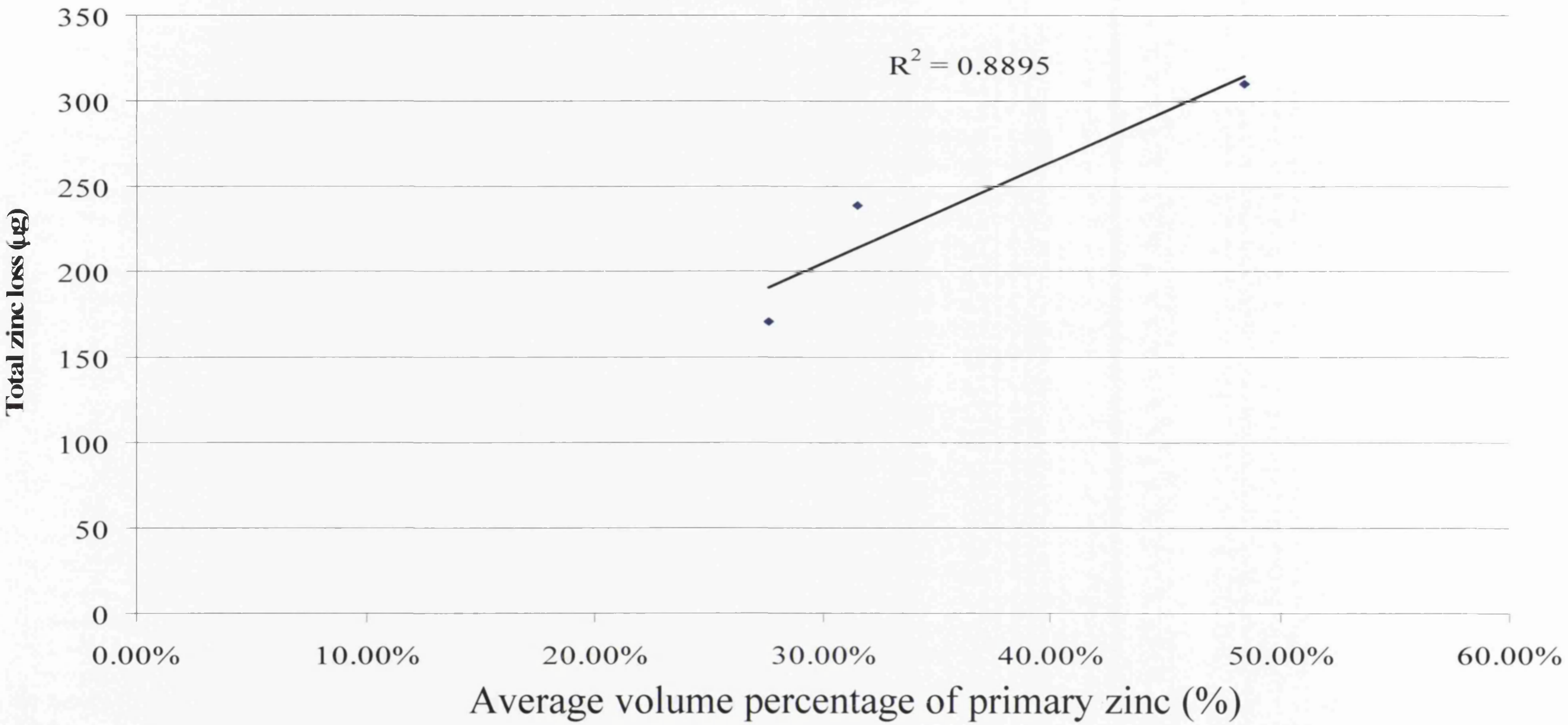

Figure 6.16. Average *tzl* as a function of volume percentage of primary zinc at the casting centre

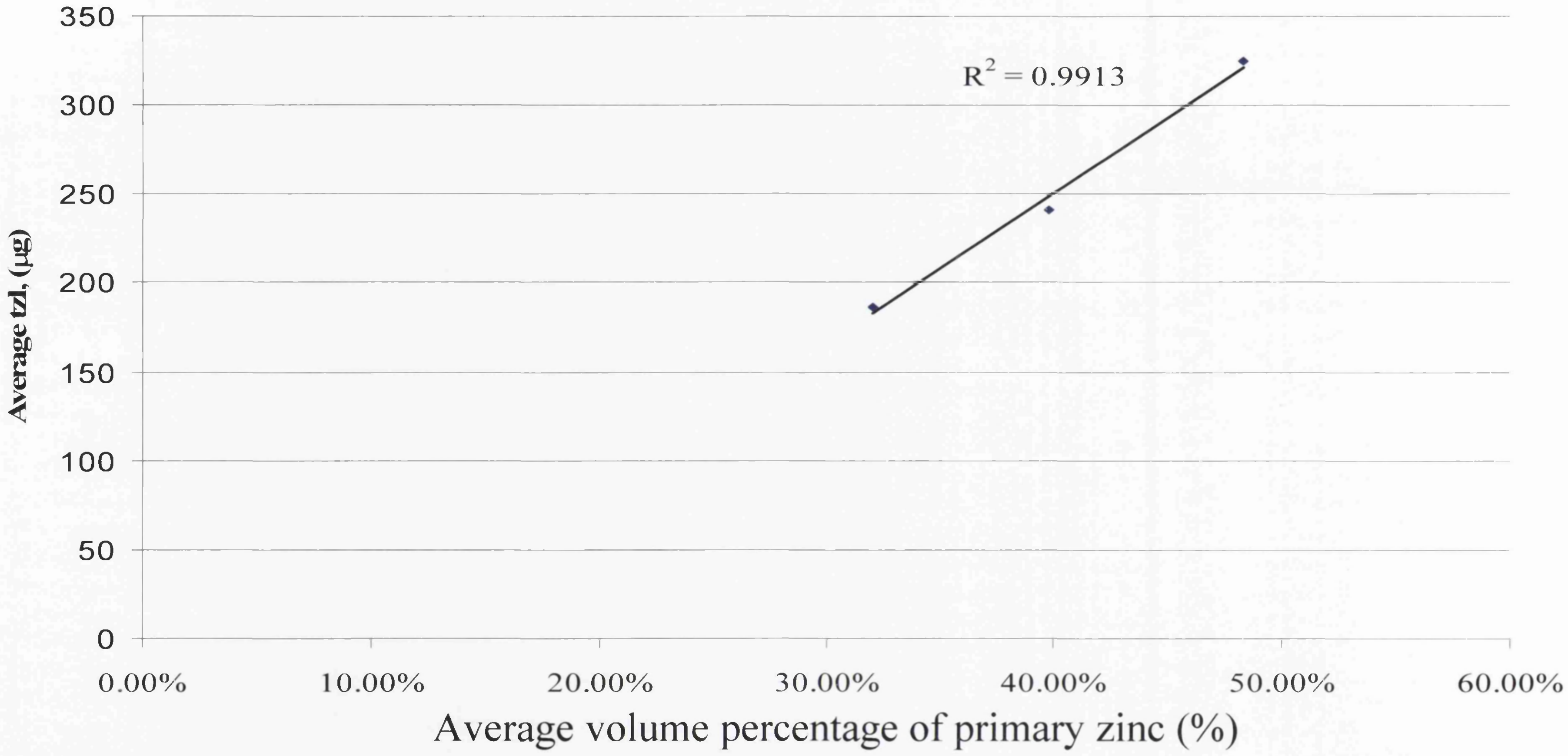

Figure 6.17. Average *tzl* as a function of average volume percentage of primary zinc for the casting

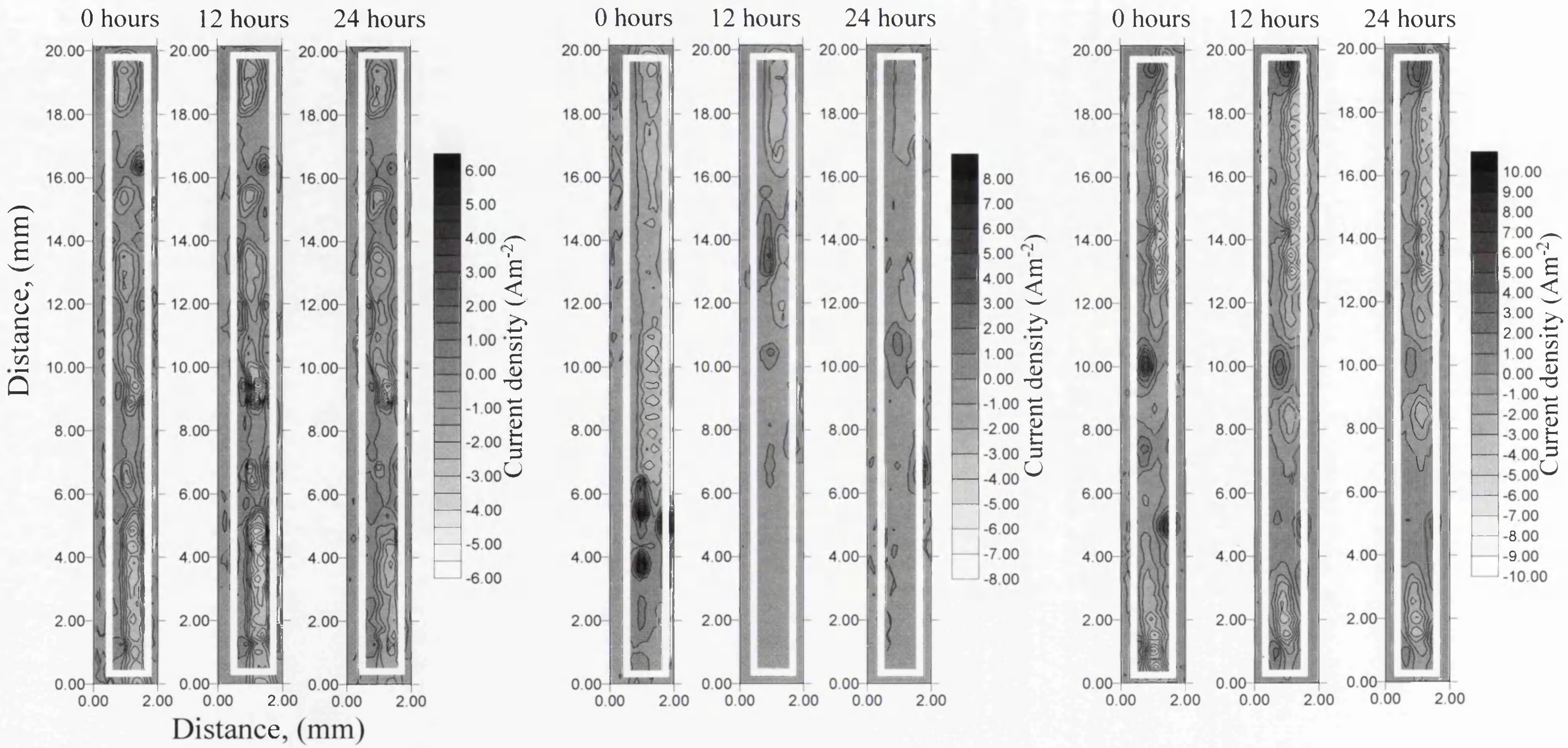

Figure 6.18. Representative SVET current density maps for cut edge samples MGHDS00 (L), MGHDS01(C) and MGHDS02 (r)

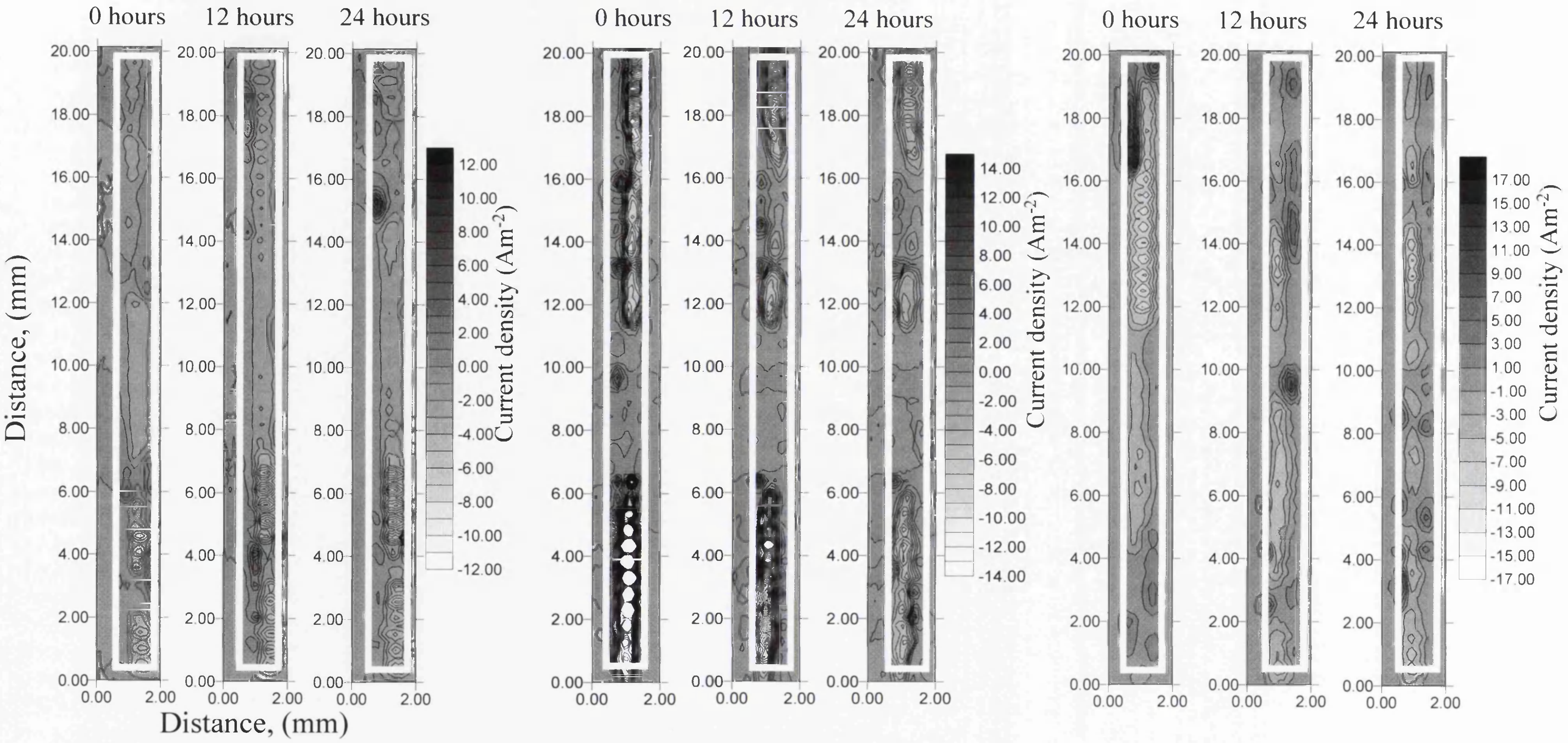

Figure 6.19 Representative SVET current density maps for cut edge samples MGHDS03 (l), MGHDS04 (c) and MGHDS05 (r)

anodes shown in these plots are indicative of the Galfan coating with previous work [2,5,15] showing preferential corrosion occurring upon the primary phase. Fig 6.20 depicts the isolation of the primary phase within the eutectic matrix along the cut edge. When observing such microstructures the point anodes witnessed on the current density maps are not surprising.

The intensity of corrosion is measured via current density (Am^{-2})[16]. Comparisons of the intensity scales of samples MGHDS00 (6 Am^{-2}), MGHDS03 (12 Am^{-2}) and MGHDS05 (17 Am^{-2}) reveals an increase in the corrosion activity upon the latter samples. Therefore, this would indicate that the changes brought about on the microstructure are having a significant effect upon the corrosion occurring.

6.1.8. The influence of Mg additions upon the zinc loss and anode lifetimes

Manipulation of the data provided by SVET (detailed in the section 2.2.2.2.) allows a calculation of the approximate zinc loss over the experimental period. Figure 6.21 shows the mean average from three separate experiments for each sample group. It is clear from these results that the addition of Mg is having a dramatic effect upon the corrosion occurring along the cut edge. The mean average *tzl* for sample MGHDS00 is 80 μg ± 3μg over the 24 hour immersion period. This figure is raised with the subsequent sequential Mg additions with values of 125 μg ± 5μg and 183 μg ± 7μg recorded for samples MGHDS03 and MGHDS05 respectively. The increase in zinc loss is in good agreement with the increase in corrosion activity previously mentioned. In addition this is a similar effect to that observed in the castings.

Figure 6.22 shows the increase in zinc loss as a function of volume percentage of primary zinc. Clearly, it can be seen that the increase in the volume percentage of the primary phase is leading to a subsequent increase in the zinc loss recorded by the

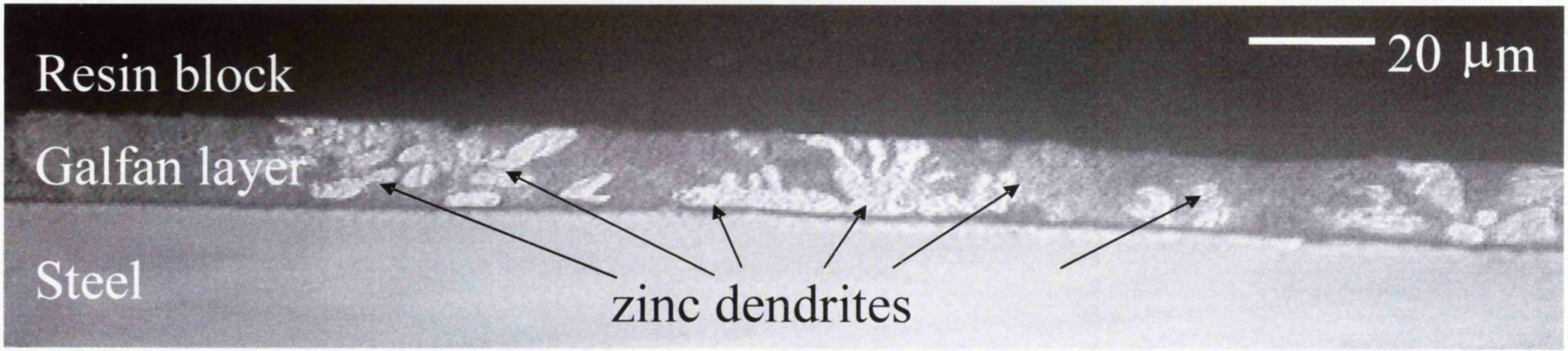

Figure 6.20 Typical galfan cut edge

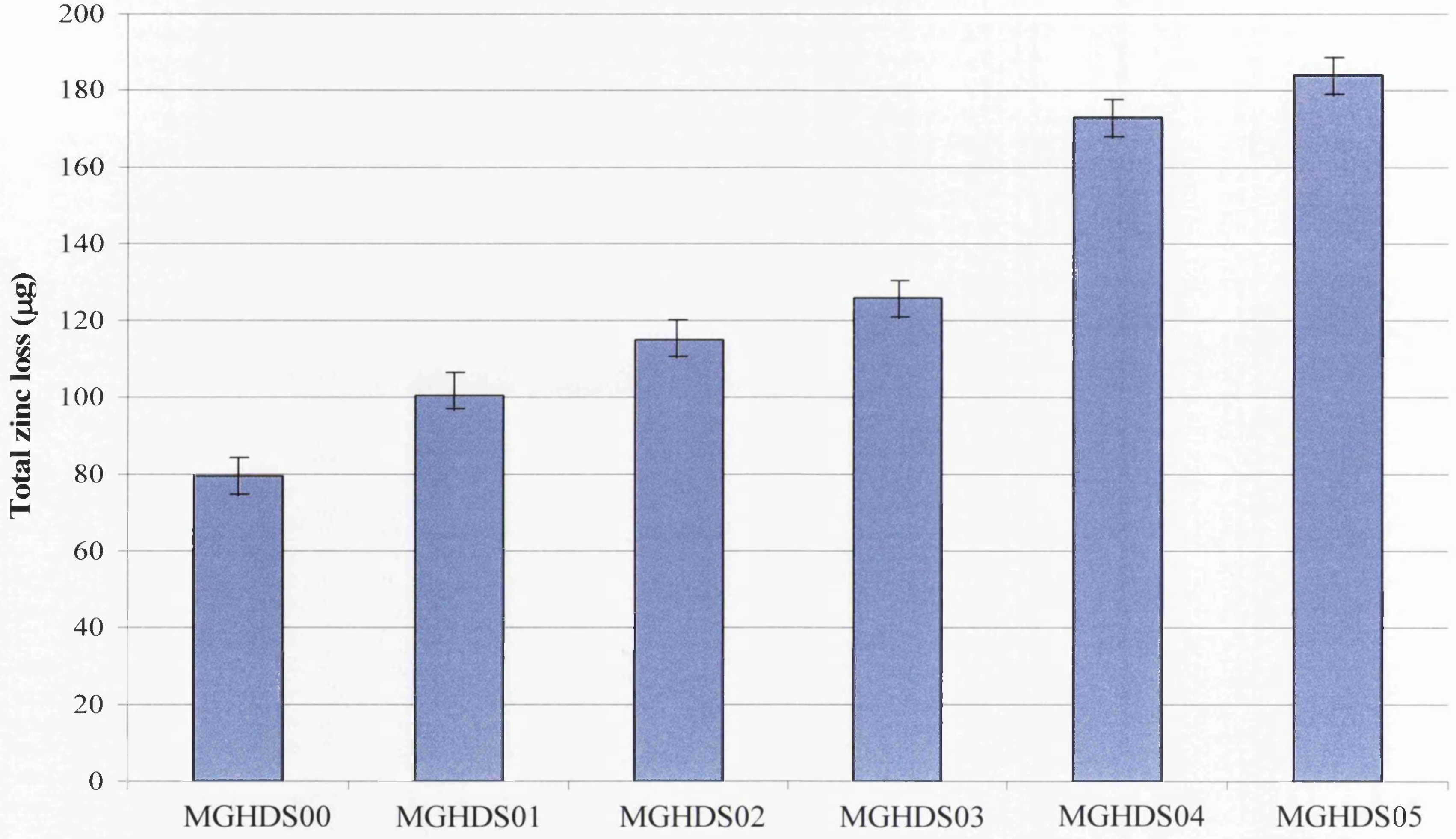

Figure 6.21 Mean average zinc loss along the cut edge over 24hr period

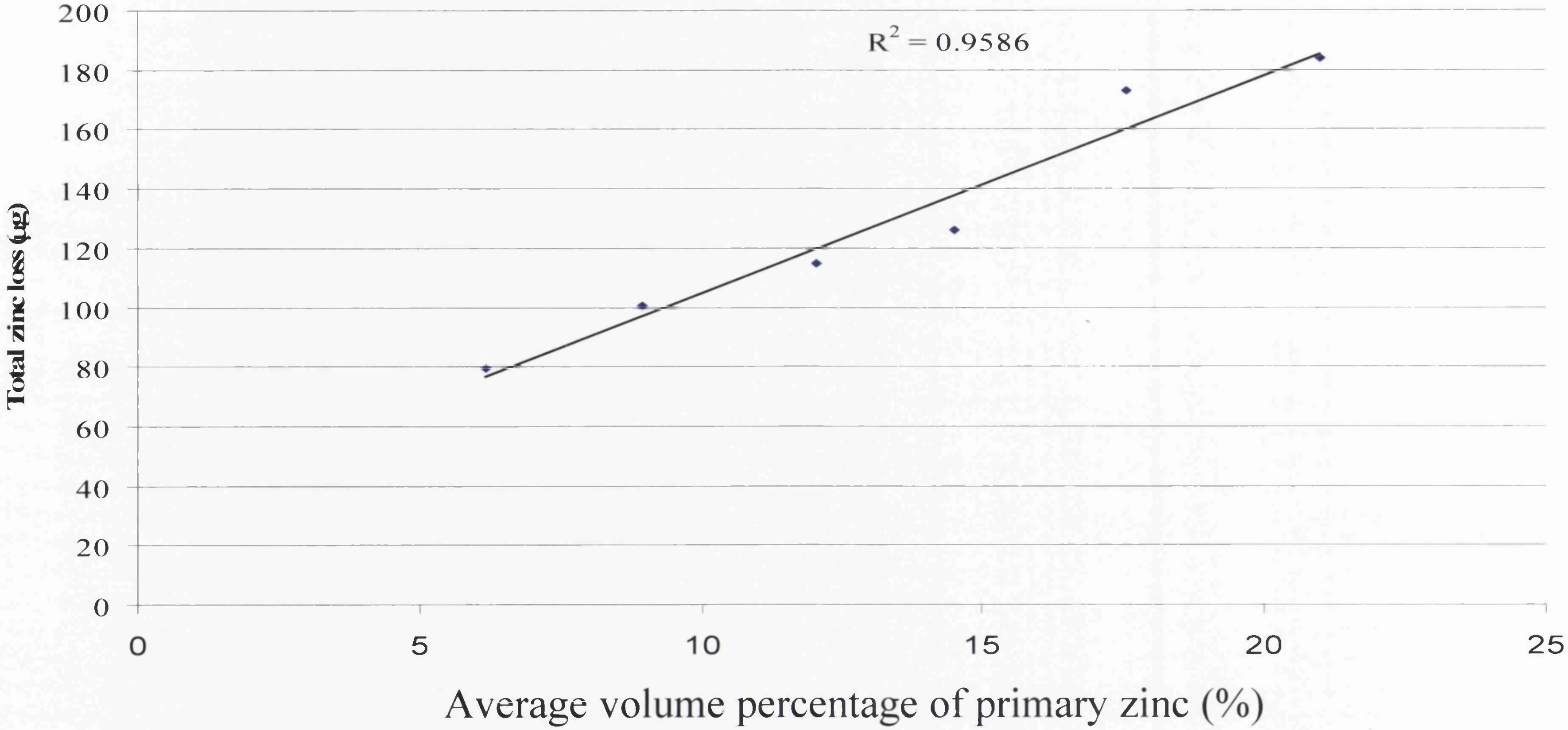

Figure 6.22. Total zinc loss recorded using SVET as a function of volume percentage of primary zinc

SVET. Hence, from this it can again be confirmed that the primary zinc is the preferential phase for initiation of anodic activity.

The hourly zinc loss for the selected individual samples is shown in figure 6.23. Firstly, from this it is obvious that the overall amount of zinc loss is greater as the Mg content is increased. However, this data also shows a reduction in the corrosion activity throughout the period of experimentation as seen in previous chapters. Taking the example of MGHDS00 the initial zinc loss over the first hour is 10 μg. As the experiment continues the zinc loss reduces to 3 μg (at 5 hours) where it stays for the remainder of the experiment. Likewise in samples MGHDS03 and MGHDS05 a similar effect is observed with reductions from 11 μg to 5 μg and 19 μg to 5 μg respectively. This passivation effect has been previously seen with Galfan[17] and is a result of the corrosion of the eutectic phase. The corrosion products formed via corrosion of the Al within the eutectic are insoluble and whilst intense corrosion occurs on the primary phase, the corrosion of the eutectic generates a passive aluminium oxide layer[18]. This layer acts as a barrier to corrosion significantly reducing the activity occurring on the surface.

Figures 6.24 and 6.25 illustrate the number of active anodes (and the associated intensity changes) as a function of immersion time. Immediately evident is the increase in the number of anodes as the Mg content is elevated. In sample MGHDS00 there are 18 active anodes increasing to 27 and 35 in samples MGHDS03 and MGHDS05 respectively. The increase in active anodes has a significant effect upon the corrosion occurring and is brought about due to the increased nucleation of the primary zinc dendrites. Further to the increase in the number of anodes there is an apparent increase in the number of long lifetime anodes in each sample up to MGHDS04. It is these anodes which have the biggest influence on the final calculated

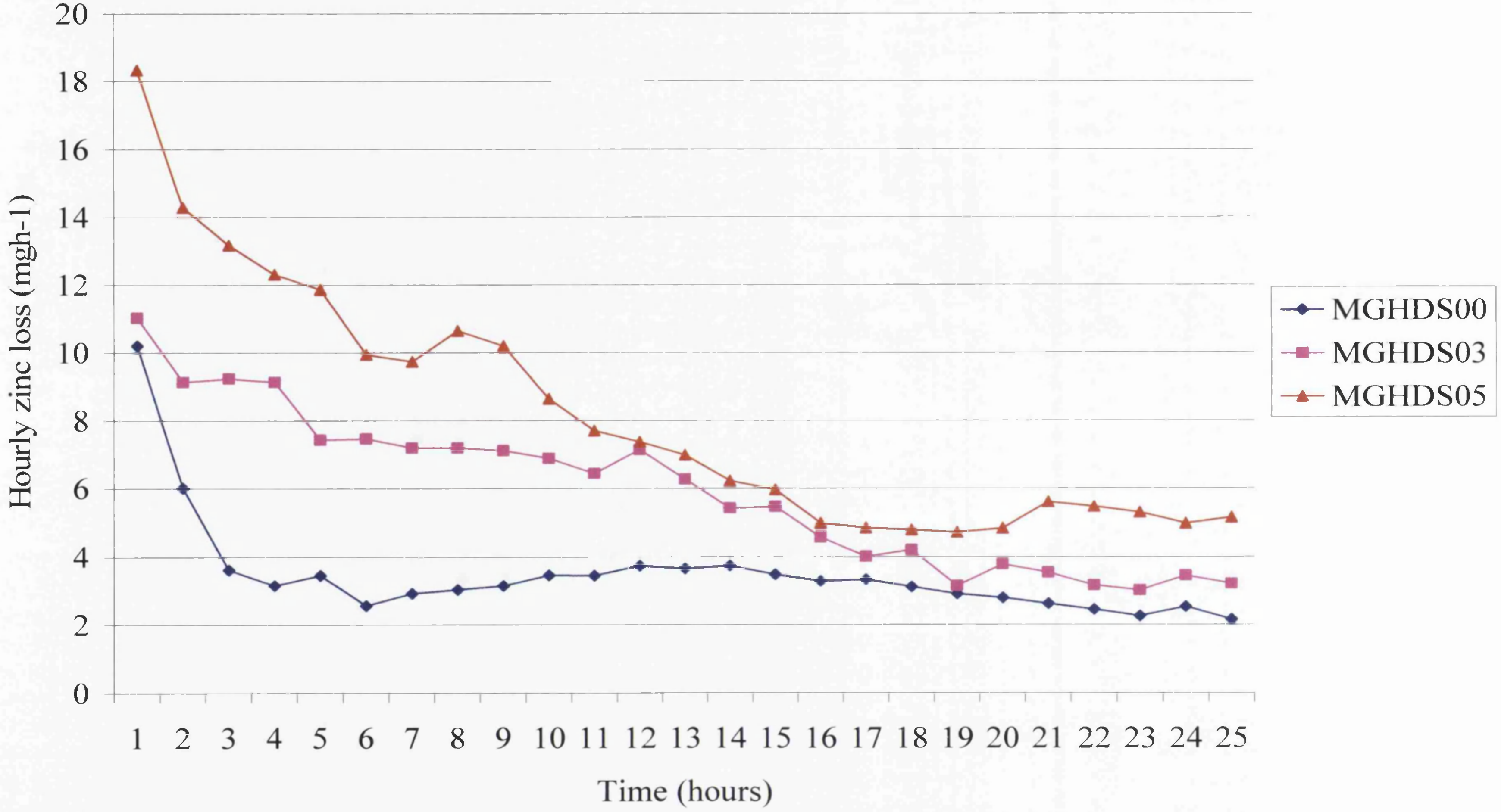

Figure 6.23. Hourly recorded zinc loss as a function of time

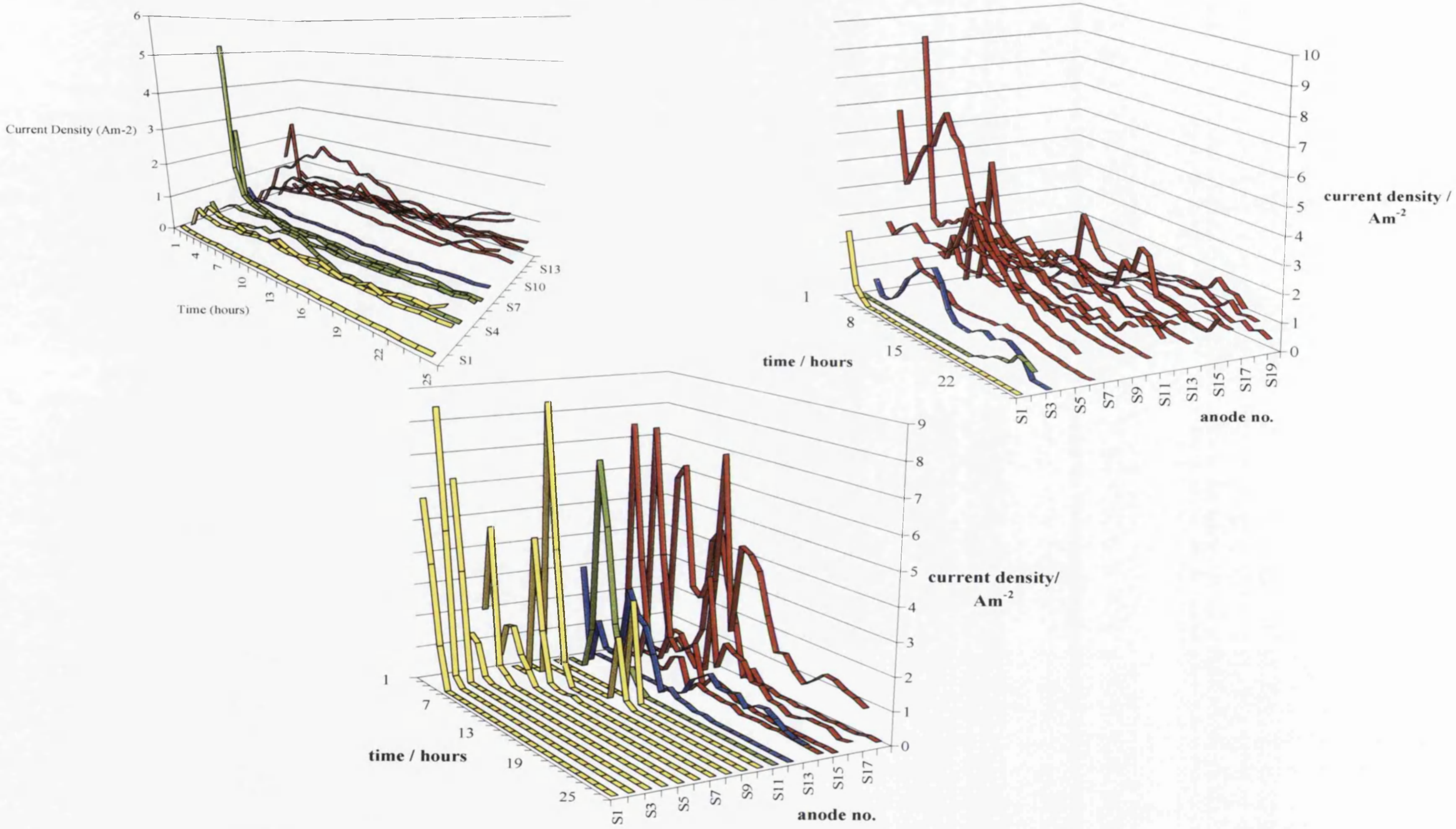

Figure 6.24. Anodic activity as a function of immersion time for samples MGHDS00, MGHDS01 and MGHDS02

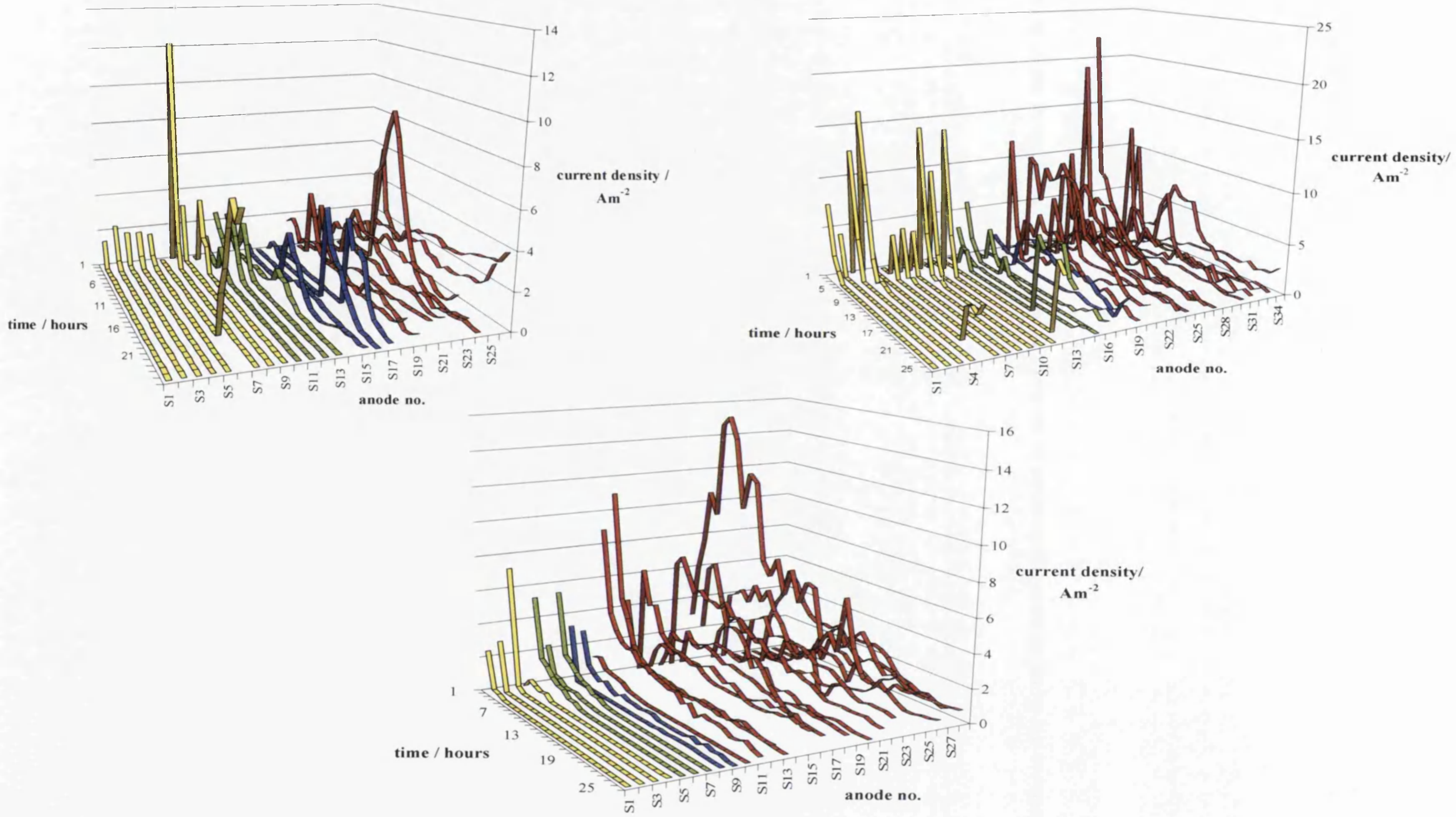

Figure 6.25. Anodic activity as a function of immersion time for samples MGHDS03, MGHDS04 and MGHDS05

zinc loss. The increase in zinc loss from samples MGHDS00 through to MGHDS04 can be ascribed to the increasing number of anodes which are corroding at higher intensities. From figure 6.26 the influence of the long lifetime anodes is seen. This plot summarises the zinc loss from each individual anode. Drawing comparison between the long lifetime anodes it can be seen that 5 anodes from MGHDS00 (anode numbers 13-18, figure 6.26) each contribute 1 – 3 μg to the zinc loss total. MGHDS04 has 17 long life (numbers 11-28, marked red in figure 6.25) anodes active throughout the experiment duration. Each of these anodes contributes between 2-16 μg to the overall total. Consequently, it is obvious that the greater number of more intensely corroding anodes in the latter samples are elevating the corrosion. Comparisons between samples MGHDS04 and MGHDS05 reveal that the number of long lifetime anodes is equivalent. In this circumstance the increase in the zinc loss is a result of two factors. Firstly, in sample MGHDS05 there is a far greater number of short lifetime (0-6 hour) anodes, 12 in total compared to only 4 in MGHDS04. Although short lived, the initial intensity of these anodes of these anodes is very high, initiating at above 15Am^{-2} compared to 8 Am^{-2} in MGHDS04. Consequently the increased number of short lived, high intensity anodes will record a greater tzl than those in sample MGHDS04. Again the contribution of these anodes is verified in figure 6.26 with the 12 short lived anodes contributing significantly more (upwards of 12μg) than the short lived anodes in MGHDS04 (upwards of 2μg). Secondly, although the number of long life anodes is equal, those in MGHDS05 are more persistent and of higher intensity.

It is apparent from these results that the intensity of corrosion is having a significant effect upon the total zinc loss. It would appear that the change in corrosion activity is a direct result of the microstructural changes. From figures 6.18 and 6.19 it

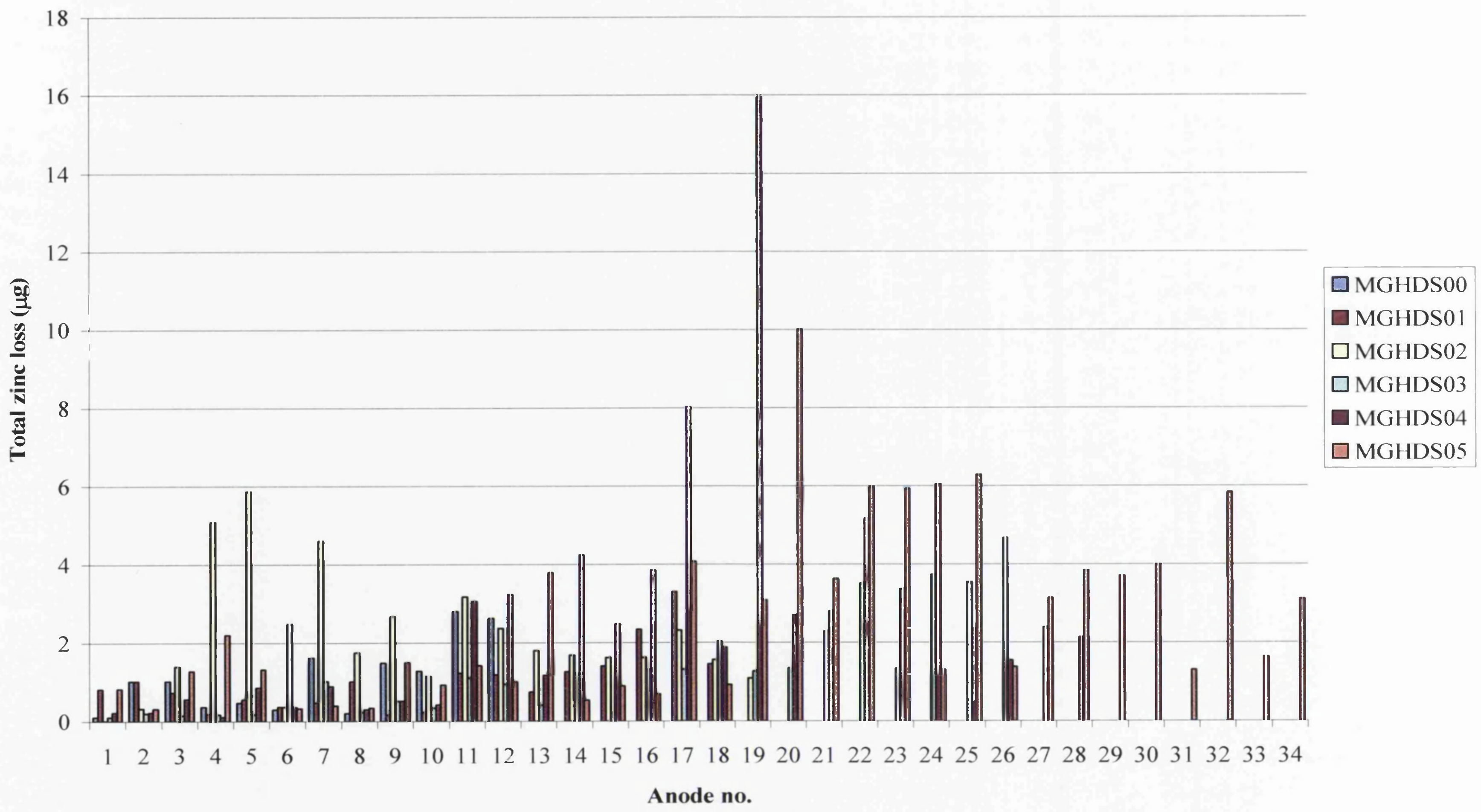

Figure 6.26. Comparison of individual anode zinc losses along the cut edge

is clear that the cathodic activity is situated on the galvanising coating as well as the steel substrate. It is known that Al is a poor cathode due to the readily formed oxide layer. As the cathodic reaction (oxygen reduction) is the rate controlling step[19] it follows that the eutectic phase is probably controlling the corrosion intensity since, as the steel gauge (upon which the majority of cathodic activity is focused) remains constant between samples the cathodic activity should be constant. The increase in the volume percentage of primary zinc is accompanied by a reduction in the volume percentage of the eutectic phase. Hence, it is believed that the reduction volume percentage of the Al containing eutectic phase allows an increase in the corrosion intensity and subsequently an associated increase in zinc loss.

6.1.9 Location and intensity of anodic activity upon the sample surface

Typical, representative current density maps are shown in figures 6.27 and 6.28 for samples MGHDS00 - MGHDS05. The maps were generated for each sample after immersion in aerated 5% NaCl after 0, 12 and 24 hours and show significant changes in the corrosion behaviour. As before, the anodic activity is shown in dark colours and the cathodic activity in light colours. The first notable feature of these plots is the change in corrosion activity exhibited. What is clear is that a slight reduction in corrosion activity occurs between samples MGHDS00- MGHDS03. This reduction in activity is also accompanied by a decrease in the number of anodic sites observed over the experimental period. The reduction in activity is consistent with previous work [18,20] and can be possibly attributed to the formation of the Galfan surface oxide layer. The oxide layer formed on the surface is enriched with Mg and Al and is significantly thicker at higher levels of Mg addition [20] . Hence this layer is more difficult to penetrate, creating a barrier upon the surface and reducing corrosion

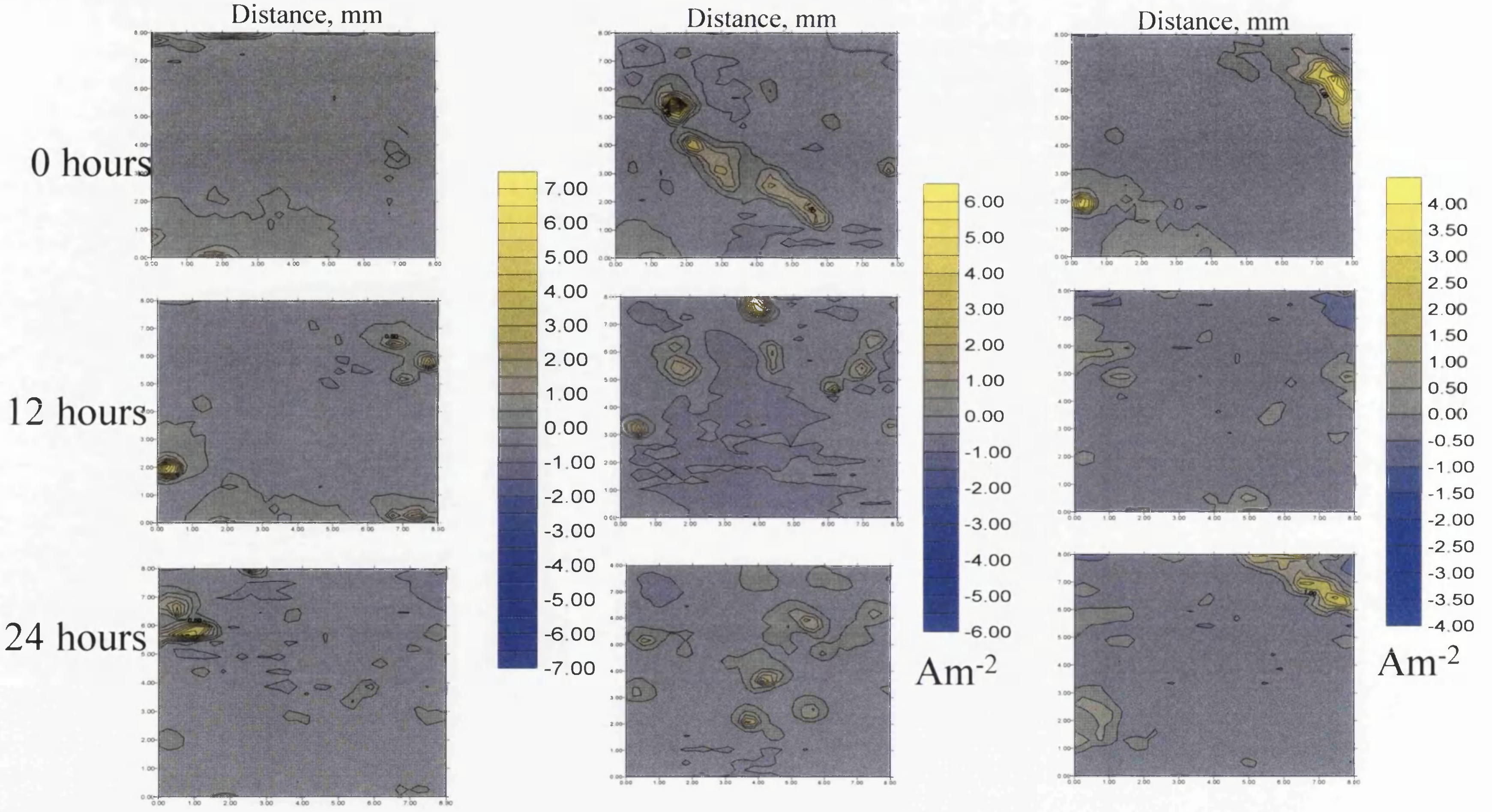

Figure 6.27. Representative iso – current cut edge maps for samples MGHDS00, MGHDS01 and MGHDS02

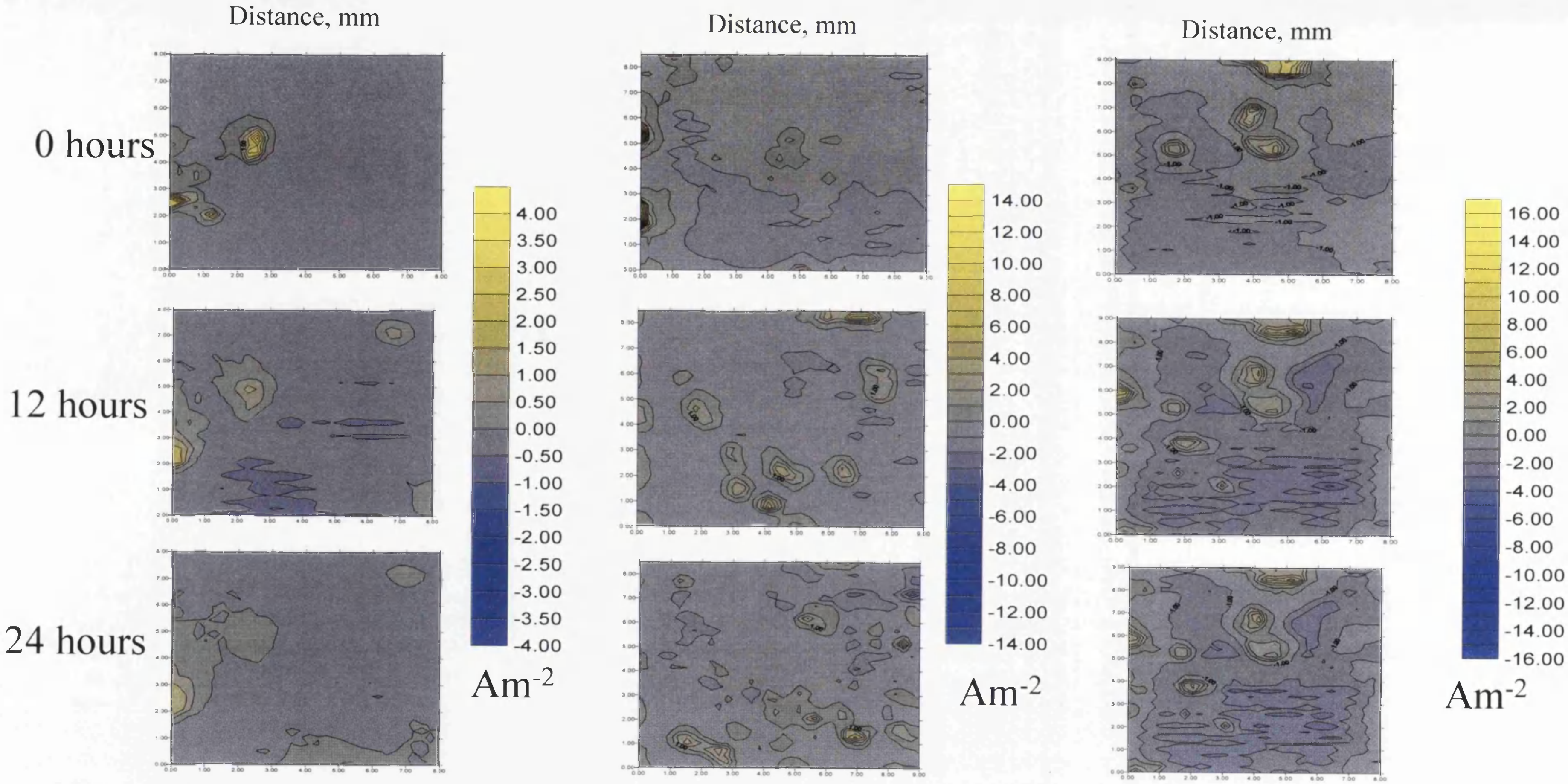

Figure 6.28. Representative iso – current cut edge maps for samples MGHDS03, MGHDS04 and MGHDS05

activity. Through samples MGHDS04 and MGHDS05 the intensity of the corrosion raises dramatically from 4 Am^{-2} (MGHDS03) to 18Am^{-2}. Distinctly in this circumstance a second mechanism is driving the corrosive activity. When the samples are exposed to electrolyte it is clear that the anodic activity is located within isolated regions.

6.1.10 Influence of Mg additions upon the anode lifetimes and associated zinc loss

As previously shown it is possible to estimate zinc losses occurring during corrosion. Figure 6.29 details the mean average zinc loss form three individual experiments for each sample group. In agreement with the changes in current density, a reduction in zinc loss is shown from MGHDS00 (138 μg) to MGHDS03 (82μg). It is likely that the reasoning for this change is twofold. Firstly the formation of the oxide layer is reported[20] to be thicker upon the samples with higher Mg contents reducing the likelihood of anodic activation. Secondly, it has also been shown that Mg increases the fluidity[12] of the Galfan spelter leading to a reduction in the solidification shrinkage and less chance of crack formation. Evidence backing this theory is detailed in figures 6.30 and 6.31. Each plot details the number of active anodes as a function of immersion time and intensity of corrosion. Figures 6.30 (a,b and c) and 6.31 d show these results for samples MGHDS00- MGHDS03 respectively. What is clear is that as the Mg content is increased the number of active anodes is decreased. Upon sample MGHDS01 there is great deal of initial activity, and a large number of short lived anodes. Comparing this with MGHDS02 and MGHDS03 it is clear that the initial activity is reduced and there are far fewer short lived anodes. This would seem to show that the number of initiation sites for corrosion is being reduced due to a combination of the above reasoning.

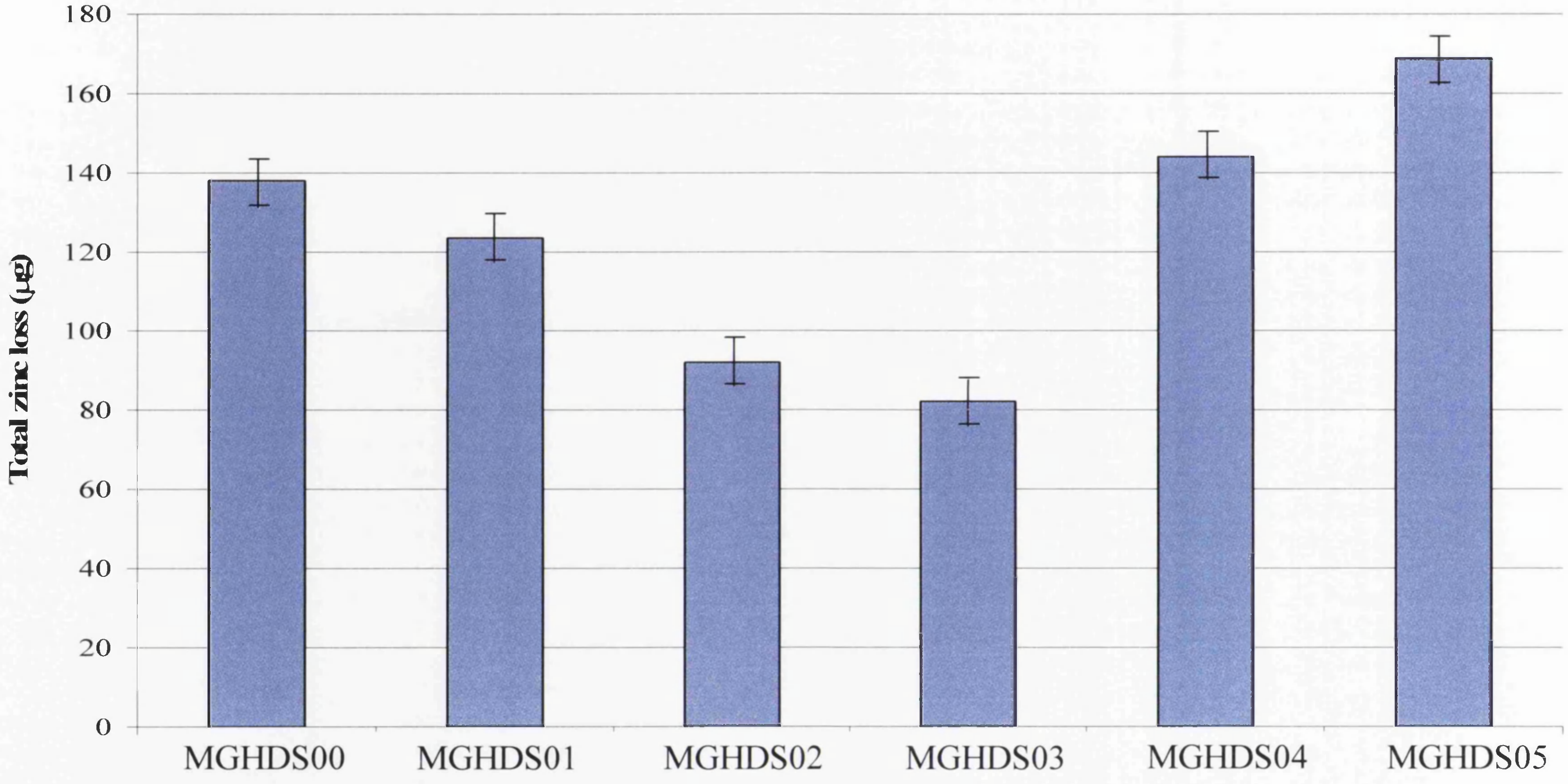

Figure 6.29. Mean average zinc loss recorded across galfan surface

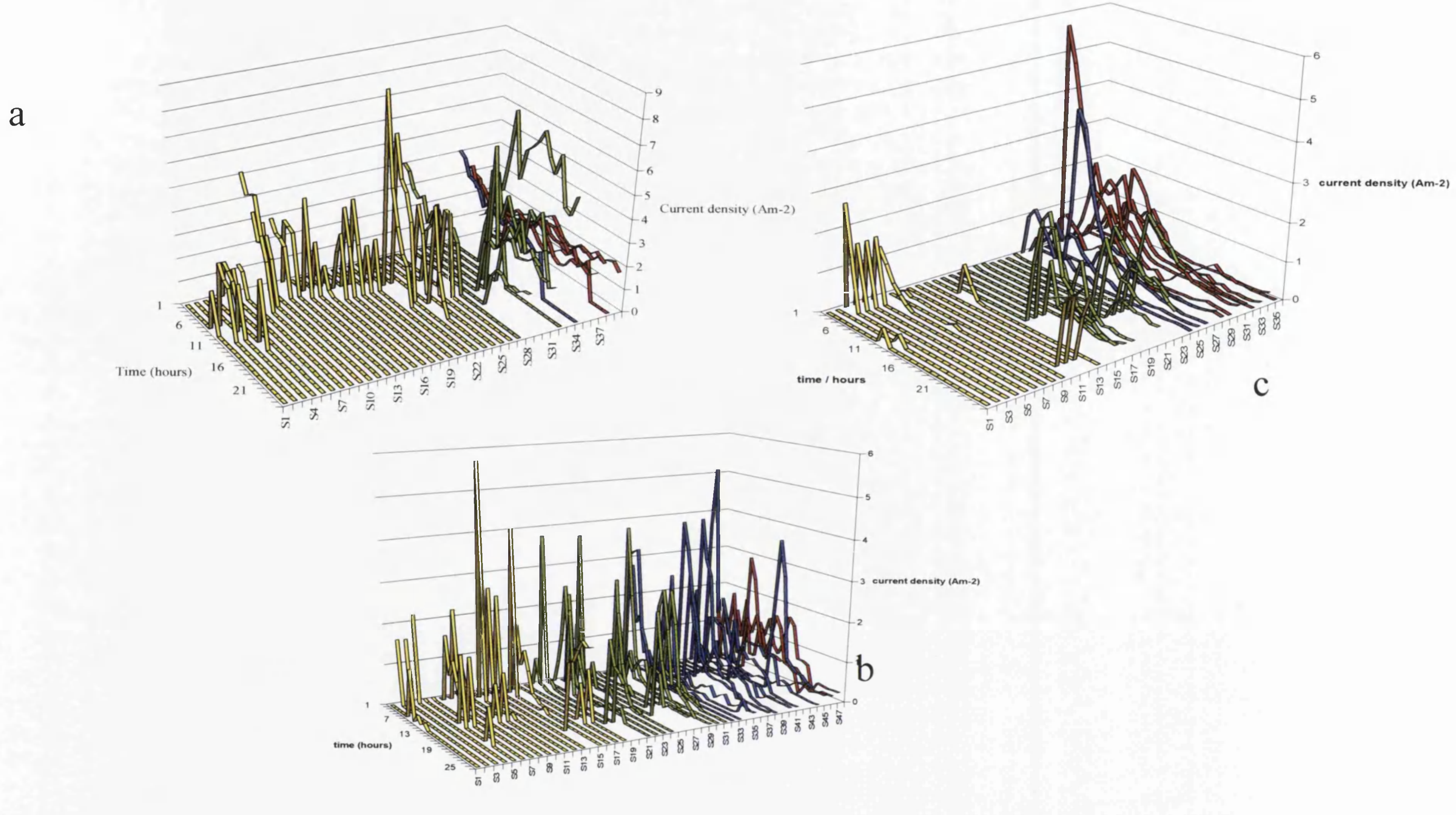

Figure 6.30. Anodic activity as a function of immersion time for samples a MGHDS00, b MGHDS01 and c MGHDS02

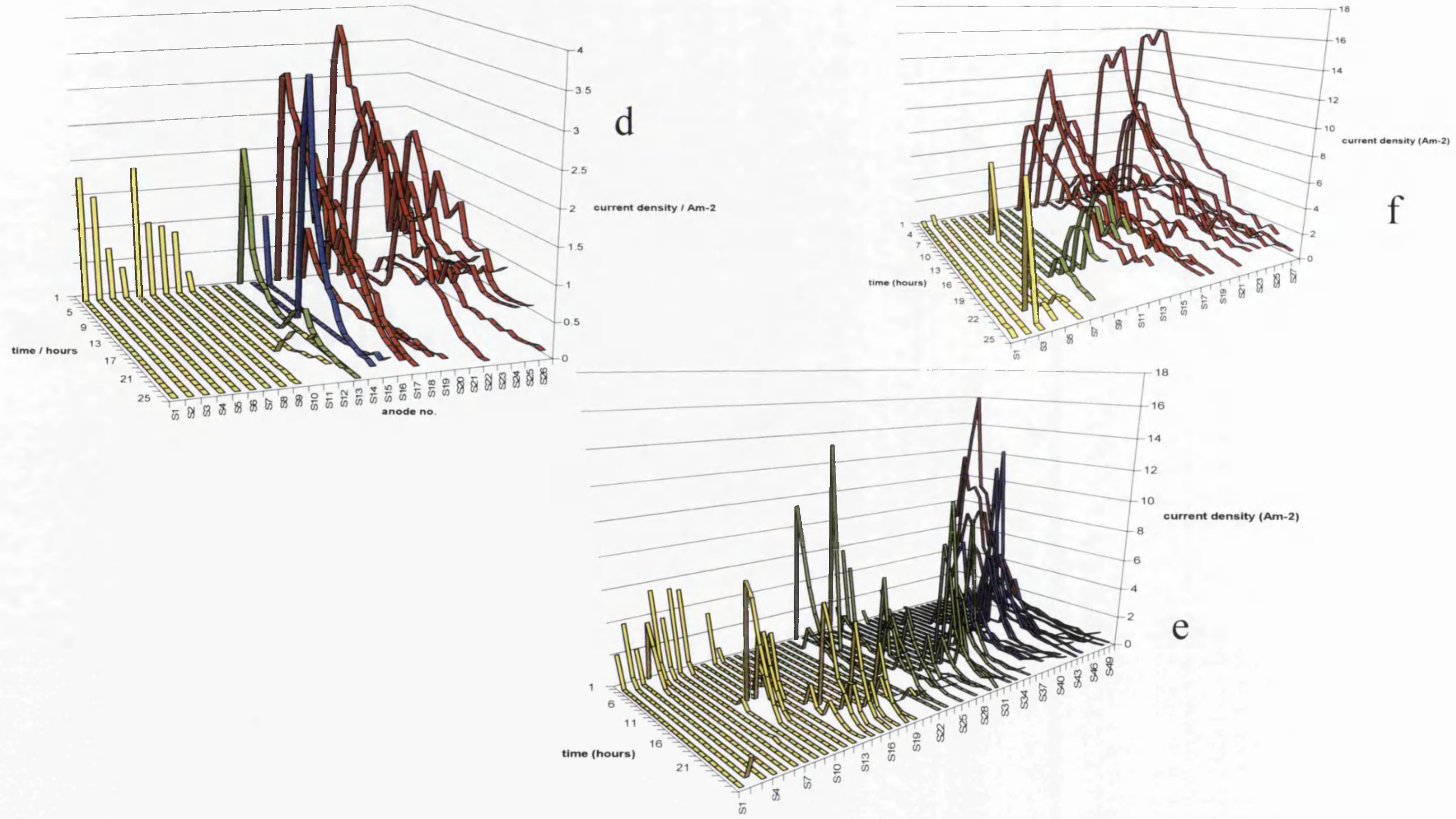

Figure 6.31. Anodic activity as a function of immersion time for samples d MGHDS03, e MGHDS04 and f MGHDS05

Interestingly a change in corrosion behaviour is seen beyond sample MGHDS03. An increase in zinc loss is recorded for MGHDS04 (142μg) and MGHDS05 (160μg). Indeed figure 6.31 (e and f) shows that the corrosion intensity has risen from $4Am^{-2}$ in sample MGHDS03 to $18Am^{-2}$ in both cases. It is believed that this is a result of a competition between the Mg content in the surface of the coating and an increase in the thickness of the oxide layer. At the lower levels of Mg content the increase in the thickness of the oxide layer reduces the cathodic driving force, consequently reducing the amount of zinc loss recorded. As the Mg content is increased (samples MGHDS04 and MGHDS05) the increasing volume percentage of primary zinc starts to dominate leading to higher corrosion rates and consequently the higher zinc losses recorded.

6.2. Conclusions

The data presented here has shown that the addition of Mg to a hyper-eutectic (<5% Al) Zn- Al binary alloy will have a dramatic effect on both the microstructure and the corrosion resistance.

The addition of Mg is believed to depress the eutectic temperature. As a result of this the volume percentage of the primary zinc solid solution is increased from 8% in MGHDS00 to 21% in MGHDS05. Likewise, in the castings the volume percentage is increased from 32% in MGC00 to 48% in MGC1.

Along with the increase in the primary phase there is also an increase in the number of primary dendrites per mm^2. Again this observation is present in both the castings and the galvanised samples. It is believed that this increase is a result of either the formation of MgO particles which subsequently act as nucleation centres or through an increase in undercooling (due to undercooling to at the depressed eutectic temperatures) promoting nucleation.

The final microstructural changes induced via the addition of mg show a change in the eutectic microstructure. The addition causes a refinement in the inter lamellar spacing from 7µm in MGHDS00 to 4µm in MGHDS02. The change is also present in the rod eutectics with a reduction from 6.7µm in MGHDS01 to 5.1µm in MGHDS05. Coupled with this change, is a transformation in the eutectic morphology from lamellar to rod. It is believed that this change is brought about by either the refinement of the eutectic structure or by the Mg reducing the surface tension of the growing phase.

The appearance of Fe_2Al_5 at the centre of eutectic cells leads to the conclusion that these particles can nucleate the eutectic cells.

In both the coatings and the castings the increase in the volume percentage of primary phase increases the corrosion rates.

Along the cut edge of the galvanised samples an increase in the corrosion is observed due to a greater number of high intensity anodes at the higher Mg contents. The increase in intensity of corrosion is believed to be a result of the reduction in volume percentage of the Al containing eutectic.

Analysis of the corrosion occurring on the surface of the samples has revealed two trends. Initially the Mg additions serve to reduce the corrosive attack through the formation of an increasingly thick oxide passive layer reducing cathodic activity. At higher Mg contents a second corrosive mechanism dominates. This is bought about by the increase in volume percentage of the primary phase. The changes induced in the microstructure (i.e. reduction in eutectic) lead to elevated corrosion rates which are more dominant that the effects of the forming oxide layer.

In summary it seems that the ternary alloy addition affects microstructure and corrosion. In the case of products for over-coating with paint, Mg additions are unsuitable since they always lead to elevated cut edge corrosion

6.3 References

---

[1] J.A. Spittle: Private communication

[2] J. Elvins, J.A. Spittle and D.A. Worsley, Corrosion Engineering, Science and Technology,38, 197,(2003)

[3] F. Hinterberger, W. Maschek and J. Faderl, Zinc Based Steel Coating Systems: Production and Performance, 281, (1998)

[4] Y. Tajiri et al: Proceedings of the International Conference on Zinc and Zinc Alloy Coated Steel Sheet GALVATECH '89, 553, (1989)

[5] D A Worsley and M Challis, British Corrosion Journal, 36, 297, (2001)

[6] K. Masuhara and F. Kumon, Proceedings of the International Conference on Zinc and Zinc Alloy Coated Steel Sheet GALVATECH '89 596, (1989)

[7] R.T. Elliot, Eutectic solidification processing, Butterworths monographs in materials, 153, 1983

[8] B.M. Thall and B. Chalmers, J. Inst. Metals, 77, 79,(1950)

[9] R.W. Smith, Solidifcation of metals, (1968)

[10] A. Knuutinen, J. Light Metals 1, 229, (2001)

[11] P.B. Crosley and L.F. Mondolfo, Mod. Castings, 49, 53,(1966)

[12] A.M. Korol'kov, Casting properties of metals and alloys, New York, Consultants Bureau,(1963)

[13] A.R. Marder, Zinc based steel coating systems: Metallurgy and Performance, 1990, Warendale

[14] N. Jestin, Thesis (Eng.D.) - University of Wales Swansea, 2003.

[15] Y. Uchiyama et al, Proceedings of the International Conference on Zinc and Zinc Alloy Coated Steel Sheet GALVATECH '89, Tokyo, Japan, p545, 1989

[16] K. Tretheway & J.Chamberlain, Corrosion for science and engineering, Harlow, Essex : Longman, 1995.

[17] Galfan technical resource manual, ILZRO

---

[18] F. Goodwin, Zinc-Based Steel Coating Systems: Production and Performance,(ED F.E. Goodwin, M. DuBois, and J-S. Kim, p.183, 1998

[19] H.N. McMurray, G. Parry and B.D. Jeffs, Ironmaking and Steelmaking,25, 210 (1998)

[20] V. Stevenson. Corus report. WL/SMP/R/DO6/4/99/D

Chapter 7

Conclusions and future Work

7.0 Conclusions and future work

From the work presented within this thesis a number of conclusions have been drawn.

Firstly it is clear that the microstructure of the Galfan coating controls the corrosion performance. Predominantly, along the cut edge, the recorded zinc loss from SVET, is related to the volume percentage of primary zinc within the coating. i.e. reducing the volume percentage of primary zinc within the coating will reduce both the recorded zinc loss and also the rate of the anodic reaction and hence improve cut edge corrosion performance. These values of zinc loss, may also provide an indication of the potential levels of zinc runoff when the coating is exposed to natural weathering (in high Cl concentration environments).

In circumstances when the volume percentage of primary zinc is constant between samples, having a greater number of smaller dendrites will provide greater corrosion resistance than fewer, larger dendrites. Evidence for this is provide when increasing the power of the cooling rig during production. Conversely, the increased nucleation created by the cooling rig is detrimental to corrosion performance across the surface due to the creation of an increased length of depressed eutectic boundary in which the corrosive activity is focused.

The addition of Mg to the Zn-Al alloy induces microstructural changes which lead to an increase in the volume percentage of primary zinc. Consequently, the sequential addition of low levels of Mg, will lead to a sequential increase in the zinc loss recorded by SVET. Initially the increase in Mg (up to 0.03wt%) is beneficial to the surface corrosion characteristics with the formation of a thick oxide layer reducing the corrosive activity observed. Above these Mg levels the change in the volume percentage of primary zinc provides a mechanism which is more dominant than the oxide film and the corrosive activity increases.

Reducing the Galfan coating weight will lead to worsened corrosion performance on both the cut edge and at the surface. The elevated corrosion at the cut edge is due to a relative increase in the volume percentage of primary zinc coupled with a decrease in the eutectic. Since it appears that the eutectic is limiting the corrosion reaction, the reduced amounts lead higher corrosion rates and subsequently greater zinc loss. On the Galfan surface the wiping action of the gas knives exposes primary zinc. As the coating weight is reduced, greater amounts of zinc are exposed which consequently elevate the corrosion occurring.

Listed below are issues raised by this project that may deem further investigation:

Processing issues:

- Chapter 3 details the zinc runoff from Galfan samples currently over 10 years old. To catalogue improvements that have been made in coating over this time period (or not), a series of experiments (similar to those in chapter 3) to categorise modern Galfan coatings would be beneficial. This work will also highlight any issues regarding the contamination of water sources from such coatings.
- Studies in chapter 4 revealed that the cut edge corrosion performance was improved by reducing the dendrite size as a direct result of increased nucleation. In this circumstance the increased nucleation was provided by the increasing the power of the cooling rig, however it is possible that increased nucleation can be provided by grain refiners. Hence studies into the addition of

grain refiners may provide a cost effective alternative to the use of the cooling rig.

- In chapter 5 it was concluded that reducing the coating weight is detrimental to both cut edge and surface corrosion resistance. This work could be extended by increasing the coating weight of the samples to elucidate any changes in the microstructure that may lead to improved corrosion performance.

Coating composition

- Mg is shown to have a significant effect upon the Galfan microstructure in chapter 6. Investigations into other alloying elements would be beneficial to determine if any can significantly improve the corrosion resistance of such coatings.
- In the majority of corrosion studies the influence of the volume percentage of primary zinc on corrosion resistance is shown. It would be interesting to increase the Al content of the coating close to the eutectic point to measure the corrosion resistance of coating containing a limited amount of the primary phase.

Further corrosion studies:

- In all corrosion studies undertaken, the effect of reducing volume percentage of primary zinc led to reduced corrosion rates. Hence studies using the rotating disc electrode to monitor oxygen reduction rates as a function of volume percentage of primary zinc would be useful to elucidate the mechanism occurring. Further to this the effect of reduction in inter-lamellar spacing should also be investigated.

Some initial work has been undertaken on the variation of Al concentration. The initial results are shown below.

7.1 Introduction

It has been shown throughout this body of work that the volume percentage of primary zinc in the Galfan coating is the preferential corrosive phase and with lower volume percentages there is less zinc *tzl.* Logically, one may assume that the removal of this phase will possibly improve the corrosion resistance of the Galfan coating.

Using the Rhesca hot dip simulator two sets of samples have been produced, both having higher Al contents than the other samples within this body of work. The compositions of these coatings are shown in figure 7.1.

Due to wetting problems during production the thickness of the coating has been limited to 8μm to ensure a continuous coating that can be analysed.

7.2 Coating microstructure

The microstructure of the sample Al4.7 displays a typical microstructure of primary zinc dendrites within the eutectic matrix. As the Al content is increased to ~8.6% the microstructure is changed as shown in figure 7.2 a & b. In this figure it can be seen that the microstructure is now of primary Al solid solution dendrites with a halo of Zn solid solution. Growth of the primary Al phase is occurring through both

Sample	Wt % Al	Wt% Zn
Al4.7	4.7	95.3
Al8.6	8.6	91.4

Figure 7.1 – The composition of the Al variation samples

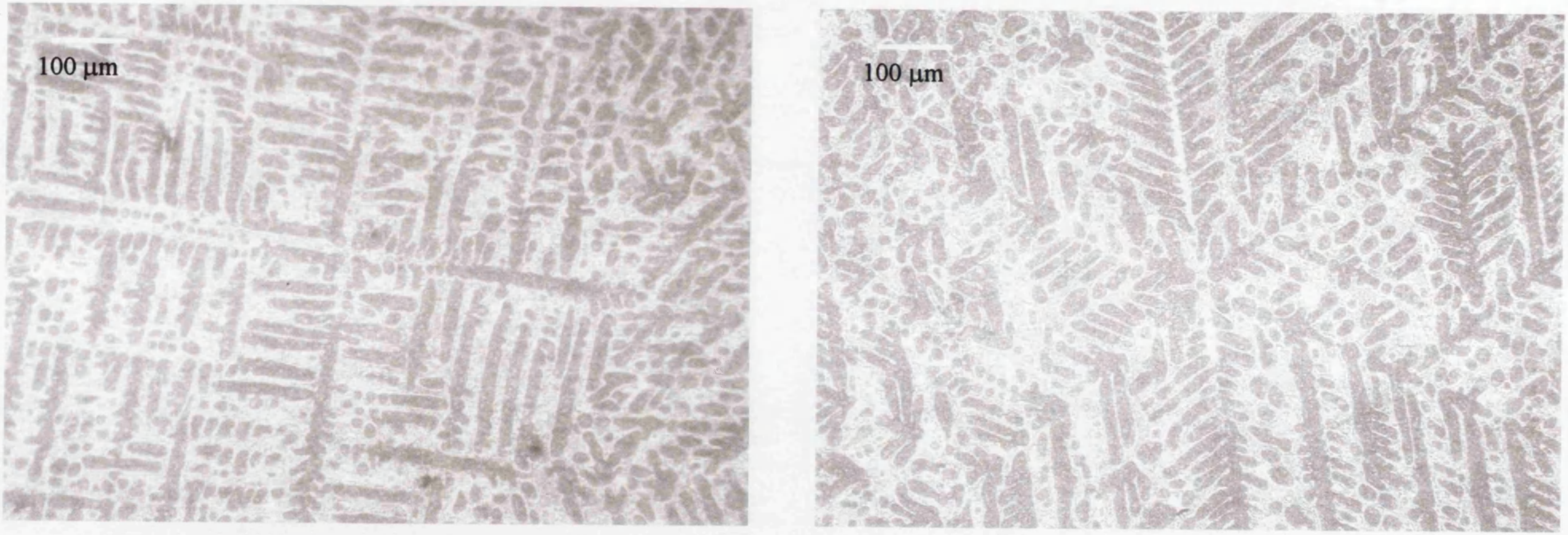

Figure 7.2 – Images of sample Al8.6 close to the steel/ coating interface

the $\langle 1\bar{1}0\rangle$ direction (figure 7.2.a) and the $\langle 11\bar{2}0\rangle$ direction (figure 7.2.b). The eutectic is of rod morphology.

7.3Initial corrosion results

Using the scanning vibrating electrode technique initial corrosion analysis has been investigated along the cut edges of the samples. Figure 7.3 details the SVET current density maps generated whilst scanning the cut edges of the two samples. The plots show representative scans after 0, 12 and 24 hours of immersion in 5% NaCl. The anodic sites (areas of metal dissolution, dark colouration) in each sample set are located proximal to the cathodic activity (areas of oxygen reduction, light coloured regions) indicating that the galvanized coating is sacrificially protecting the base steel substrate.

The mean average total zinc loss (*tzl)* from these coating is shown in figure 7.4. The average *tzl* from sample Al4.7 is 277μg compared with 363μg from the Al8.6 sample. This is consistent with the higher current density values observed from the iso-current plots. It would therefore appear that the corrosion performance of the coating with a small increase in Al gets worse. However further investigations in this field are required.

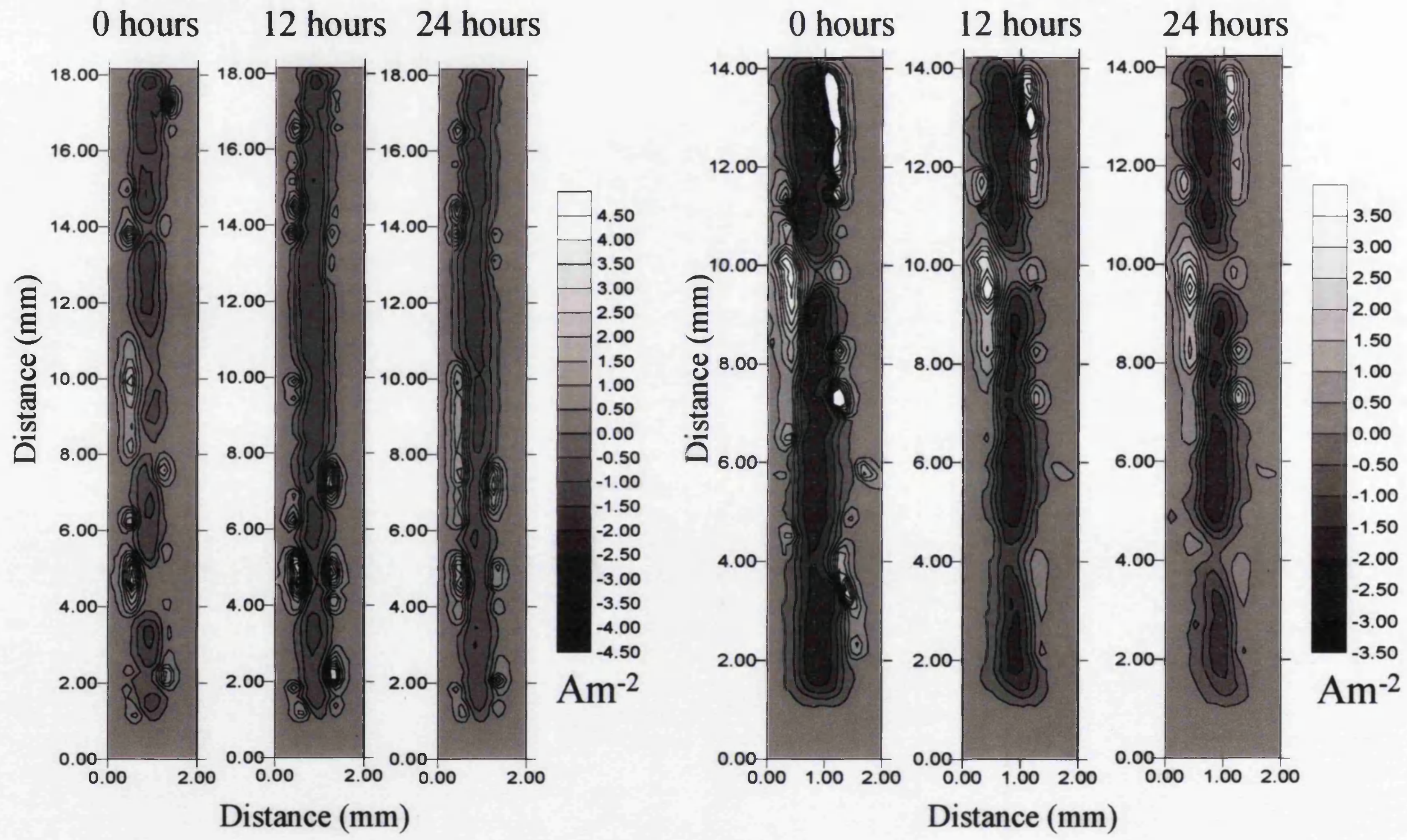

Figure 7.3 – Representative current density maps for samples Al8.6 (l) and Al4.7(r)

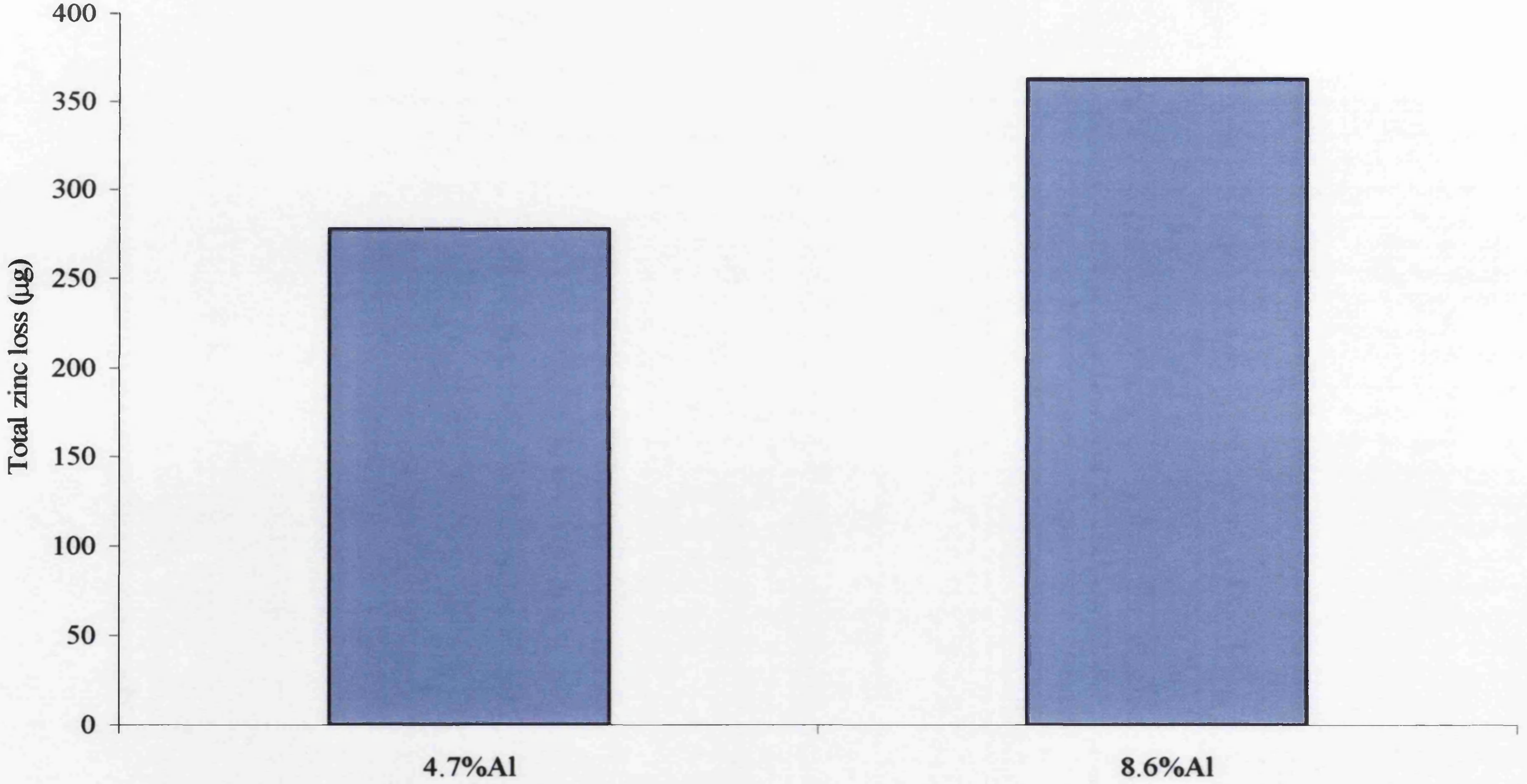

Figure 7.4 – Initial tzl from samples Al4.7 and Al8.6

DECLARATION

Declaration: This work has not previously been accepted in substance for any degree and is not being concurrently submitted in candidature for any degree.

Signed: Date:

Statement: This thesis is the result of my own investigations, except where otherwise stated. Other sources are acknowledged by footnotes giving explicit references.

Signed: Date:

Statement: I hereby give consent for my thesis, if accepted, to be available for photocopying and interlibrary loan and for the title and summary to be made available to outside organisations.

Signed: Date: